Ultrafast Laser Microwelding of Glass-to-Glass and Glass-to-Opaque Materials

Jianyong Chen

A dissertation submitted for the degree of Doctor of Philosophy

Heriot-Watt University

School of Engineering and Physical Sciences

November 2016

Abstract

Techniques for joining materials, especially glass to dissimilar materials, while maintaining their surface and optical properties are essential for a wide range of industrial applications. Current techniques rely on adhesives or interlayers which can exhibit issues with creep, out-gassing or aging. Ultrafast laser welding based on nonlinear absorption in transparent material offers an attractive solution to this problem. Bringing two material surfaces into close (optical) contact and focusing the ultrafast laser onto the interface allows for localised melting and rapid resolidification, forming strong bond and welding the two surfaces together. The highly localised nature of this absorption means that welds can be created whilst avoiding significant heating of the surrounding material — important for joining materials with significantly different thermal expansion coefficients.

Using a picosecond laser system (Trumpf TruMicro), a range of welds between similar material (borosilicate glass to borosilicate glass, fused silica to fused silica, borosilicate glass to fused silica) and highly dissimilar materials (sapphire to stainless steel, fused silica/borosilicate glass to silicon/aluminium/copper/stainless steel) have been demonstrated. Theoretical simulations were carried out to investigate the aberrations that occur to a laser beam focused inside material and to describe the behaviour of the generated plasma. With the guidance of theoretical work and developed experiment setup, a large range of parameters related to welding were investigated both in bulk material and welding for different materials and surface conditions. Shear strength tests on welds shows a maximum value could be obtained between parameters resulting in barely welded seams, for low power, and obvious cracking, for higher power. Optimised welding for borosilicate to borosilicate glass creates stronger bonds (108.8 N/mm^2) than traditional joining methods (adhesive, typically 15~25 N/mm^2). Parameter maps were made for different surface separation and surface conditions to determine a successful weld. In order to weld highly dissimilar materials, different welding patterns were designed to relax residual stress and eliminate cracks. Welding with galvo-scanner was also introduced as an alternative method for industrial applications which provides a high scan speed and flexible patterns. To increase welding strength and expand the parameter tolerance for a successful welding, focus vibration methods were proposed to reduce the residual stress. Finally, welding of example industrial parts was demonstrated for different application requirements.

Acknowledgements

I have been fortunate to carry out my PhD in the AOP group at Heriot-Watt University, to have high power laser applications as my career, to be surrounded by and to work with great people, whom I would like to give great thanks in this page.

Professor Duncan Hand was a wonderful supervisor and colleague. From the day I was introduced to the AOP group 3.5 years ago, his broad knowledge and invaluable expertise has helped me a lot for in my work and career. My second supervisor Dr Robert Thompson has always provided good ideas and gave me lots of fantastic suggestions for my research. Dr Richard Carter worked with me all through my PhD, his passion for work and attitude to science always inspired me and set a good example for my research. For this PhD project, we four had hundreds of meetings together, which will prove a benefit in my professional and non-professional activities for the rest of my life.

Special thanks to my industrial collaborator, Renishaw plc, for funding and technical support for this PhD project; particularly Nick Weston, and Marcus Ardron. Monthly meeting with them have helped a lot in this project, their fresh ideas and industrial viewpoint ensured that this project has been productive and eye-opening.

I would also like to thank to Mr Neil Ross for cutting and etching glass for this project. He did a really good job even while moving his clean room, without his input, this project would not have progressed quickly as it did. Also thanks to Mr Adam Lancaster to work with me on the femtosecond laser parameter investigations, I learnt a lot from Adam and their lab during that time.

When I first came to UK four years ago, far away from home, without fluent English, the friendly environment in the AOP group quickly drove my loneliness away. Many thanks to all the AOP group members for their kind help and useful discussions, I had great pleasure in work with them, they have been always willing to pause and discuss a vexing issue or interesting problem, in science or life in general.

Finally, thanks to my parents and my pregnant wife for the endless support throughout these many years of my study.

ACADEMIC REGISTRY

Research Thesis Submission

Name*:*	Jianyong Chen		
School/PGI:	School of Engineering and Physical Sciences		
Version: *(i.e. First, Resubmission, Final)*		Degree Sought (Award **and** Subject area)	Doctor of Philosophy in Physics

Declaration

In accordance with the appropriate regulations I hereby submit my thesis and I declare that:

1) the thesis embodies the results of my own work and has been composed by myself
2) where appropriate, I have made acknowledgement of the work of others and have made reference to work carried out in collaboration with other persons
3) the thesis is the correct version of the thesis for submission and is the same version as any electronic versions submitted*.
4) my thesis for the award referred to, deposited in the Heriot-Watt University Library, should be made available for loan or photocopying and be available via the Institutional Repository, subject to such conditions as the Librarian may require
5) I understand that as a student of the University I am required to abide by the Regulations of the University and to conform to its discipline.

* *Please note that it is the responsibility of the candidate to ensure that the correct version of the thesis is submitted.*

Signature of Candidate*:*		Date:	

Submission

Submitted By *(name in capitals):*	JIANYONG CHEN
Signature of Individual Submitting:	
Date Submitted:	

For Completion in the Student Service Centre (SSC)

Received in the SSC by *(name in capitals):*

Method of Submission
(Handed in to SSC; posted through internal/external mail):

E-thesis Submitted (mandatory for final theses)

Signature: Date:

Table of Contents

List of Symbols & Abbreviations

3D	Three Dimensional
Alicona Infinite Focus	Surface Measurement Product from the Alicona Company
AOP	Applied Optics Group in Heriot Watt University
BK7	Borosilicate Glass (Crown glass) from Schott
BOROFLOAT®33	Borosilicate Glass from Schott
CCD	Charge Coupled Device
fs	Femtosecond
FWHM	Full Width at Half Maximum
HAZ	Heat Affected Zone
Instron 3367	Stress Measurement Machine from Illinois Tool Works Inc
IR	Infrared
LBW	Laser Beam Welding
LIPSS	Laser Induced Periodic Surface Structures
MEMS	Micro Electro Mechanical Systems
MPI	Multiphoton Ionisation
NA	Numerical Aperture
ND filter	Neutral Density Filter
OC	Optical Contact
P240, P600, P1200, P4000	ISO Grit Designation for Sandpaper
ps	Picosecond
Ra	Profile Roughness Arithmetic Average
SEM	Scanning Electron Microscope
SS	Stainless Steel
TAG lens	Tunable Acoustic Gradient Index of Refraction Lens
ULE	Ultralow Expansion
UV	Ultra Violet

List of Publications

Journal Publications:

J. Chen, R. M. Carter, R. R. Thomson, and D. P. Hand, "Avoiding the requirement for pre-existing optical contact during picosecond laser glass-to-glass welding" Opt. Express, vol. 23, no. 14, p. 18645, 2015.

R. M. Carter, **J. Chen**, J. D. Shephard, R. R. Thomson, and D. P. Hand, "Picosecond laser welding of similar and dissimilar materials" Appl. Opt., vol. 53, no. 19, pp. 4233–4238, 2014.

Publication in Preparation:

J. Chen, R. M. Carter, R. R. Thomson, and D. P. Hand, "Scanning strategies of ultrafast laser Welding of dissimilar materials" in preparation

Conference Contributions:

J. Chen, R. M. Carter, R. R. Thomson, and D. P. Hand, "Surface Separation Investigation of Ultrafast Pulsed Laser Welding", Photonics West, Laser Source Technologies and Industrial Lasers and Applications Conference (LASE16), 2016, San Francisco, USA.

J. Chen, R. M. Carter, R. R. Thomson, and D. P. Hand, "Ultrashort Pulsed Welding", EPSRC Centre for Innovative Manufacturing (EPSRC-CIM), 2015, Edinburgh, UK.

J. Chen, R. M. Carter, R. R. Thomson, and D. P. Hand, "Welding of highly dissimilar materials using ultrashort (few picoseconds) laser pulses" Industrial Laser Applications Symposium (ILAS), 2015, Coventry, UK

J. Chen, R. M. Carter, R. R. Thomson, and D. P. Hand, "Ultrafast laser localised welding of similar and dissimilar materials", photon14, 2014, London, UK.

By uniting we stand, by dividing we fall

― John Dickinson (1732-1808)

Chapter 1 Introduction

An important property of light is that it has no volume and photons have no electronic charge, so when they are concentrated into a very small space, they do not collide with each other like negative charged electrons. This is an important property especially for ultrafast machining [1]. Important applications of glass in optics, MEMS, mechanical, electrical, and the biomedical field require the bonding of glass to glass or glass to silicon or metal [2][3][4][5]. However, stable joining techniques still remain a technological challenge, and glass joining relies on techniques using adhesive agents (like glues) or an interlayer, which may cause poor mechanical, thermal or chemical durability [6][7][8]. Traditional laser fusion welding is considered to be one of the best techniques for melt joining of many kinds of materials, since joining is accomplished without an intermediate layer or mechanical contact [9]. Yet it has not been accepted for glass welding in production, because it relies on linear absorption and a large volume of material is melted, this usually causes changes to the properties of the original materials [2][10].

1.1 Aims and Objectives

There are unique advantages in ultrafast laser micromachining of transparent materials over other optical device fabrication techniques. Firstly the nonlinear nature of the absorption confines any induced changes to the focal volume. This spatial confinement combined with laser-beam scanning or sample translation, makes it possible to micromachine geometrically complex structures in three dimensions. Secondly, the absorption process is independent of the material, enabling optical devices to be fabricated in compound substrates of different materials. Thirdly, ultrafast laser micromachining can be used for fabricating optical parts separately and bonding those optical parts together with interconnections to a single transparent substrate [11].

Due to its very high peak power, when ultrafast laser pulses are focused on the surface of or inside bulk transparent materials, a sufficiently high intensity in the focal volume induces nonlinear absorption which causes localized melting and rapid resolidification of the material. This technique has been widely applied to the fabrication of photonic devices on the surface or inside the bulk of transparent materials. Development of techniques for joining materials, especially glass to glass or glass to dissimilar materials (metal, sapphire, silicon, ceramic etc.), while maintaining the surface and optical

properties are essential for many modern industrial products. Due to the localized properties of nonlinear absorption, localized bonds can be created between the two materials while minimising the residual thermo-mechanical stresses in the joint volume.

This PhD aims to develop an ultrafast laser (ps laser) welding process as an industrially relevant technique for laser manufacturing of high value components or parts. The work uses a picosecond laser (Trumpf TruMicro 5x50) in the Applied Optics and Photonics group (AOP) at Heriot-Watt University to investigate the basic understanding of ultrafast laser interactions with transparent materials, and welding samples or industrial parts of different materials and/or geometries with the investigated welding parameters. This programme investigates ultrafast laser welding of transparent material to transparent material as well as transparent material to metals or silicon. Potential problems such as sample surface treatment and residual thermo-mechanical stresses are investigated and different welding methods developed for a variety of component conditions.

1.2 Thesis Outline

This thesis is organized based on the sequence of study on a scientific problem: introduction and literature review (Chapter 1), theoretical preparation (Chapter 2), experimental setup and sample preparation (Chapter 3), experiment parameter test and welding measurements (Chapter 4), welding limitation determination (Chapter 5), welding pattern considerations (Chapter 6), ultrafast laser welding applications (Chapter 7), and last conclusions and future work (Chapter 8).

Chapter 1: An introduction to this project and a brief literature review of the history of ultrafast laser machining, techniques of material joining and the development of ultrafast laser welding.

Chapter 2: Theoretical background is reviewed and deduced for ultrafast laser machining inside bulk material. Linear and nonlinear propagation inside material is discussed, along with energy transportation and a comparison of short and long pulses is presented.

Chapter 3: An ultrafast laser welding setup for our experiments is introduced and the differences from traditional laser welding are discussed. The different materials and surface conditions (with different preparation methods) before and after welding are introduced and discussed. Finally the welding process is discussed in detail.

Chapter 4: Test and measurement of the ultrafast laser welding parameters required for a successful weld are presented. The welding requirements of laser absorption, pulsed laser energy, material properties and sample surface conditions for a successful weld are first discussed. Secondly a laser absorption model is proposed based on laser parameter tests and morphology analysis of weld seams. Thirdly strength tests are carried out to statistically determine the weld strength characteristics with different welding parameters and scanning patterns. Finally fluorescence testing of different/similar materials welds is presented to determine material exchange and compound formation inside weld seams.

Chapter 5: Weld limits are investigated for given specific sample conditions. Surface defects, interface stress and its influence on the welding process are discussed and experimentally observed. Two methods, cylindrical lens and etched grooves are introduced which provide controlled gaps to investigate the capability for ultrafast laser welding to weld with significant surface separation.

Chapter 6: Residual stresses introduced at the weld area due to thermal process are investigated and discussed. Several methods to relax stress and eliminate cracks are evaluated, which include: decreasing laser power and increasing seam spacing; dual power welding; scan sequence adjustment; and discrete welding (or spot welding). Two methods to generate discrete welding patterns are discussed and demonstrated. To generate different welding patterns and get better welding results, welding with galvo-scanner and focus vibration are also introduced and discussed.

Chapter 7: Ultrafast laser welding of industrial parts for a number of application requirements are demonstrated, including welding a large area; hermetic bonding; welding through a thin or thick piece of glass; and non-perpendicular incidence welding.

Chapter 8: The conclusions and main findings of this thesis and outlook are presented.

1.3 Literature Review

1.3.1 Ultrafast Laser Machining

The evolution of the ultrafast laser has spawned many new fields of scientific investigation. Most of this research relies on three unique features of ultrafast laser pulses. First, a short pulse can be used to measure a very fast process. Such diverse phenomena as electron-phonon scattering, phonon vibration and chemical bond

breaking can all be directly time-resolved with femtosecond laser pulses. Second, a short pulse can create extreme non-equilibrium conditions. For example, because lattice ionic cores respond much more slowly than electrons do, an ultrafast pulse can excite electrons to a very high temperature while the ion core temperature is still low. Finally, an ultrashort pulse can provide extremely high laser intensity, usually working with high-NA lens. Electric field strengths that exceed the electric field binding valence electrons to their core atoms are easily produced with an ultrafast laser system leading to nonlinear absorption. For nonlinear absorption to occur, the electric field strength in the laser pulse must be approximately equal to the electric field that binds the valence electrons in atoms—of the order of 10^9 V/m, corresponding to a laser intensity of $5\times10^{20}\ W/m^2$ [12].

Ultrafast laser machining of transparent materials focuses on the last situation. Usually when light propagates through a transparent material, nothing happens to either the material or the light. With high intensity pulses, however, both the material and the light can be dramatically changed by the interaction [13][14]. Despite significant study much still remains to be learned about the fundamental mechanisms that govern the interaction of ultrafast laser pulses with transparent materials. Applications have been greatly developed since ultrafast laser micromachining was firstly demonstrated in 1994, when a femtosecond laser was used to ablate micrometre-sized feature on silica and silver surfaces [15][16].

During the past two decades, ultrafast lasers have been widely adopted for high resolution and high accuracy micromachining purposes including both high precision surface micromachining and 3D internal structuring [17][18][19][20][21]. Due to the ultrashort timescale and the ultrahigh laser intensity with high numerical aperture (NA) lenses, nonlinear absorption induced at the focus leads to highly localised material ablation or modification, this assures high precision clean processing [20][22][23][24][25]. A lot of effort has been expended to discover feasible applications and machining mechanisms [26][27][28][29][30].

1.3.1.1 Pulse Duration

"Ultrafast" is not a strict term. It usually refers to laser systems with pulse durations ranging from several fs to tens of ps [31]. Three regimes of material modifications are accessed depending on whether the pulse duration is shorter, comparable or longer than the time required by the hot electrons to transfer their energy to the lattice via electron-

phonon scattering [32]. For a pulse duration $\tau \gg \tau_{e-ph}$ (τ_{e-ph} is the electron-phonon coupling time; for the case of silica glass, it is around 1 ps), electrons and lattice reach thermodynamic equilibrium on the time scale of the pulse duration. Damage, preferentially by phase explosions, occurs when the rate of energy extraction from the focal volume is smaller than the energy deposition rate. For this reason nanosecond pulses are the most suitable for applications requiring material removal such as laser deep drilling and cutting [33].

Conversely, femtosecond laser pulses, for which $\tau \ll \tau_{e-ph}$ leads to strong non-equilibrium conditions as electrons in the conduction band are heated much faster than they can cool by phonon scattering. The energy is transferred to the lattice after the pulse has passed on a time scale much shorter than the heat diffusion time, producing a permanent modification in the material with essentially no collateral damage. In silica glass, the low collateral damage associated with the processing by femtosecond pulses is proving invaluable for optical waveguide inscriptions; for 3D-precision machining; and for the generating of birefringent optical elements [20][22][25][30].

A theoretical framework for pulse durations $\tau \cong \tau_{e-ph}$ is not available due to the intrinsic complexity. It is known, however, that in the 1~20 ps pulse range, the fluence damage threshold departs from the thermally driven $\sqrt{\tau}$ dependence associated with longer pulses, which indicates that the Joule heating of the electrons excited at the beginning of the pulse is responsible for the optical damage [32][34]. During single pulse bulk modification of silica glass, Burakov *et al.* showed that a long exposure time was correlated to material expansion leading to a negative refractive index change in the irradiated zones [35]. The generation of pressure waves—resulting in stress accumulation and positive index change in the region surrounding the focal volume — occurs as a consequence of the material expansion [36].

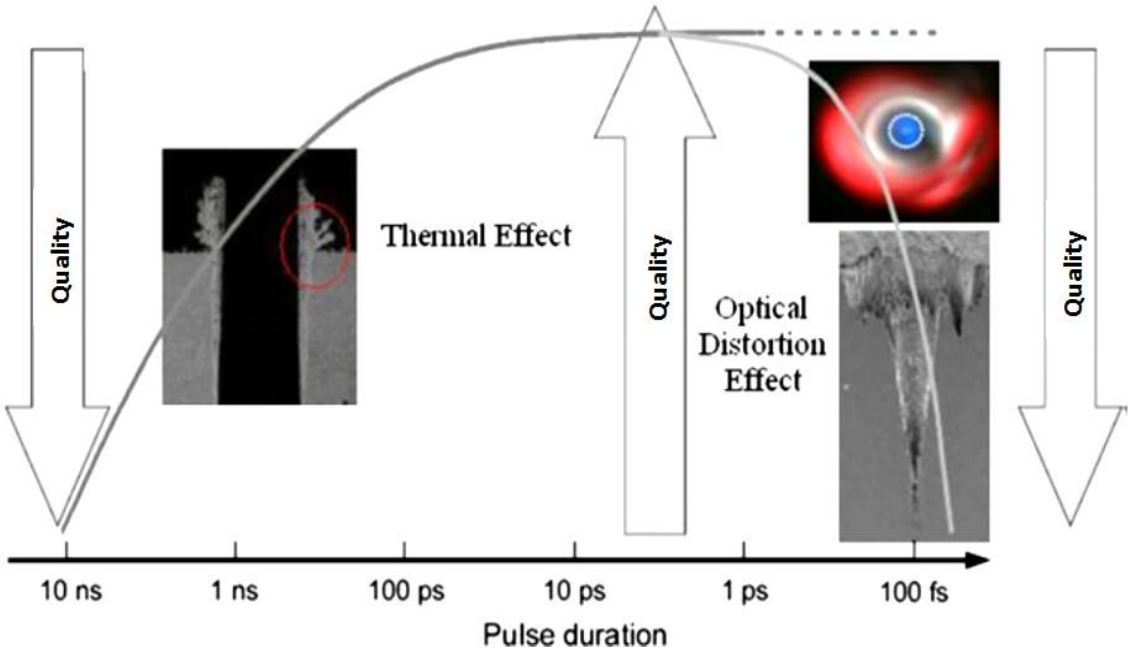

Fig 1.1 Schematic illustration of the machining quality dependence of pulse duration in machining of metals [22] with a pulse duration ≧200 ps, thermal effects seriously affects the laser micromachining quality while optical distortion may also result in bad ablation morphology with laser pulse durations down to ~100 fs.

Fig 1.1 gives an overview of micromachining quality dependence on laser pulse duration and suggests $1\,ps \leq \tau \leq 10\,ps$ favours high machining quality. With laser pulse duration reducing from ns down to fs, thermal effects become less apparent while optical distortion effects become more apparent. On one hand, the melting and recast layer will shrink with pulse duration but cannot reach zero even at pulse durations down to the fs regime. On the other hand, due to the ultrahigh laser intensity, a strong deformation of the laser light can occur near the focal plane (shown in Fig 1.1, the top right image for detail). This is caused by self-focusing and its interaction with the ambient air, which may seriously affect the machining accuracy [22].

1.3.1.2 Machining in Bulk Transparent Materials

Owing to their high purity and large transparency window, glasses and crystals are commonly used as base materials. Ultrafast laser micromachining has been used to fabricate photonic devices using a variety of transparent substrates, including glasses, crystals and polymers. A wide variety of femtosecond-laser micromachined devices, have been demonstrated using glasses and crystals, including waveguides, diffractive elements, active devices, microfluidic devices and rapid prototyping.

1.3.1.2.1 Optical Waveguide

Waveguide fabrication was one of the first demonstrations of the potential of ultrafast laser micromachining for photonic applications [37][38]. Femtosecond laser micromachined waveguides can serve as interconnects in a variety of host glasses and have opened up the possibility of three dimensional layering of waveguides. The pulse energy required for fabricating devices can be as low as a few nanojoules [39][40].

The spatial profile of the refractive index of waveguides is strongly dependent on material and processing conditions (close to that of a fibre for fused silica substrates) [39][41][42]. The transmission losses are of the order of 0.5~1.0 dB/cm for a wide variety of material and processing conditions [43][44][45][46]. Optical connected waveguides have already been fabricated in bonded doped and undoped phosphate glass, and also through multiple pieces of glass separated by air gaps [47][48].

1.3.1.2.2 Filters and Resonators

In principle, devices fabricated with planar lithographic techniques can be fabricated with ultrafast laser micromachining. Indeed, couplers, filters and interleavers have already been demonstrated [39][41][47][49]. The three-dimensional freedom permits the fabrication of vertical resonators, and vertical or lateral splitters [47][50][51]. Femtosecond laser micromachining of fibre Bragg grating filters in bulk material was first demonstrated using multiple exposures [52], recently 90% efficiency Bragg gratings have been fabricated in fused silica [53]. The long-term stability of the laser-induced index change makes femtosecond laser micromachining attractive for fabrication of both long-period fibre gratings [54][55] and Bragg gratings [56][57]. Recently, femtosecond laser 3D direct writing found important applications in quantum circuits to replace the bulk optics in complex quantum optical system [58][59]. Crespi et al. have constructed a multimode interferometer realising an arbitrary 5×5 mode transformation with femtosecond laser writing for photonic boson sampling [59], as shown in Fig 1.2.

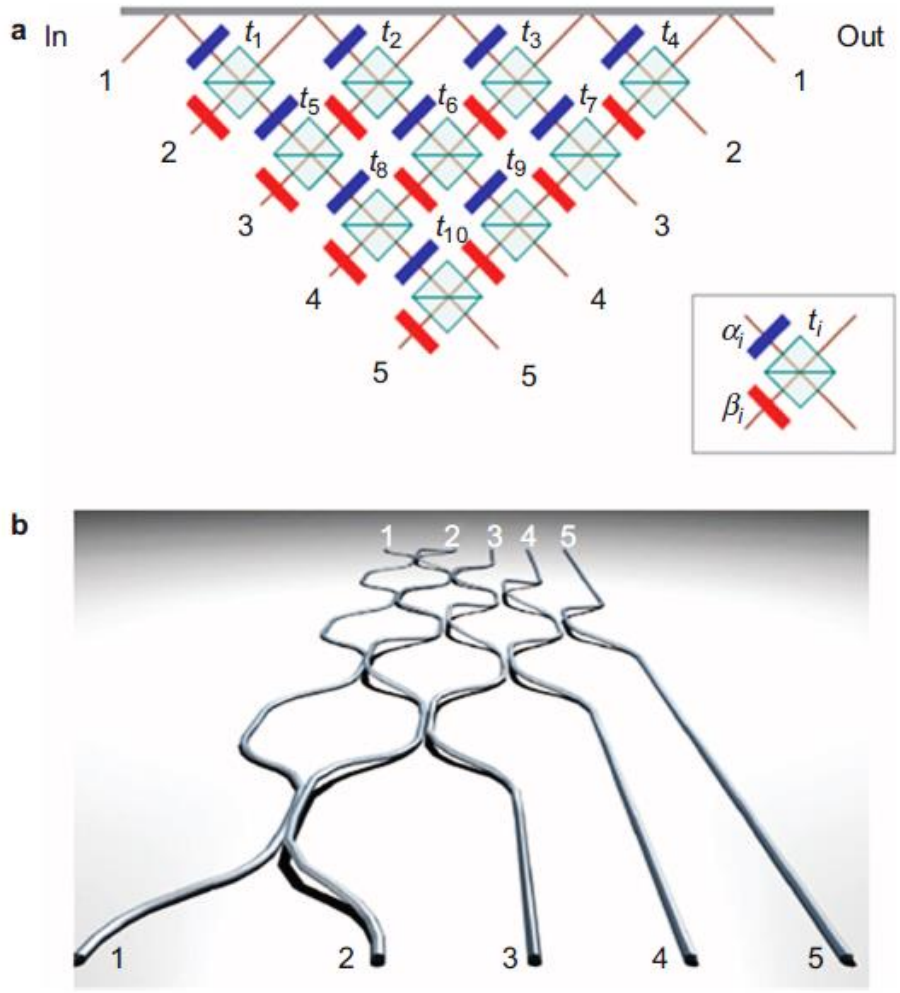

Fig 1.2 (a). Layout of a multimode interferometer for realisation of an arbitrary 5×5 mode transformation using a network of beam splitters with different transmissivities. (b). The same interferometer realised in a glass substrate using a laser writing technique [59][60].

1.3.1.2.3 Microfluidic Structures

Ultrafast lasers can also be used to fabricate microfluidic structures in glass materials by spatially selective precision modification inside glass materials through nonlinear optical absorption. Currently, there are two main strategies for this application. The first strategy employs femtosecond laser modification inside glass or crystal materials followed by wet chemical etching [61][62]. The other strategy is to perform femtosecond laser 3D drilling from the rear surface of the glass in contact with distilled water (the water introduced into the microchannel can help to remove the ablated debris) [63][64]. The former approach has advantages that include larger scale microfluidic structures and improved smoothness on inner walls, whereas the latter approach allows for the fabrication of 3D microchannels in an almost limitless variety of materials with

smaller channel diameters. In particular, microfluidic channels with arbitrary lengths have recently been produced in porous glass immersed in water using water-assisted femtosecond laser drilling [65]. This approach has also enabled the fabrication of 40 mm long nanofluidic channels with widths of 40 nm [66][67], while this is impossible to be realised by longer laser pulses, as shown in Fig 1.3.

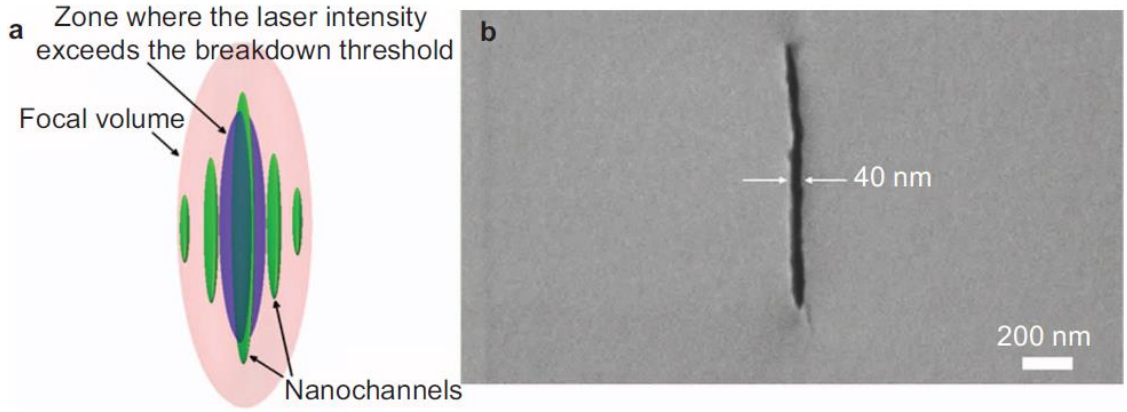

Fig 1.3 (a). Schematic diagram of the concept employed to realise the formation of a narrow channel width far beyond the optical diffraction limit. (b). Cross-sectional SEM micrograph of a nanochannel fabricated in porous glass [67].

1.3.1.3 Surface Processing

1.3.1.3.1 Microdrilling and Cutting

Ultrafast lasers suppress thermal diffusion and thus reduce HAZ formation, even in high thermal conductivity materials such as metals. Fig 1.4a and Fig 1.4b show scanning electron microscopy (SEM) images of holes drilled in 100 μm thick steel foils by ablation using laser pulses with widths of 200 fs and 3.3 ns, respectively [68]. The femtosecond laser produces an ablated hole with a sharp edge and a steep wall with little formation of HAZ. In contrast, nanosecond laser ablation produces significant swelling around the ablated hole due to melting.

Ultrafast lasers can perform high quality micromachining of even brittle materials such as glass. Fig 1.4c and Fig 1.4d show SEM images of a micromachined surface and glass cut by femtosecond laser. Both images reveal that clean ablation with sharp edges was achieved without the formation of cracks.

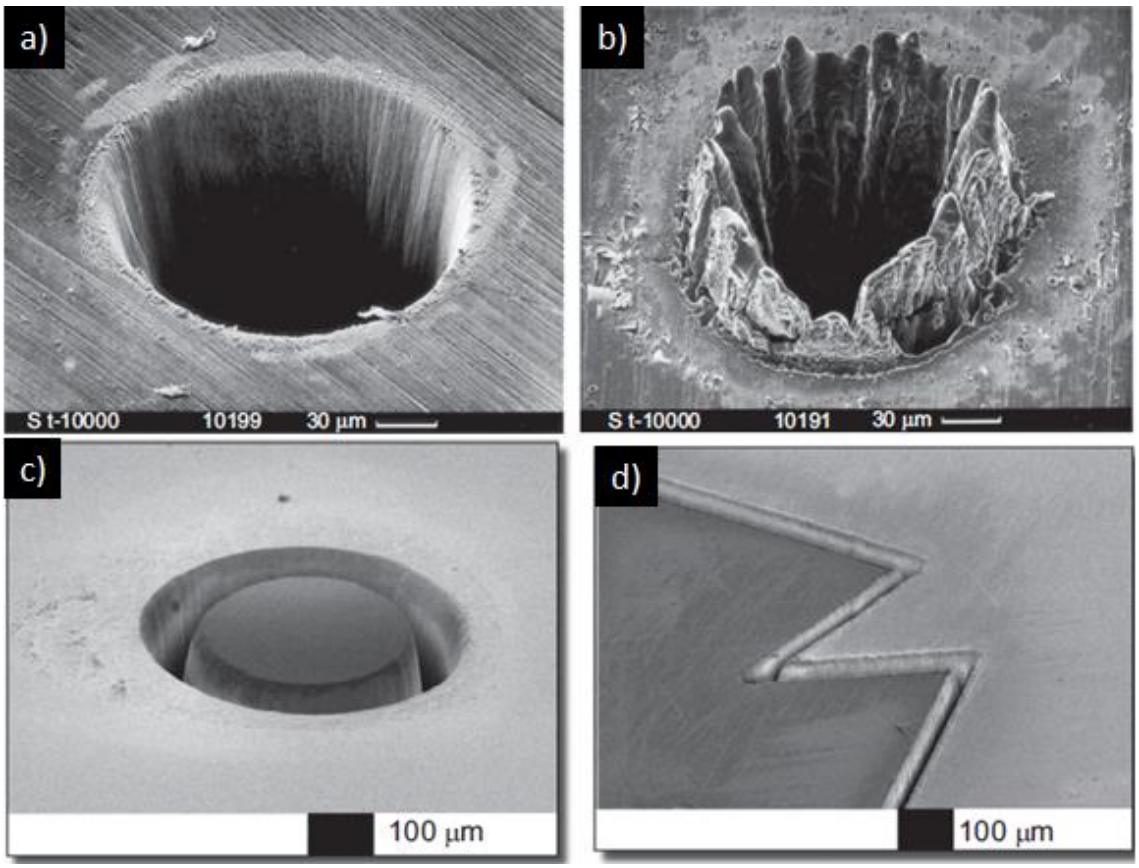

Fig 1.4 Holes drilled in 100 µm thick steel foils by ablation using laser pulses with the following parameters: (a). Pulse width: 200 fs, pulse energy: 120 µJ, fluence: 0.5 J/cm^2, wavelength: 780 nm; (b). Pulse width: 3.3 ns, pulse energy: 1 mJ, fluence: 4.2 J/cm^2, wavelength: 780 nm [68]. (c). SEM images of a micromachined glass surface and (d). A glass material cut by femtosecond laser ablation [60].

1.3.1.3.2 Surface Structuring

Femtosecond direct laser machining can create structures on the nanometre scale. Nanostructures can appear alone or they can be associated with microstructures, also they can be random nanostructures or periodic nanostructures.

Random structures: Nanostructured surfaces consist of one or more of the following entities: nanopores, nanoholes, nanocavities, nanoprotrusions, nanobumps, and nanorims. Nanopores and spherical nanoprotrusions on Ti, Au, Cu, and Pt were observed near the ablation threshold and at a very low number of pulses [69][70]. Vorobyev et al. noticed that nanostructuring on copper, at the centre of the beam spot, is possible below a fluence of 1.5 J/cm^2 [69]. Stratakis et al. obtained nanobumps on Al with a periodicity of 200–300 nm by fs laser machining (180 fs, 800 nm) in both ethanol and water, whereas Al machined in air showed irregular nanoentities of 100 nm in size

[71]. Coloured metals can be fabricated by producing nanostructures on the surface. Such structural colours can be attributed to the specific nanostructures formed on the metals that induce higher plasmonic absorbance at certain wavelengths [71]. A range of different mechanisms have been proposed to explain the formation of laser-induced nanostructures, such as hydrodynamic processes that originate from localized nanoscale melt, bubble cavitation, and nanoparticle redeposition [72][73][74].

Periodic nanostructures: Laser-induced periodic surface structures (LIPSS), also termed ripples or nano-ripples, were first observed in 1965 [75]. LIPSS are periodic nanostructures constituted of alternate crests and troughs. which are formed by ultrafast laser irradiation with a fluence near the ablation threshold with linearly polarized nanosecond or longer laser pulses [76].

LIPSS produced by long-pulsed lasers have smooth features, whereas LIPSS densely covered with nanostructures are reported for fs pulses [77]. The low-spatial-frequency LIPSS (LSFL) have a periodicity close to the laser wavelength. LSFL are perpendicular to the polarization of the incident laser beam. High-spatial-frequency LIPSS (HSFL) have a periodicity much smaller than the laser wavelength and the orientation can be parallel or perpendicular to the beam polarization [78]. Fig 1.5 shows both types of LIPSS on Ti.

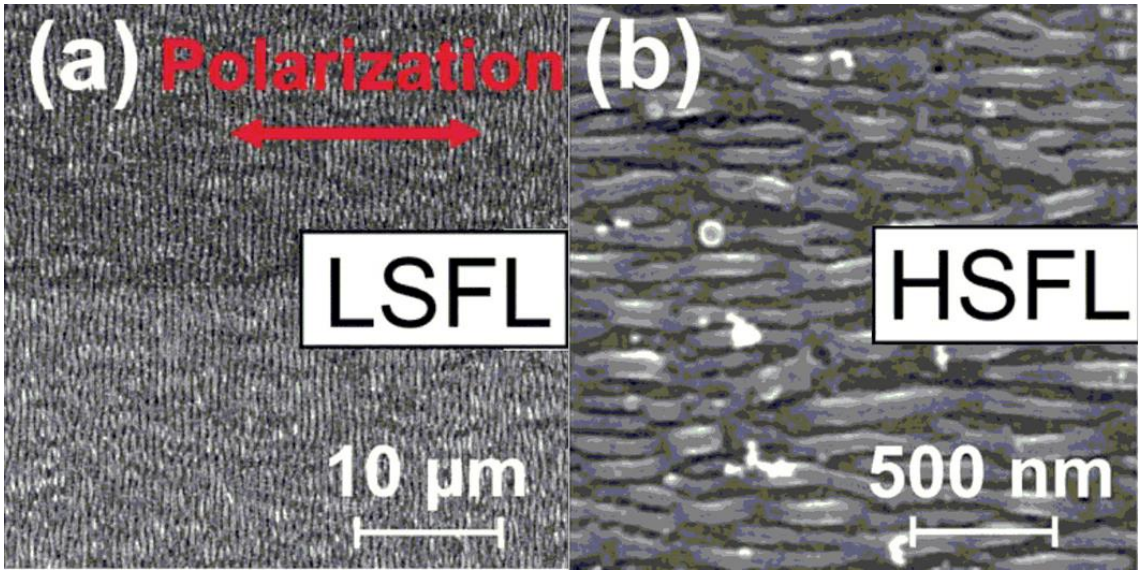

Fig 1.5 SEM images of (a). Low-spatial-frequency LIPSS (LSFL) and (b). High-spatial frequency LIPSS (HSFL) on Ti irradiated with 790 nm fs laser [78]. The double-sided arrow indicates the polarization of the laser beam.

For low spatial frequency LIPPS, the structures are understood to be formed by interference of the incident laser with the reflected (scattered) light. Consequently, ripples are generally oriented perpendicular to the incident polarization. The spacing of the fabricated structure is given by $\lambda/n\,(1 \pm sin\theta)$, where λ is the laser wavelength, θ is the laser incident angle and n is the refractive index of the material [79]. Therefore, the spacing is always in the order of the wavelength or greater. In contrast, periodic grating structures formed by femtosecond lasers have a spacing much smaller than the laser wavelength (typically 1/10–1/5 of λ) [80]. Various mechanisms, including the self-organization of surface instability [81], second-harmonic generation [82], refractive index change [83], nanoplasma formation [84] and the excitation of surface plasmon polaritons [85] have been proposed for the formation of nanoripples.

Another interesting and useful texture formed by ultrafast laser irradiation is regular arrays of conical microstructures, which can be produced on *Si* by irradiation with hundreds of femtosecond laser pulses in a halogen atmosphere (e.g., SF_6 or Cl_2), as shown in Fig 1.6 [86].

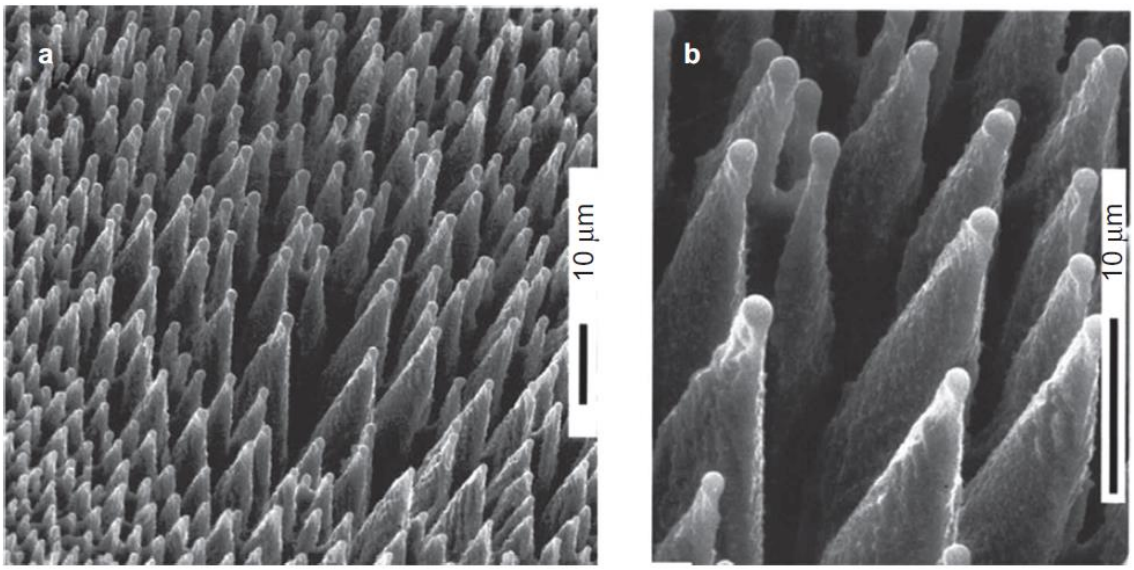

Fig 1.6 (a). Array of sharp conical spikes produced on Si by irradiation with 500 fs laser pulses in SF_6, (b). Magnified image of (a) [86].

1.3.2 Traditional Bonding Techniques

Bonding is carried out for a variety of technical reasons, mechanical attachment, thermal contact, electrical contact, gas or liquid seal and any or all combinations thereof. The choice of bonding method depend on the intrinsic properties of the bonding

materials (i.e. hermetic, electrical conductance, thermal conductance, thermal coefficient of expansion, adhesive bond strength related to the intrinsic fillers, mechanical properties, and their adhesive and cohesive strength).

1.3.2.1 Mechanical Attachment

Mechanical attachment is commonly used. For example, camera lenses are usually fixed with mechanical mounting (clamp). Optical contact (OC) is another type of mechanical bonding method—when surfaces or molecules are close enough, the intermolecular force (Van der Waals forces, hydrogen bonds, and dipole-dipole interaction) will keep the two surfaces together. But optical contact bonding is typically not sufficiently strong to hold two apparently conformal rigid bodies together, since the forces drop off rapidly with distance (in the order of $1/distance^2$) , and the actual area in contact between the two bodies is small due to surface roughness and minor imperfections [87].

1.3.2.2 Adhesive Bonding

Adhesive bonding (also referred to as gluing) describes a wafer bonding technique with an intermediate layer connecting substrates of different materials. Adhesive bonding has the advantages of less stringent requirements on the quality of the bond interfaces, a greater choice of substrate materials, considerably lower bonding temperatures and no electric fields are required for successful bonds. The elastic properties and, often, liquid-like behaviour of the intermediate layer during the bonding process results in a low stress within the materials being bonded. The thickness of the intermediate layer can be varied from tens to hundreds of microns, which means it can be used not only as the bonding layer but also as a spacer to form cavity-style packages [88][89].

A wide range of polymers, including methyl methacrylate (PMMA), parylene, SU-8 and benzocyclobutene (BCB), have been applied successfully to full wafer bonding, packaging of micro-fluidics devices, MEMS devices (especially RF-MEMS), and IC and CMOS packaging [90][91][92]. Low melting temperature glass frit or a metallic intermediate layer is also used as adhesive bond by heating the samples and intermediate layers to a temperature below the substrate melting point and above the frit or metallic intermediate layer melting point. Resolidification of the intermediate layer will form strong bond at interface of the substrates [93][94][95].

1.3.2.3 Solder Bonding

Solder bonding is a versatile lower temperature bonding process which is used in joining a range of metals, ceramics, glasses and metals. Solders are joining filler metals that melt below 450 ˚C, and brazing above 450 ˚C. Solder bonding is typically used in the assembly of structures where a good thermal and/or electrical contact is required. Compared to bonding with epoxy adhesives, solder bonding can provide better thermal and electrical conductivities, but requires higher temperatures including direct contact of molten metal to the bonding surfaces [96].

1.3.2.4 Direct Fusion Bonding

The term “direct bonding” implies that these bonding processes do not require any additional intermediate bonding layers. It has been shown that this places a high demand on the surfaces to be bonded with respect to roughness and cleanliness. For industrial applications, techniques include resistance bonding, anodic bonding, ultrasonic welding and friction bonding.

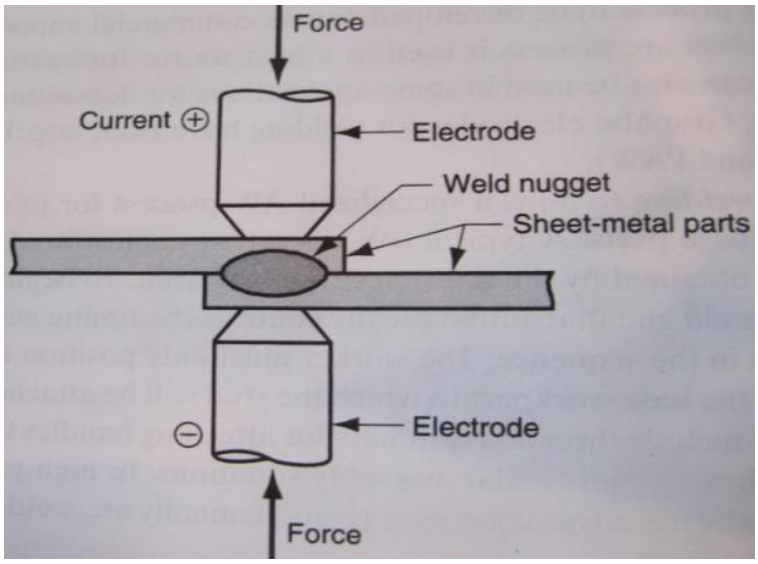

Fig 1.7 Diagram of resistance welding

Resistance welding is a thermo-electric process in which heat is generated at the interface of the parts to be joined by passing an electrical current through the parts for a precisely controlled time and under a controlled pressure. The name “resistance” welding derives from the fact that the resistance of the workpieces and electrodes are used to generate the heat at their interface. Small pools of molten metal are formed at the point of the highest electrical resistance (the connecting or "faying" surfaces) as an electrical current (100–100,000 A) is passed through the metal, Fig 1.7 shows the

diagram of typical resistance welding. In general, resistance welding methods are efficient and cause little pollution, but their applications are limited to relatively thin and conductive materials, and the equipment cost can be high [97][98].

Anodic bonding, which is also referred to as field assisted bonding, was first reported by Wallis and Pomerantz [99] in 1969. Initially developed for sealing of glass to metals, it is currently applied to the bonding of glass to silicon for packaging applications in the production of microsystems and MEMS, e.g. encapsulating of sensors [100][101]. Typically where bonding a silicon wafer to a glass wafer – both polished and particle free – the parts are placed into intimate contact and a typical temperature of around 400 °C to 450 °C and a voltage ranging from 400 V to 1200 V is applied. A strong bond (15-25 MPa) is formed between the two surfaces in an electrochemical reaction.

Ultrasonic welding is an industrial technique whereby high frequency ultrasonic acoustic vibrations are locally applied to workpieces held together under pressure to create a weld. It is accomplished by converting high-frequency electrical energy into high-frequency mechanical motion. The mechanical motion, along with applied force, creates frictional heat at the components' mating surfaces (joint area) and the material will melt forming a molecular bond between the parts. It is commonly used for plastics, and especially for joining dissimilar materials [102][103].

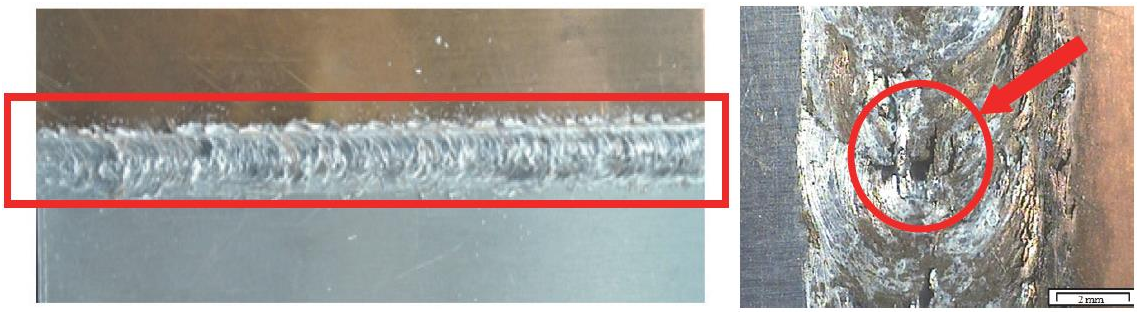

(a) (b)

Fig 1.8 Friction stir welding of aluminium alloy and copper with: (a) welding surfaces and (b) surface void defects [106].

Friction welding is a solid-state joining process that uses a third body tool to join two facing surfaces. Heat is generated between the tool and material which leads to a very soft region near the friction surface. It then mechanically intermixes the two pieces of metal at the joint, with the softened metal joined using mechanical pressure. Technically, because no melt occurs, friction welding is not actually a welding process in the traditional sense, but a forging technique. However, due to the similarities

between these techniques and traditional welding, the term has become common. It is primarily used on aluminium, most often on extruded aluminium (non-heat treatable alloys), and on structures which need superior weld strength without a post weld heat treatment [104][105][106].

1.3.2.5 Laser Welding

Laser welding involves the application of a high power laser beam to fuse and join two solids of similar or dissimilar natures. It is a currently widely used method using a laser as a heat source to join materials. As a comparison to ultrafast laser welding it is discussed here.

The advantages of laser joining over conventional fusion or arc welding processes include high welding speed, small heat affected zone (HAZ), low distortion, ease of automation, single pass joining of thick sections and higher design flexibility with controlled seam size [107]. The special interest in laser joining lies in its capability to fusion join dissimilar materials with different section thicknesses, compositions and/or physical/chemical properties for industrial scale applications particularly in the automotive and aerospace industry [9][108][109].

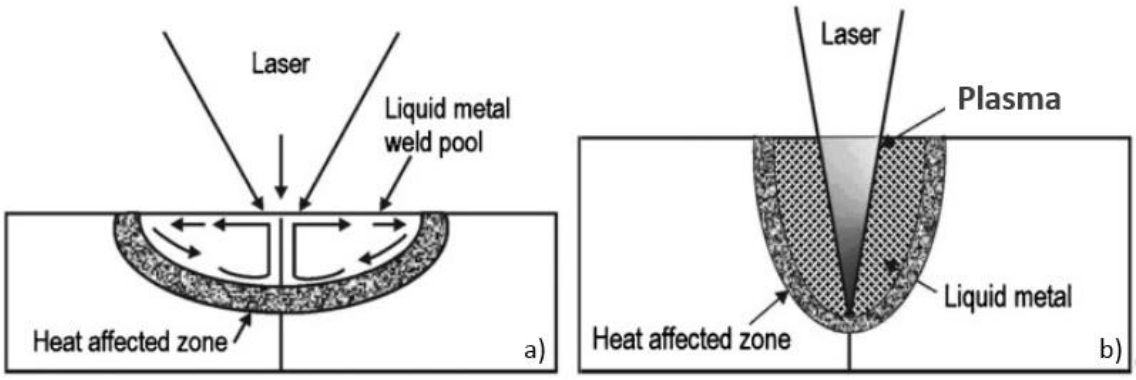

Fig 1.9 Schematic of (a). Conduction melt pool (semi-circular) and (b). Deep penetration (keyhole) fusion zone and weld [9].

There are two fundamental modes of laser welding depending on the beam power/configuration and its focus with respect to the workpiece: (i) conduction welding and (ii) "keyhole" or deep penetration welding (Fig 1.9a and Fig 1.9b). Conduction welding occurs when the power density is insufficient to cause boiling at the given welding speed (i.e. the focus of the beam is above the surface or laser intensity is low). In deep penetration or keyhole welding, the beam focus lies below the surface so that sufficient energy per unit area is available to cause evaporation and formation of a hole

in the melt pool. The “keyhole” behaves like an optical black body in that the radiation enters the hole and is subjected to multiple reflections before being able to escape. The transition from conduction mode to deep penetration mode occurs with increasing laser intensity and duration of laser pulse applied to the workpiece.

There are two main problems in laser welding: lack of penetration or the inverse. These are the boundaries for a good weld for a given power. Welding efficiency can be expressed in terms of the power (or energy) transfer coefficient η, where η is the ratio between the laser power absorbed by the workpiece and the incident laser power. η is usually very small but can approach unity once a keyhole has been established. The melting efficiency or melting ratio ε is given by [110]:

$$\varepsilon = \frac{vdW\Delta H_m}{P} \qquad \text{Eq 1.1}$$

P is the incident laser power, v is the welding speed, d is the sheet thickness, W is the beam width, and ΔH_m is the enthalpy or heat content of the metal at the melting temperature. The maximum values of ε are 0.48 and 0.37 for penetration welds and conduction welds respectively. The quality and properties of the laser weld depend on laser pulse time, power density, laser spot diameter/penetration, traverse speed of the laser beam across the substrate surface, shielding gas, melt area, melting ratio and material properties such as absorptivity, specific heat, density, etc.

It has been found that the arc from a TIG torch mounted close to the laser material interaction point will automatically lock onto the laser generated hot spot. Steen et al. [111] indicated the temperature only has to be around 300 ^{o}C above the surrounding temperature for this to happen. The combination of laser beam with metal inert gas or tungsten inert gas (TIG) arc (so called hybrid technique) seems promising from the viewpoint of bead formation except for occurrences of large blowholes or voids. The process has found new applications for faster welding in tailored blank lines, thicker section welding for shipping and automotive applications [112][113].

A large variety of metals and alloys have been welded with pulsed or CW lasers. The earliest study on deep penetration laser beam welding (LBW) was outlined by Brown and Banas [114], and Schubert et al. [115] gave a brief overview on the potential applications of high power CO_2 and Nd:YAG lasers to create lightweight structures in automotive, aerospace and aeronautic industries.

1.3.3 Development of Ultrafast Laser Welding

In 1.3.2, most of the conventional methods of welding similar or dissimilar materials for industrial applications were introduced, but none of those methods are suitable for directly welding of glass to glass or glass to other materials.

Transparent dielectrics (glass) have several distinctive features. Firstly, they have a wide optical band-gap (it ranges from 2.2–2.4 eV for chalcogenide glasses up to 8.8 eV for sapphire) that ensures transparency in the visible or near infrared spectral range at low light intensity. In order to induce material modification with moderate energy pulses, the laser intensity should be increased to induce a strongly non-linear response from the material and to assure plasma formation. This requires intensities in excess of 10^{14} W/cm^2 where most dielectrics can be ionised early in the laser pulse.

A second feature of dielectrics is their relatively low thermal conductivity characterized by the thermal diffusion coefficient, α, which is typically ~10^{-3} cm^2/s (compared with a few cm^2/s for metals). Therefore micron-size l regions will cool in $t \sim l^2/\alpha$~10 μs. This opens the opportunity for a multipulse effect: the energy deposed by a sequence of several laser pulses focused into the same point in a dielectric will accumulate if the period between the pulses is shorter than the cooling time [36].

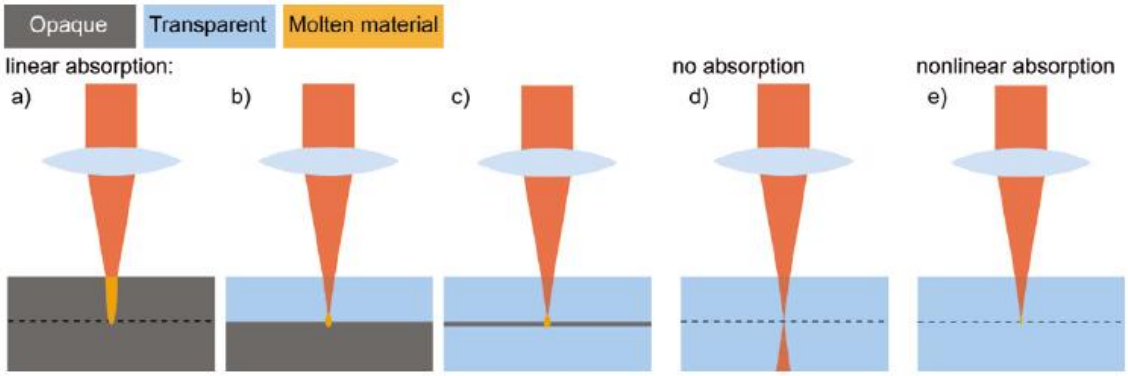

Fig 1.10 Comparison of laser induced melting of different material combinations using linear absorption (a-c) and nonlinear absorption (e). Linear absorption requires an opaque material, nonlinear absorption occurs even in transparent materials at high energy densities [4].

Fig 1.10 shows laser welding of different material combinations. Ultrafast pulses can generate extremely high peak powers with a modest pulse repetition rate and can be used to locally melt the interface of transparent materials [2][8][10]. Longer pulses or CW laser relying on the linear absorption at the interface of opaque material leads to

melting of large volumes of glass plates so that cracks propagate in the molten region due to the thermal stress, this usually causes damage to the original properties of the materials (see Fig 1.10a-c). For the bonding of transparent materials laser absorbed by an opaque intermediate layer may be used [7][116] (Fig 1.10c), however, this technique is not suited for the bonding of two transparent materials without an absorption layer (Fig 1.10d).

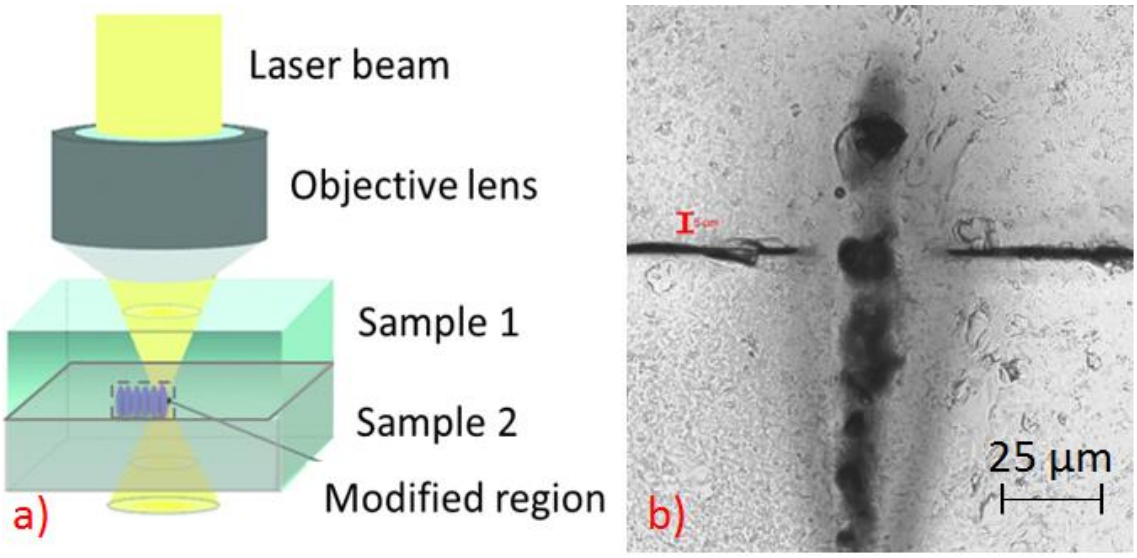

Fig 1.11 (a). Schematic of laser welding of transparent material and transparent material, and (b). A typical weld of fused silica with fused silica. (Pulse energy 18 µJ, pulse duration 6.9 ps of a 400 kHz pulses, with scan speed 2 mm/s of a 2 µm surface separation).

A typical ultrafast laser weld is shown in Fig 1.11. For ultrafast laser bonding to work, the peak intensity of the focused laser beam must be sufficiently high to generate free electrons in the focal volume through nonlinear absorption processes (either multi-photon or tunnelling) [32]. These free electrons then act as seed electrons for single photon absorption (Joule heating), avalanche ionisation, and plasma formation. Ideally, the laser must also exhibit a sufficiently high pulse repetition rate (100's of kHz) for heat to accumulate in the weld region. This heat accumulation results in more efficient energy absorption, through phonon assisted absorption, and increases the physical size of the melt volume, known as the heat affected zone (HAZ). The melt region fills up the original gap between the two surfaces and, by subsequent resolidfication, joins the two materials. The size of the HAZ, and hence the cross-sectional area of the resultant weld, depends on the parameters used, such as sample translation speed, laser power and pulse repetition frequency.

Ultrafast laser welding has great advantages (seen in Chapter 7) compared with traditional welding methods for applications in optics, MEMS, electrical and biomedical fields [4][7][116][117][118][119]. Tamaki et al. [120] in 2005 demonstrated welding between two silica glass plates without a light-absorbent intermediate layer using a low repetition rate (1 kHz) femtosecond laser. In reference [8] Watanabe et al. reported on welding of dissimilar transparent materials using the same laser, and also investigated the parameters that resulted in joining by varying laser pulse energy and translation velocity. Sören Richter et al reported a promising application of ultrafast pulse laser welding to manufacture micro-optical devices [4]. High repetition ultrafast laser pulses as local heat sources can solve the thermal expansion problem. Alexander Horn [5] using ultrafast laser joining offered a very precise process with dimensions smaller than 50 μm, the welding strength measurements and gas/humidity tests shows a strong and reproducible sealing process. Research on ultrafast welding mainly includes the following three methods:

1. Welding parameters investigation
2. Welding strength and thermal tests
3. Morphology analysis

1.3.3.1 Welding Parameters Investigation

1.3.3.1.1 Laser Parameters

Due to multi-photon absorption within the confocal area there is little operational difference when welding with long or short wavelengths. Glasses show transparency to the laser pulses, but there is another factor affecting absorption. When a plasma is formed, electrons are free to absorb photons and hence the plasma can block the beam; also the hot plasma will disperse the beam due to the plasma density changes and hence change the refractive index. Furthermore, the plasma can scatter the light going through it. All of these processes contribute to plasma absorption which will help to sustain the plasma. The absorption coefficient has been deduced by Raiser [121] to be:

$$\alpha_{bremm} \approx n^2 \lambda^2 T^{3/2} \qquad \text{Eq 1.2}$$

n is gas density, λ is the wavelength, *T* is the absolute temperature of the plasma, so a short wavelength will be less absorbed and hence generates cooler and less absorbing plasmas.

In pioneering work Tamaki et al. used low repetition rate femtosecond laser pulses to weld two fused silica pieces together in 2005 [120]. In their experiment, because there was no heat accumulation due to the low repetition rate and therefore no melting of material outside the focal volume, the weld region was confined to the focal region, about 5 μm. Furthermore, the low repetition rate laser limited the welding speed to only 5 μm/s.

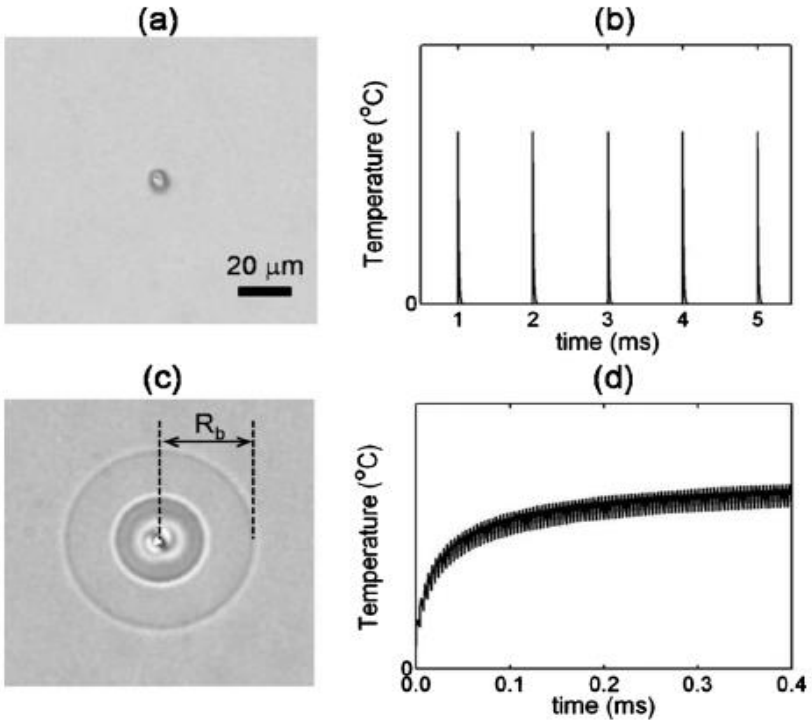

Fig 1.12 Optical microscope images of modifications by laser irradiation at (a) 1 kHz and (c) 250 kHz. (b) shows the simulated temperature change at the focus for the 1 kHz case and (d) for the 250 kHz case. The pulse energy was 2.0 μJ in both cases [10].

Lan Jiang and Hai-Lung Tsai's theoretical deduction and experiment work [122] gives a clear view the influence of pulses separation times and energy. Laser pulses temporally close enough can transiently vary free electron densities of the irradiation area, which in turn determines the optical and thermal properties. The building-up of free electrons by the first pulse greatly enhances the free electron generation through avalanche ionisation during the second pulse. Based on the simulation, for the same average power of

different repetition rates, the maximum cycle temperature due to pulse mode near the heat source region increases with decreasing repetition rate, due to decreasing pulse energy, as seen in Fig 1.13 [117].

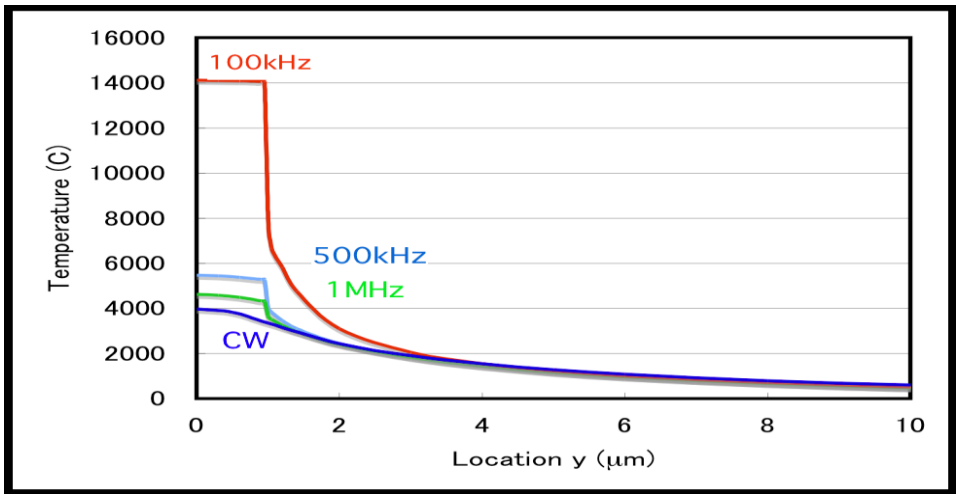

Fig 1.13 Statistic simulation of maximum cycle temperature (temperature when next pulse arrives) along the x-axis vs. y at z=0 calculated by pulse and CW models (average power 0.2 W, a=1 μm, h=10 μm, v=100 mm/s) [117].

M. Shimizu et al. [10] reported a heat-modification region dependence on pulse energy, exposure times and ambient temperature. The threshold temperature of heat-modification becomes lower with increasing laser exposure time and ambient temperature, as shown in Fig 1.14.

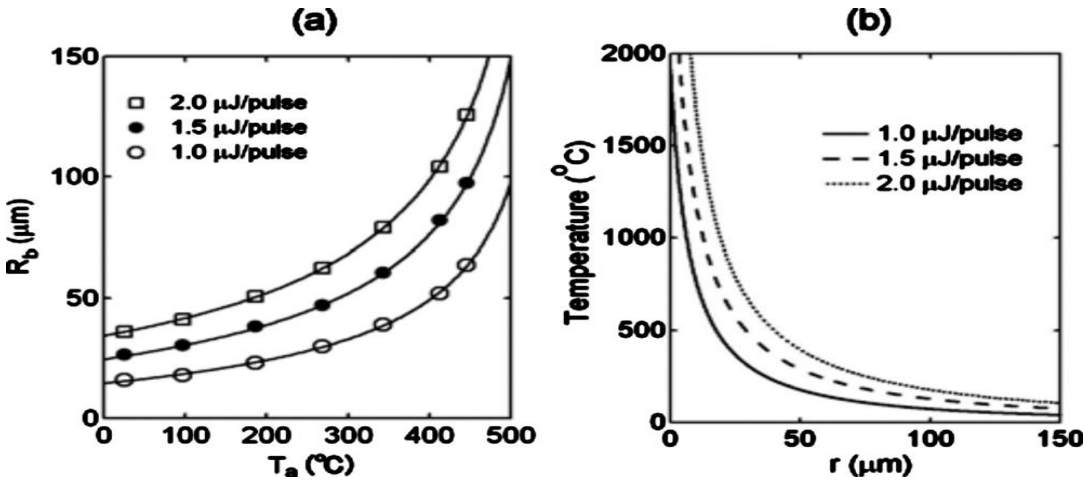

Fig 1.14 (a). The radius of the heat-modified regions (R_b) plotted as a function of ambient temperatures (T_a) for different pulse energies. (b). Temperature distributions just after the laser exposure has stopped [10].

For direct welding, whether glass to glass, glass to transparent semiconductor substrates or glass to metal, nanosecond lasers, picosecond lasers and femtosecond lasers were

used. Isamu Miyamoto et al. [3] compared the picosecond and femtosecond regime and concluded that picosecond lasers are more attractive due not only to the simplicity of the laser system but the higher melting and joining efficiencies as picosecond regime provides higher nonlinear absorption due to larger contribution from avalanche ionisation. As seen in Fig 1.15 [117], comparing the conditions of 0.5 μJ-100 kHz, the nonlinear absorptivity of 10 ps is 2~3 times higher than that of 406 fs pulses inside D264 (Schott), although the laser intensity of 10 ps is approximately 30 times lower than that of 325 fs. This is because 10 ps pulses are long enough for the growth of the electron density in the conduction band by the avalanche ionisation.

Using ns and fs pulsed lasers for direct welding of glass and copper was presented by Yasuyuki Ozeki [3], which demonstrated that ns-pulses require much higher pulse energy for the same joining strength and result in a wider heat affected zone compared to that with fs-pulses, so that fs-pulses are more suitable for precisely controlling the welded region by suppressing the excess heat.

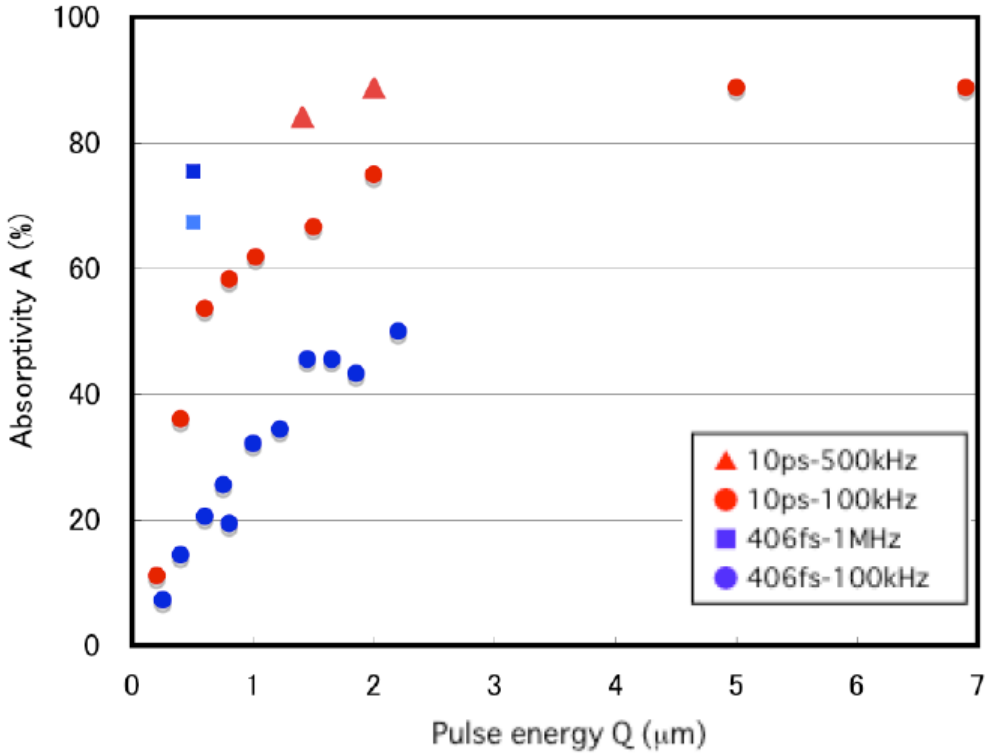

Fig 1.15 Nonlinear absorptivity vs. pulse energy with laser 10 ps and 3 μJ at 100 kHz in Schott D264 [117].

1.3.3.1.2 Welding Clamp

Direct bonding is accomplished when a substantial part of the area between two bonding surfaces is in optical contact, when the sum of Van der Waals forces across the

area results in a relatively strong bond. However, a direct bond is poor at resisting short and long-term elastic or plastic deformations e.g. due to the application of large thermal and mechanical loads.

During welding therefore a clamp is required to maintain close contact of the samples to be welded. Takayuki Tamaki [2] reported their clamp rig with the schematic diagram shown in Fig 1.16. Two substrates are carefully cleaned, stacked one on another, and pressed together by three bolts and a lens held in a fixture to create an optical contact area, so the ultrafast laser translates in this area and weld through filamentary propagation. However, a substantial amount of bending moment is left inside the samples, leading to residual joint strength or even breakage of the welds. Another clamp rig is used to cope with this problem [3] as shown in Fig 1.17. The samples are pressed with a rubber plate and a slide glass so that the pressure is applied over a wider area, leaving a reduced bending moment.

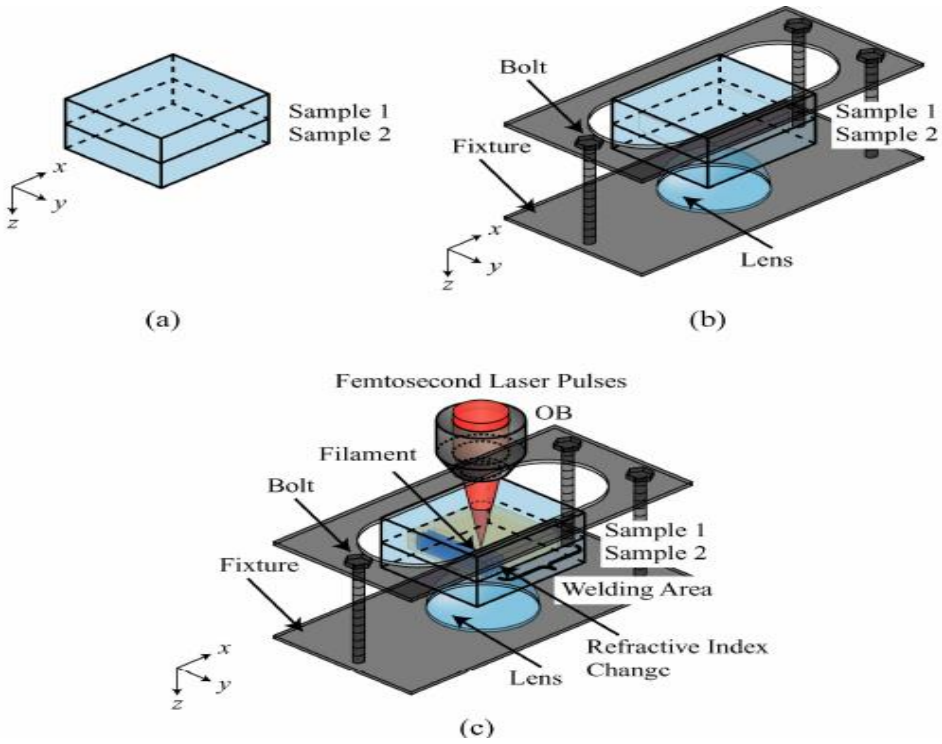

Fig 1.16 Schematic diagram of laser micro-welding of two substrates. (a). Two stacked substrates. (b). Fixing of two substrates using sample holder and a pressing lens. (c). Welding of two substrates by focusing femtosecond laser pulses at the interface between the two substrates [2].

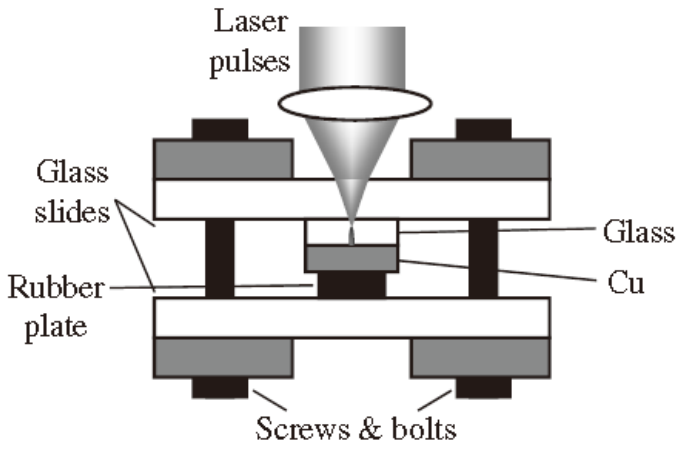

Fig 1.17 Schematic of the fixture for holding samples to be joined [3].

1.3.3.2 Welding Strength Test and Thermal Test

1.3.3.2.1 Welding Strength Test

The ultrafast laser welding strength was evaluated in early papers as merely staying joined, as W. Watanabe [8] said "When raising the samples and holding one of them at a certain height the other sample did not fall", till more recently the welding strength has been demonstrated to reach 95% of the bulk material for borosilicate glass to borosilicate glass welding [118]. Miyamoto et al. [123] evaluated the mechanical strength of laser-melt zone using a three-point bending test, and showed that the strength in that zone was as high as the un-irradiated base material. For strength measurements of two piece welding there are tensile strength measurement [2] (Fig 1.18a), shear strength measurement [124] (Fig 1.18b) and bend strength measurement [4][125] (Fig 1.18c).

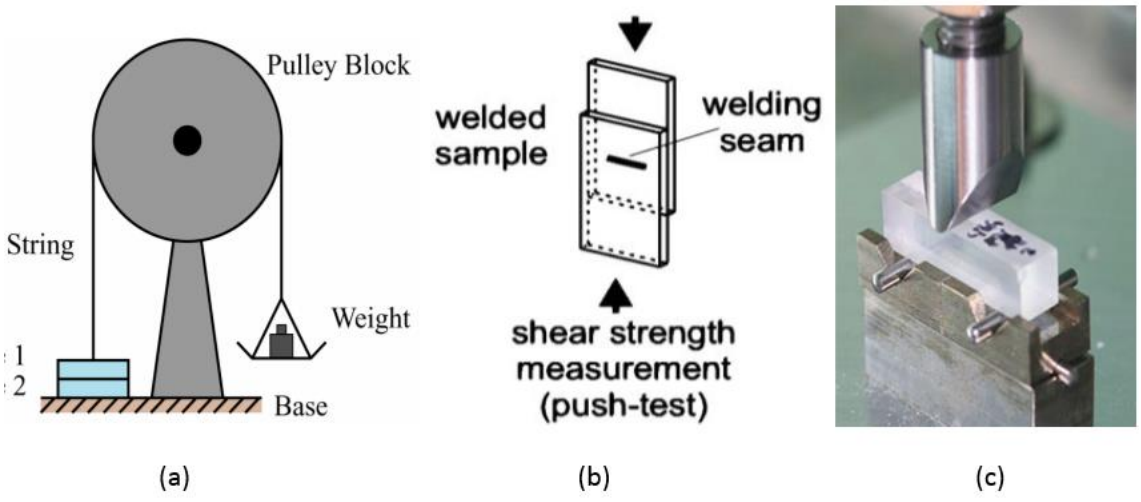

Fig 1.18 strength test setups for different kinds of joining forces((a) from [2], (b) from [124], (c) from [4]).

The first setup uses adhesive to join one sample to a base and the other to a string, which is hard to carry out because the joint force may be unbiased and the adhesive strength may be small compared with the ultrafast laser joint. The shear strength test encounters the problem of van der Waals forces between the two surfaces, especially if there is a large optical contact area. Also the glasses are prone to bend because of the push force acts on the edge of the glass sample. For the three points bent test one needs to cut the glasses into rods first, and defects and scratches during the cutting process often introduce uncertainties to the test. Furthermore if the rod joint area is non-uniform, the resultant cantilever effect will make the test unreliable, so the estimated error of breaking stress measurement is up to 25%.

1.3.3.2.2 Thermal Test

When electrons transfer their energy to ions hydrodynamic motion begins and a shock wave emerges from the energy deposition zone [126][127]. This is driven by pressure gradients in the absorption volume built up by deposited energy. Most of the shock wave propagation is confined within cold material. Therefore, most of the material inside the absorption volume is compressed and transformed into a post-shock state. Also the diffusion of thermal energy generates a heat affected zone (HAZ), which may lead to a smooth refractive change with a number of defects (cracks) around the focal volume [37]. Obviously, the weld seam area is subjected to different types of loading such as tension, shear force etc. Brittle materials deform elastically up to failure under the action of tensile stress, with the fracture beginning in a direction approximately perpendicular to the maximum tensile stress. Welding two materials with different thermal expansion coefficients is likely to magnify the influence of the tensile stress area.

Thermal shock analysis was carried out by David Hélie et al. [119] to test different inscription patterns of different materials. The welded samples were deposited on a steel plate preheated inside an oven, which simulated a fast temperature rise in the lower material. Samples taken out of the oven were immediately dipped into water to produce a fast temperature drop. These thermal tests showed that samples using ultrafast laser welding can greatly enhance the resistance to thermal shocks compared with those only were bonded with optical contact, as seen in Fig 1.19.

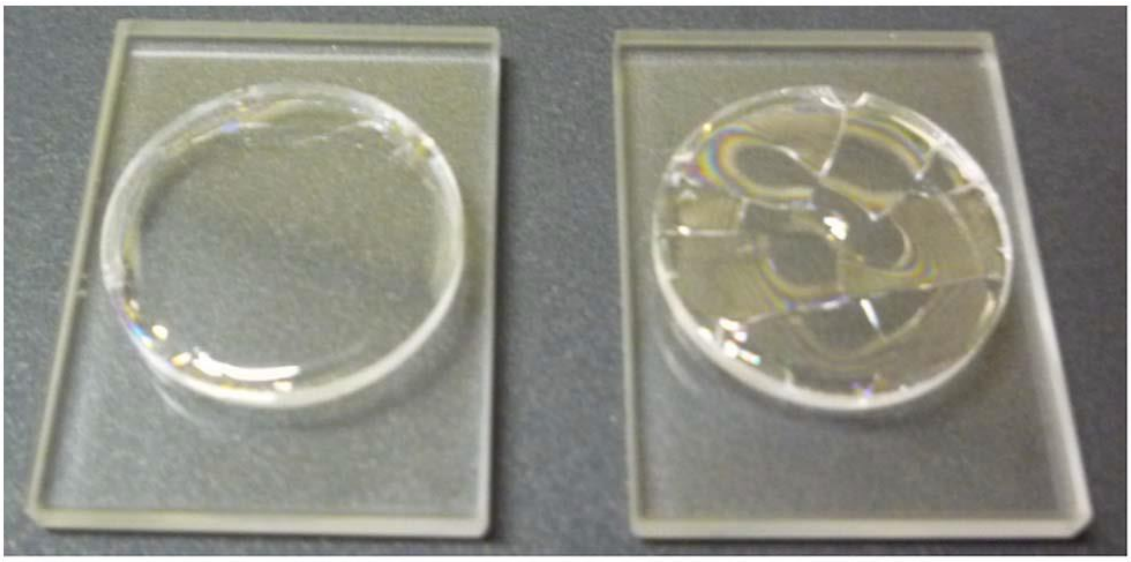

Fig 1.19 Photograph of two direct bonded fused silica–BK7 assemblies reinforced by circular weld lines after thermal shock treatments, inducing a brittle rupture of material. The circular 50 weld line seam (left) preserved the optical contact inside the sealed area after a thermal shock of 250 °C. To the right, the optical contact was broken at a temperature of 200 °C for a similar sample reinforced with 11 weld lines [119].

1.3.3.2.3 Residual Stress and Crack Analysis

Defect generation during welding was observed for a broad range of welding conditions, in this section a general summarization of defects formation and their origins analysis is presented.

In paper [128] Kristian Cvecek et al. investigated many types of cracks, and categorize them into two groups. The first group consists of cracks generated when the material is too cold and therefore brittle. Three types of crack occur in this group: the first one is when a high repetition rate ultrafast laser irradiates the material, cracks appear at the longitudinal orientation of the tear shape HAZ area along the laser beam path and a defect is formed at the bottom of the molten zone rather than at the top. As shown in Fig 1.20a; the second type is incorrect positioning of the laser beam focus leading to the formation of cracks inside the welding seam and to the deformation of the joining surface in Fig 1.20b; the third kind of crack is caused by non-uniform heating within the welding process. The bottom plate doesn't get enough energy to reach its melting point in the irradiated area; the surface can be deformed but there remain certain surface tensions which prevents joining of the plates.

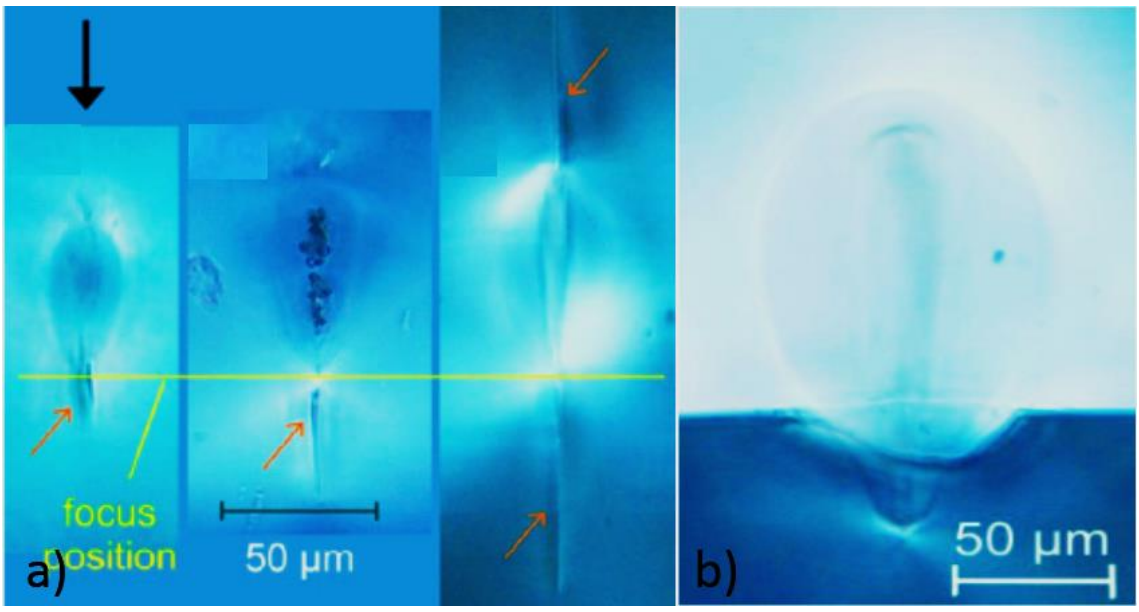

Fig 1.20 Sample cross-sections of HAZ carried out in different glass materials. Cracks, identified by the red arrows [128].

The second group of cracks happen where the volume of the molten zone grow so large that the thermal expansion and subsequent contraction leads to crack formation [128], as shown in Fig 1.21. These tunnel-like cracks extend around the molten zone or run perpendicular to the welding direction. This crack formation is most prominent for processing conditions where a high average power or low feed rate has been used as the thermal expansion and shrinkage stresses cause this type of crack. These cracks have been observed in all types of tested glass except fused silica since fused silica has a comparably low thermal expansion coefficient.

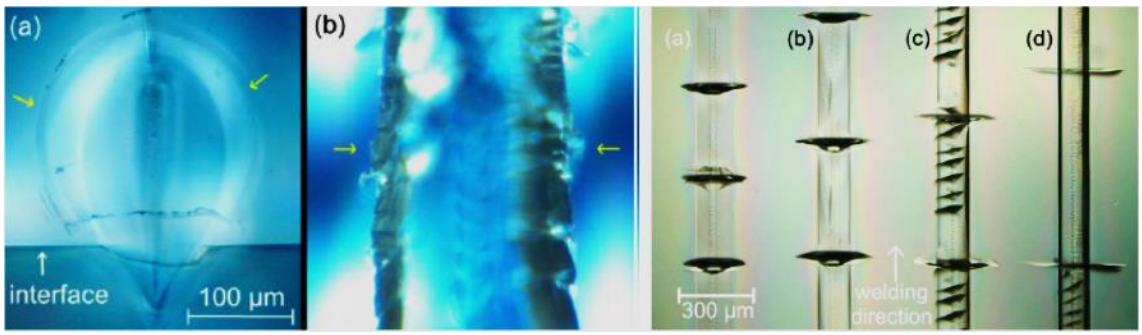

Fig 1.21 The cracks in D263 glass caused by over-powered, indicated by the yellow arrows around the molten zone [128].

1.3.3.3 Morphology Analysis

The size and shape of the HAZ depends on many factors, including laser parameters, material properties, welding parameters and surface conditions. To investigate the

morphology, the welded samples need to be cross-sectioned and an optical microscope or SEM is used. For a wide range of processing parameters, a welding seam formed by joining two substrates is significantly larger than the focal volume, indicating a thermal mechanism. Cross-section for a typical thermally induced modification shape at different laser repetition rates was shown in [125] by S. Richter, which indicates the absorption starts at the lowest point of the bulb shape suggesting the location of the focal point. Fig 1.22 shows decreasing molten volume with decreasing repetition rate due to lower heat accumulation. Because of the large thermal conductivity of fused silica, no melt occurs in the material surrounding the focal volume at or below a repetition rate of 1 MHz. However, voids can be formed due to the high peak power at the focus.

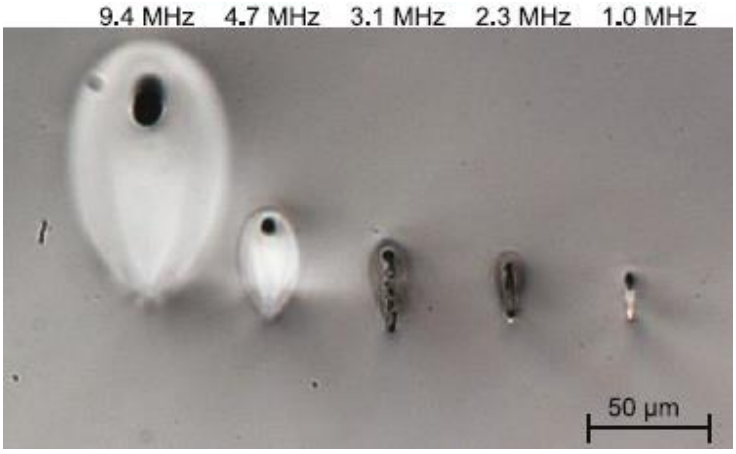

Fig 1.22 HAZ, voids, cracks, height width with different laser repetition rates [125].

Optical transmission images and reflectance images have typically been used to investigate the joining area of the two pieces of glass [127], images are shown in Fig 1.23. The transmission image in Fig 1.23c indicates a complex pattern of refractive index gradients, and here the fusion of glass penetrates up to 50 µm into each substrate. Fig 1.23c shows the gap of the two surfaces is completely eliminated in the seam area, so the two pieces of glass are fused together without significant damage.

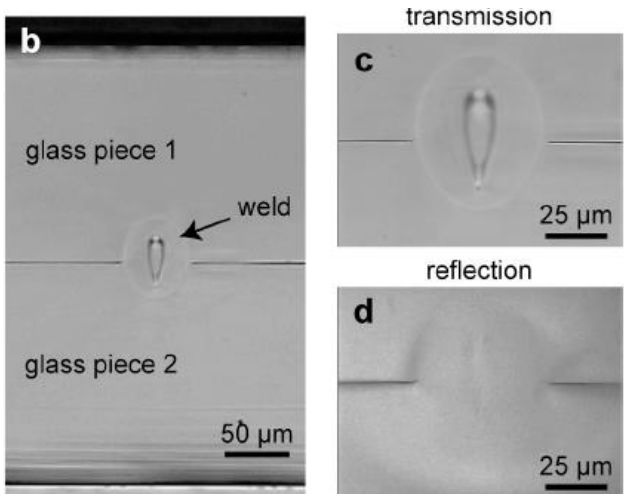

Fig 1.23 Transmission and reflection images of a weld seam between the two surfaces [127].

The absolute HAZ area related to each parameter is still hard to fix because the laser and beam parameters vary with different laser systems, but the trend of HAZ size changes with different laser parameters is still worth investigating.

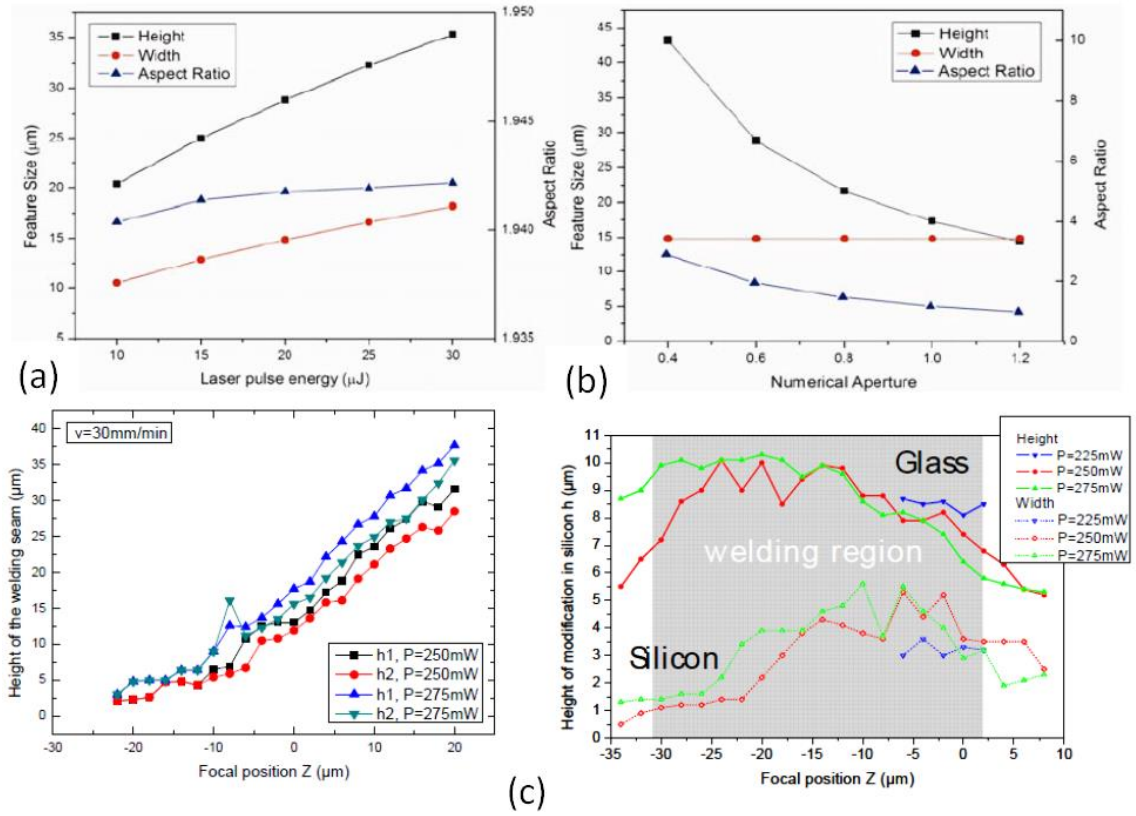

Fig 1.24 Welding seam sizes Vs different parameters ((a) and (b) from [129] NA=0.6 and laser pulse energy=20 μJ. (c) from [5]).

The results show a quite similar trend from different investigators [5][127][129]. Fig 1.24 illustrates the relations between HAZ sizes and (a) pulse energy; (b) numerical

aperture of the lens; and (c) focal positions of the two surfaces for different powers. The laser intensity and energy density play important roles for the HAZ size, with HAZ height changes more rapidly than HAZ width.

1.4 Summary and Conclusion

In this chapter the aims and objectives of this PhD work were presented. Ultrafast laser micromachining of transparent materials has unique advantages over other optical device fabrication techniques. Firstly the nonlinear nature of the absorption confines any induced changes to the local focus area. Secondly the absorption process is independent of material, enabling optical devices to be fabricated in different materials.

Due to its very high peak power, an ultrafast laser focused on the interface of two materials causes localized melting and rapid resolidification due to nonlinear absorption. Minimised thermal distortion and localised spatially selective melting mean that ultrafast laser sources are ideal for welding of glass to glass or glass to highly dissimilar materials like metals, semiconductors or ceramics. This PhD aims to develop an ultrafast laser (ps laser) welding process as an industrially relevant technique for laser manufacturing of high value components or parts.

A literature review was presented including three parts: ultrafast laser machining, traditional bonding techniques and the development of ultrafast laser welding. The influence of laser pulse duration on machining was discussed and the literature of ultrafast laser machining in bulk transparent materials and surface processing were reviewed. Traditional bonding is done for a variety of technical reasons, mechanical attachment, thermal contact, electrical contact, gas or liquid sealing and any or all combinations thereof. The choice of bonding method will therefore depend on the intrinsic properties of the bonding materials which include mechanical attachment (clamp or optical contact), adhesive bonding, soldering, and direct bonding such as resistance welding, anodic bonding, ultrasonic welding, friction welding and laser welding (longer pulse or CW laser).

Development of the ultrafast laser welding began in 2005 (Tamaki et al. [120]), since then ultrafast laser welding has been extensively developed. Research on ultrafast welding includes the following 3 methods: welding parameter investigations, welding strength/thermal tests, and morphology analysis. For ultrafast laser bonding to work, the peak intensity of the focused laser beam must be sufficiently high to generate free

electrons in the focal volume through nonlinear absorption processes (either multi-photon or tunnelling). These free electrons then act as seed electrons for single photon absorption (Joule heating), avalanche ionisation, and plasma formation. Ideally, the laser must also exhibit a sufficiently high pulse repetition rate (100's of kHz) for heat to accumulate in the weld region. This heat accumulation results in more efficient energy absorption, through phonon assisted absorption, and increases the physical size of the melt volume (HAZ). The melt region fills up the original gap between the two surfaces and, by subsequent resolidfication, joins the two materials. The size of the HAZ, and hence the cross-sectional area of the resultant weld, depends on the parameters used, such as sample translation speed, laser power and pulse repetition frequency.

Chapter 2 Ultrafast Pulse Irradiation of Transparent Materials

There are two different ways to create optical property changes in transparent materials using a laser. First, non-destructive phase transitions can be induced by lasers at an intensity below the damage threshold [32]. Second, irreversible structural changes may be produced at high intensities above the optical breakdown threshold. We concentrate on this latter regime in this chapter. To achieve this, the laser beam must be focused into a small volume inside the material using a high numerical aperture (NA) optic. Light-matter interactions become nonlinear when the focused volume contains a sufficiently high energy density ($>6\times10^{12}$ W/cm^2) [36][126]. The plasma generated in the focal region increases the absorption coefficient. Local temperature rise and accumulation is eventually balanced by heat conduction.

In this chapter, the equations describing propagation of electromagnetic waves in a dielectric material are firstly reviewed. Then a number of key results from linear and nonlinear optics are presented dealing with the focusing of Gaussian beams. Finally, nonlinear propagation and absorption theory is compared with experimental results to evaluate the impact of thermal accumulation by high repetition rate ultrashort pulses. In addition thermal conduction theories are briefly described.

2.1 Gaussian Beam Focused into Material

In discussing laser beam propagation, the most frequently discussed beam shape is a Gaussian transverse intensity profile, as most laser resonators can produce such a mode, and a (fundamental) Gaussian is the minimum diffraction beam shape.

Propagation of an electromagnetic wave in a medium is governed by the Maxwell equations [130][131]. Combining the four Maxwell equations, and considering only the dipole response of the material, the wave equation for the electric field of the electromagnetic wave in dielectric material:

$$\nabla^2 \boldsymbol{E} + \frac{1}{c^2}\frac{\partial^2 \boldsymbol{E}}{\partial t^2} + \mu_0 \frac{\partial^2 \boldsymbol{P}}{\partial t^2} = 0 \qquad \text{Eq 2.1}$$

where $\boldsymbol{E}$ is the electric field vector, $\boldsymbol{P}$ is the induced electric polarisation. μ_0 is the vacuum permeability, ε_0 is the vacuum permittivity, and $1/c^2 = \varepsilon_0\mu_0$, with c the speed of light in vacuum. To complete the description, a relation between P and E is needed (if the material does not have memory):

$$\boldsymbol{P} = \varepsilon_0(\chi^1\boldsymbol{E} + \chi^2\boldsymbol{E}.\boldsymbol{E} + \chi^3\boldsymbol{E}.\boldsymbol{E}.\boldsymbol{E} + \cdots) \quad \text{Eq 2.2}$$

where χ^j $(j = 1,2,3 \ldots)$ is the j^{th} order susceptibility. Each of the electric fields on the right hand side of Eq 2.2 can have different frequency components, and there will be a nonlinear polarization produced at the sum or difference of these frequency components. Generally, the orders over the 3rd in Eq 2.2 are negligible, moreover, in all the materials with inversion symmetry, χ^2 vanishes and Eq 2.2 can be simplified to

$$\boldsymbol{P} = \varepsilon_0\chi^1\boldsymbol{E} + \varepsilon_0\chi^3\boldsymbol{E}.\boldsymbol{E}.\boldsymbol{E} = \boldsymbol{P}_L + \boldsymbol{P}_{NL} \quad \text{Eq 2.3}$$

where P_L and P_{NL} are the linear and nonlinear polarisation. Including all three permutations of the fields which contribute to the nonlinear polarisation, Eq 2.3 becomes

$$\boldsymbol{P} = \varepsilon_0\left(\chi^1 + \frac{3}{4}\chi^3|E|^2\right)\boldsymbol{E} \quad \text{Eq 2.4}$$

Hence Eq 2.1 can be simplified to

$$\nabla^2\boldsymbol{E} + \frac{n^2}{c^2}\frac{\partial^2\boldsymbol{E}}{\partial t^2} = 0 \quad \text{Eq 2.5}$$

where *n*, the refractive index is given by

$$n = \sqrt{1 + \chi^1 + \frac{3}{4}\chi^3|E|^2} \quad \text{Eq 2.6}$$

Taking the nonlinear term to be small compared to the linear susceptibility and expressing the electric field strength in terms of the laser intensity *I*, Eq 2.6 becomes

$$\mathrm{n} = \mathrm{n}_0 + n_2 I \quad \text{Eq 2.7}$$

with the laser intensity

$$I = \frac{1}{2}\varepsilon_0 c n_0 |E|^2 \qquad \text{Eq 2.8}$$

The linear refractive index n_0 and the nonlinear refractive n_2 are

$$n_0 = \sqrt{1+\chi^1}$$
$$n_2 = \frac{3\chi^3}{4\varepsilon_0 c n_0^2} \qquad \text{Eq 2.9}$$

This nonlinear refractive index gives rise to self-focusing and self-phase modulation, and explains many of the features in the propagation of loosely-focused short laser pulses in transparent materials.

If assumed that there are no free charges and that the susceptibility is spatially independent, the nonlinear refractive index becomes zero, and Eq 2.5 describes the propagation of optical radiation in linear optics [12].

2.1.1 Beam Propagation and Focusing in Air

From Eq 2.5 the propagation of time-harmonic beams can be described as a scalar field with one direction vector

$$\boldsymbol{E}(r,t) = \hat{\boldsymbol{n}}\psi(x,y,z)e^{i\omega t} \qquad \text{Eq 2.10}$$

and the electric field can be described as a scalar wave equation

$$\nabla^2\psi + k^2\psi = 0, k^2 = \frac{n^2}{c^2}\omega^2 \qquad \text{Eq 2.11}$$

A general solution to Eq 2.11 can be written as a sum of plane waves $e^{-ik_x x}e^{-ik_y y}e^{-ik_z z}$. The paraxial approximation implies that, if $\frac{\sqrt{k_x^2+k_y^2}}{k} \ll 1$, the k-vectors are assumed to be roughly in the k_z direction and the solution can be greatly simplified as a scalar field

$$\psi(x,y,z) = u(x,y,z)\exp(-ikz) \qquad \text{Eq 2.12}$$

Fresnel diffraction theory seeks to express the amplitude distribution $u(x,y,z)$ for all $z > 0$ as a convolution of the initial amplitude distribution $u_0(x,y)$ with a propagator $h(x,y,z) = \frac{i}{\lambda z} e^{-ik\left[{(x^2+y^2)}/{2z}\right]}$, in a Green function approach. The evolution of an arbitrarily-shaped beam as it propagates through space can then be determined from just its initial transverse profile.

Consider a Gaussian beam with waist *w*,

$$\mu_0(x,y) = A\exp(-\frac{x^2+y^2}{w^2}) \qquad \text{Eq 2.13}$$

Propagation through a thin lens will not immediately affect the amplitude distribution, but will introduce a phase delay that decreases in the radial direction. Hence, after passing through the lens, the beam becomes

$$\mu_1(x,y) = A\exp(-\frac{x^2+y^2}{w^2})exp\left[i\frac{k}{2f}(x^2+y^2)\right] \qquad \text{Eq 2.14}$$

The free space propagation of the beam is then accomplished with the Fresnel diffraction integral and a new Gaussian waist and phase curvature can be obtained as

$$w(z)^2 = \frac{4z^2w^2}{k^2}\left[\frac{1}{w^4} + \frac{k^2}{4}\left(\frac{1}{z}-\frac{1}{f}\right)^2\right], \frac{1}{R(z)} = \frac{1}{z} - \frac{\frac{k^2}{4z^2}\left(\frac{1}{z}-\frac{1}{f}\right)}{\frac{1}{w^4}+\frac{k^2}{4}\left(\frac{1}{z}-\frac{1}{f}\right)^2} \qquad \text{Eq 2.15}$$

The new waist position is obtained when the phase fronts are again flat ($R(z) = \infty$), the new Gaussian waist position is

$$z = f\left[1+\left(\frac{f\lambda}{\pi w^2}\right)^2\right]^{-1} \approx f - \frac{f^3\lambda^2}{\pi^2 w^4} \qquad \text{Eq 2.16}$$

The Gaussian waist is slightly in front of the actual lens focus, but this value is so small that we usually ignore it (for example, given a focusing conditions of f = 10 mm, w = 12.7 mm, and λ =1.03 μm, $\frac{f^3\lambda^2}{\pi^2 w^4}$ is just 4.1×10^{-12} m).

It is straightforward to obtain the size of the waist at the focus (the focus spot size) from Eq 2.15 as

$$w_0 = \frac{f\lambda}{\pi w} \qquad \text{Eq 2.17}$$

and the beam size near the focus is

$$w(z)^2 = w_0^2\left[1 + \left(\frac{z}{z_R}\right)^2\right], z_R = \frac{\pi w_0^2}{\lambda} \qquad \text{Eq 2.18}$$

where the z_R is the Rayleigh length, the distance from the focus at which the radius has increased by $\sqrt{2}$, and hence the intensity has been halved [131].

Considering a previous Gaussian beam divergence when it reaches the focal lens, the focus spot size can be write as [9]

$$w_0 = \frac{2M^2 f\lambda}{\pi D_L} \qquad \text{Eq 2.19}$$

here M^2 represent the laser beam divergence quality, and D_L is the beam diameter when it reaches the lens.

2.1.2 Beam Focused in Materials

The preceding results are Gaussian beams focused in air, the deduction and experiments described in this part concern beams focused into transparent material.

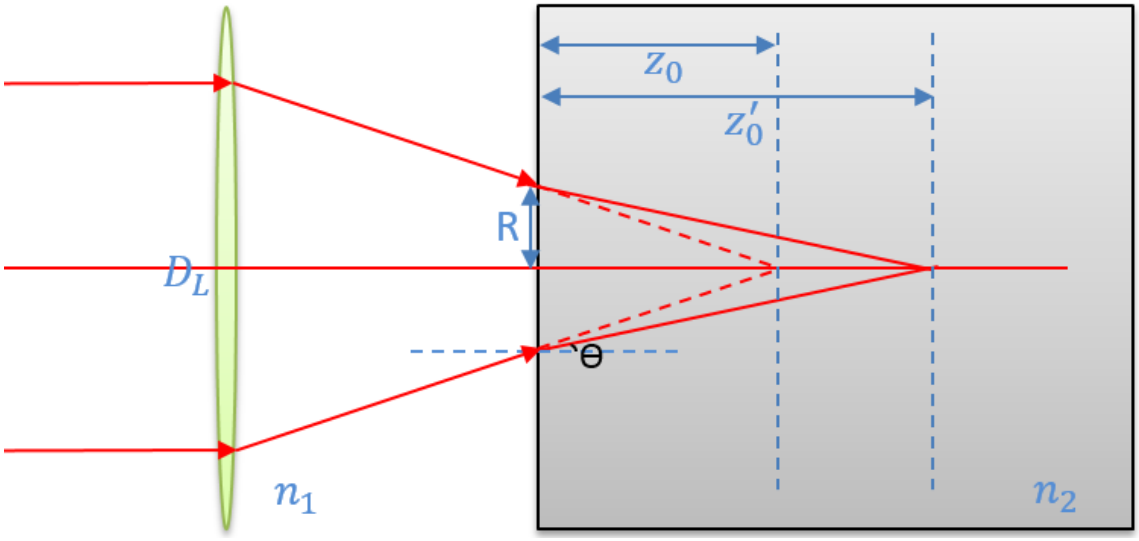

Fig 2.1 Beam focused into transparent material. Paraxial focusing across an interface. The beam makes a spot of radius R on the front surface of the material, and the focus moves from z_0 to z_0' with refractive index change from n_1 to n_2.

Based on Snell's law and the geometric relations from Fig 2.1, the relation between z_0 and z_0' is

$$z_0' = z_0 \frac{n_2}{n_1} \sqrt{\frac{D_L^2(n_2^2 - n_1^2)}{4n_2^2 f^2} + 1} \qquad \text{Eq 2.20}$$

and with an ABCD matrix method, the focal spot size and Rayleigh range inside the material becomes [131]:

$$w_{material} = \frac{\lambda f}{\pi w} \; and \; z_{material} = n z_R \qquad \text{Eq 2.21}$$

From Eq 2.21 the waist in material is the same as that in air and the Rayleigh range becomes *n* times larger, since $z_R = \frac{\pi w^2}{\lambda}$ and the wavelength in the material is scaled by *n*. However, the ABCD matrix method only works when it is paraxial, i.e. for a tightly-focused beam, Ulanowski and Ludlow [132] presented an exact (closed form) solution which matches an initially paraxial Gaussian beam focused with a high-NA lens, and reduces to a paraxial Gaussian beam as the numerical aperture is lowered.

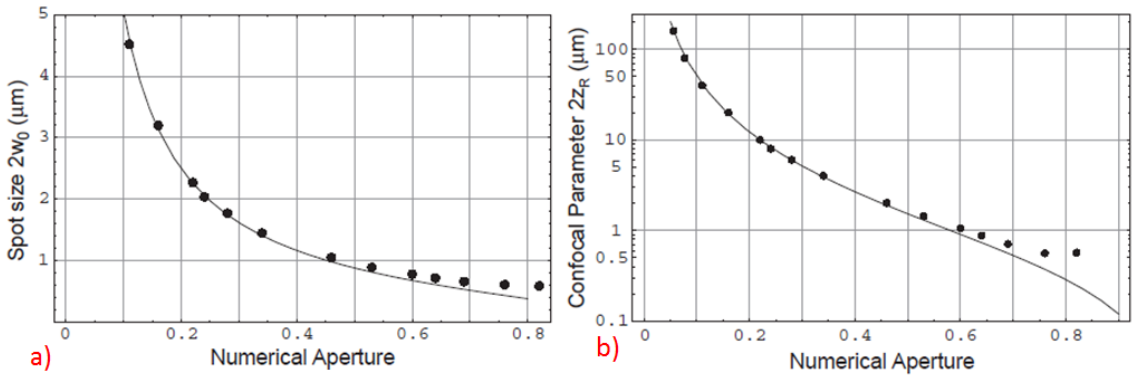

Fig 2.2 Comparison of predicted spot size of non-paraxial solution of Ulanowski and Ludlow [132] *(points) to a paraxial approximation (curve) [133].*

The simulation results [133] show the deviation of real value and the paraxial value of the spot size and Rayleigh range are not that large, as shown in Fig 2.2. For focal lenses used in this thesis, numerical apertures of 0.54, 0.28 and 0.14 were used, the deviations are limited based on the simulation (deviations are only 8% and 10% for focal spot size and Rayleigh range respectively for numerical aperture NA = 0.54), therefore the Eq 2.21 is used in this thesis.

2.1.3 Aberrations

2.1.3.1 Spherical Aberration

Because of the relatively ease of manufacture, the spherical lens is by far the most common and readily available. However, a spherical lens only images perfectly in the paraxial limit (for ray optics, this is the limit where $sin\theta$ is well approximated by θ, where θ is the angle of the refracted ray relative to the optic axis). The non-ideal focusing of non-paraxial rays results in aberrations, which are grouped by their order in the Taylor expansion of $sin\theta$ at which they are taken into account [134]. Spherical aberration cause marginal rays parallel to the optic axis to come to focus before the focus of rays close to the optic axis, and hence the ideal ray optic point focus is blurred into a spot of finite radius. This blur increases with increasing numerical aperture. J. Ashcom [133] shows that for typical parameters, a plano-convex lens (made of BK7, n=1.51 at 800 nm) cannot be used for numerical apertures greater than about 0.16 as the simulation is shown in Fig 2.3.

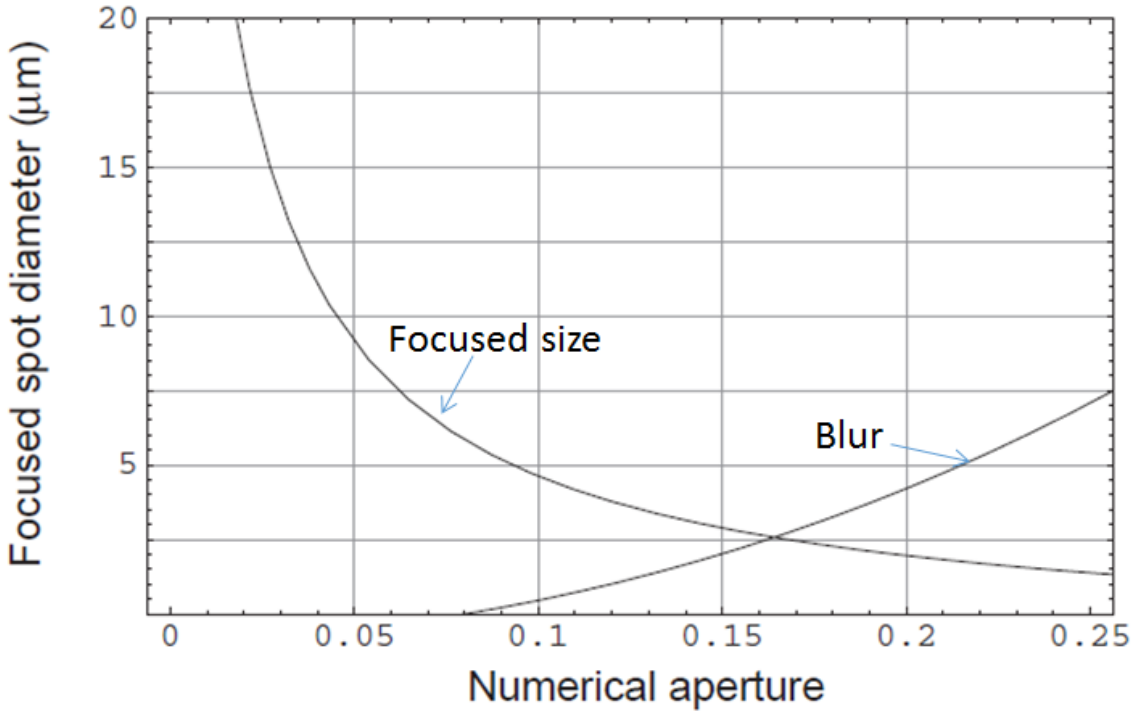

Fig 2.3 The blur in the focused spot caused by spherical aberration of a plano-convex lens, and is greater than the diffraction limited Gaussian spot at roughly NA= 0.16 [133].

2.1.3.2 Angled-Incidence Aberration

Additional aberrations can occur if the laser beam impinges on the material at non-normal incidence. Since we will make use of this abnormal incidence in Chapter 7, this

type of aberration will be discussed in this part. For simplicity, we consider a 20 mm lens focusing into borosilicate glass with an incident angle θ, as shown in Fig 2.4. The beam diameter at the lens is $D_L = 12.7\ mm$, and the lens focuses at a depth d in the material.

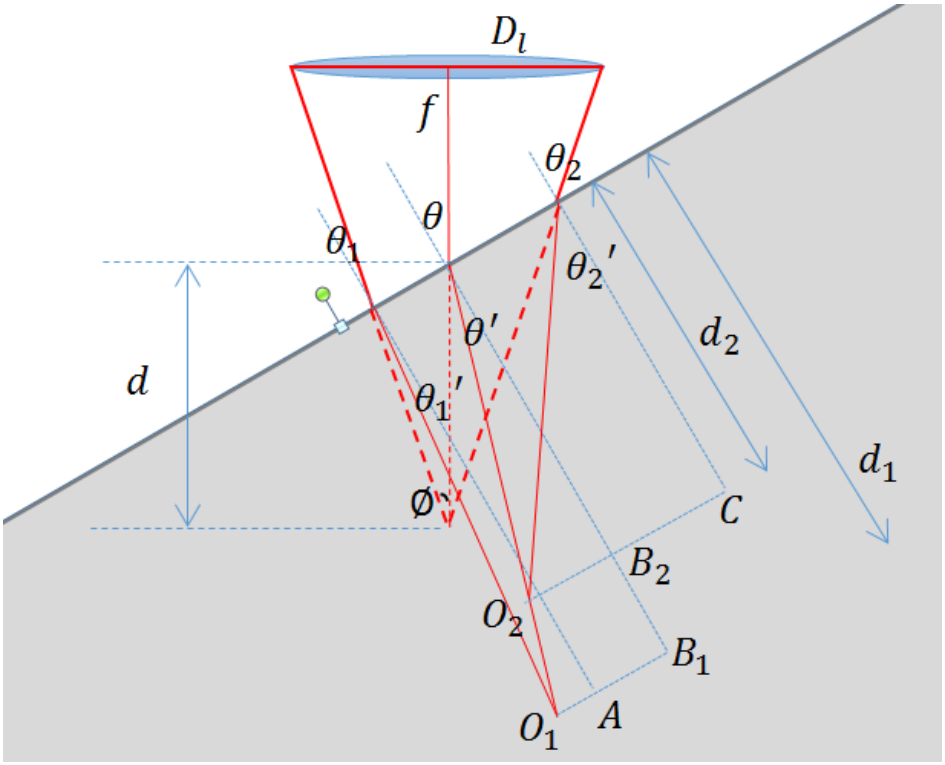

Fig 2.4 Diagram of laser beam focused into an angled material.

By calculating the marginal rays focal position based on their geometric relations (Eq 2.22), the focus lies between O_1 and O_2, and the distances d_1 and d_2 can be calculated with Eq 2.22. The relation of $d_1 - d_2$ representing the aberration length can be calculated as shown in Fig 2.5.

$$\emptyset = arctan\left(\frac{D_L}{2f}\right)$$

$$\theta_1 = \theta - \emptyset\,, \theta_2 = \theta + \emptyset$$

$$B_2C = \frac{dsin\emptyset}{cos\theta_2}, B_1A = \frac{dsin\emptyset}{cos\theta_1} \qquad \text{Eq 2.22}$$

$$tan(\theta') = \frac{O_1B_1}{d_1} = \frac{O_2B_2}{d_2}$$

$$\tan(\theta_2') = \frac{O_2B_2 + CB_2}{d_2}, \tan(\theta_1') = \frac{O_1B_1 - AB_1}{d_1}$$

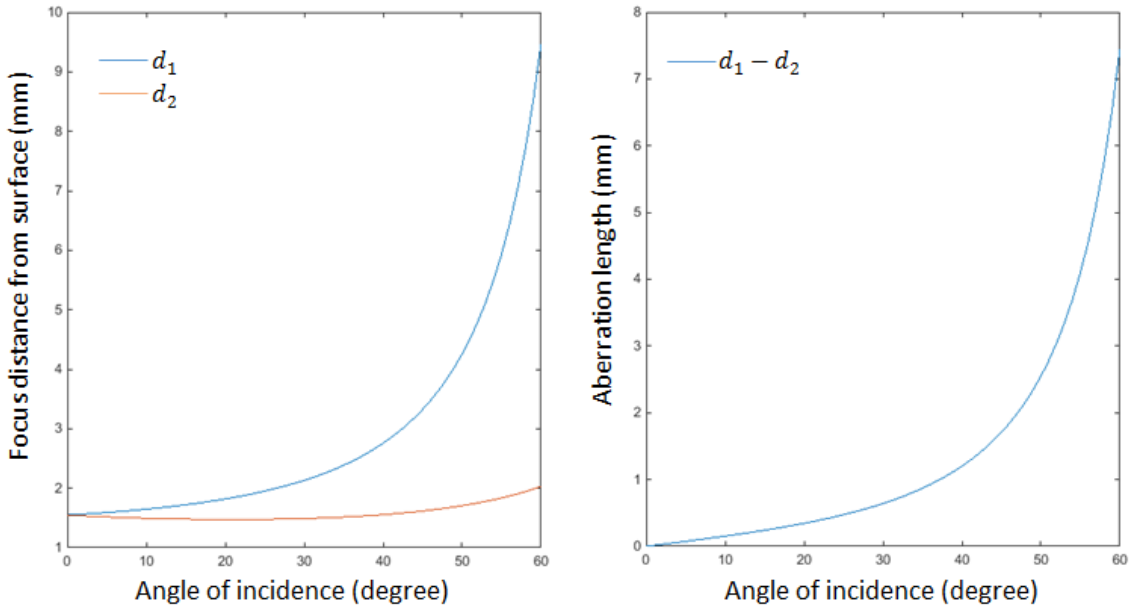

Fig 2.5 (a). Focus distance related with different incident angle, and (b). Aberration length ($d_1 - d_2$) with different incident angles.

From the graph, the aberration length increases rapidly with the material surface tilt, which will greatly influence the welding parameters required, as examined experimentally in section 7.5.

2.1.3.3 Material Aberration by High-NA Lens Focused inside Material

Even with a perfect zero aberration lens and a normal incidence, when the laser is focused into material, it will still induce aberrations when it propagates through the air-glass interface. Based on Snell's law for a highly-focused beam, the diagram of high-NA lens focusing inside material is shown in Fig 2.6. The graph shows that the marginal rays actually focus late, which results in a blur similar to that discussed for spherical aberration in Section 2.1.3.1 (but note that spherical aberration causes marginal rays to focus before the paraxial focus, not after). By considering the caustic around the focus, the aberration length can be calculated based on Eq 2.20 to be Eq 2.23 for a laser beam incident from air into glass

$$d = z_0 \left(\sqrt{\frac{D_L^2 (n^2 - 1)}{4f^2} + n^2} - n \right) \qquad \text{Eq 2.23}$$

here z_0 is the length of the laser focus dip into the material, n is the refractive index of the glass, D_L is the beam diameter, f is the focal length. For our 10 mm focus length lens

into borosilicate glass with a beam diameter of 12.7 mm, the aberration length d is $0.162 \times z_0$. As we can see the aberration increases with the focused depth (z_0). The experimental result of the focal region position related to different nominal focal place is shown in Fig 7.5 (NB not all the aberration length can generate permanent phase change inside borosilicate glass; the experiment only presents a trend).

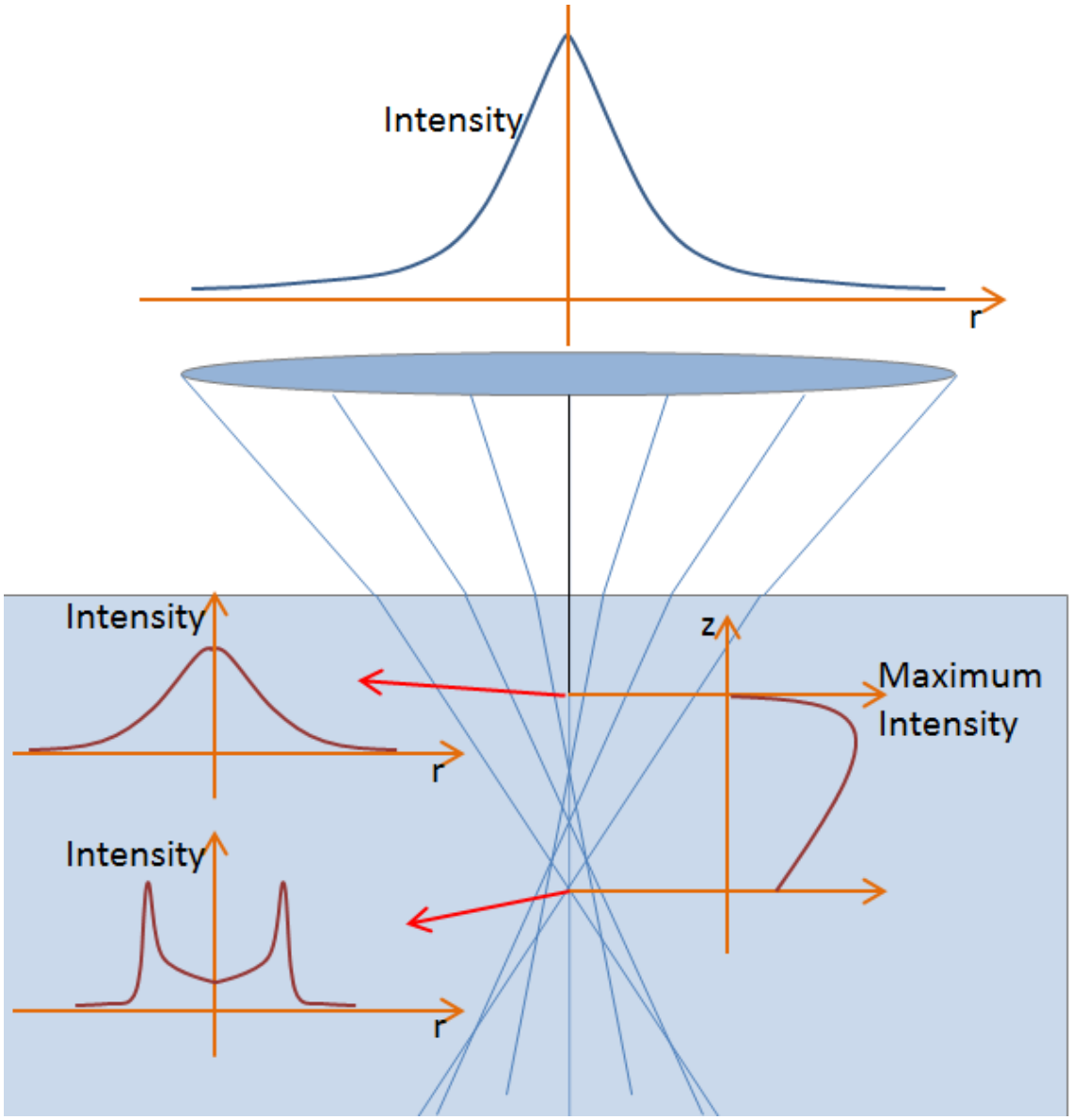

Fig 2.6 High-NA lens beam focused inside a material. Aberration and intensity distribution at different depth positions are based on calculations (laser wavelength 1030 nm, material refractive index is 1.507, beam diameter 12.7 mm and focal length 10 mm with a NA of 0.54).

For a fixed focal position inside glass, the laser intensity at different depths shows a different distribution, as shown in Fig 2.6. Consider the laser beam at the lens is a Gaussian beam (laser power is 1 W), divide the laser beam into numerous light rays,

and move the glass sample 2 mm up such that the focus is located at *2n* mm below the front surface (*n* is the refractive index of the glass). At the beam axis (*r* = 0), the intensity distribution (light across the centre) is shown in Fig 2.7, the highest intensity position is located around 90 μm below the *2n* mm (0 in the graph) position.

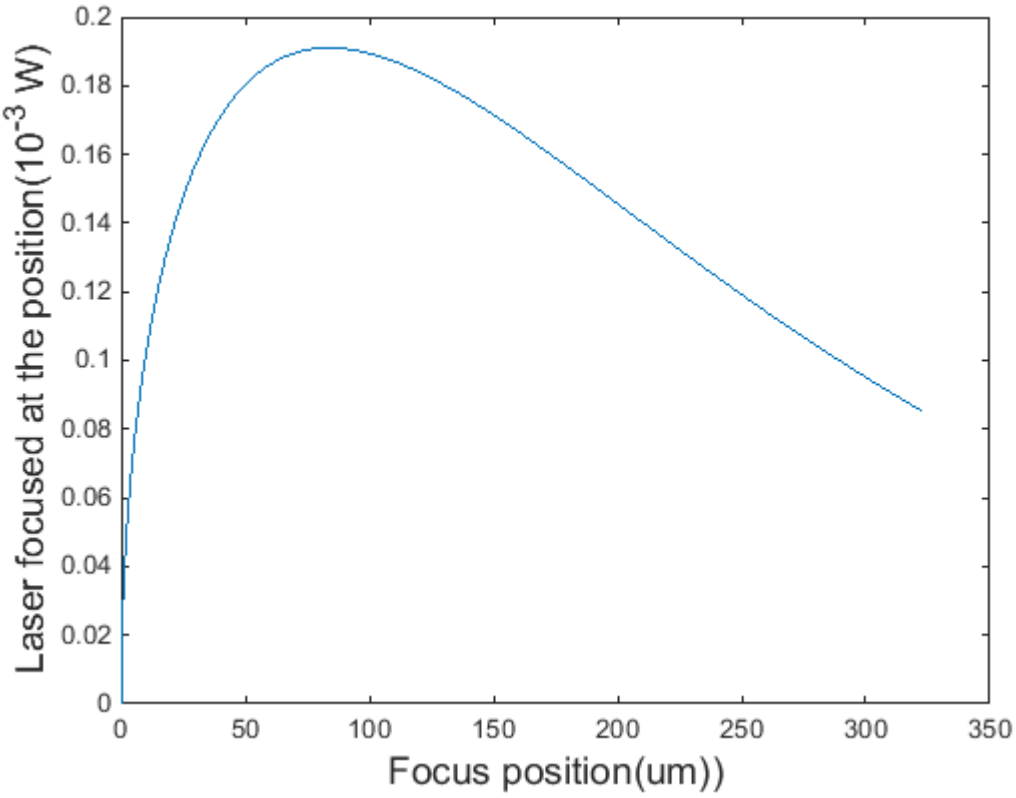

Fig 2.7 Laser intensity distribution inside borosilicate glass with focus inside 2n mm (laser power 1 W, focal lens f is 10 mm and beam diameter is 12.7 mm), the 0 position of x axis represents z position start from 2n mm inside (normal focus position) and downward (+ of the x axis).

Based on ray optics, Gaussian beam passes through a 10 mm lens and is focused into 2 mm inside borosilicate glass, the light intensity distribution at a fixed z position vary rapidly along the z axis due to the material aberration. Fig 2.8 shows the simulation results for the laser density distribution images of a laser beam highly-focused inside borosilicate glass in the *r* direction (x-y plane) at a certain z place around the focus (a. 50 μm above the focus, b. at the focus, c. 50 μm below the surface). Note that because the simulation is based on ray optics, the profile around the focus is not 100% accurate. Fig 2.9 shows the profile of laser intensity in a much large scale. If we follow the beam propagation direction, the laser intensity distribution changes from a Gaussian beam to a donut shape and then to a tent shape. The laser intensity becomes extremely high at the

focus, and after the focus, the beam is dispersed to a donut shape with high intensity appearing as a circle centred at the main axis. This donut shape lasts for about 1.5 mm and then the laser intensity profile becomes a tent shape with laser peak intensity appearing at the main axis again. For a real case, when the high peak power pulses are focused inside the material, the laser energy will be absorbed around the focus before it propagates to a donut shape or a tent shape.

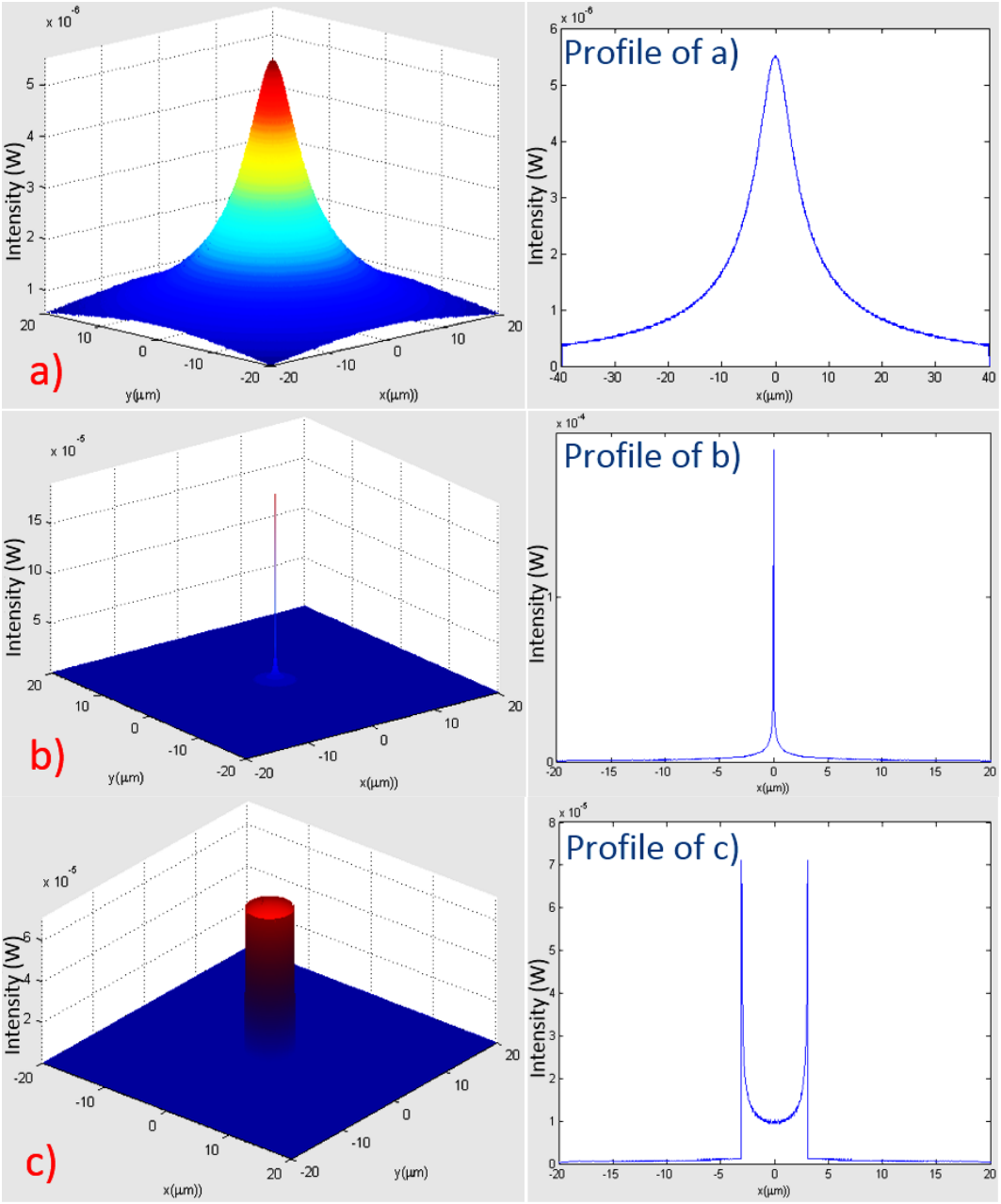

Fig 2.8 Simulated intensity distribution in the radial direction around the focus. (a). 50 μm above the focus, (b). At focus, (c). 50 μm below the focus. (Laser power 1 W, focal length 10 mm, laser beam diameter 12.7 mm and focus into borosilicate glass 2n mm.)

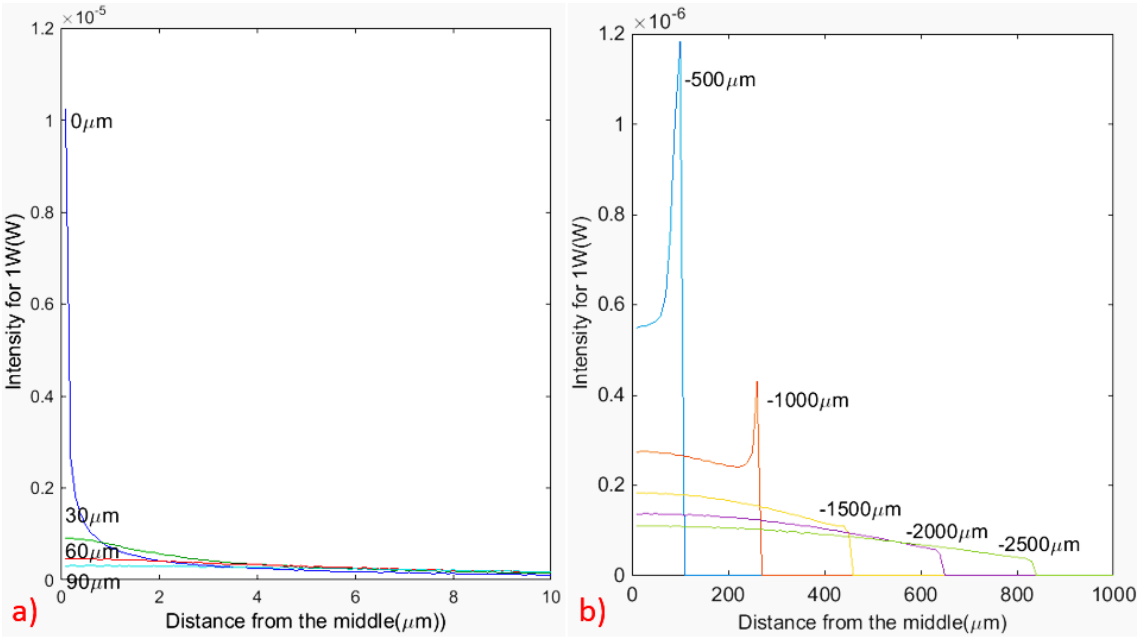

Fig 2.9 Profile of Simulated intensity distribution in r direction over a large z range (a). From 90 μm to 0 μm (the focus), (b). From -500 μm to -2500 μm)

A Zemax program simulation based on the ray optics of the high-NA focal lens was used to evaluate the spherical aberration and aberration by passing through surface of the transparent material (typically glasses). The simulation begins by constructing the collection of rays focused to a point in air, and then introduces an interface with a given index of refraction. The lens used is a 10 mm plano-convex lens (Thorlabs, LA1116, BK7, *NA=0.54*) and the irradiation laser wavelength is 1030 nm, focused perpendicularly into borosilicate glass (*n=1.51*). The simulation results are presented in Fig 2.10. The simulation sets peak intensity of 1 W/mm^2 (continuous wave) in front of the focal lens and the total laser power is 9.8 W. At the focus the intensity increases to 2.16×10^5 W/mm^2 (in air) and 1.94×10^5 W/mm^2 (in glass). The beam waist diameters keep the same value of 1.3 μm both in air and in glass but the Rayleigh range changes from 5.2 μm to 7.9 μm, as predicted in Eq 2.21. When we zoom into the region around the focus area (Fig 2.10b and Fig 2.10c), the rays no longer come to focus at a single point on the axis. The marginal rays focus first and the rays in the middle focus late, which results in the blur similar to the discussion in [133].

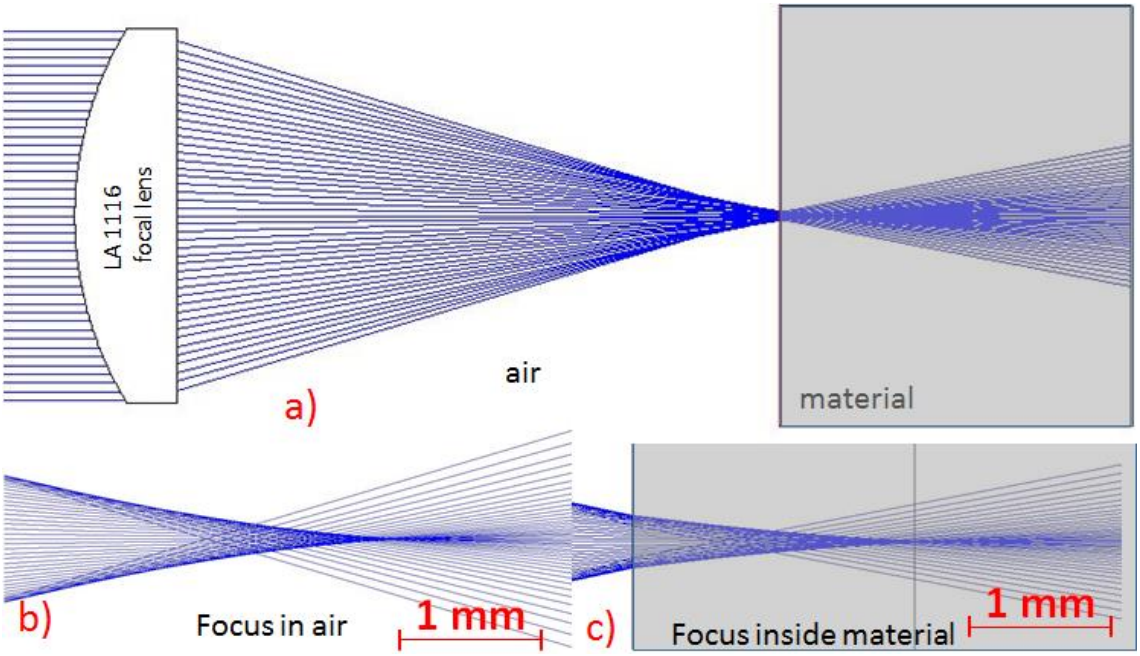

Fig 2.10 Zemax simulation of 10 mm lens (NA=0.54), (b).focused in air and (c).inside material (borosilicate glass). The laser wavelength 1030 nm and the peak intensity in front of the focal lens is 1 W/mm^2.

By considering the caustic (aberration of spherical lens), the curve formed by the outermost rays, reaches a minimum, we can estimate the minimal spot size to be 110 μm in air and 90 μm in glass, and the distance between the marginal ray crossing and the central ray crossing can be as long as 1 mm.

2.2 Nonlinear Propagation and Nonlinear Absorption

2.2.1 Self-Focusing

The phenomenon of self-focusing is a result of the intensity-dependent refractive index of the material, given by Eq 2.7. If a material exhibits an index that increases with the intensity of the applied field, then a propagating pulse that is more intense at its centre than at its edges (for example, a pulse that has a Gaussian transverse intensity profile) will experience a larger index at its centre, as shown in Fig 2.11. The pulse then effectively passes through a graded index lens, thus the pulse is focused. For ultrashort pulses the laser peak power can be extremely high, resulting in beam filamentation if the focusing effect is stronger than the beam divergence, which occurs above a certain critical power [12].

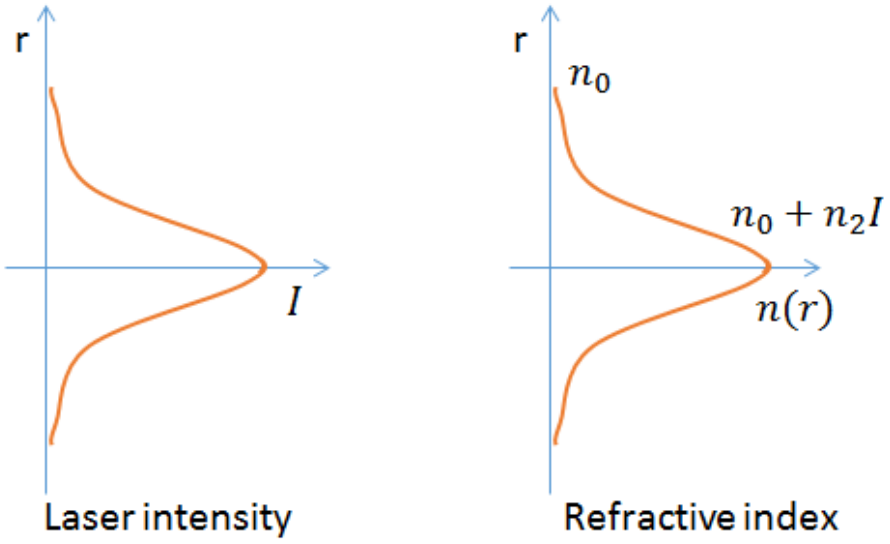

Fig 2.11 Material with an intensity-dependent refractive index. For a Gaussian beam, the middle of the beam experiences higher refractive index than the surround.

Although the refractive index varies depending on the laser peak intensity, the strength of the self-focusing lens depends only on the peak power of the laser pulses. the critical power P_{cr} for self-focusing is given by [135]:

$$P_{cr} \sim \frac{\pi \lambda^2}{8 n_0 n_2} \qquad \text{Eq 2.24}$$

where λ is the laser wavelength, n_0 and n_2 are the linear refractive index and second order nonlinear refractive index. P_{cr} is typically on the order of a few MW [136]. Self-focusing is a frequent cause of optical damage in transparent materials with ultrashort pulsed lasers. In real materials, other mechanisms halt the beam collapse caused by self-focusing inside material. In particular, as the laser beam self-focuses, the laser intensity increases and is eventually strong enough to be nonlinearly absorbed inside the material. A plasma is formed, and it contributes a negative refractive index change (because the free electrons contribute negatively to the refractive index), which compensates the positive refractive index change produced by the intensity-dependent refractive index and prevents further self-focusing [137].

2.2.2 Nonlinear Absorption

The energy of a photon is $E = h\nu$ based on Planck-Einstein equation [138]. For a wavelength of 500 nm, the energy of a photon is 4×10^{-19} J or 2.5 eV, which is

insufficient to excite an electron from the valence band to the conduction band for a pure material which has a forbidden band gap larger than this, so the material shows transparency to this wavelength. In laser materials processing this can be overcome in different ways. The first solution is simply heating the opaque materials through absorption of laser energy, which is a thermal or pyrolytic process. Secondly higher energy photons (like UV) can be used which can break the chemical bonds directly; this is a photolytic process. The third option is using a high power laser that delivers so many photons at a time that electrons interact with several photons simultaneously. This method of absorption is called nonlinear absorption and is the reason ultrafast laser pulses are used for machining of transparent materials. In this case the photon energy, and hence the wavelength, is less important because energy is transferred by multiple photons simultaneously. There are two different nonlinear excitation mechanisms, photoionisation and avalanche ionisation, which plays different roles at different absorption stages.

2.2.2.1 Multiphoton Ionisation

Photoionisation refers to excitation of electrons from the valance band into the conduction band by a laser. The material can be either ionised through a tunnelling effect or multiphoton absorption depending on the laser frequency and intensity [14]. In tunnelling ionisation, the electric field of the laser suppresses the Coulomb well that binds a valance electron to its parent atom, seen in Fig 2.12a. If the electric field from the laser field is very strong ($|E| > 10^9\ V/cm$), the Coulomb well is supressed sufficiently that there is a significant probability that the bound electron can tunnel through the barrier and become free.

On the other hand, multiphoton ionisation (MPI) occurs when the electron simultaneously absorbs two or more photons whose combined energy is sufficient to exceed the material band gap [139], seen in Fig 2.12c. The transition point between multiphoton ionisation and tunnelling ionisation was worked out by Keldysh [140], the Keldysh parameter γ is defined as:

$$\gamma = \frac{\omega}{e}\left[\frac{mcn\varepsilon_0 E_g}{I}\right]^{1/2} \qquad \text{Eq 2.25}$$

where ω is the laser frequency, I is the laser intensity at the focus, m and e are the reduced mass and charge of the electron, c is the speed of light, n is the refractive index

of the material, E_g is the band gap of the material, and ε_0 is the permittivity of free space. When the Keldysh parameter is larger than around 1.5, photoionisation is a multiphoton process, while tunnelling is dominant when this parameter is smaller than around 1.5. In the intermediate regime, the photoionisation is a mix of the two, seen in Fig 2.12b.

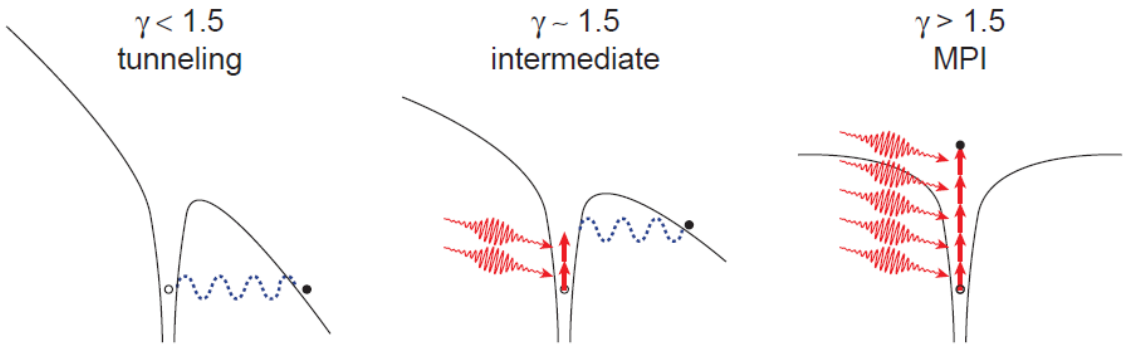

Fig 2.12 Schematic diagram of photoionisation for different Keldysh Parameter [14].

The photoionisation rate depends strongly on the laser intensity. In the multiphoton ionisation regime, the rate is

$$\left(\frac{d\rho}{dt}\right)_{MPI} = \sigma_N I^N \qquad \text{Eq 2.26}$$

here σ_N is the N-photons absorption coefficient. The N number is determined by the smallest integer that satisfies the relation $\frac{Nhc}{\lambda} \geq E_g$. Generally speaking, tunnelling ionisation dominates for strong laser fields and low (far IR) optical frequencies. At high frequency (visible or near IR), multiphoton ionisation becomes the dominant mechanism.

2.2.2.2 Avalanche Ionisation

An electron in the conduction band of a material exhibits linear absorption of other incident laser photons. The collision of this high energy electron with a valence electron may result in two excitation electrons (in the conduction band), each of which can absorb laser photons and subsequently ionise additional valence band electrons. As long as the laser field is present, the electron density in the conduction band grows according to

$$\left(\frac{d\rho}{dt}\right)_{Av} = \eta(E)\rho \qquad \text{Eq 2.27}$$

where $\eta(E)$ is the avalanche ionisation rate and E is the electric field of the laser. Avalanche ionisation requires some seed electrons in the conduction band. These initial electrons are either provided by thermal excitation and defect states, or by photoionisation. The diagram of avalanche ionisation is shown in Fig 2.13.

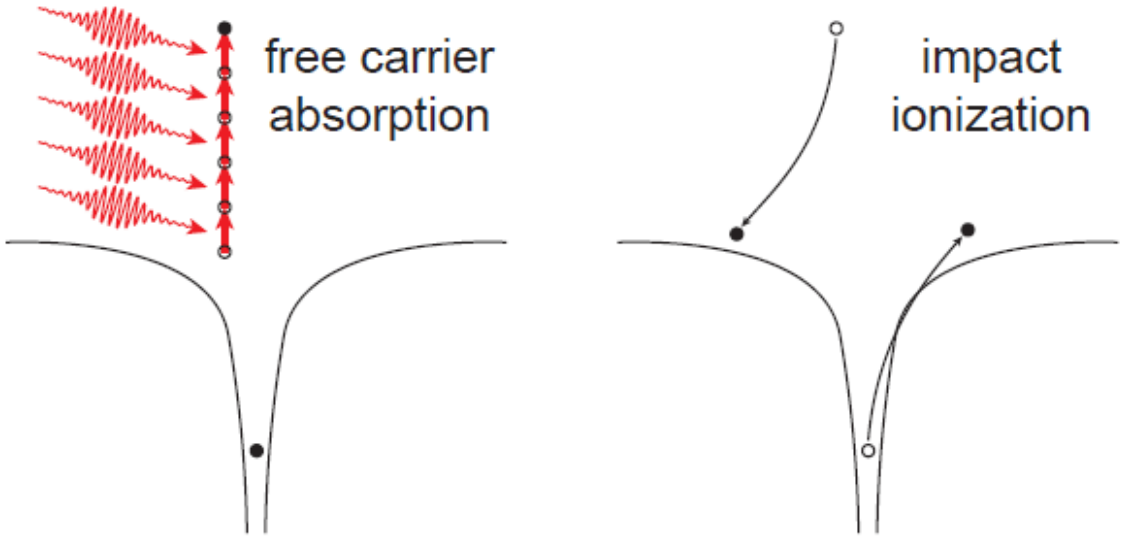

Fig 2.13 Schematic diagram of avalanche ionisation. An initial free electron linearly absorbs several laser photons, then impact ionises another electron [136].

2.2.2.3 Plasma Absorption

The plasma formed by multiphoton and avalanche ionisation can strongly absorb laser radiation when the plasma density becomes sufficient. Plasma density *N*, grows until the plasma frequency reaches the laser frequency, then the absorption becomes very efficient. The plasma frequency given by:

$$\omega_{\mathrm{p}} = \left[\frac{Ne^2}{\varepsilon_0 m}\right]^{1/2} \qquad \text{Eq 2.28}$$

and the plasma absorption coefficient is given by

$$\kappa = \frac{\omega_p^2 \tau}{c(1+\omega^2\tau^2)} \qquad \text{Eq 2.29}$$

where ω is the laser frequency, and τ the phenomenological Drude scattering time (usually around 0.2 fs) [141]. From Eq 2.29 the plasma absorption coefficient is proportional to the plasma particle density. Since the plasma is confined by the cold material around it (where the laser has been focused inside the material), the plasma density easily achieves a high level. Experimental investigations of plasma absorption are presented in section 4.1.4.1 and section 6.2.2.4.

At the onset of nonlinear absorption, one can imagine most of the laser power will pass through the materials as the nonlinear absorption is weak. The weak and nonlinear absorption deposits energy in the absorption volume will cause defects in the material which provide an efficient route to faster the absorption.

Once the critical plasma density is reached, the originally transparent or semi-transparent material becomes opaque, and a large percentage of the absorbed laser energy is deposited in a thin plasma surface layer [142]. Hence, the laser threshold fluence can be considered as the minimal fluence to create the critical density. The plasma eventually becomes self-sustainable so it grows up and expands out of the focal region (mainly towards the incident laser direction).

2.3 Energy Transportation inside Material

Ultrafast laser interactions with materials can be divided into two stages: (i) photon energy absorption, mainly through free electron generation and heating, and (ii) the redistribution of the absorbed energy to the lattice leading to material melting [122].

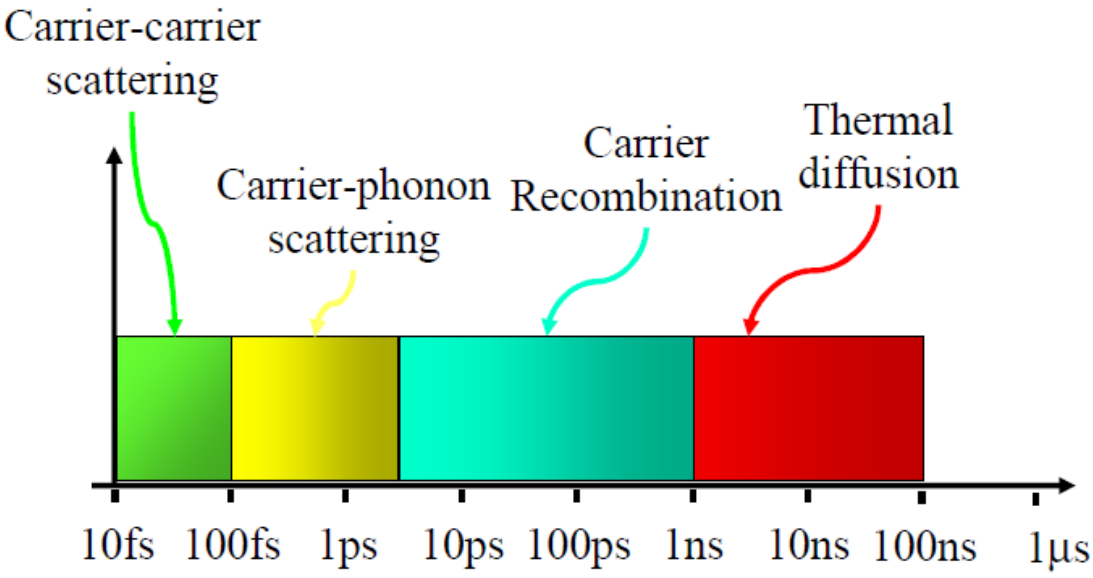

Fig 2.14 Schematic diagram of the time scale of electronic interactions [143].

The previous section presented how nonlinear absorption leads to the ionisation of the transparent material. This first stage is completed in such a short time that the lattice temperature remains unchanged within the subpicosecond regime. Once excited, the electrons quickly relax through a number of processes such as thermalisation, carrier removal, and thermal diffusion/structural changes. Fig 2.14 shows the time scales for a number of relevant physical processes involved in ultrafast laser micromachining. Thermal transportation takes three steps from energy absorption of an ultrashort pulse to distribution in the material:

2.3.1 Free Electron-Material Equilibrium

After excitation, electrons and holes are redistributed throughout the conduction and valance bands via carrier-carrier scattering and carrier-photon scattering. Carrier-photon scattering does not change the number of carriers, however, their energies decrease due to spontaneous emission, which transfers energy to the lattice. It takes many scattering processes and a timescale of a few picoseconds before the temperatures of the free electrons and the material are in equilibrium [11].

2.3.2 Carrier Recombination

Once the carrier and the material are in equilibrium, the material is at a well-defined temperature, meanwhile, there is still an excess of free carriers compared to thermodynamic equilibrium. The excess carriers are removed either by recombination of electrons and holes or by diffusing out of the excitation region. Free carrier recombination can either be radiative or non-radiative. This process lowers both the energy and density of free carriers, and takes place in a timescale of nanoseconds [144]. A pressure or a shock wave driven by the condensed plasma appears around the focal volume [126][145][146].

2.3.3 Thermal Diffusion

When free carriers and the material reach an equilibrium temperature and the free carriers have been dissipated due to recombination, the material is essentially the same as that heated by conventional means. On a nanosecond to microsecond timescale, the thermal energy diffuses out of the energy absorption region. At a sufficiently high energy these processes cause melting or non-thermal ionic motion. Resolidification or condensation ensues as the temperature falls below the melting points, and leaves permanent structural changes [10][36].

2.4 Thermal Stress Model for Dissimilar Material Welding

In order to better understand the thermal stresses induced during ultrafast laser welding, a simple model (based on W. Chen etc. [164]) is introduced here to evaluate the interface shear stress due to differential thermal expansion of the two materials.

2.4.1 Continuously Welding Model

Assuming that the two materials are directly bonded together at the whole interface region, thermal processes during welding or ambient temperature changes will induce stress.

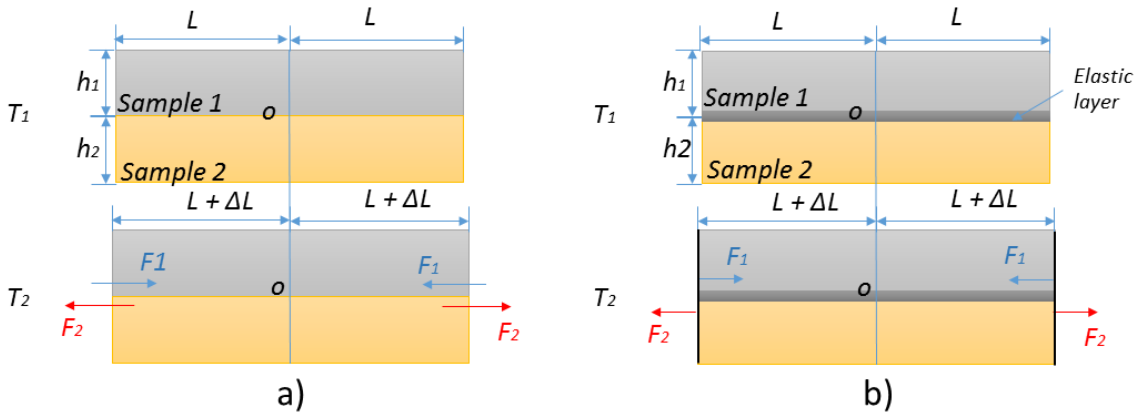

Fig 2.15 Schematic model interface force analysis of welding different materials. (a). No surface deformation, (b). Surface elastic deformation.

The model is constructed as shown in Fig 2.15. For the two samples bonded together have a uniform cross-section area (length $2L$ and width W, with thickness h_1 and h_2), elastic moduli (E_1 and E_2), and thermal expansion coefficients (α_1 and α_2). It is assumed that no bending or deformation occurs during the thermal process and at temperature T_1 the interface is stress free, at temperature T_2, the force at the surface of the two samples due to the thermal expansion are F_1 and F_2. If we making the assumption that there is no elastic deformation (Fig 2.15a), the shear force between the two surfaces is easy to be deduced from Young's modulus and the thermal expansion formula:

$$F = \frac{EA\Delta L}{L} \text{ and } \frac{\Delta L}{L} = \alpha \Delta T \qquad \text{Eq 2.30}$$

as

$$F = \frac{E_1 E_2 A_1 A_2 (\alpha_2 - \alpha_1)(T_2 - T_1)}{(E_1 A_1 + E_2 A_2)} \qquad \text{Eq 2.31}$$

Compared with Eq 2.30 and Eq 2.31, the stress does not depend on the length as the two samples combines as a whole with an effective elastic moduli-area to be $(EA)_{eff} = \frac{E_1 E_2 A_1 A_2}{(E_1 A_1 + E_2 A_2)}$, for a uniform format of $F = (EA)_{eff}(\alpha_2 - \alpha_1)(T_2 - T_1)$.

But in a real situation the interface is not as rigid as the conditions above. There are some micro-deformations during the thermal expansion (or contraction) that make the interface elastic. We assume the elastic layer has a thickness *d* and shear modulus *G* (Fig 2.15b). The shear stress of the surface τ and the forces F_1, F_2 are related through equilibrium of the forces and the stress-strain-temperature relations [164], the shear stress at the interface is given by

$$\tau = \frac{(\alpha_2 - \alpha_1)(T_2 - T_1) G \sinh \beta l}{\beta d \cosh \beta L} \qquad \text{Eq 2.32}$$

where $\beta^2 = \frac{Gw}{d}\frac{(E_1 A_1 + E_2 A_2)}{E_1 E_2 A_1 A_2}$, and *w* is the width of the weld seam [164].

Physically the shear stress is zero at the centre (zero position in Fig 2.15b), and increases gradually to a maximum at the free edge. The maximum stress is (if βL is small),

$$\tau = \frac{(\alpha_2 - \alpha_1)(T_2 - T_1) LG}{d} \frac{\tanh \beta L}{\beta L} \approx \frac{(\alpha_2 - \alpha_1)(T_2 - T_1) LG}{d} \qquad \text{Eq 2.33}$$

For glass-metal welding, the glass has quite high rigidity (or shear modulus *G*) and low deformation (smaller *d*) compared with metal. From Eq 2.33 the interface shear stress of the two different materials bonding increases with the weld size (*L*). The sample usually cracks at the edge of the weld if a large continuous area is welded.

2.4.2 Discrete Welding Model

Initially a spiral pattern was used for welding glass to metal. A model is setup based on stress-strain-temperature relations of the spiral pattern. For simplicity, consider a one dimensional situation illustrated in Fig 2.16, the spiral has *n* revolutions from the cross-section (only 4 revolutions of seams are presented in Fig 2.16), and each seam has an elastic layer thickness *d*, seam width *X* and shear modulus: *G*. Again, thermal processes

during welding or an ambient temperature change will induce stress at the weld seams because of the different thermal expansion coefficients of the two material. Assume no bending or deformation during thermal process (Fig 2.16) and at temperature T_1 the interface is stress free.

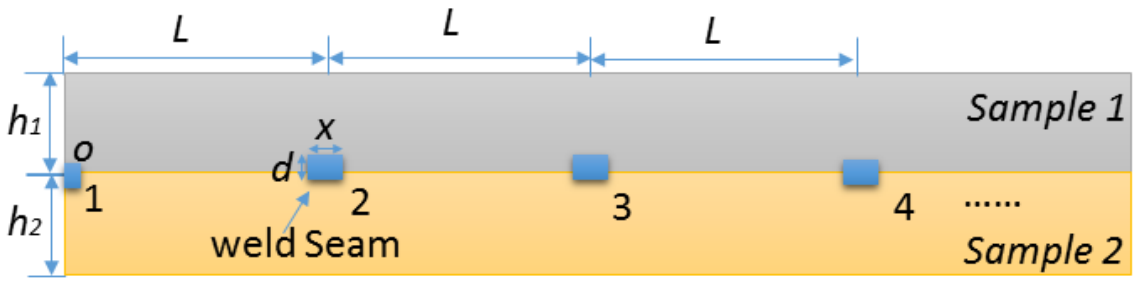

Fig 2.16 One dimension model for spiral pattern welding.

The distance between adjacent weld seams is L, and it is assumed that there is no shear force in the non-welded area. The material parameters are:

Sample 1: Young's modulus: E_1, sample thickness: h_1, thermal expansion: α_1.

Sample 2: Young's modulus: E_2, sample thickness: h_2, thermal expansion: α_2.

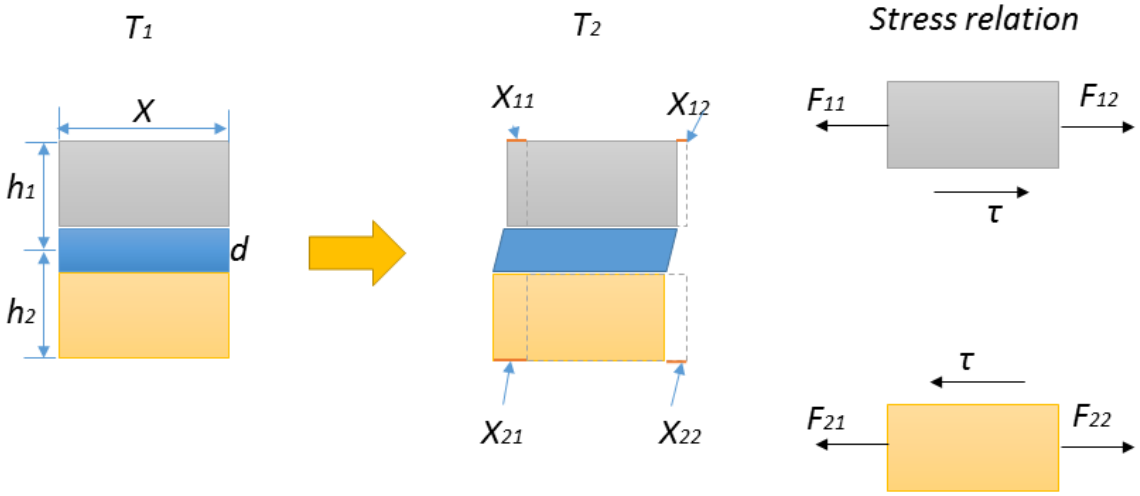

Fig 2.17 Length and force relation on the seam area.

The stress-strain-temperature relations for each of the seams are (τ: pressure of the area N/mm^2):

$$F_{12} - F_{11} + \tau A = 0$$
$$F_{22} - F_{21} - \tau A = 0$$

Eq 2.34

A is the weld area of the seam, and

$$X_{12} - X_{11} = \frac{F_{11}X}{E_1 A_1} + \alpha_1 \Delta T X$$
$$X_{22} - X_{21} = \frac{F_{21}X}{E_2 A_2} + \alpha_2 \Delta T X \quad \text{Eq 2.35}$$

and

$$(X_{22} - X_{21}) - (X_{12} - X_{11}) = \frac{\tau d}{G} \quad \text{Eq 2.36}$$

and the force

$$F_{11} = \frac{E_1 A_1}{L}(\alpha_1 \Delta T L - X_{11})$$
$$F_{21} = \frac{E_2 A_2}{L}(\alpha_2 \Delta T L - X_{21}) \quad \text{Eq 2.37}$$

For each of the seams (blue square represents the cross-section view in Fig 2.16), we have the same formulas as above (areas:$A = w_1.X, A_1 = w_2.h_1, A_2 = w_2.h_2$), $w_1$is the length of the seam, w_2 is the width of the samples.

At the outer boundary seam, the boundary condition of the force changed to:

$$F_{1n} = F_{2n} = 0$$

As there is no force applied to the material outside the seam. The outer boundary seam (the n^{th} seam) shear stress can be calculated as:

$$\tau_n = \frac{(\alpha_2 - \alpha_1)\Delta T X}{(\frac{d}{G} + DX^2)} \quad \text{Eq 2.38}$$

where define: D $= \left(\frac{1}{E_1 h_1} + \frac{1}{E_2 h_2}\right)\frac{w_1}{w_2}$, and the shear stress of the m^{th} seam is

$$\tau_m = \frac{(\alpha_2 - \alpha_1)\Delta T X - DX^2(\tau_{m+1} + \tau_{m+2} + \cdots \tau_n)}{(\frac{d}{G} + DX^2)} \quad \text{Eq 2.39}$$

Assume: $w_2 = 25\ mm\ and\ w_1 = 2.5\ mm$, and put in the parameters of fused silica and aluminium into the simulation. Material thickness $h_1 = h_2 = 1\ mm$, $d = 0.1\ mm$ (related to the HAZ height), temperature difference $\Delta T = 500\ K$.

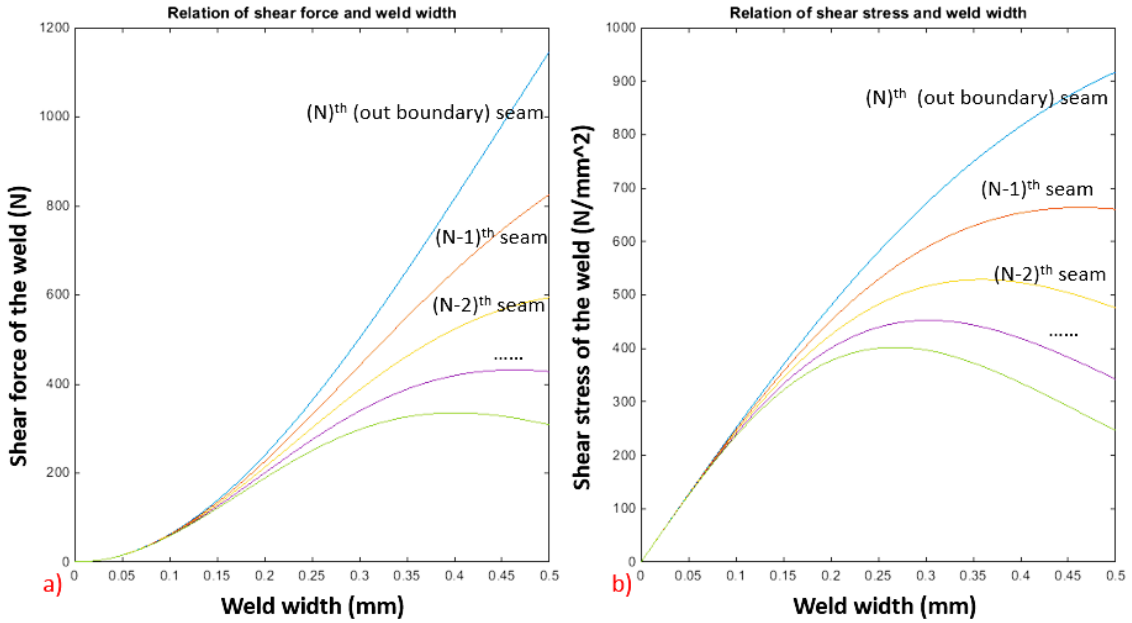

Fig 2.18 Simulation of shear force (a) and shear stress (b), average value of different seam numbers related with different seam width (assume ΔT=500 K, material: borosilicate glass and aluminium).

From the calculation, the outer boundary of the spiral weld suffers the largest shear force and stress, which gradually decreases as the spiral seam number of spiral revolutions decreases (from Fig 2.16). The shear force increases with the seam size (HAZ width) for all the seams, and then decreases (except the shear force of the n^{th} seam, which remains a maximum value as the seam width increases) at some seam width. In real weld, the width of glass-metal weld lies between 10 μm to 30 μm. Thus the outer boundary of shear stress is around 60 N/mm^2.

The outer boundary shear force and shear stress are plotted as a function of weld width for temperature difference (ΔT) in Fig 2.19. High energy deposition into a specific volume will induce huge temperature changes which causes a large shear stress increase. Note that material break stresses (for borosilicate glass, 113 N/mm^2) will crack the sample, which restricts the weld seam width and ΔT. Based on the deposited energy and thermal diffusion of the weld region, a temperature increase can be calculated for a 0.8 W laser absorbed in a 2.5 mm diameter region of a 25 mm ×25 mm ×1 mm material (an averaged maximum temperature increase in the weld region) as 216 K for borosilicate

glass, 184 K for fused silica, 31 K for aluminium and 41 K for stainless steel 304 (temperature calculations are based on the simulation of the material/circumstance conditions with Comsol software).

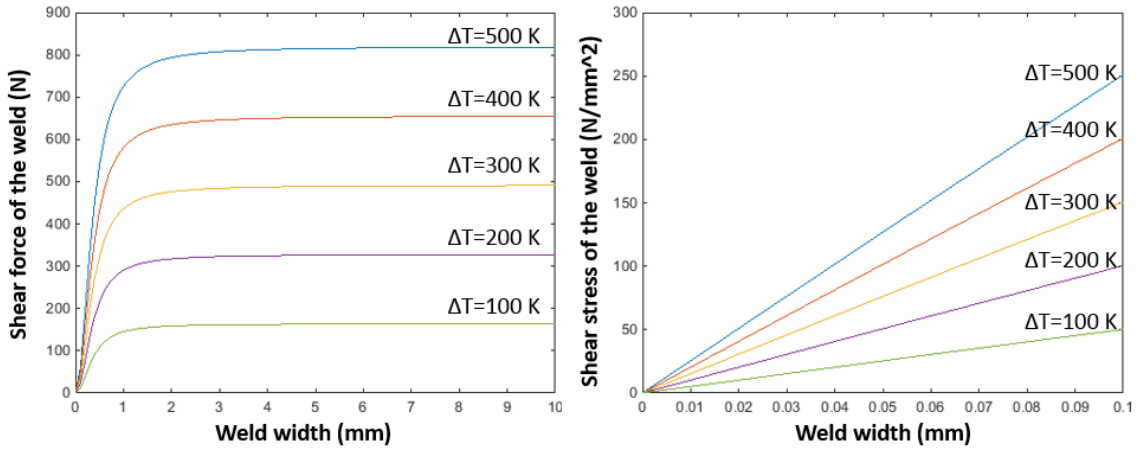

Fig 2.19 Simulation of relation of shear force and shear stress (average value) of the nth (out boundary) seam and different seam width with different deposited temperature (average temperature during the process, material simulated: borosilicate glass and aluminium).

2.5 Ultrashort Pulse and Longer Pulse Comparison

Understanding the different timescales involved in converting the laser pulse energy into structural change provides an insight into why ultrashort laser pulses are well suited for micromachining applications. For longer pulse durations, energy is being transferred from the laser excited electron plasma to the material on a timescale of the pulse duration. The hot electrons rapidly equilibrate with the material through phonon emission and sufficient excitation will melt the irradiated region. In the long pulse regime, the absorbed energy is carried out of the focal volume by thermal diffusion. Furthermore, the peak laser intensity required to produce the damage is not high enough to directly photoionise electrons, so either thermal excited electrons or impurity and defect states provide the initial seed electrons for the avalanche ionisation. Since the breakdown relies on impurity or defect states, its threshold has a non-deterministic nature. For a constant laser fluence near to the threshold some laser shots produce damage while other do not, depending on how many seeds electrons are in the focal volume of each shot, as can be seen from our weld with an angle test in section 7.5.

Conversely, as discussed previously, in the ultrashort regime, the pulse duration is much shorter than the time required for energy transfer to the lattice, hence decoupling the absorption and lattice heating processes [32]. Photoionisation plays an important role in the generation of conduction band electrons for ultrashort laser pulses. Photoionisation on the leading edge of the laser pulse provides the seed electrons for avalanche ionisation during the rest of the pulse [32]. This self-seeded avalanche makes short-pulse breakdown less dependent on defects in the material than longer pulse breakdown and therefore makes the threshold for short pulse damage very deterministic. For very short laser pulses, photoionisation can dominate avalanche ionisation and produce a sufficient plasma density to cause damage by itself [147], and high density plasma is formed, while the material remains at low temperature. Only after the pulse is gone, is the energy transferred to the material.

2.6 Summary and Conclusion

Optical property changes in transparent materials induced by laser pulses can be non-destructive phase transitions or irreversible structural changes. For ultrafast laser welding to work, the laser beam must be focused into a small volume inside the material using a high-NA optic to generate high laser intensities above the optical breakdown threshold (10^{12} W/cm^2 ~10^{14} W/cm^2).

This chapter reviewed and discussed the equations describing propagation of electromagnetic waves in a dielectric material. A theoretical description of a Gaussian beam focused into material using a high numerical aperture lens with paraxial and non-paraxial approximations was provided. The focal spot size could be obtained for a specific focus lens based on these calculations, from which a guide of laser power/pulse peak power could be made for nonlinear absorption inside material. A number of key results from linear and nonlinear optics are presented dealing with the beam propagation and absorption mechanisms inside transparent materials. The focal position for the laser beam focusing through the front piece of glass to the interface can be theoretically calculated based on Snell's law (Eq 2.20). And the actual focus size difference from theoretical calculation can be evaluated based on the paraxial and non-paraxial approximation. Aberrations introduced though different situations (spherical lens, abnormal incidence and beam highly focused into material) were evaluated and discussed and the laser intensity distribution inside material around the focus was simulated. Aspherical lenses are usually used to replace spherical one to reduce the

spherical aberration, and from the analysis, the deterioration of the focus increases with the amount of material focused through, it is instructive to estimate the depth at which focusing at a given NA is no longer diffraction limited. Although this ray-tracing technique is not the most rigorous possible, it does draw attention to possible problems when using such tight focusing. A spiral pattern stress model was built up and the stresses of each revolution related with weld width and temperature change ΔT was plotted. Based on the simulation, welding of specific materials with specific, different thermal expansions, sets the limit of the weld seam width and temperature deposition during the welding process for a successful weld. Finally thermal transportation in an ultrashort time scale was described and the thermal dynamics of short and longer pulses were compared which showed in fs to ns scale the advantage of short pulses for micromachining.

Chapter 3 Ultrafast Laser Welding Setup

Ultrafast laser welding permits direct welding of glass with glass, or glass with opaque materials of significantly different thermal expansion. The heat affected zone (HAZ) introduced during the ultrafast laser welding process can be as small as 10's of micrometres which enables high precision micro-joining without thermal distortion issues within the bulk material. Ultrafast laser welding, which allows absorption inside transparent material based on nonlinear absorption, enables welding between transparent materials without any intermediate layers. Unlike tradition methods, absorbing energy at the front surface of the material where it diffuses to the interface for welding (i.e. conduction mode welding), or generates a keyhole penetration deep into the material (keyhole welding) [148], ultrafast laser pulses are absorbed directly at the interface, which allows the top surface remain intact. Ultrafast laser welding requires quite a different optical setup from traditional laser welding, the following points should be considered:

For ultrafast laser welding of two transparent materials, the laser beam needs to be tightly focused into a spot to generate high laser intensity. This, together with the ultrashort laser pulses, concentrates light spatially and temporally, bringing about nonlinear absorption and hence local joining. Thus a high-NA lens is required to generate peak intensity above the material breakdown threshold.

This high laser intensity, inducing nonlinear absorption within a small volume at the focus, acts as the initial absorption mechanism and is followed by plasma absorption and other linear absorption processes (i.e. defect absorption), this results in the pulse energy deposition in a 100 μm scale tear-drop shaped area. High precision stages are required to make sure the focus stays at, or around, the interface during welding and a feedback/monitoring system with a position resolution of less than 20 μm is needed to trace the focal position during this process.

The mechanics of directly welding two close surfaces together without frit or interlayer also requires a special clamp rig to keep the two surfaces in firm optical contact during welding.

This ultrafast laser welding project is based on our Trumpf TruMicro 5x50 picosecond laser system. Before this PhD project started, a fundamental setup was built up by Dr Richard Carter, a research associate in our group. The setup includes:

Optical system: ultrafast laser, a polarisation attenuator, a beam expander and a lens together with two reflecting mirrors mounted in support cages;

Sample holder: a sample clamp comprising a three point loading cover and a piston with a single ball on top (Fig 3.10);

Stage and control: three axes stages (Aerotech Pro115 stages) and stage control software (Aerotech Ensemble).

This setup was successful in producing proof of principle demonstrations. In the following sections the experiment setup will be presented in details. Laser parameter requirements will be discussed with components and parameters considered for successful welding. Sample preparation and arrangement methods will be introduced for a clear view of ultrafast laser direct welding. The welding procedure will be described and discussed commenting on the differences for glass-glass welding and glass-metal welding.

3.1 Setup Introduction

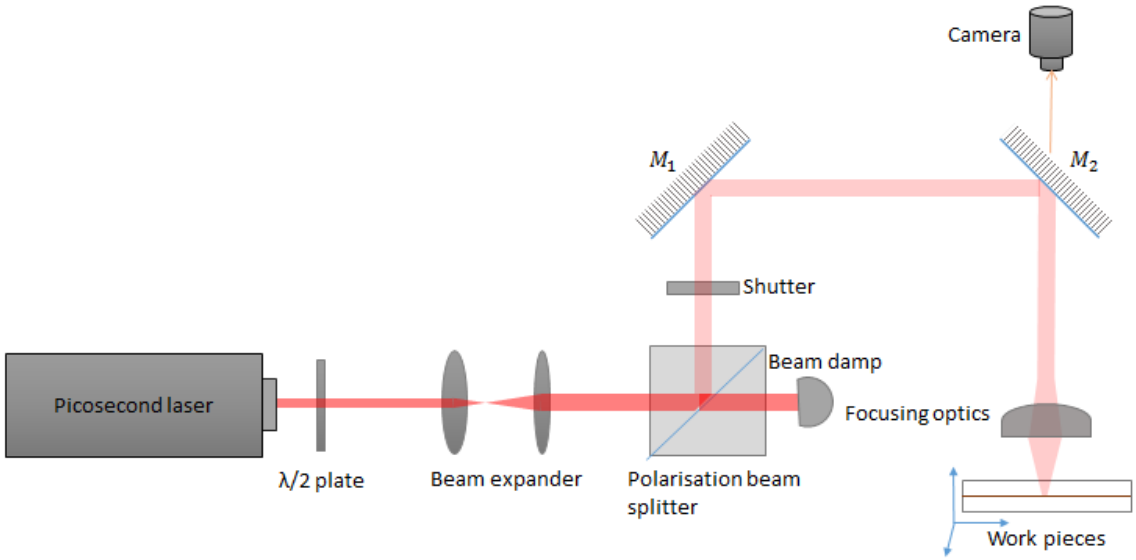

Fig 3.1 Schematic of ultrafast laser welding setup. Laser output polarisation perpendicular to the paper plane. λ/2 plate and polarisation beam splitter form a laser power attenuator. M_1 and M_2 are fixed mirrors. Working pieces (samples) are scanned by motion of the 3-axes stages.

A schematic diagram for the ultrafast laser welding setup is shown in Fig 3.1. Experiments were carried out using a Trumpf TruMicro 5x50 picosecond laser with a pulse duration of 5.9 ps and repetition rate of 400 kHz. The laser beam passes through

an attenuator consisting of a $\lambda/2$ plate and a polarisation beam splitter. A beam expander gives a ~×2 beam diameter to a 12.7 mm (all the beam sizes are described in FWHM in this thesis and the beam intensity profiles were measured with a CCD). The laser beam is focused into the work piece using a high-NA spherical or aspherical lens. A CCD camera is used to monitor the reflection and scattered light at the focus location. Both the focusing optics and laser pulse energy are chosen to provide a suitable power density, dependent on the material composition and conditions. Before welding, the 3-axes stages adjust the sample height based on the camera image to ensure the laser is focused at the interface. Beam translation is realised by moving the work piece in the x-y plane in a pattern defined by various laser scanning strategies.

In addition to our picosecond laser system, two femtosecond lasers, a Bluecut 10 and a Pharos both from Photonic Solutions Ltd. (laser details shown in Table 3.1), were used for testing laser pulse durations and repetition rates. The test setups share the same layout as in Fig 3.1, but the output beam diameters of the femtosecond lasers are smaller compared with the picosecond laser, thus the beam expanders were altered to provide beam diameters of 6 mm after expansion.

3.1.1 Parameter Consideration

For a successful weld many factors need to be considered for different materials:

1. Laser pulse parameters—energy, duration, and repetition rates
2. Lens and beam parameters—beam diameters, focal length, and focal spot size
3. Scanning parameters—scan speed and focal position
4. Surface parameters—roughness and interface separation

These parameters may have interactions with each other. So during the parameter tests, usually only one or two parameters are altered while the other parameters are kept the same. These tests observed their influence on the weld appearance or HAZ after being cross-sectioned.

The reflection at the interface is relatively unimportant for ultrafast laser welding as the high power pulses will destroy the surface after only a few pulses as a result of the interface melting. The upper surface reflection of the optical material is important, however, in particular for a high refractive index contrast.

The laser repetition rate mainly influences thermal accumulation around the focal region. Heat builds up based on the relation between the thermal diffusion time and the ultrafast pulse interval. Based on this thermal accumulation, pulsed laser micromachining can be roughly divided into two regimes:

Low repetition rate regime (kilohertz or below): The laser pulse separation time is far larger than the time required for heat to diffuse out of the focal volume for typical glasses. The focal volume thus returns to normal temperature before the next pulse arrives. Structural changes are hence localized in the laser focal region because as they are only based on the localised nonlinear absorption [149].

High repetition-rate regime (megahertz): Thermal accumulation effects occur. The laser pulses collectively act as a point source of heat at the focal volume within the bulk material when the time interval between successive pulses is much shorter than the time scale for diffusion of heat out of the focal volume. The temperature increases due to accumulated heat and the diffusion of that heat enlarges the modified volume. This process can be useful for decreasing the thermal gradient, which is quite important for localised brittle material processing.

How much laser power is enough for ultrafast laser welding? Generally speaking, the average power should be high enough to generate HAZ (i.e. a melt region) while not cracking the material. Peak power must be high enough to generate nonlinear absorption inside glass, leading to plasma generation. The plasma will then dominate the laser absorption process. In general, a higher laser power gives larger welding seams, whilst excessive energy introduces high residual stresses, and also generates bubbles or voids in the joining area, which makes the bond weak or, in severe cases is enough to crack the sample.

The Trumpf Trumicro 5x50 is an industrial level high average power laser system for high quality microprocessing with material drilling, cutting and ablation. The maximum output power of the laser in the infrared (1030 nm) is 50 W. A polarisation power splitter was inserted in the beam path to attenuate the laser power (Fig 3.1), to provide a flexible adjustment of laser power.

To obtain sufficient laser power density for nonlinear absorption, a high-NA lens was used to focus the beam into a small spot. For a Gaussian beam focus (assuming no aberrations), the spot diameter can be calculated using:

$$d = \frac{4M^2 f\lambda}{\pi D}, NA = \frac{D}{2f} \quad \text{Eq 3.1}$$

here D is the beam diameter, λ the wavelength and f is the focal length of the lens. For our laser system (1030 nm, a beam diameter of 12 mm and $M^2 = 1.4$) an $f = 10$ mm achromatic lens will produce a focal spot diameter of 1.3 µm. For the smallest spot, the beam diameter D is adjusted to be the same of the lens aperture. The lenses used in our experiments had focal length of 10 mm (*NA=0.54*, spot diameter 1.3 µm, Rayleigh length 1.8 µm), 20 mm (*NA=0.28*, spot diameter 3.1 µm, Rayleigh length 7.3 µm) and 40 mm (*NA=0.14*, spot diameter 6.2 µm, Rayleigh length 29.3 µm). The influence and testing of different lenses will be discussed in Chapter 4.

The stages are Aerotech Pro115 mechanical-bearing ball-screw linear stages with a motion programmable Aerotech software interface. The stages move with bidirectional repeatability of 1 µm and maximum travel speed of 300 mm/s. In our ultrafast laser welding experiments a scan speed of 1 mm/s to 10 mm/s was used to ensure a suitable pulse overlap for linear absorption, nonlinear absorption and thermal accumulation. Precise positioning and movement control is essential in order to ensure that the beam is focused at the interface of the two samples. Due to the small Rayleigh range of the focus (~7.3 µm for the 20 mm lens) combined with the HAZ generated by the laser pulses, the focus needs to be less than 50 µm from the interface. The stages movement is controlled by software: Aerotech Ensemble motion controller. A shutter placed in the beam path controlled by the software provides a flexible method to synchronise the laser and the stages.

Before laser welding, a laser back reflection is detected via a CCD camera for laser focus positioning. A high neutral-density ND filter is put in front of the CCD camera to ensure that a back reflection is only obtained when the laser focused near the surface of the workpieces (which has the highest back reflection intensity). Our CCD camera has no focusing optic, which means that when a spot is focused onto the camera the laser is not focused on the sample surface. This helps prevent damage when to the sample surface when imaging on the CCD. The smallest, and brightest focus on the CCD, ($z = 0$ µm) occurs where the focus is slightly above the surface, as we can see from the schematic in Fig 3.2. This method gives a resolution of less than 5 µm although it is qualitatively by eye (as seen in Fig 3.13).

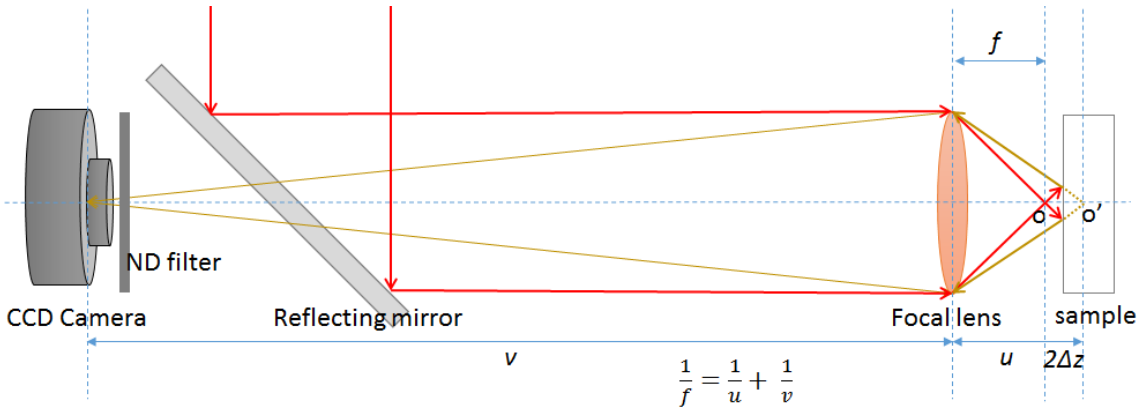

Fig 3.2 Optical relation of CCD camera focus positioning

When laser is focused on the surface of the sample, the reflected laser light will take the same beam path back as the irradiation beam, based on the standard thin lens formula:

$$\frac{1}{f}=\frac{1}{u}+\frac{1}{v} \qquad \text{Eq 3.2}$$

$$u = f + 2 * \Delta z$$

where u is the object distance, v is the image distance and f is the focal length of the lens, Δz is the distance between the focal plane and the sample surface. For our system, v = *1.8 m*, and usually 10 mm, 20 mm and 40 mm lens are used, so Δz can be easily calculated as 0.028 mm, 0.112 mm and 0.455 mm respectively, although this also depends on how well collimated the incident laser beam is. Thus after obtaining the image position, a stage movement of Δz upward is required to focus the beam on the sample surface.

Table 3.1. Ultrafast lasers used for the laser welding experiments

Parameter	TruMicro 5x50	BlueCut 10	Pharos SP
Wavelength	1030 nm/515 nm/343 nm	1030 nm	1028 nm ±5 nm
Average power	50 W/30 W/15 W	6 W	6 W
Beam quality M^2	1.3	< 1.25	< 1.3
Max. pulse energy	125 µJ/75 µJ/37.5 µJ	10 µJ*	12 µJ
Pulse duration	5.9 ps	300 fs	190 fs to 10 ps
repetition rate	400 kHz	100 kHz to 5 MHz	500 kHz

**For Blue cut laser the output limitation is maximum pulse energy 10 µJ or maximum average power of 6 W.*

For a comparison of laser repetition rate and pulse duration time, two femtosecond lasers were also used with similar experimental setups, a Bluecut 10 femtosecond laser and a Pharos laser, with the parameters listed in Table 3.1. From the table the pulse energy of the Bluecut 10 is quite low for a high repetition rate (i.e. only 1.2 μJ pulse energy for 5 MHz repetition rate), so during testing we kept the laser average output power the same (as opposed to the same pulse energy) and a dynamic polarisation adjustment was used to obtain a suitable laser power.

3.1.2 Material Properties

Material properties including: melting temperature, lattice structure, specific heat capacity, thermal expansion and thermal conductivity etc. greatly influence thermal process and hence laser welding parameters must be selected appropriately. For ultrafast laser welding, the brittleness of the transparent material (typically glass) is also very important, as is its initial surface condition (which should allow sufficiently good contact between the two materials), and the residual stress induced by the thermal process, determine if a successful weld can be formed without cracking. Surface roughness requirements for ultrafast laser welding are discussed in detail in section 3.2.2.

Ultrafast laser is mainly used for welding between different glass types or glass to opaque materials like aluminium or silicon, which have highly dissimilar optical, thermal and mechanical properties to the glass. For ultrafast laser welding, besides the material optical and thermal properties, different mechanical properties determine their different welding behaviours. Table 3.2 lists some relevant materials with properties related to ultrafast laser welding.

Table 3.2. Thermal and mechanical properties of different materials [118]

Material	**Coefficient of thermal expansion [10^{-6}/K]**	**Thermal conductivity [W/(m K)]**	**Heat capacity [J/(g K)] (25°C)**	**Melting point [^{0}C]**	**Density [g/cm^3]**	**Young's modulus[10^3 N/mm^2]**	**Tensile strength [N/mm^2]**
Fused silica	0.5	1.31	0.79	1600	2.2	72	92±13
Borosilicate glass	3.25	1.2	0.83	820	2.2	64	113±15

Material	Coefficient of thermal expansion [10^{-6}/K]	Thermal conductivity [W/(m K)]	Heat capacity [J/(g K)] (25°C)	Melting point [^{0}C]	Density [g/cm^3]	Young's modulus[10^3 N/mm^2]	Tensile strength [N/mm^2]
BK7	7.1	1.1	0.86	719	2.51	82	113±15
ULE	<0.001	1.31	0.77	1490	2.21	67	94±14
Sapphire	8.4	27.21	0.77	2040	3.98	345	1900
Zerodur	<0.1	1.46	0.82	1000	2.53	90	164±30
Aluminium	23.1	237	0.9	993	2.70	70	300
silicon	2.6	149	0.7	1414	2.33	165	7000
Stainless steel (304)	16-18	14-17	0.53	1723	8	151	860

3.1.3 Optical Contact

If two glass surfaces are pressed together, the area in close contact can easily be distinguished since both surfaces exhibit reflection and thus interference fringes appear with different colours observed due to the relation of surface separation and wavelengths of light, as seen from Fig 3.3. Optical contact occurs where two surfaces are sufficiently close, this means the surface separation is less than a quarter wavelength of visible light and no light is reflected from either of the surfaces. When the surface separation reaches the optical contact level, Van der Waals forces (between molecules or atomic groups) will rise and keep the two surfaces together, the Van der Waals force can be calculated as [150]:

$$F_{VW}(r) = -\frac{AR_1R_2}{6(R_1+R_2)r^2} \sim \frac{1}{r^2} \qquad \text{Eq 3.3}$$

where R_1 and R_2 are the assumed uniformed radii of molecules or atomic groups, A is the Hamaker coefficient ($\sim 10^{-19} - 10^{-20}$ J) which depends on the material properties (it can be positive or negative in sign depending on the intervening medium), and r is the distance between the two surfaces. From Eq 3.3 the Van der Waals force increases with surface separation decreasing, and disappears rapidly with surface separation r up to the micrometre level.

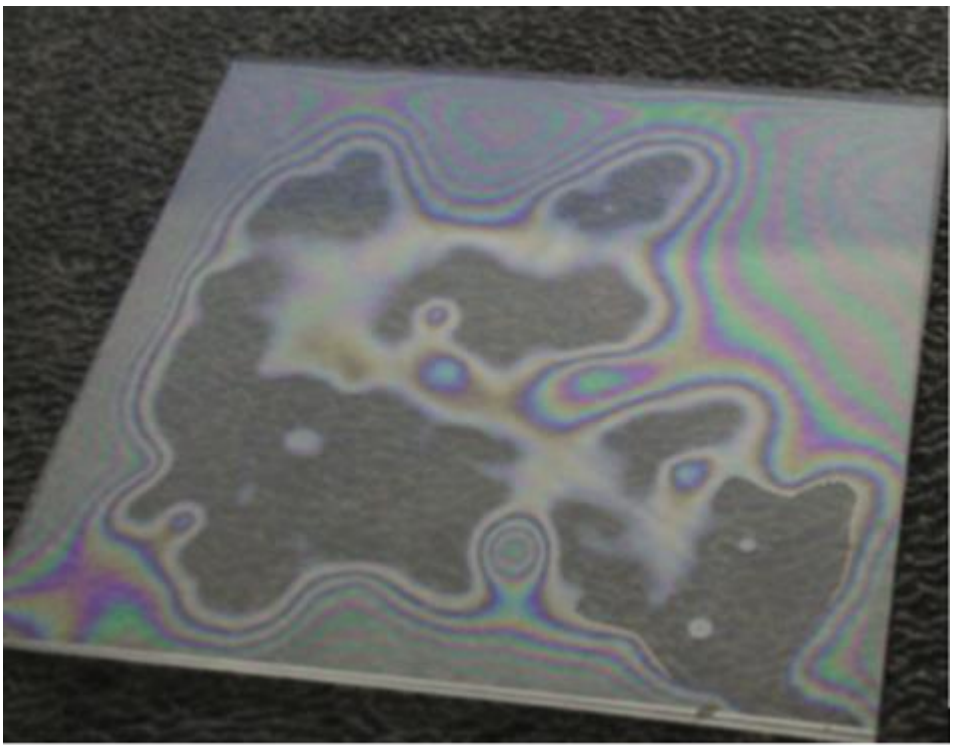

Fig 3.3 Photo of two pieces of glass close together. Optical contact, interference fringes and contaminants caused non-optical contact islands (with interference fringes around).

Direct bonding is accomplished by Van der Waals force when a substantial part of the area between two bonding surfaces is in optical contact. However, a direct bond does not well resist short and long-term elastic or plastic deformations following the application of large thermal or mechanical loads.

A particular issue with ultrafast laser welding is an assumed requirement for close contact between the surfaces to be joined. Previous reports on ultrafast laser welding have identified a requirement for the gap to be ~ 100-500 nm [2][10][151], in order to avoid cracking or ablating at the interface. Such close contact can be obtained by pressing two flat, smooth and clean surfaces together. But this method appears not stable for irradiating with ultrafast lasers as the heat induced deformation and shock waves introduced by laser pulses. So usually sample clamping is needed to maintain close contact at the interface during the welding process.

3.2 Sample Preparation

Accurate welding generally requires low surface roughness and high cleanness. Ultrafast laser welding, however, takes this to a much higher level. As a surface-surface

direct joining method, it demands the surface separation to be at μm or sub-μm level, and hence the surface roughness and smoothness must be less than this. Polished surfaces are thus typically required to provide a suitable small gap, preferably optical contact.

3.2.1 Surface Cleanliness

In addition to surface roughness issues, the sample surface needs to be cleaned before welding. Residual contaminants of even a couple of μm size would prevent close surface contact of a large area. Also contaminants of different materials may influence the miscibility of the two materials to be joined. A surface cleaning procedure is therefore followed, this starts with an acetone wash followed by wiping with clean lens tissue; the surface is then washed in acetone followed by methanol. If the method above is not sufficient, an acetone ultrasound bath is also used.

3.2.2 Surface Preparation Methods

A rough surface will disturb the beam wavefront passing through and thus distort the beam focusing quality as the beam is focused slightly beneath the interface. The gap between two joint surfaces also dramatically influences the welding e.g. reducing the welding strength or causing cracking.

Commercial glass surfaces are usually smooth and flat. For example, Schott BOROFLOAT®33 glass which is commonly used in our experiment is described as "an excellent mirror-like surface, a high degree of flatness and an outstanding optical quality", and the typical micro roughness of surface is less than 3 nanometres. For the glass surface, we only need to deep clean the surface using the procedure described above and it is good to use.

However, for ultrafast laser welding of glass to metal the surface of industrial parts or commercial products are usually not that good. Some surface treatment needs to be done before welding. In our lab the surface preparation methods include: workshop milling, grinding, polishing, and tumbling. In the figure below are pictures of the different metal surfaces tested for glass to metal welding.

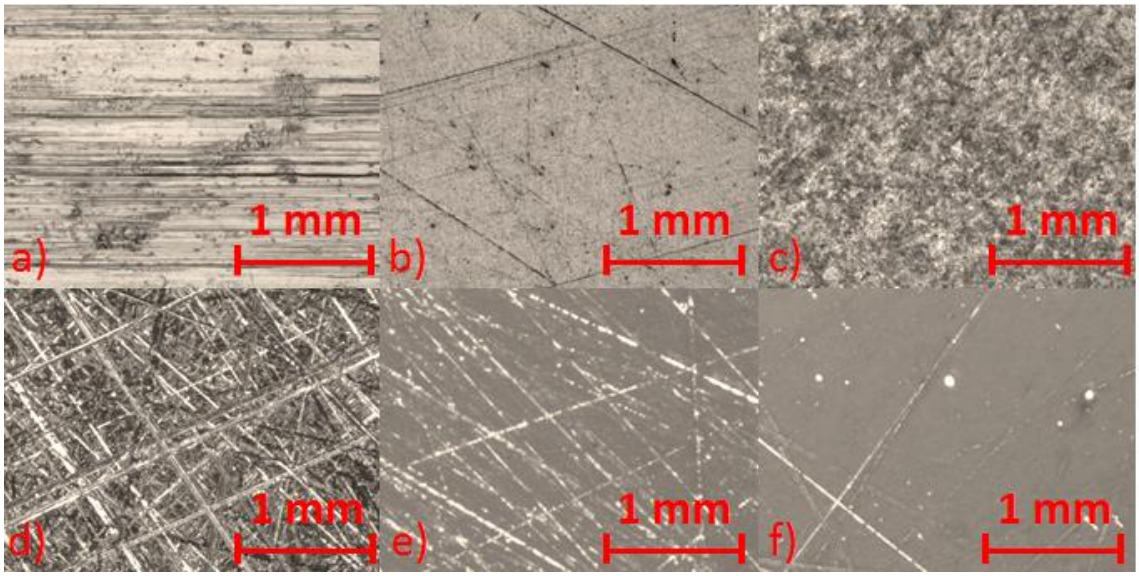

Fig 3.4 Optical microscope graphs of surface texture (on aluminium sheet) of different surface preparation methods: raw aluminium sheet surface (a), finely milled surface (b), tumbled surface (c), ground surface with P240 grit (seen in 3.2.2.1) (d), ground surface with P800 grit (e), ground surface with P4000 grit (f).

Surface flatness over a large scale of the sample is equally as important as the local roughness for a close contact. It needs to be noted that different surface preparation methods provide different surface flatness and smoothness, i.e. a polishing process with a rotating method can provide low local roughness but is less flat over a large scale.

Table 3.3. Surface Ra for different materials or polishing method (samples prepared in our lab and measured with Alicona InfiniteFocus).

Treatment method	**Roughness (*Ra*)**
Milling surface	1~3.5 um
Treating with laser	0.5~3 um
Glass surface	Less than 5 nm
Polished with 1 um diamond suspension	Less than 100 nm

3.2.2.1 Polishing

Polishing is a process to create a smooth surface by mechanical abrasion, chemical reaction or, more recently, through laser polishing. Polishing or buffing machines use an abrasive glued to a rotating wheel, which is brought into contact with the workpiece with a constant force. High rotating speeds (more than 20 m/s) with a fine grit (> P600)

can provide a surface roughness of less than 1 μm. A Struers Labopol-5 polishing machine with water lubricate/cooling is used in our lab for both grinding and polishing of the metal surface. *SiC* grinding paper and/or a polishing cloth with diamond suspension are used for different surface roughness. Table 3.4 shows a list of grit designation and diamond suspension grain size and their working particle sizes.

Table 3.4. Grit designation and diamond suspension grain size

SiC grit designation	**Mean diameter in μm**		**Diamond suspension**	**Diamond grain size in μm**
P60	269		**6**	6
P120	125		**3**	3
P220	68		**1**	1
P600	30.2		**1/4**	0.25
P1200	18.3			
P2500	10.3			
P4000	8.4			

Grinding is the first stage in mechanical material removal. Proper grinding removes damaged or deformed surface material while introducing as little new deformation as possible. When preparing sample surfaces for polishing, plane grinding (large grit) and fine grinding (small grit) are usually carried out to flatten the surface. The grinding process always begins with plane grinding. Plane grinding ensures that the surfaces of all samples are in the same condition before the preparation continues, and that the surfaces of all samples in a sample holder are at exactly the same level. Fine grinding must remove the deformation from cutting or plane grinding and produce a surface that is ready for polishing. Steps are carried out with smaller and smaller grit sizes *SiC* paper.

Fig 3.5 Photo of grinding/polishing machine.

To remove deformations from fine grinding and obtain a surface that is highly reflective, polishing is carried out on cloths of differing resilience with different abrasives. In our lab cloth with diamond suspension of different grain sizes are adopted for surface polishing. Diamond suspension sizes from 6 μm downward are sufficient for laser welding. Surface roughness of different grinding or polishing levels is measured with Alicona is presented below (Fig 3.6 and Table 3.5).

Table 3.5. Surface preparation methods and measured roughness (Alicona)

Surface preparation	**Roughness *Ra* (nm)**
Raw surface	623.1
P240 grinding surface	402.3
P600 grinding surface	263.5
P1200 grinding surface	140.4
P4000 grinding surface	64.2
Polished with diamond suspension	< 50

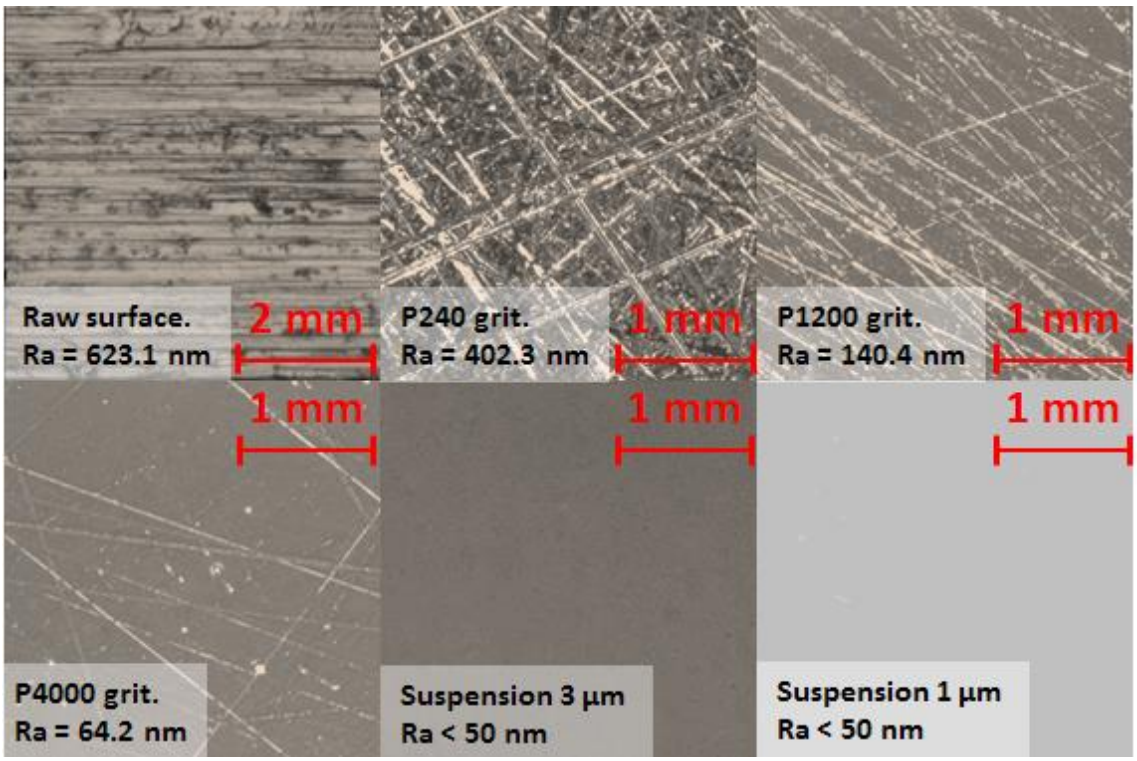

Fig 3.6 Grinding and polishing surfaces of different levels.

3.2.2.2 Milling

Milling covers a wide variety of different operations and workshop machines. Essentially it is the machining process of using rotary cutters to remove surface material from a workpiece feeding in a particular direction. It is one of the most commonly used processes in industry and machine shops for machining parts to precise sizes and shapes. The milling surfaces usually contain scratches along the rotation direction (see in Fig 3.7), which are due to the feeding speed and rotation rpm. With the advent of computer numerical controlled milling machines, high quality milling surfaces can be machined by feeding speed and rotation rpm control based on surface quality inspection. Table 3.6 shows the measured surface roughness of normal milled surface and finely milled surface prepared in our workshop.

Table 3.6. Surface roughness of milling in our lab (mean value, Alicona)

Surface	**Roughness *Ra* (nm)**
Milling surface	525.7
Finely milling surface	125.7

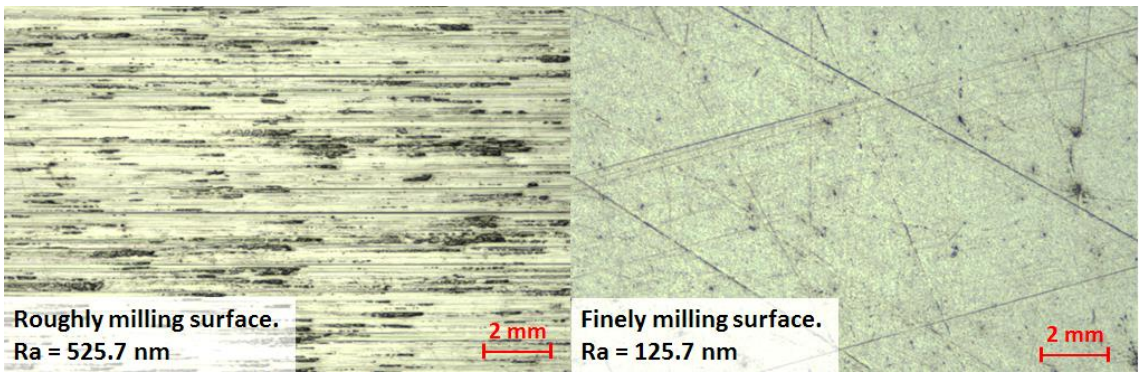

Fig 3.7 Normal milling surfaces and finely milling surface.

3.2.2.3 Tumbling

Tumble finishing is a common technique for smoothing a rough surface on relatively small parts. A plastic or rubber barrel is loaded with a consignment of parts, all of similar or the same hardness and size, some abrasive grit, and a liquid lubricant. Silicon carbide grit is commonly used, and water is a universal lubricant. The barrel is horizontally placed upon rotating rail with the optimal rotation speed depend on the size of the tumbler barrel and material involved. As the barrel is rotated the material rises until gravity causes the uppermost layer to landslide down to the other side. A well-chosen speed for polishing causes the parts within the barrel to slide past each other, with the abrasive grit between them. The result of this depends on the coarseness of the abrasive, and the duration of the tumble. Tumbling is usually most efficient with the barrel half full. The disadvantages of this process are that the abrasive action cannot be limited to only certain areas of the part. Fig 3.8 shows a typical barrel tumbling machine and the abrasive grit.

Fig 3.8 Typical tumbling machine (left) and abrasive grit (right).

The tumbled surface usually reaches a roughness (*Ra*) of 150 nm to 300 nm. The advantage of this process is a consistently similar roughness over a large area. One set of optimised welding parameters could potentially weld a large area without fault due to the highly uniform surface condition. Fig 3.9 shows the example tumbling surfaces, produced (i) using our tumbling system, and (ii) sample tumbled in Renishaw plc, who collaborates in this project.

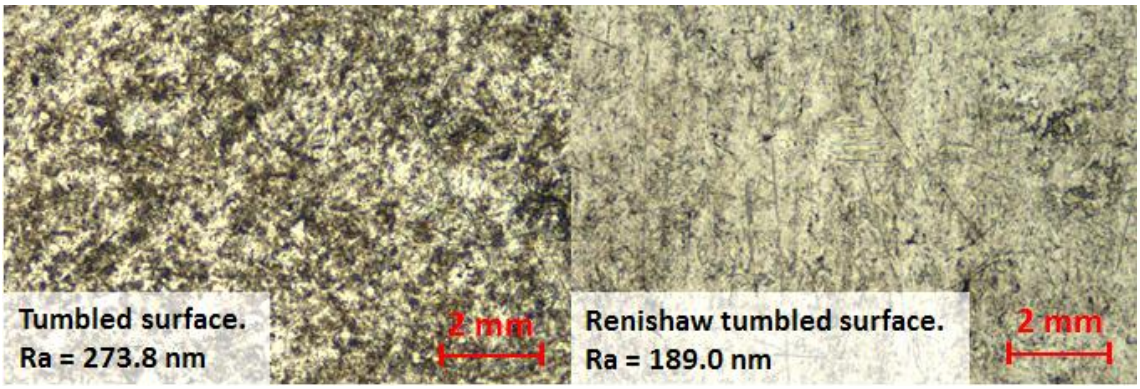

Fig 3.9 Our tumbled surface (Ra =273.8 nm) and surface tumbled in Renishaw (Ra = 189.0 nm).

3.2.3 Sample Cross-Section

To investigate the morphology properties of the weld area, a clear sectional view is needed under an optical microscope. It would be simple for transparent materials with mirror flat surfaces, but in most situations the samples need to be cross-sectioned to expose the weld region, due to phase disturbance from refractive index variations or dirt/faults around the weld region. Cross-section process is in two steps: cut and polishing. For ultrafast laser welding, the welds are usually small and the glass is brittle, so violent cut methods could not be used. A diamond saw with coolant is used for a smooth cut. Samples need to be mounted firmly and be cut a little bit in front of the weld because the cut might not be perfectly flat, smoothing and polishing afterward will remove this material polishing back to the region we want to observe. Welding samples vary in shape, so they require firm mounting to protect the weld area (i.e. to prevent welds breaking during cutting). In order to mount the samples in the polishing machine the samples were set into cold mount resin with a uniform shape for cutting and polishing.

3.2.4 Sample Clamp

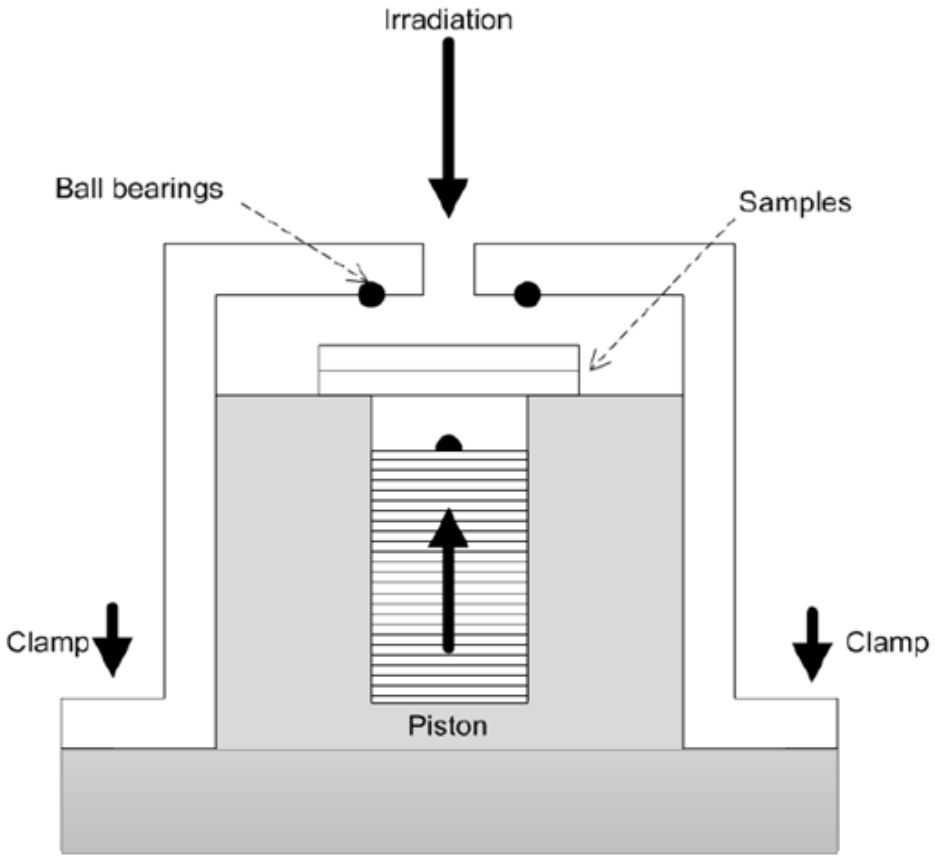

Fig 3.10 Illustration of welding clamp.

After the sample surface has been prepared and cleaned, the samples to be welded must be clamped to generate the small gap necessary for welding and avoiding cracking or ablation at the interface. The gap requirements are investigated in Chapter 5. For very flat surfaces, such close contact can be obtained by directly pressing two surfaces together, and exploiting the Van der Waals force to create an optical contact. However, it is difficult to obtain optical contact across a large area, even with highly polished surfaces and rigorous cleaning processes. Meanwhile, Van der Waals forces are not reliable or perhaps not strong enough to keep two samples pieces together. A suitable sample clamp is needed to maintain the small gap for the welding process. Other researchers reported using bolts together with lens held in a fixture to press two surfaces together [2], or using two large piece of glass to push the samples together fixed using bolts [3]. However those methods are not flexible, and the force applied on the samples is hard to control, and perhaps as high as 100 MPa, which would lead to a strong residual stress and hence, cracks or microcracking is inevitable.

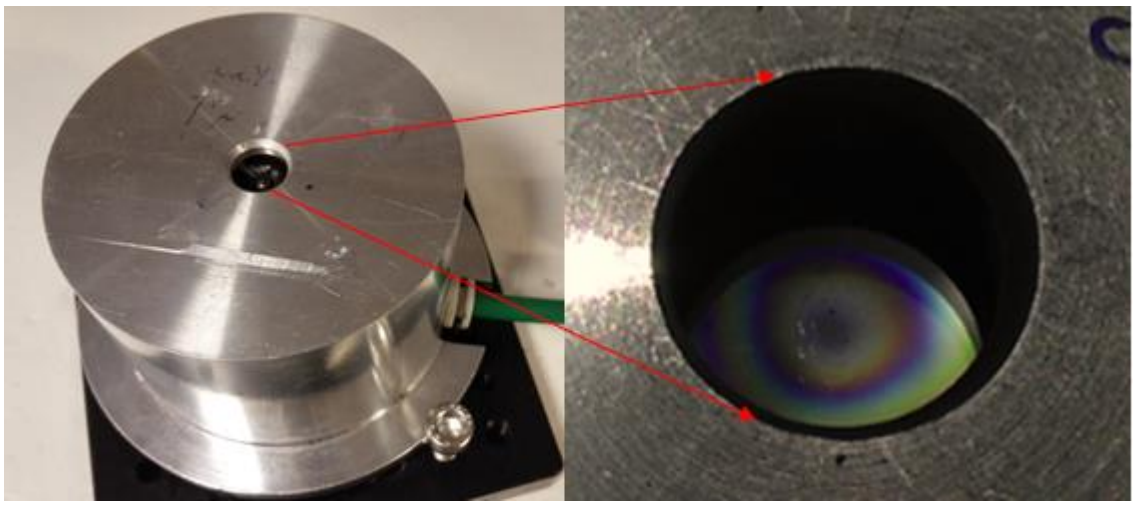

Fig 3.11 Clamp and optical contact (Newton's ring) when piston pressure applied.

In our lab a pneumatic piston structure is adopted to apply a substantial force, ideally at a point. A clamp structure is designed using a four point loading system with a piston to control the applied force. Fig 3.10 shows a schematic diagram of the clamp arrangement used for welding. Here a single ball bearing is pushed into the back of the two samples via a piston. This then lifts the sample onto three equilaterally positioned ball bearings on a cover plate. This provides a symmetric force centred on the region where the weld is desired. It is possible to qualitatively evaluate the clamping and contact region by observing interference fringes (Newton's rings) while changing the pressure inside the piston (Fig 3.11).

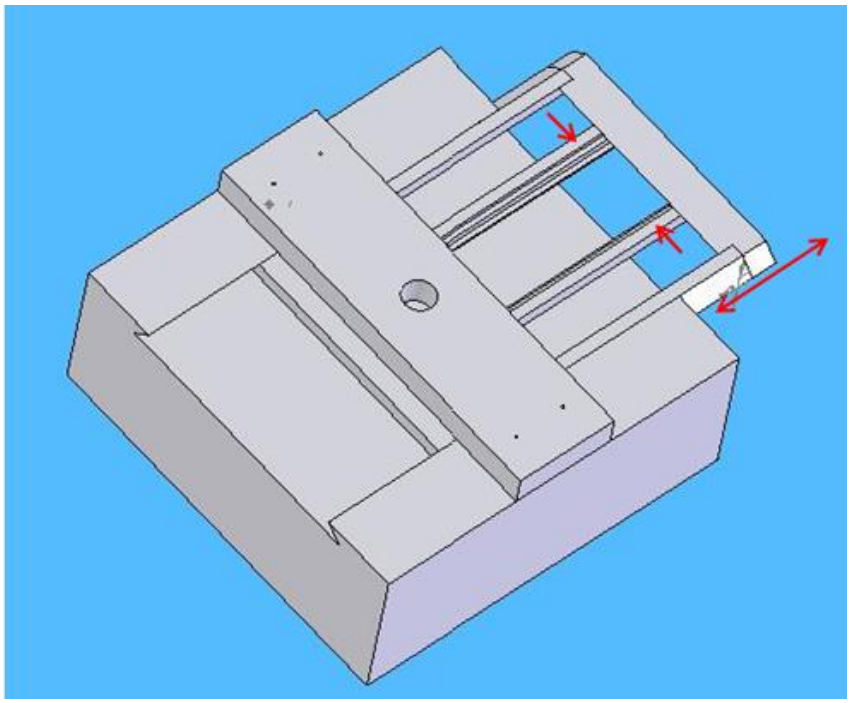

Fig 3.12 Illustration of multi-spots welding clamp.

By applying an appropriate force on the samples, an optical contact region can be obtained around the central area. Laser irradiating this area through a hole makes the welding process more reliable, but in this method the weld area is restrict by the hole on the top and the ball beneath the samples. A second clamp structure was designed and built to solve this problem, with a moveable frame that carries the samples horizontally in both x and y, as shown in Fig 3.12. The ultrafast laser irradiates from the top hole to the material, and when the welding area is chosen through moving the frame, the piston underneath will be aerated and a single ball on top of the piston presses the sample together for welding. After a weld has been generated, the piston pressure is released and by moving the frame to another area for another weld.

3.3 Welding Procedure

In previous subsections the experiment setup and sample preparation work were discussed. A scan head would be ideal to scan the required weld geometry which could give a flexible scan pattern and fast scan speed, however, a scan head with a sufficiently small focal spot (several μm) was not available. In our lab the sample clamp is mounted on x, y, z translation stages (Areotech pro115 with ~6 μm accuracy) to position and translate the sample through the laser focus. The translation stages were controlled to provide different irradiation patterns. For flexible interaction between laser and stage movement, a shutter (Thorlabs shutter controller 10) was inserted in the beam path and was programme controlled.

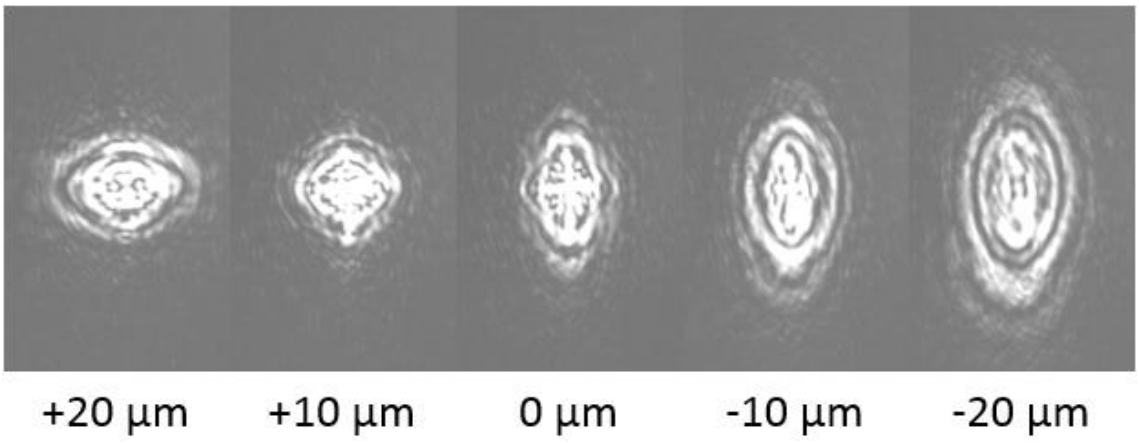

Fig 3.13 Camera view of different patterns from different focal positions around the surface (+ represent position above the interface, and - represent position below the interface).

The focus position was observed through the CCD camera which receives a focused image when the focus is close to an interface. Different patterns are formed if the focus is at different positions (Fig 3.13).

The interface between the samples usually exhibits no reflection because of optical contact. For welding therefore, the laser is first focused on the upper surface of the upper sample, and when this position is located, a certain distance will be moved downward based on the calculation of the thickness of the upper sample:

$$d' = \frac{d_{thickness}}{n_1} \qquad \text{Eq 3.4}$$

$d_{thickness}$ is the thickness of the upper sample and $n_1$is its refractive index.

The welding starts with samples put in the clamp rig which is mounted on the 3 axes stages; the laser, with limited power, is fired to adjust the focus, locating the middle of the hole on the clamp rig. The focal position is then properly adjusted based on the pattern on the CCD camera. Finally the laser power and repetition rate are set based on the samples and the program controls the stages movement based on a particular welding pattern with the shutter controlling the laser output as required. An outward spiral pattern is most commonly used as this allows the welding process to begin within the central optical contact area. Discrete welding patterns are also often adopted in glass-metal welding to prevent crack propagation while helping to release accumulated heat and residual stress for welding materials of highly different thermal expansion coefficient. Different welding patterns will be discussed in chapter 6.

3.4 Summary and Conclusion

In this chapter an ultrafast laser welding setup was introduced and the differences between traditional laser welding were discussed. Samples of different materials and surface conditions with different preparation methods were discussed.

Unlike traditional methods, energy absorption at the front surface of the material where it diffuses to the interface for welding (i.e. conduction mode welding), or a keyhole penetration deep into the material (keyhole welding), ultrafast laser welding, which allows absorption directly at the interface based on nonlinear absorption, enables welding between transparent materials without any intermediate layers. The heat affected zone (HAZ) introduced during the ultrafast laser welding process can be as

small as 10’s of micrometres which enables high precision micro-joining without thermal distortion issues within the bulk material. Meanwhile, ultrafast laser welding requires a quite different optical setup from traditional laser welding. High-NA lenses and different beam translation methods are needed for high laser intensity and relatively large scan range, also high precision stages with a focus position monitoring system should be adopted for the small weld seam.

Analysing the welding parameter requirements provide us a guide for parameter/component selection during the welding process. For a successful weld many factors need to be considered for different materials:

1. Laser pulse parameters—energy, duration, and repetition rates
2. Lens and beam parameters—beam diameters, focal length, and focal spot size
3. Scanning parameters—scan speed and focal position
4. Surface parameters—roughness and interface separation

These parameters may have interactions with each other. So during the parameter tests, usually only one or two parameters are altered while the other parameters are kept the same. These tests observed their influence on the weld appearance or HAZ after being cross-sectioned. A systematic analysis of those parameters is presented in the following chapters.

Material properties including: melting temperature, lattice structure, specific heat capacity, thermal expansion and thermal conductivity greatly influence thermal process and hence laser welding parameters must be selected appropriately. For ultrafast laser welding, the brittleness of the transparent material (typically glass) demands the welding residual stress be as small as possible. The initial surface conditions (which should allow sufficiently good contact between the two materials) and the residual stress induced by the thermal process, determine if a successful weld can be formed without cracking.

Commercial glass surfaces are usually smooth and flat which only need to be deep cleaned. However, the surfaces of industrial parts or commercial products are usually not that good. Some surface treatment needs to be done before welding. In our lab the surface preparation methods include: workshop milling, grinding, polishing, and tumbling, the preparation procedures were hence provided and the surface roughness

was measured in this chapter. Based on our experiments (Chapter 5), metal surface roughness (*Ra*) of less than 300 nm is required for a successfully weld, this is obtainable using those simple and less expensive surface preparation methods talked above for the industrial applications.

After the sample surface has been prepared and cleaned, the samples must be firmly carefully clamped to a close contact to avoid cracking or ablating on the interface. In our lab a pneumatic piston clamp was designed using a three point loading system (Fig 3.10), which provides a symmetric force centred on the region where the weld is desired and it is possible to qualitatively evaluate the surface separation at the contact region by observing interference fringes (Newton's rings) while changing the pressure inside the piston.

The quality of the successful weld can be identified by observing if the two samples are still bonded after removing the clamp, and the seams can be observed under an optical microscope to see if the welds are at the right position and massive cracks appear after a couple of days. Further analysis can be done in the form of a cross-section morphology analysis or strength test. Even when welding with the same parameters and conditions, the breaking strength can vary significantly from sample to sample because of the distribution of physical flaws in brittle material. As a result, a statistical technique is needed to determine the typical weld strengths.

Chapter 4 Test and Measurement

4.1 Parameter Investigation

As a direct welding method for identical or different materials with different optical or material properties, ultrafast laser microwelding requires the welding parameters to be carefully considered.

First consider the material. Glass is usually brittle, and is easily cracked during the welding process, especially at the surface where more defects are distributed. Stresses generated by heat induced deformation, localised heating or thermal expansion can crack the material. More residual stress is observed with more deposited energy [152][153].

Secondly nonlinear laser absorption, unlike laser absorption at the material surface as in traditional laser welding, plays an important role in ultrafast laser welding. This enables local absorption both inside bulk material and at the interface. However, nonlinear absorption only occurs where the power density is above a specific threshold (the breakdown point), which means a certain amount of laser energy cannot be absorbed (i.e. transmitted) due to the beam distribution (Gaussian or other) at the focus. A weak plasma, initially generated by nonlinear absorption, scatters incident light (negative refractive index effect), but as more laser energy is absorbed, the stronger plasma becomes absorbent and the main absorption mechanism transfers from nonlinear to linear plasma absorption, which will rapidly expand and covers a larger area above the focus. The time required to transfer from nonlinear absorption to plasma absorption depends on the pulse energy and peak power. This can happen within a single pulse. Furthermore if the time interval between pulses is comparable or smaller than the thermal diffusion time, energy will accumulate and help electron or photon assistant absorption in the following pulses.

Thirdly, power density (light intensity) needs to be significant for nonlinear absorption. An ultrashort pulsed laser and high-NA lens are required for welding because they allow for a laser intensity which is extremely high at the focus by condensing light temporally and spatially. These high intensities result in a range of nonlinear effects.

Self-focusing is the most important nonlinear effect that we must consider when determining bulk ionisation thresholds. As the power in the laser pulse is increased, the

laser beam will self-focus when the power exceeds the critical power. The critical power is given by Eq 2.24. In our laser system, if a $\lambda=1030$ nm wavelength is used, for a material such as fused silica, $n_0 \approx 1.453$, $n_2 \approx 2.4\times10^{-20}$ m^2/W, the critical power is 4.6 MW. For our laser system, assuming a flat-top pulse shape, the average power required to reach critical power is:

$$E_{Ave} = P_{cr} f \tau = 10.8\, W \qquad \text{Eq 4.1}$$

here f is the laser pulse frequency (400 kHz), and τ is pulse duration (5.9 ps). In reality, the pulse is not a flat-top, so an average power lower than this value will reach the critical power.

The threshold for self-focusing depends on the peak power while the threshold for optical breakdown and damage depends on the laser intensity. If the laser pulse is tightly focused into the material using a high-NA lens, the intensity for optical breakdown can be reached with a power that is below the critical power for self-focusing. Self-focusing should be avoided during our process. A crude estimation can be made on how tightly we must focus the laser beam to produce breakdown with power below the self-focusing critical power by assuming the beam has a flat-top spatial profile. Then we have

$$I = \frac{P}{\pi(d/2)^2} \qquad \text{Eq 4.2}$$

where d is the diameter of the laser spot at the focus, p is the peak power of the laser pulse, and I is the laser intensity. From the formula the laser must be focused to a spot small enough to achieve breakdown with a laser power that is below the self-focusing critical power. With high numerical aperture (NA) microscope objectives, focal spot diameters of less than 2 μm can be achieved, allowing the threshold for optical breakdown to be reached with power that is more than an order of magnitude below the self-focusing critical power.

The fourth parameters are sample surface conditions and surface separation. The surface preparation methods have been discussed in Chapter 3. A rough surface prevents the two materials from forming a close contact. Surfaces that are not smooth and flat also introduce stress which pulls the two surfaces apart. For a large surface separation, more

energy should be deposited in an area in order to generate more plasma to bring material into the gap. However for a rough surface, the surface separation in a localised area changes rapidly depending on the peaks or valleys of the rough area. During welding it inevitably causes overheating locally at peaks and under heating at valley areas. This is critical in glass to metal welding even if the glass surface is flat enough, the non-uniformed heating will act on glass surface and will introduce surface cracks. This cannot be quantitatively measured and specific parameters and will be discussed in Chapter 5.

For the parameter investigations, inscription inside bulk glasses were carried out with borosilicate glass and fused silica (both from Schott). Measurements were made using a microscope and, usually, sample cross-sections were needed for a morphology analysis.

4.1.1 Different Lenses

Lenses with different numerical aperture (NA) were used for generating light intensities above the optical breakdown threshold. We measured the HAZ with differences in laser power and scan speed for lenses of focal length 10 mm, 20 mm and 40 mm. For our laser system, the M^2 value is 1.4 and beam diameter is 12.7 mm after the beam expansion, the important calculated parameters for different lenses are shown in Table 4.1.

Table 4.1. Useful parameters for different lenses working in the laser system (in air)

Focal length(mm)	**NA**	**Focus diameter (µm)**	**Rayleigh length (µm)**	**Intensity at focus (W/m^2)***
10	0.54	1.3	1.8	225×10^{15}
20	0.28	3.1	7.3	56.2×10^{15}
40	0.14	6.2	29.3	14.0×10^{15}

**The intensities were calculated with 1 W average power output from the laser.*

An experiment measuring HAZ generation using different lenses was carried out by drawing individual lines inside glass (borosilicate or fused silica) with a speed of 1 mm/s. The HAZ width could then be observed under the microscope, and samples were cross-sectioned for morphology analysis. Cross-sections of the HAZ dimensions inside borosilicate glass for different lenses are presented in Fig 4.1, which gives a first impression of what the HAZ looks like for different focal lengths. It was observed, as

expected, that higher pulse energies were required to induce nonlinear absorption (and hence HAZ) for larger spot sizes. It was also clear that as the focal length increased, the HAZ cross-section shape changes from a tear-drop to more prolonged appearance (Fig 4.1a and Fig 4.1b) as predicted in the simulation above. In each case the vertical dimensions are much larger than the Rayleigh range (29.3 µm for the 40 mm focal length; 7.3 µm for the 20 mm; and 1.8 µm for the 10 mm). Although the HAZ with 20 mm or 40 mm lenses is large compared with that induced using the 10 mm lens, fewer cracks were observed in these cases as a smaller thermal gradient appears as the area of heat absorption is larger compared with the 10 mm lens, so less internal stress is accumulated within the HAZ. As seen from Fig 4.1, different heat affected layers can be clearly seen in those large HAZ, which is due to a large amount of thermal diffusion to the surrounding area.

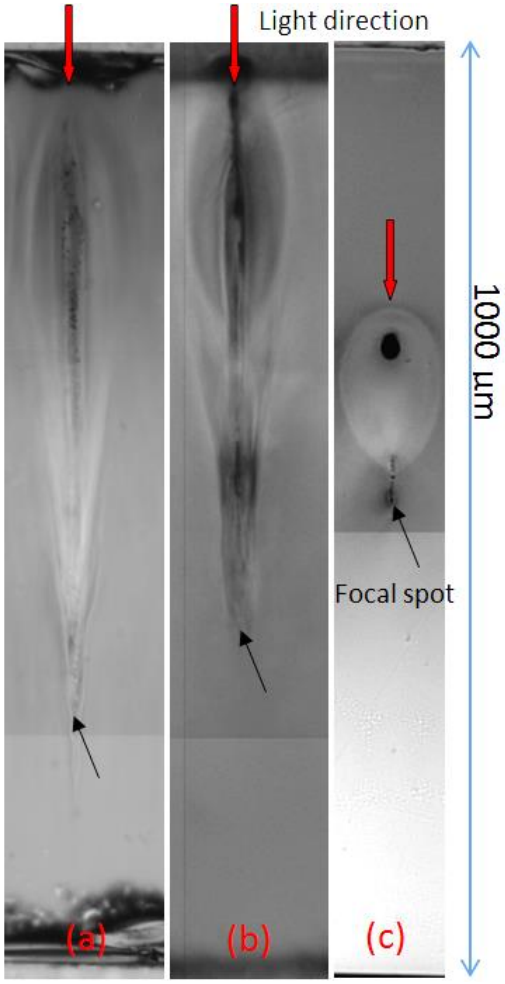

Fig 4.1 HAZ of different focal length lenses generated with different power in borosilicate glass. The length/width ratios are 5.3, 4.35 and 2.17 for (a). 7.5 W with 40 mm lens, (b). 4.65 W with 20 mm lens and (c). 1.09 W with 10 mm lens.

For both fused silica and borosilicate glass, the graphs show the same trend, other than the borosilicate glass obtaining larger HAZ compared with fused silica for the same laser parameters (see Fig 4.3). The graphs below show HAZ features inside fused silica generated with different lenses.

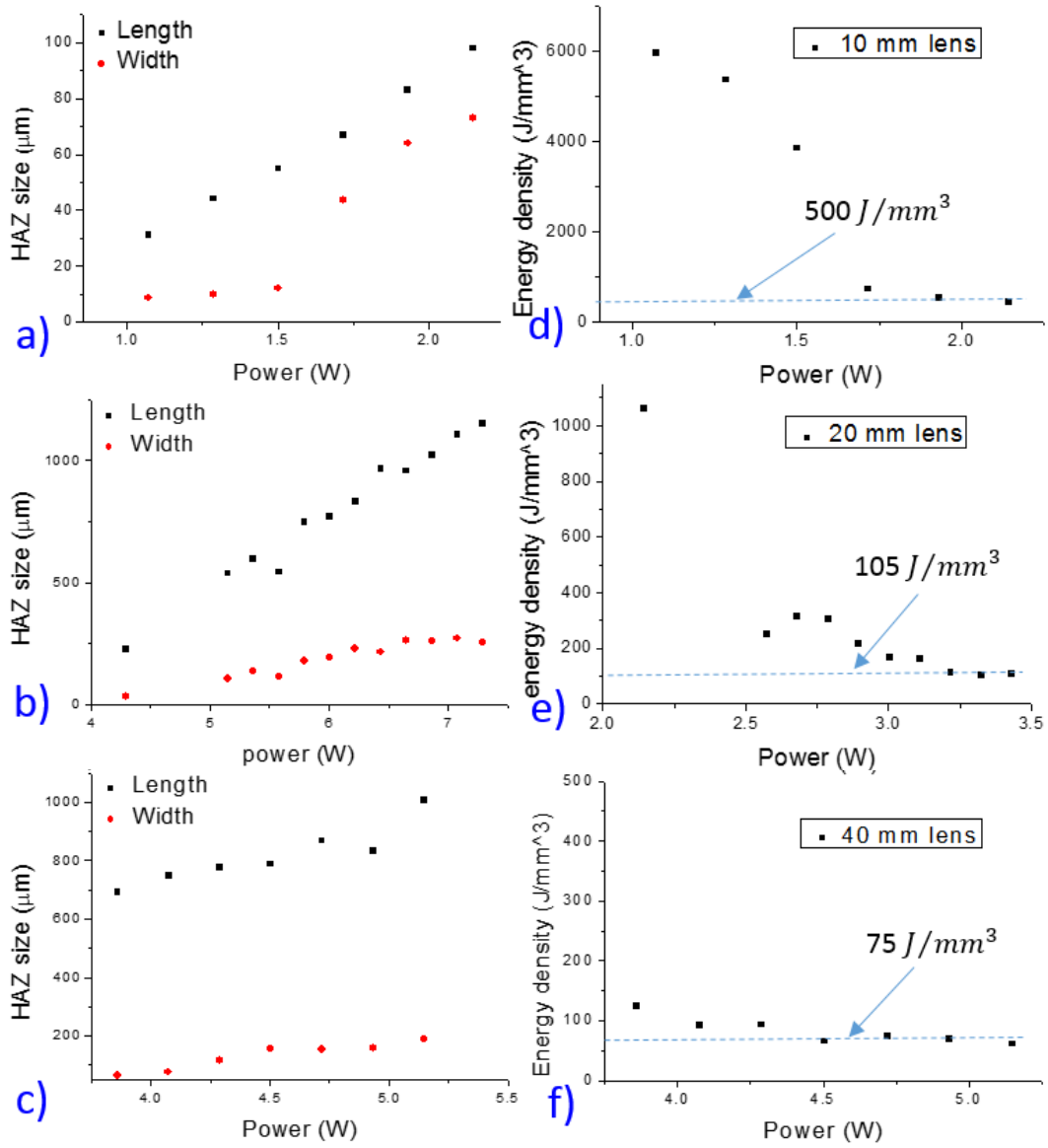

Fig 4.2 Comparison of HAZ inside fused silica for focus length (a). 10 mm, (b). 20 mm, and (c) 40 mm with scan speed 1 mm/s and pulse repetition rate 400 kHz. The right hand side shows the deposited energy density as a function of laser average power with different focal lenses of (d). 10 mm lens, (e). 20 mm lens, (f). 40 mm lens.

After the samples were cross-sectioned, both the width and length of the HAZ were recorded to evaluate the laser power absorbed inside glass, as shown in the left side of Fig 4.2. A leap of the HAZ width by increasing the laser power from 1.5 W to 1.75 W in Fig 4.2a is indicative of an absorption mechanism change from nonlinear absorption

to plasma absorption. As the HAZ lines were always scanned with a speed of 1 mm/s, the line energy density (energy deposited per unit HAZ length) instead of the volume of HAZ is used for comparison. From the cross-section the HAZ area could be measured for different laser powers. The deposited energy density (laser energy/HAZ volume) inside the HAZ for different laser average power used for welding could be calculated and the results are presented in Fig 4.2 (d, e, f). These graphs are based on the calculation that all the laser power was absorbed. In a real situation most of the power is absorbed at higher power (when plasma absorption is established), but at low power, large amounts of laser energy is not absorbed (i.e. transmitted) [124]. The calculation result in Fig 4.2 (d, e, f) is a poor approximation, especially for lower average powers, thus the energy density calculated at the lower power is much larger than those at higher powers. The energy density at higher laser power becomes stable (approximately 500 J/mm^3 for 10 mm lens, 105 J/mm^3 for 20 mm lens and 70 J/mm^3 for 40 mm lens), which is also implied from the laser absorption model in 4.2.1. The laser energy is highly focused for the 10 mm lens resulting in a condensed absorption region, and during the thermal diffusion after irradiation the extra hot absorption centre and surround area establish a thermal diffusion balance that stop the HAZ expansion.

4.1.2 Different Power

Absorbed laser energy plays a quite important role during the welding process, delicate control of laser power is essential for ultrafast laser welding. In this section different methods were used to generate a better understanding of laser power interactions with materials (i.e. fused silica and borosilicate glass). The experiments involved focusing the laser inside bulk glass with different average powers and a specific speed.

As with the other tests presented in this chapter, the results after processing were observed under a microscope for HAZ characterisation. The power used here is always above the material breakdown threshold and thus a permanent change (defects or HAZ) is induced, Fig 4.3 shows the relation of width of the HAZ and laser power inside borosilicate glass and fused silica, while keeping the other parameters the same (10 mm lens, and scan speed 1 mm/s). The results are quite straightforward, the HAZ size expands as the laser power increases, there is a linear relationship for both of the materials, but the gradient of the two graph are quite different, and the breakdown (average) power of borosilicate glass is around 0.3 W (pulse energy of 0.75 μJ) compared with 1.72 W (4.3 μJ pulse energy) for fused silica. One may also see the

difference in the HAZ width-power relation of the two materials for the same laser average power. For laser power of 2.5 W (6.25 μJ), the HAZ line width of borosilicate glass is 390 μm which is more than 4 times that of fused silica (only 90 μm). The laser absorption and HAZ size depend on the wavelength, local intensity, and pulse duration, as well as on the electronic structure of the material. For better understanding of the HAZ appearance differences, we present the material properties in Table 4.2. One needs keep in mind that once the HAZ is generated, above 90 % of the laser power would be absorbed [124]. From the table, the thermal properties of the two materials are more or less the same except the softening point softening point (the temperature at which a material softens beyond some arbitrary softness) and transformation temperature (the temperature at which a change in phase occurs in material during heating or cooling), which is quite likely accounting for the huge HAZ width difference.

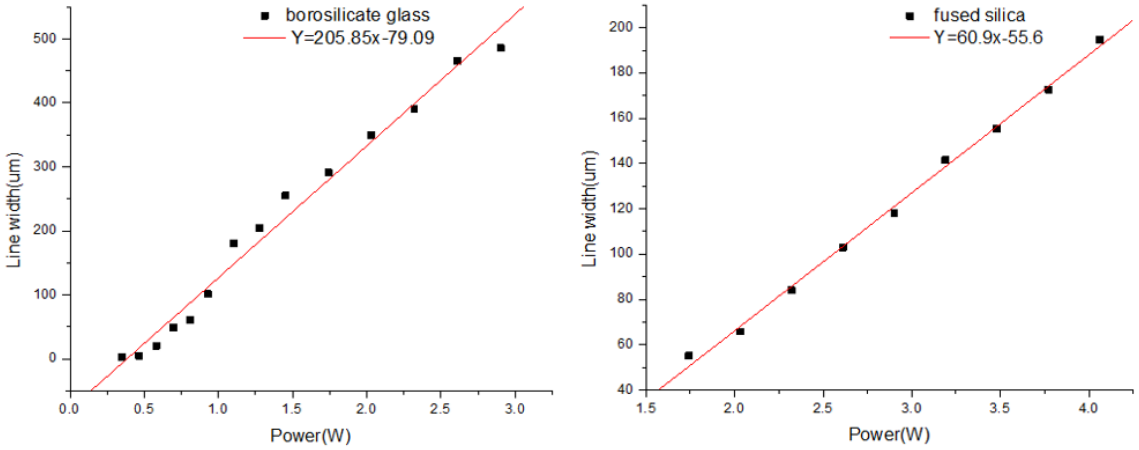

Fig 4.3 HAZ line width of borosilicate glass and fused silica with different powers (10 mm lens, scan speed = 1 mm/s). Comparison of line width with different laser power focused inside the material.

Table 4.2. Comparison of thermal properties of borosilicate and fused silica glasses

Material	Borosilicate	Fused silica
Density(25ºC) [g/cm^3]	2.2	2.2
Specific Heat Capacity [J / (kg.K)]	830	790
Thermal conductivity [W/(m. K)]	1.2	1.31
Softening point [ºC]	820	1600
Transformation Temperature [ºC]	525	~1200

**Parameters from the brochure of Schott materials, softening point and transformation temperature represent different viscosity conditions.*

The cross-section views of the different power HAZ gives more detail on how the laser power influences the material phase transformation. Fig 4.4 shows the HAZ inside borosilicate glass for various incident powers with a 20 mm lens. The laser inscribed from the top with the same focal position. From the image the HAZ can be seen to expand around the focus as the power increases, however it mostly expands towards the incident laser.

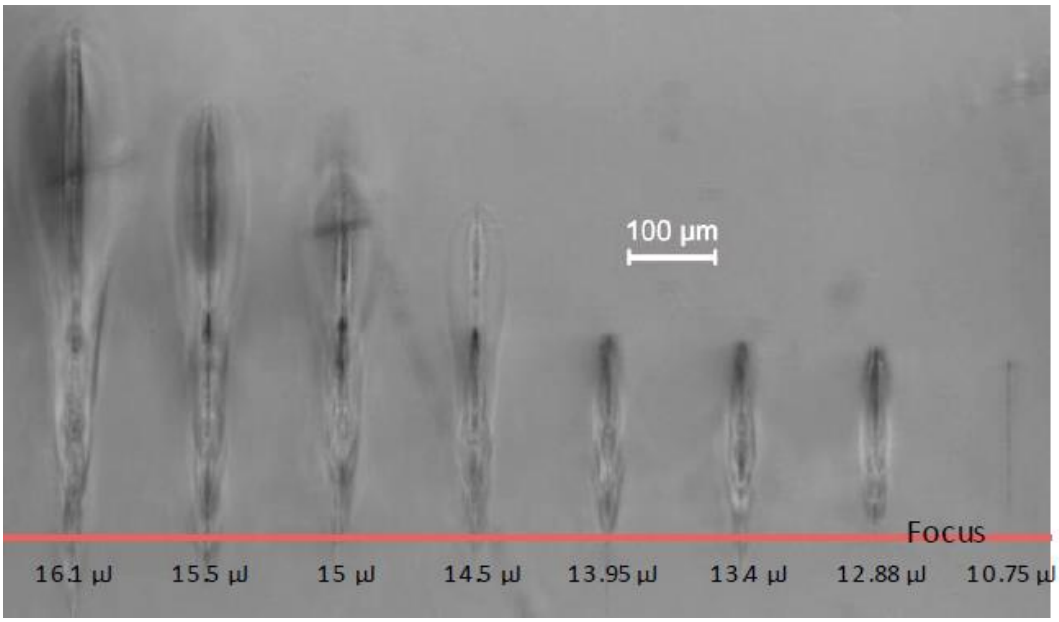

Fig 4.4 Cross-section view of HAZ of different pulse energy with 400 kHz repetition rate (with 20 mm focal lens and 1 mm/s scan speed).

When the pulsed laser power is low, material chemical bond breaks (defects) or cracks appear around the focus with limited HAZ around the plasma region. As the laser pulse energy increases, the plasma expands with further increasing energy absorption following the laser irradiation direction, this results in a filament like modification. When the laser pulse energy increases to a certain level (14.5 µJ in Fig 4.4), the plasma becomes stronger and the laser absorption mainly occurs within the upper part of the plasma. This results in a bulb-shape HAZ. Once the plasma expands to a position, sufficiently far from the focus, where the focusing beam diameter is large (resulting in lower laser intensity) (Fig 4.15) absorption drops to an un-sustainable level and the process begins again at the focus. As a focused laser beam scans laterally inside the material with a certain pulse energy and translation speed, the plasma oscillates between the focus and this threshold position. A HAZ is created as the heat transfers from plasma to the surround area, and a chain-shape seam appears along the scanning

direction for each plasma absorption oscillation. The HAZ is located above the focal point with the height based on the laser power, as seen from Fig 4.4.

4.1.3 Different Speed

The laser power, scan speed and repetition rate are all effective ways to change the energy density absorbed along the inscription line. Fig 4.5 shows the relation of the HAZ size and laser scan speed inside two different materials. From the graph, both length and width of the HAZ decrease with scan speed increasing, but the decrease is not as rapid compared with changes in power.

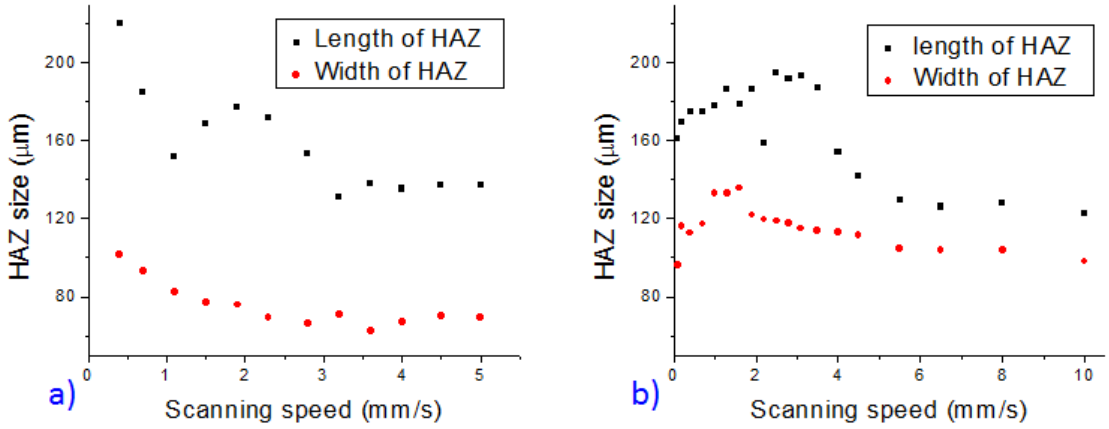

Fig 4.5 Relation of HAZ size and laser scan speed (a). Fused silica (laser average power 2.35 W and pulses repetition rate 400 kHz), (b). Borosilicate glass (laser average power 1.04 W and pulses repetition rate 400 kHz).

For both the measurement of HAZ size of various powers and scan speeds, there are always some testing errors as the size of HAZ is non-uniform along the scanning line. This can be seen in Fig 4.6. Different patterns can be observed by changing speed or power. The reasons for those dot or dash line patterns can be explained through different absorption mechanisms, which will be discussed in detail in section 4.2.

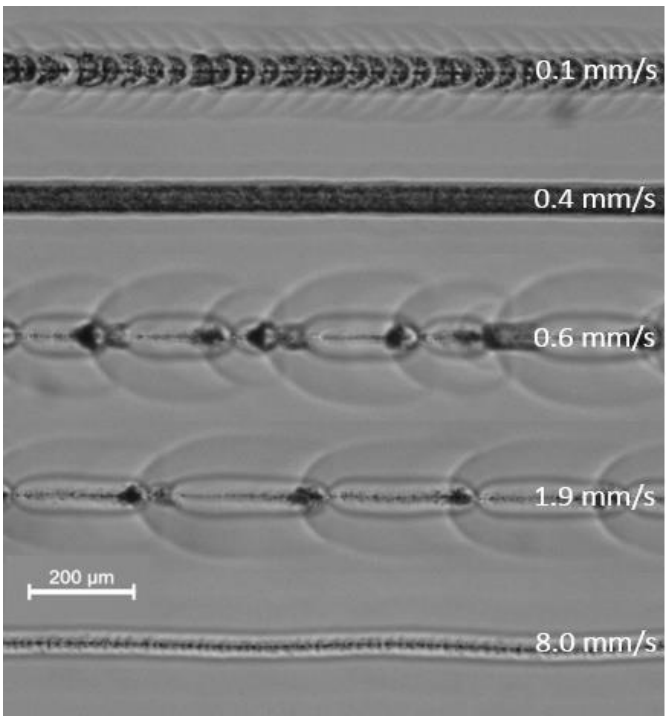

Fig 4.6 Different patterns introduced by different scan speed (laser average power is 1 W, with 10 mm lens).

Increase in laser power and decrease of scan speed can result in the same line energy density (laser energy deposited for a unit scan length). Compared with Fig 4.2 and Fig 4.5, higher power obtains larger HAZ compared with slower scan speed for the same line energy density. Even if laser pulses are scanned with the same linear energy density, different pulse overlap (spatial interval) and pulse separation time (time interval) will greatly influence the HAZ or welding results. For example, laser scanning parameters of:

①1 mm/s and 1 W average power (pulse energy: 2.5 μJ) with 400 kHz pulse repetition rate

②2 mm/s and 2 W average power (pulse energy: 5 μJ) with 400 kHz pulse repetition rate

③1 mm/s and 1 W average power (pulse energy: 5 μJ) with 200 kHz repetition rate

Even though they have the same line energy density, for a 10 mm line, ① and ② takes 10 seconds while ② only 5 seconds, and for ② and ③ pulses are spatially separated and the pulse energies are doubled, for a clear diagram view see Fig 4.7. Ultrafast laser welding needs to carefully consider the time and space intervals. Previous reports indicate the absorption and thermal effects of a pulse are dependent on the initial conditions of the material (temperature, free electron density etc.) and time interval

between pulses [10]. The energy of a single pulse is quite low, and the energy will be dispersed gradually (in the scale of ~10^{-6} s) although a very high electron temperature ($\sigma_e = 5 \times 10^{23}$ /cm^3) [154] can be obtained in a local area inside the glass. Pulses with high repetition rates will greatly increase thermal accumulation inside the material, and a 2.5 μs and 5 μs time interval will lead to a great HAZ difference as the free electron density and thermal diffusion change rapidly in this time scale [155][156]. For a scan speed of only a few millimetres per second, the pulse overlaps are quite high for our laser system (400 kHz), for a 1 μm diameter focus, the pulse overlaps are 99.8% and 98.4% for 1 mm/s and 10 mm/s scan speed respectively. In this experiment we change the scan speed and observe the HAZ afterward.

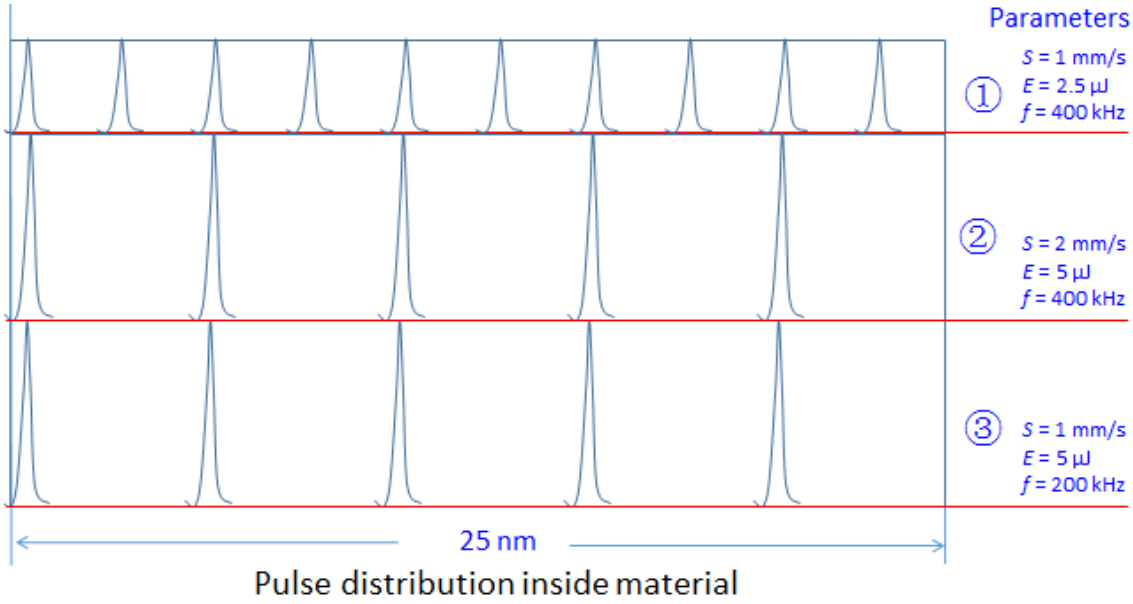

Fig 4.7 Diagram of laser pulses of different parameters (scan speed S, pulse energy E and pulse repetition rate f) with the same line density ①. 1 mm/s and 1 W average power (pulse energy= 2.5 μJ) with 400 kHz pulse repetition rate, pulse time interval: 2.5 μs. ②. 2 mm/s and 2 W average power (pulse energy= 5 μJ) with 400 kHz pulse repetition rate, pulse time interval: 2.5 μs. ③. 1 mm/s and 1 W average power (pulse energy= 5 μJ) with 200 kHz repetition rate, pulse time interval: 5 μs.

4.1.4 Different Repetition Rate

For our laser system, the pulses repetition rate is 400 kHz, which is high enough for thermal accumulating for laser welding, and the repetition rate can be adjusted through the software control panel with a rate of *400×1/n* kHz, *n=1,2,3*…. However pulses repetition rates below 200 kHz are insufficient for thermal accumulation inside most of

the glasses used in our lab, as the thermal diffusivity of glass is around a few mm^2/s, and for low repetition rate, energy is diffused to the surrounding area before next pulse arrives. For the first part of this experiment we kept the sample stationary and fired a certain number of pulses into the bulk observing the change to the HAZ to evaluate how the energy accumulates inside glass thermally. In the second part we used a femtosecond laser with a maximum repetition rate of 5 MHz to observe the HAZ features when the laser was scanned inside samples.

4.1.4.1 Stationary Pulses inside Glass

Keeping the sample immobile under the focused laser pulses, the laser fired a certain number of pulses (in a pulse train). The sample was then moved and another pulse train was produced. The picture in Fig 4.8 is the top view of the HAZ produced in borosilicate glass. The parameters used are indicated on the figure, and the number of irradiated pulses is calculated and individually labelled on this map. The detailed HAZ size and cubic HAZ size information is measured and presented in Fig 4.9. The cubic HAZ size represents volume information as we assume the length and width of the HAZ increase to the same value and the width in x and y direction are the same. From Fig 4.8 and Fig 4.9, it is further clear that for the same pulse repetition rate, the HAZ size increases with the pulse train duration and for the same pulse train duration, the HAZ size decreases with the pulse repetition rate.

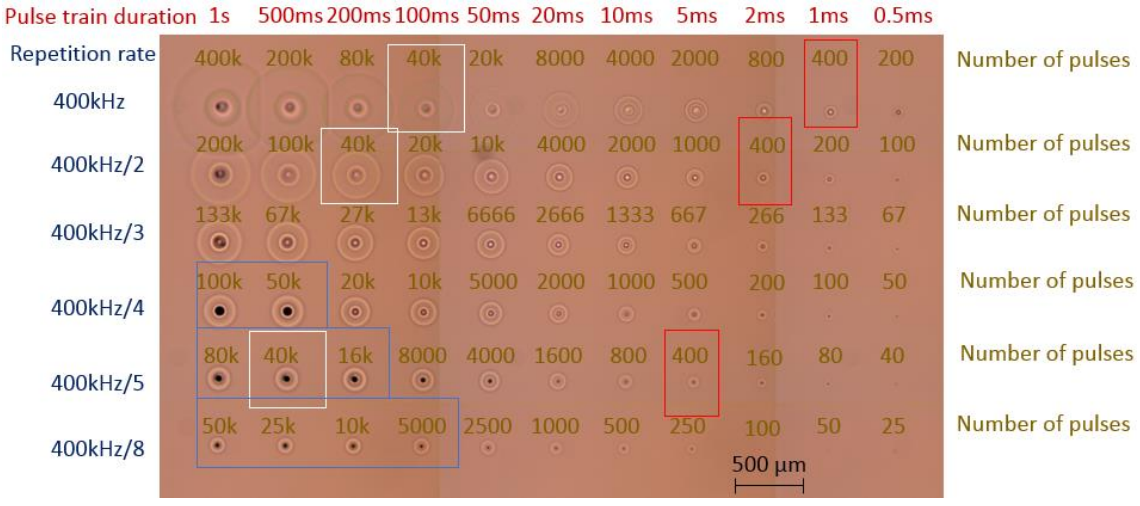

Fig 4.8 HAZ map of different number of pulses and different laser pulse repetition rate inside borosilicate glass with stationary laser pulses (pulse energy: 29.2 µJ). Squares of different colours indicate the HAZ of different thermal accumulation features (White: thermal accumulation, red: absorption not stably established, blue: the HAZ size saturation).

Meanwhile, the difference of thermal accumulation for the same number of pulses represents the effect of thermal accumulation features. Taking the irradiating of 40000 pulses inside the sample, for example, (indicated by the white square in Fig 4.8), the HAZ diameters are 443.6 μm (400 kHz pulse frequency), 356.7 μm (200 kHz pulse frequency) and 169.5 μm (80 kHz pulse frequency) which is an apparently declining trend as the frequency decrease which indicates the relation of the time interval between adjacent pulses and thermal accumulation.

On the other hand, for irradiating of 400 pulses inside the sample (indicated by the red square in Fig 4.8), the HAZ diameters are 79.2 μm (400 kHz pulse frequency), 86.5 μm (200 kHz pulse frequency), and 76.7 μm (80 kHz pulse frequency). For smaller number of pulses (400 or less), even irradiating with different laser pulse repetition rate, the HAZ diameters are similar. To explain: 400 or less pulses could not generate stable plasma absorption inside borosilicate glass (the plasma is not sustained between pulses, and when next pulse comes in, the free electrons are insufficient to quickly help the plasma absorption build up). Thus nonlinear absorption dominates the process; which only happens around the focus, and the heat diffuses to the surrounding area after irradiation. Thus the HAZ is similar in size for different frequency. More than 400 pulses are required to transfer the main absorption mechanism from nonlinear absorption to plasma absorption, and then the absorption area quickly expands as the plasma grows. Furthermore pulse trains with higher frequency accumulate heat more quickly which helps plasma grow.

As the blue squares indicated in Fig 4.8, the HAZ diameters turn to a saturated feature as the pulse train duration increases for the same repetition rate. To explain this: for longer pulse trains, the laser absorption acts as a continuous heat source inside the material, a dynamic equilibrium was established for the heat coming in and diffusing out, so the phase change of the material (i.e. HAZ) stops expanding.

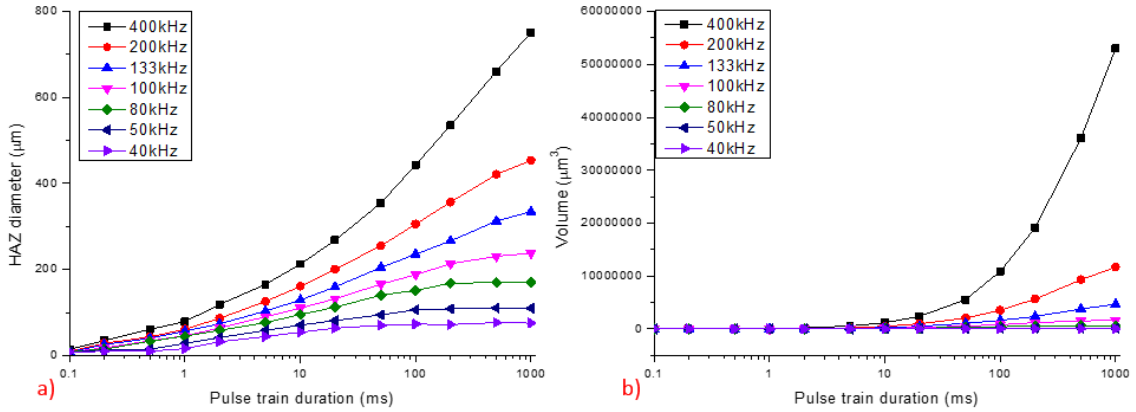

Fig 4.9 Graph of (a). HAZ width and (b). HAZ volume related with pulses train duration of different laser repetition rate.

4.1.4.2 Scanned Pulses inside Glass (Femtosecond Laser)

To determine the influence of higher pulse repetition rates we used a femtosecond laser (Bluecut 10 from Photonic Solutions). The frequency can be continuous adjusted from 100 kHz to 5 MHz. A similar laser setup is used as before except the focal lens we used has a high-NA objective (NA: 0.6) to compensate for the smaller laser beam diameter from the laser to give a similar focal spot size. For this experiment we want to keep the same output power and observe the HAZ differences, but the laser output power has the limitation of a maximum output power of 6 W and a maximum individual pulse energy of 5 μJ, so the laser average powers and pulse energies shown below were used:

Table 4.3. Table of femtosecond laser parameters used for repetition rate investigation

Pulse repetition rate [kHz]	**100**	**200**	**333**	**500**	**1000**	**2000**	**3000**	**5000**
Laser average power[W]	0.453	0.89	1.2	1.2	1.2	1.2	1.2	1.2
Pulse energy[μJ]	4.5	4.45	3.6	2.4	1.2	0.6	0.4	0.24

Cross-sectional view of the HAZ lines shows similar result for 100 kHz, 200 kHz and even 333 kHz; the HAZ size increases with the pulse repetition rates. The relation between pulse repetition rate and HAZ size for the same laser average power is shown in Fig 4.10. For the same average power, the HAZ size shows a sharp declining trend. That is because for higher repetition rates, the energy of individual pulses is lower compared with pulses of lower repetition rate (from Fig 4.13), which leads to a lower

absorption rate for those individual pulses, even if the overall laser energy is the same, most of the energy is either transmitted or dispersed.

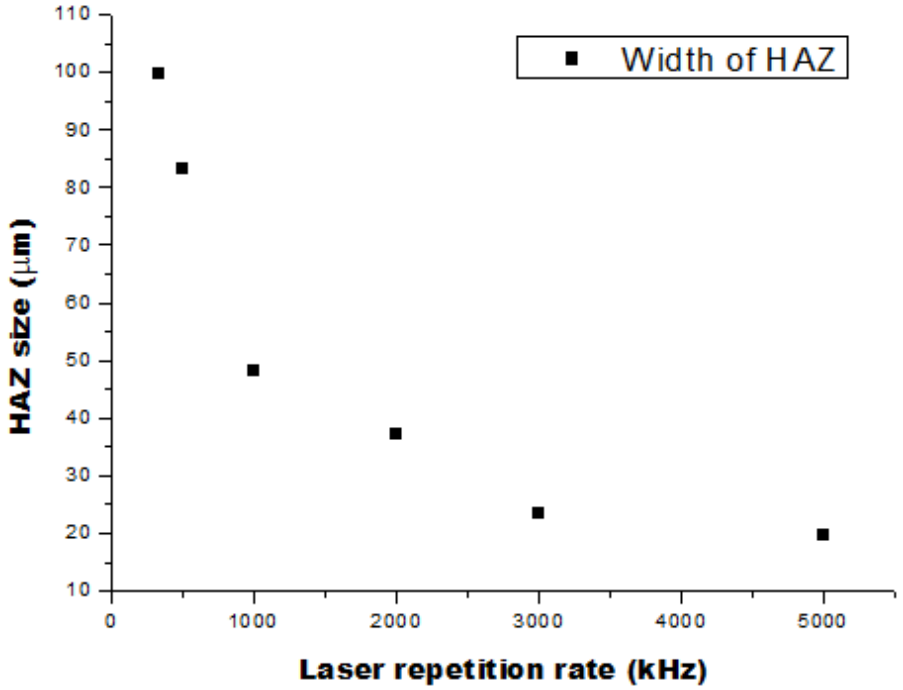

Fig 4.10 Relation of laser repetition rate and scanning HAZ size inside borosilicate glass with the same laser average power (Bluecut 10, 300 fs, focal lens NA = 0.6, beam diameter = 6 mm).

4.1.5 Different Pulse Duration

Measurement of the influence of different pulse durations was carried out use the Pharos laser system from Photonics Solutions, with pulse duration continuously adjustable from 162 fs to 10 ps. In this experiment the setup is the same as the one in 4.1.4.2 with laser power fixed as 1.5 W and pulse repetition rate 500 kHz. For each of the pulse durations, we drew lines inside borosilicate glass with speeds of 1 mm/s, 6 mm/s and 11 mm/s, and then the sample was cut and cross-sectioned for measurement, and the results are shown in Fig 4.11. From the graph, the HAZ slightly decreases as the pulse duration becomes longer, which is quite easy to understand as during the experiments we kept the pulse energy the same, so a longer pulse means lower peak power, and a pulse with higher peak power can excite nonlinear absorption more easily and needs less time to form plasma absorption, thus less energy is transmitted as the absorption becomes stable.

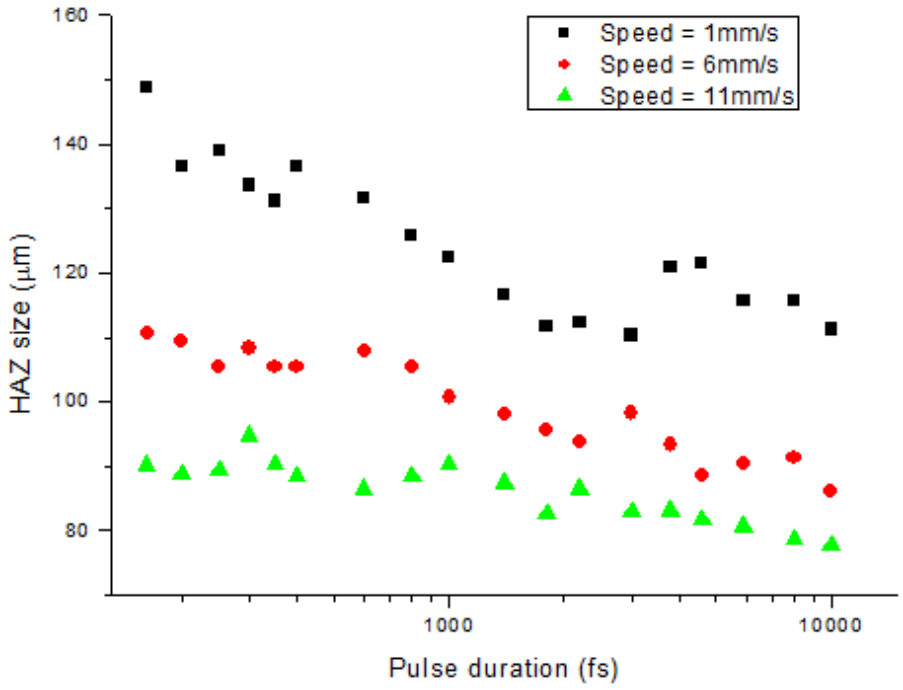

Fig 4.11 Relation of HAZ size and laser pulse duration (with laser average power 1.5 W and pulse repetition rate 500 kHz).

4.2 Morphology Analysis

In this section we will discuss about the morphology analysis of the welding area in the same or different materials. Ultrafast laser welding HAZ width could be measured or analysed under a microscope. Cross-sections (described in Chapter 3) are usually necessary for a detailed analysis of the HAZ features.

4.2.1 Morphology Model

For a better understanding of the HAZ variations with laser power and scan speed for different focal lenses, a focused Gaussian beam is considered:

$$I(r,z) = I_o \left(\frac{\omega_o}{\omega(z)}\right)^2 \exp\left(-\frac{2r^2}{\omega^2(z)}\right) \qquad \text{Eq 4.3}$$

with I_o the laser intensity at the focus, ω_o the beam waist (focal radius size) and $\omega(z)$ the radius at which the field amplitudes fall to 1/e of their axial values, in the plane perpendicular to the beam axis z, with $\omega(z) = \omega_o\sqrt{1 + \left(\lambda z/\pi\omega_o^2 n_g\right)^2}$ and $\omega_o = 2M^2\lambda f/\pi D$, with f the focal length of the lens and D the beam diameter, n_g is the refractive index of the material (n_g =1.507 for borosilicate glass at 1.03 μm). Here we

only consider the highest intensity i.e. along the axis ($r = 0$) and the position z_1 that is just above the breakdown threshold, then Eq 4.3 becomes:

$$I_{th} = I_o \left(\frac{1}{1+\left(\frac{\lambda z_1}{\pi \omega_0^2}\right)^2} \right) \qquad \text{Eq 4.4}$$

I_{th} is the breakdown threshold of the material.

For a clear view of the breakdown length a simulation graph is presented for the relation of I_o/I_{th} and the breakdown length in Fig 4.12, the breakdown length (the length of laser intensity above the breakdown threshold along the beam direction) increases with the laser intensity. Assuming the laser intensity at focus I_o is 3 times of the intensity of the material breakdown threshold (welding of borosilicate is around 1.3 W, and from 6.2.2, a breakdown threshold of 0.453 W inside borosilicate glass was measured), then the breakdown length from the focus to z_1 (here only positive z is required as the laser energy is absorbed before focus), are 4.77 μm, 19.1 μm and 76.4 μm respectively for a 10 mm, 20 mm and 40 mm focus length. For the welding work of borosilicate to borosilicate the breakdown length is much longer than the Rayleigh range of the lens, which gives an impression of the filament length expected due to different lens without the involvement of a HAZ (for examples, see 10.75 μJ case in Fig 4.4 and single pulse situation in Fig 4.16).

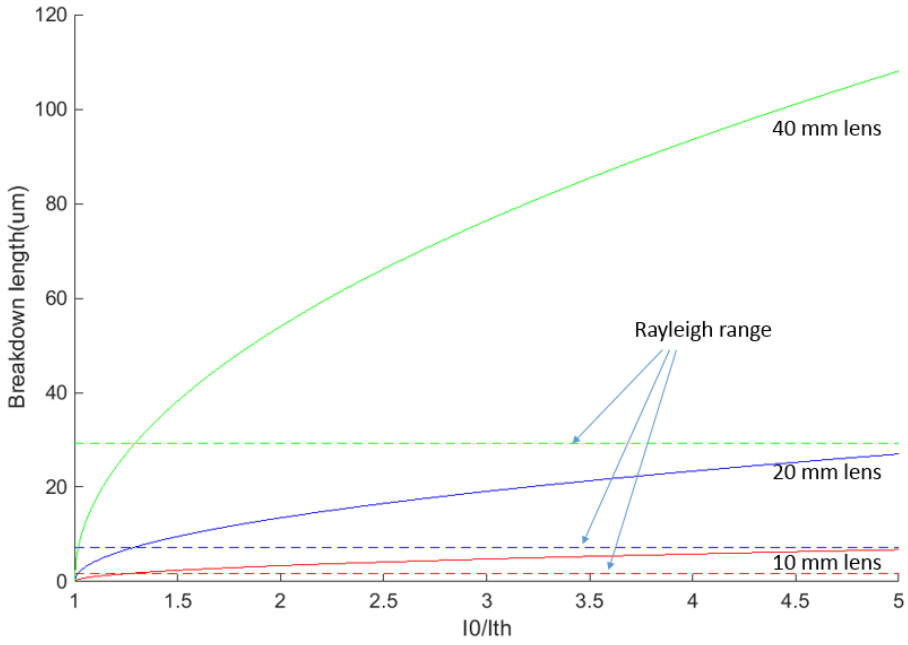

Fig 4.12 Calculated relation of I_o/I_{th} and the breakdown length for different focus lenses. The Rayleigh ranges are also drawn with the same colours.

As more laser pulse energy is deposited, HAZ appears around the absorption region, and plasma plays a dominant role and further elongates the length of the HAZ. The range of the laser intensity that can sustain a plasma (i.e. the expected extent of plasma around the focus) is obtained from Eq 4.3:

$$I_{plasma} = I_o \left(\frac{\omega_o}{\omega(z)}\right)^2 \exp(-\frac{2r^2}{\omega^2(z)}) \qquad \text{Eq 4.5}$$

I_{plasma} is the laser intensity threshold which can sustain plasma (the absorbed laser energy can allow the plasma to survive provided plasma already exists). Assuming the laser intensity at focus I_o is 1000 times the intensity of I_{plasma} for the 10 mm lens, and keeping the same laser power for the 20 mm and 40 mm lenses (and considering only the positive z as before). Then the maximum plasma widths are all 32.3 μm in width and 100.1 μm, 200 μm and 398.9 μm in length for 10 mm, 20 mm and 40 mm lenses respectively, as the calculated results shown in Fig 4.13.

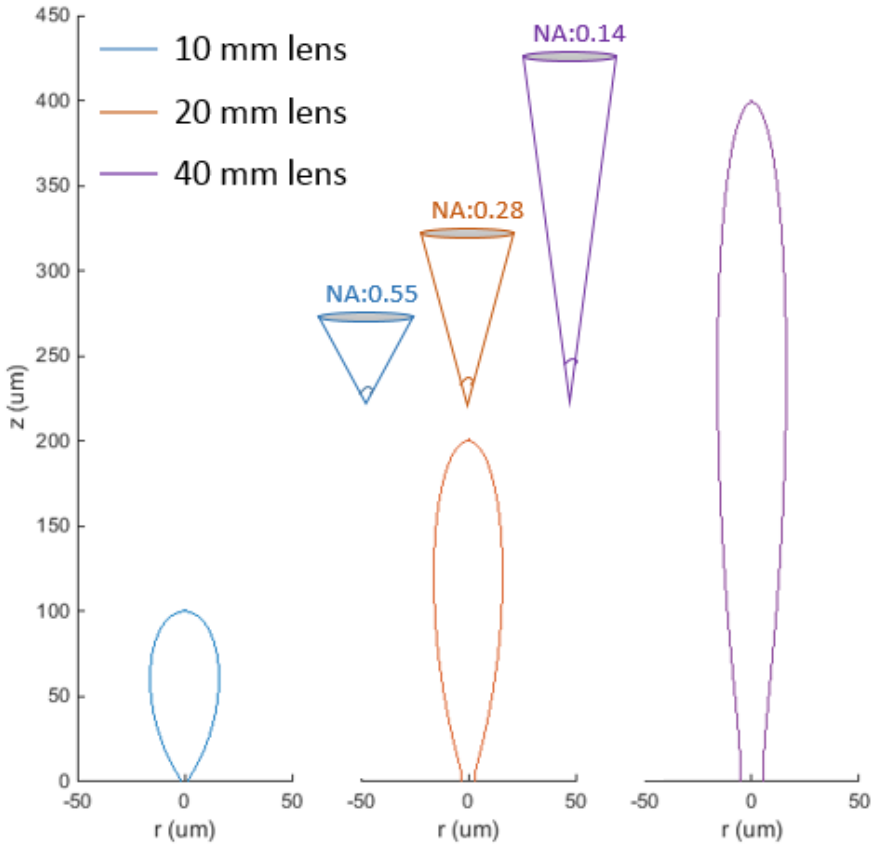

Fig 4.13 Calculation of the plasma sustainable cross-sectional area for different focal length lenses (assuming laser intensity at the focus of the 10 mm lens is 1000 times that of the plasma sustainable intensity. The calculation is based on the same laser average power for those 3 lenses).

As the same average power is used for the calculation of the 10 mm, 20 mm and 40 mm lenses in Fig 4.13, the plasma region expands over a much larger area for the longer focus lenses. Which means the plasma is more intense for the 10 mm lens compared with the longer focus lenses, so the absorbed energy density is much higher, and more voids (defects) and smaller HAZ are generated in side material or welding. The HAZ created in the experiments of different focus lenses (Fig 4.1 and Fig 4.2 in section 4.1.1) can be explained by the model above.

Combining Eq 4.4 and Eq 4.5 will give us a laser energy absorption region based on laser power and focal lens. If we further consider different scan speeds, which will influence the energy deposition rate, the HAZ (melted region by heat diffusion after laser absorption) region of different shape will be formed.

4.2.2 Cross-section

The size and shape of the modified region (HAZ) depends on the laser and material parameters as well as the sample translation velocity and, most importantly, the focal length of the lens. Cross-sections perpendicular to the inscription line for typical HAZ generated by different focal length lenses are shown in Fig 4.1, and cross-sections along the HAZ line are shown below (Fig 4.14).

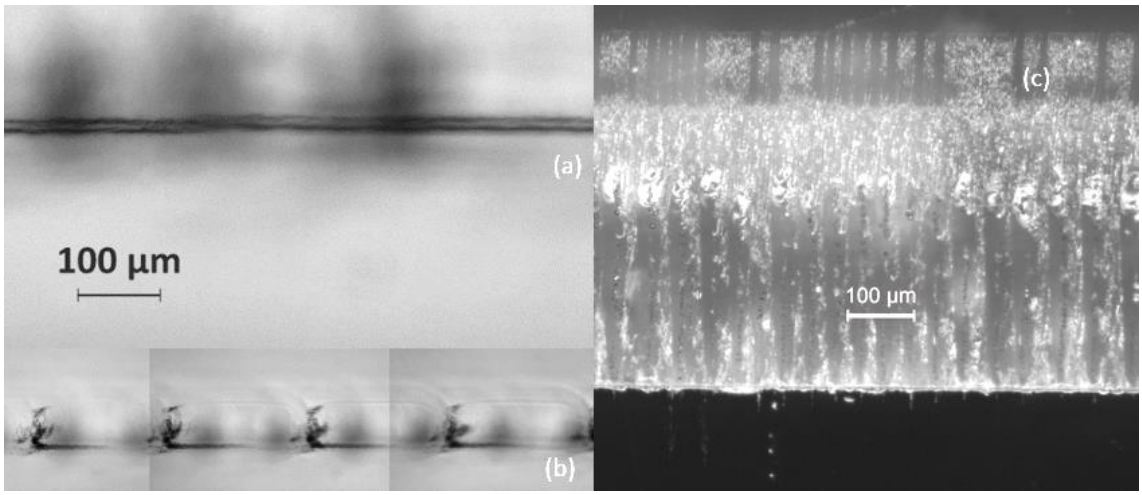

Fig 4.14 Cross-section of ultrafast laser HAZ along the (a). Continuous HAZ line, (b). Dashed HAZ line (both top view seen in Fig 4.6) of 10 mm lens, and (c). Welding line with 20 mm lens.

The cross-section view gives us a clear understanding of the laser absorption mechanism of different parameters. When ultrafast laser pulses are focused inside glass, nonlinear absorption will firstly occur at the focus, which appears as an elongated line

along the laser vector, (can be seen from Fig 4.4 and Fig 4.16 for lower power or smaller numbers of pulses). This is usually caused by localized chemical bonds breaking by nonlinear absorption, but the absorbed energy is not sufficient to melt the region when it diffuses to the surrounding area.

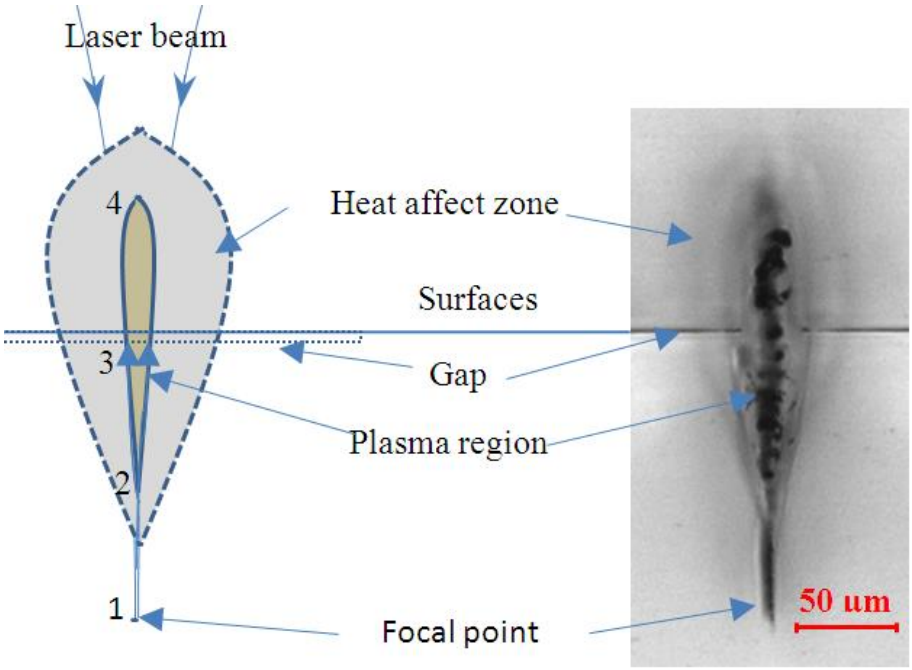

Fig 4.15 Diagram of welding formation between two surfaces (the insert welding figure: fused silica to fused silica, 7.29 W, 2 mm/s with a 2 µm gap).

Fig 4.15 shows a typical cross-section of a weld, the leading ledge of the pulse has only enough energy to exceed the intensity threshold for breakdown at the laser focus, and therefore forms the tip of the tear-drop (Fig 4.15(1)), subsequent pulses have enough energy to produce breakdown further from the laser focus, with the help of both nonlinear absorption and linear (i.e. defects) absorption. Breakdown occurs further and further upstream from the focus, forming a defect line larger than the Rayleigh range of the lens (Fig 4.14c, explained in Fig 4.12). As laser power increases or more pulses come in, plasma is formed and expands to form a cone structure. Both laser beam expansion and plasma expansion lead to a structure that extends over a region much larger than, and above, the focal volume of the lens, and spans a wide range of material modifications (Fig 4.15(2)). NB as the pulses separation time is larger than the plasma lifetime, the subsequent pulses are more readily absorbed by defect or photon assistant absorption and the absorption region moves incrementally closer to the source rapidly expanding the plasma affected region along the laser beam axis.

As the absorption region moves upwards there is eventually sufficient thermal diffusion to form a HAZ and this begins to expand laterally (Fig 4.15(3)). This process continues until the absorbing region has moved so far out of focus that absorption drops to an un-sustainable level (Fig 4.15(4)). At this point the formation terminates and the process begins again at the geometric focus as the laser is translated laterally (Fig 4.14b and Fig 4.6), or the plasma absorption becomes self-sustainable at this height and a continuous line is formed as the laser is laterally translated (Fig 4.14a and Fig 4.6). During this process material in the plasma affected region mixes and a true weld is formed in this area [157]. Thermal diffusion generates a HAZ but the limited mixing of material is insufficient to form a true weld (seen from the right inset of Fig 4.15).

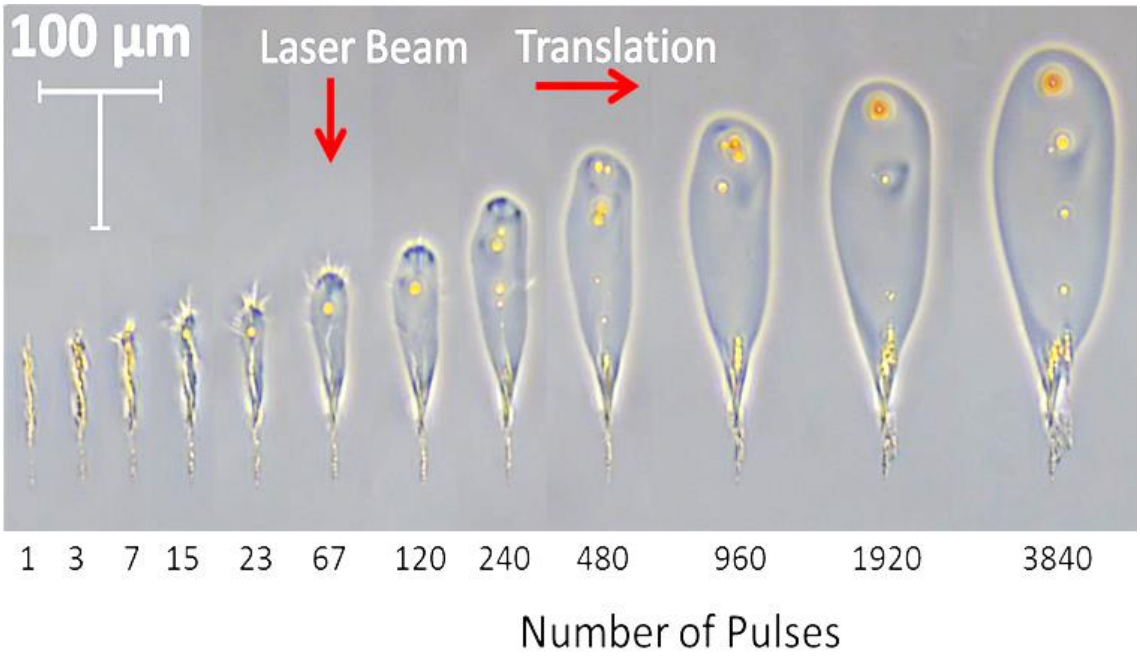

Fig 4.16 Evolution of plasma affected region and HAZ with increasing incident pulses of 21.25 µJ in a single fused silica sample. Phase contrast imaging has been used to provide clearer images.

For welds at the interface, especially of different materials, the material properties play quite an important part, not just the thermal properties discussed in Chapter 2, there are several points to consider:

Plasma material exchange: During the welding process, plasma moves up from the focus and expands laterally to form a conical plasma region and eventually heat is diffused to a tear-drop HAZ. Inside the plasma region material from the upper material and from the bottom sample move upward and downward and are finally mixed together and form a bond at the interface (for detailed please see section 4.4). However

out of the plasma region, even inside the HAZ, a limited bond is observed from the cross-section (right part of Fig 4.15)

Surface tension: Thermal diffusion generates a melting pool around the plasma region, but cross-sectioning of the weld region indicates that this melt region might not create a bond as shown in Fig 4.15, in which the surface tension of the melting surfaces prevents the two materials maxing together and forming a true bond.

Transition temperature and thermal expansion: Unlike metals, glasses (amorphous materials) have transition temperature (close to their annealing points), at which the material temperature above this point will result in a change from a hard and relatively brittle state into a soft and flexible rubber-like state. The transition temperature is always lower than the melting temperature (or softening point for amorphous materials). So around the melt pool glass becomes soft which may not directly affect welding of the same material but will affect welding of different materials, as shown in Fig 4.17. Different thermal expansions of the rubber-like states of the two materials will result in one intruding into the other, which results in a non-flat interface.

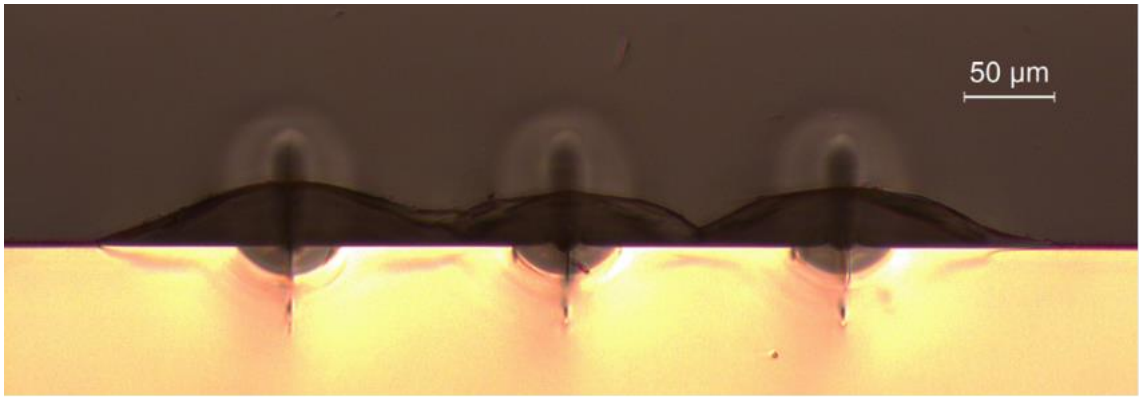

Fig 4.17 Welds of two different glasses of different transition point. (Upper glass: Nd doped borosilicate glass, bottom glass: borosilicate glass. Laser parameters: 1 W average power with 1 mm/s scan speed).

Brittleness: The brittleness of glass makes it easy to crack after localised heating through ultrafast laser pulses, although some reports say the heat enhances the fracture toughness of the material inside the welded region [5][136]. At the same time heat introduces more residual stresses [158]. Cracks and residual stress can usually be observed inside cross-section views of both HAZ and welding (Fig 4.18). The residual stress mainly comes from the heat and shock waves generated as laser pulses are incident, which compresses the surrounding material. When the HAZ is melted or

softened, it releases the stress in the molten region (e.g. compare different number of pulses in Fig 4.16), and, after processing, the solidification introduce residual stresses as well. Those residual stresses can be minimised by optimising the different welding parameters.

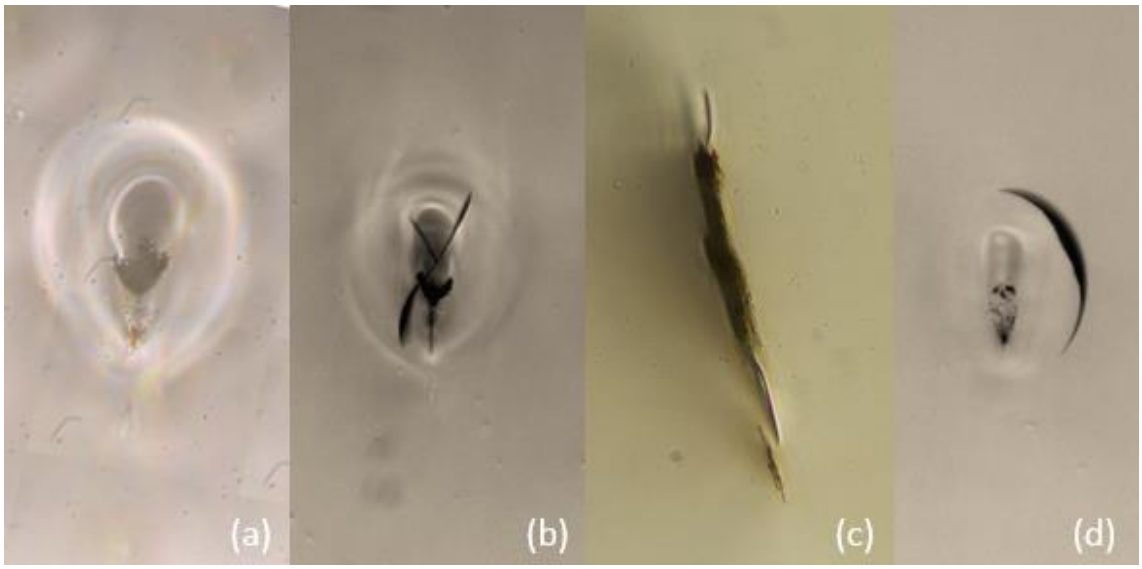

Fig 4.18 Residual stress and residual stress induced cracks. (a). Refractive index changes inside the HAZ, (b). Cracks inside borosilicate glass, (c). Crack induced by small amount of laser power, (d). Cracks inside fused silica.

4.2.3 Welds Peeling

Apart from cross-sectioning after welding, peeling is another way to investigate the welding area is morphology analysis. The extension stress is not that easy to measure for small samples, so for our experiment we didn't carry out extension strength tests for peeling, instead we observed the morphology after breaking. When separating the two samples after welding, it is hard to predict where the cracks start and what the broken area looks like for glass to glass welding, as both the samples are brittle, and it is hard to know where the defects will become fatal. For breaking glass to metal welds, however, the broken area seems quite consistent for the same welding parameters.

The experiments carried out consisted of firstly welding a piece of borosilicate glass to a polished stainless steel surface (R_a <50 nm), with a laser average power of 0.7 W and scan speed 1 mm/s. The samples were broken and then brought under a microscope for observation, with the 3D scanning method "montage" of a Leica DM6000M Microscope, a 3D surface shape can be constructed around the broken seam. In the photos and graphs, the weld seams are scanned in a spiral pattern with the laser

scanning direction clearly indicated from the break pattern. Arc ripples of glass remain on stainless steel surface indicating the weld strength is sufficiently high to act as a pivot when the sample was peeled off, the force then aggregates closed to the welds causing cracks or breaks.

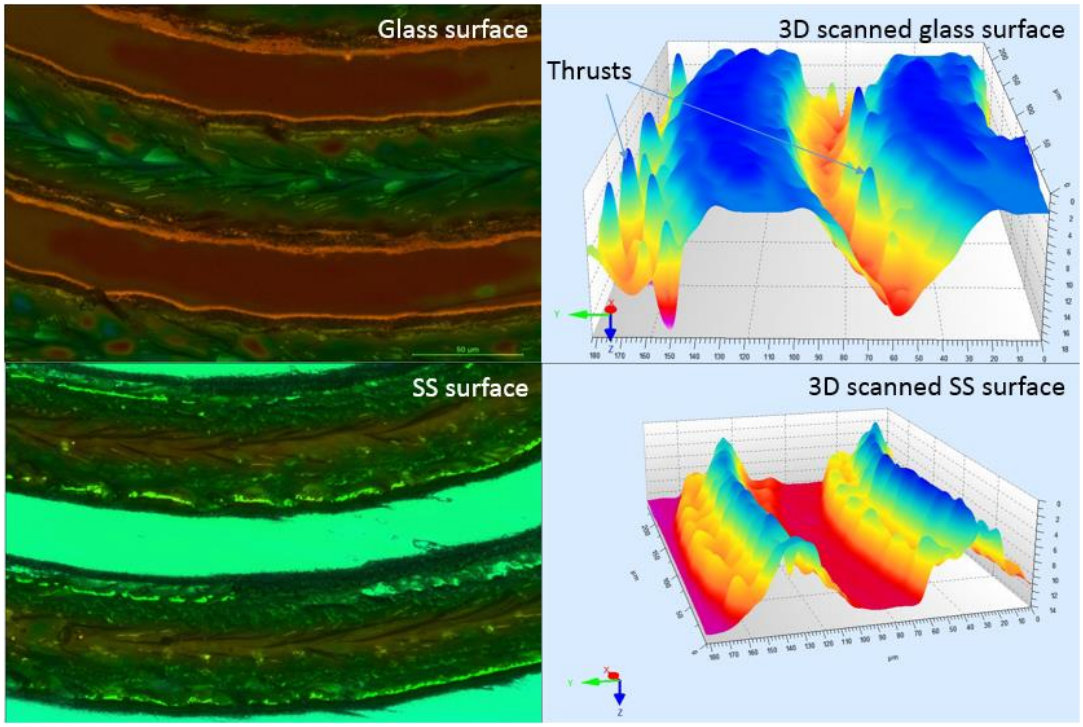

Fig 4.19 Borosilicate glass and stainless steel surface after the welds have been broken and 3D constructed image under the microscope. Note that due to the low diffraction of the glass surface, the thrusts on the top-right image are not entirely real (laser average power 0.7 W and scan speed 1 mm/s with a 20 mm lens and the seam separation is 100 μm).

4.3 Bonding Strength Test

As mentioned above, it is hard to measure the extension break strength of the weld as the sample is not easy to hold while applying a force, but it is relatively straightforward to measure the shear strength. For shear strength tests samples of uniform size and weld location are prepared with a sample frame to reduce the uncertainty of the results, as shown in Fig 4.20. Samples of borosilicate to borosilicate glass welding were used for the test with borosilicate samples cut into 25×25 mm and 20×20 mm square pieces. The 25 mm square sample and 20 mm square sample were then put into the frame inside the clamp for welding (Fig 4.20). The welded samples were then put to a strength test rig in a strength test machine (Instron 3367) for strength test, as shown in Fig 4.21.

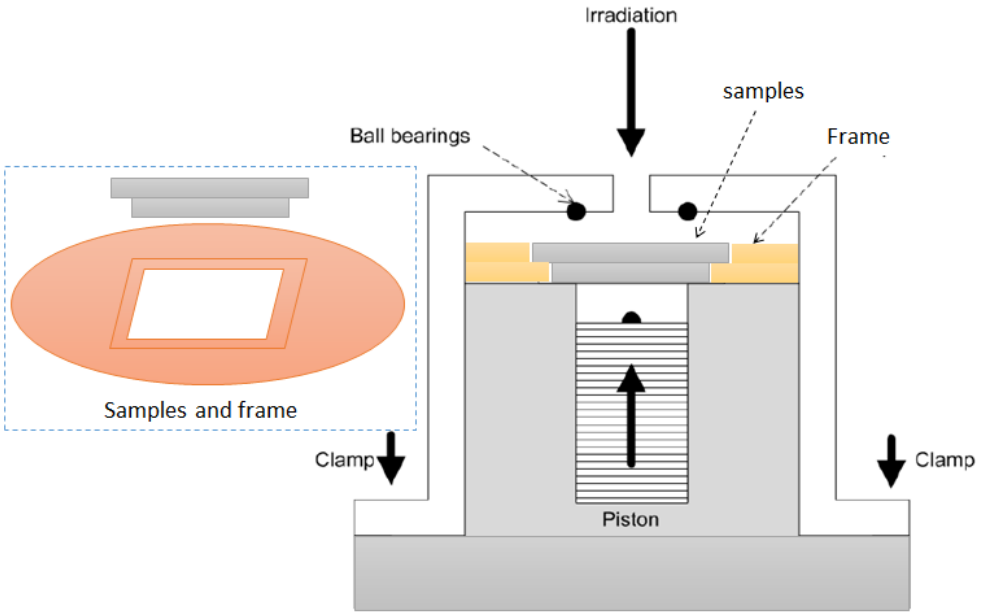

Fig 4.20 Samples and sample frame in the clamp to maintain the relative position of the two samples and same welding position.

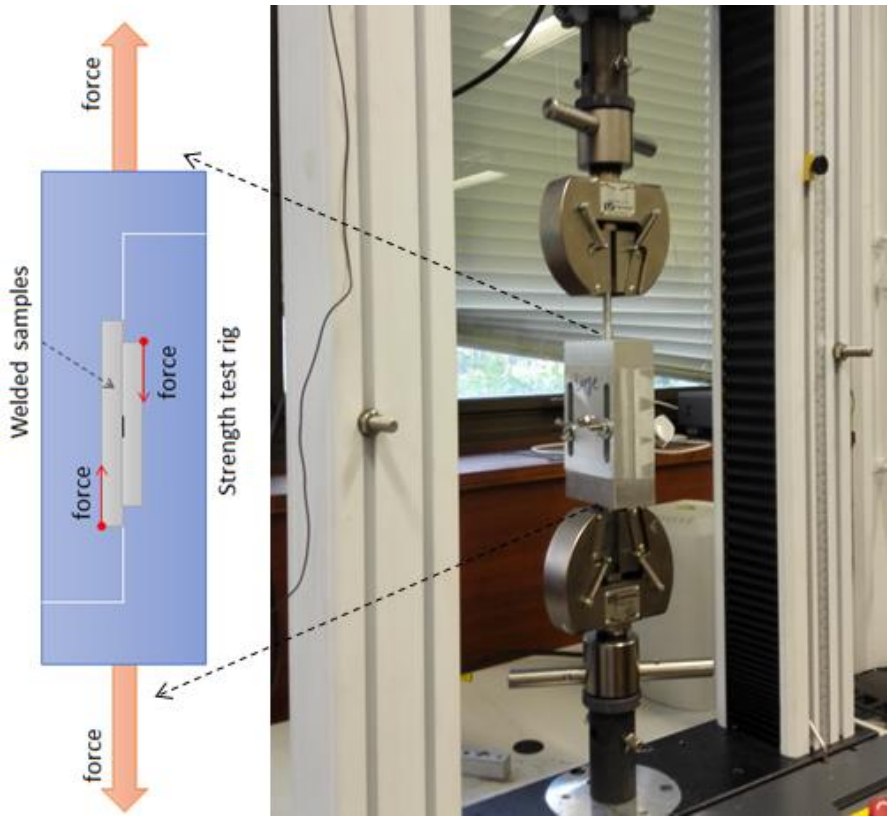

Fig 4.21 Diagram view of shear break testing rig and photo of rig in the strength test machine. Two differentially sized pieces of glass fit into machined recesses in an aluminium block. The block is loosely held with sliding bolts and pulled apart along an axis normal to the weld plane.

For ultrafast laser direct welding of glass to glass, optical contact is easy to achieve as the surfaces are usually extremely flat, which is good insofar as the Van der Waals force can enhance the strength of bonds. For consistent strength testing, however, we need to reduce the influence of Van der Waals force as much as possible as the optical contact area varies for different samples during the clamp and welding process. The Van der Waals force is quite small compared with the welded force, as we measured for 5 samples with only optical contact, the strength of Van der Waals force is 1.04±0.05 N/mm^2 (compared with welding strength of around 100 N/mm^2 in the test). The optical contact area was measured after weld and the Van der Waals force was subtracted after the overall force was obtained. Note that the Van der Waals force is highly dependent on the separation of the two surfaces, but the distance is hard to measure or evaluate after the samples have been welded, for simplification we take all the Van der Waals forces the same for a unit optical contact area during the test.

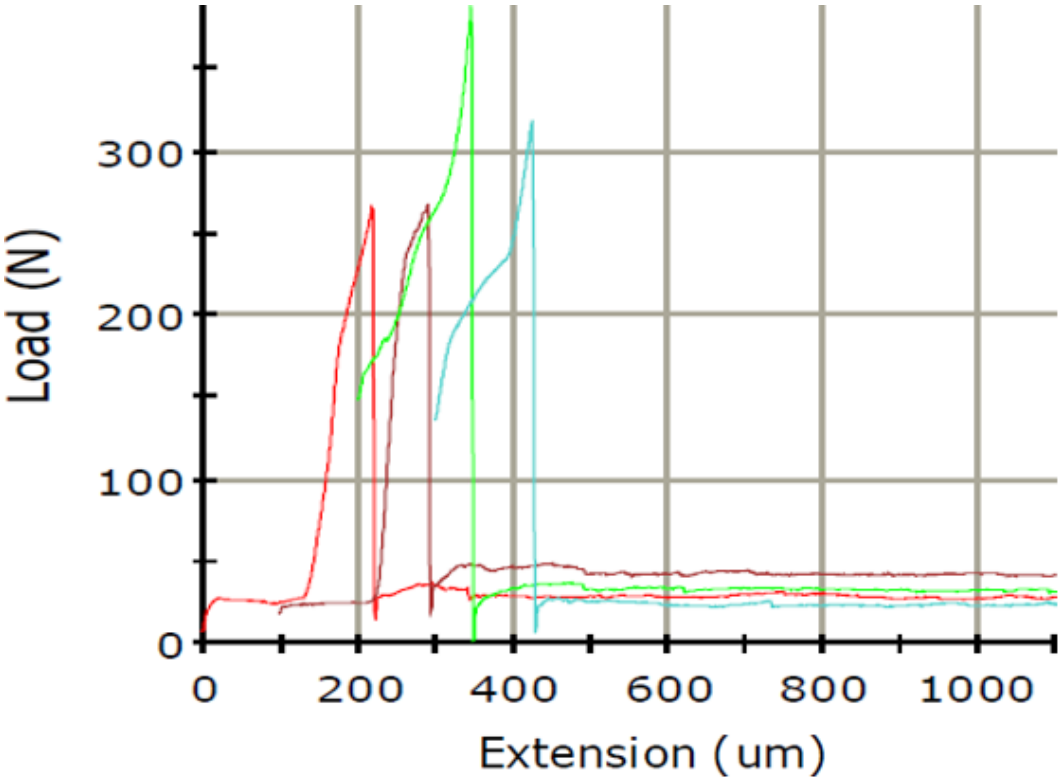

Fig 4.22 Typical shear extension and load strength relation for ultrafast laser welding samples.

The force applied to pull the two parts of the shear rig apart is in the direction shown in Fig 4.21. The typical shear extensions and load strength are shown in Fig 4.22, the load (initially just half the mass of the shear test rig) increases as the machine arm is pulled.

The load strength increased to a maximum with an abrupt break indicating a brittle material failure.

The test data includes "Load at break" for the initial strength shown on the machine when no force applied (F_{Break}), and "Maximum load" for the maximum force load to break the samples ($F_{Maximum}$), the weld strength was measured:

$$F_{Weld} = F_{Maximum} - F_{Break} - S_{oc} * P_{oc} \quad \text{Eq 4.6}$$

S_{oc} is the optical contact area of the sample and P_{oc} is the stress per unit area required to break the optical contact as previously measured. For brittle materials the maximum stress measured may vary for different samples due to the distribution of physical flaws, so usually a number of samples are tested for a statistic result.

4.3.1 Different Parameters

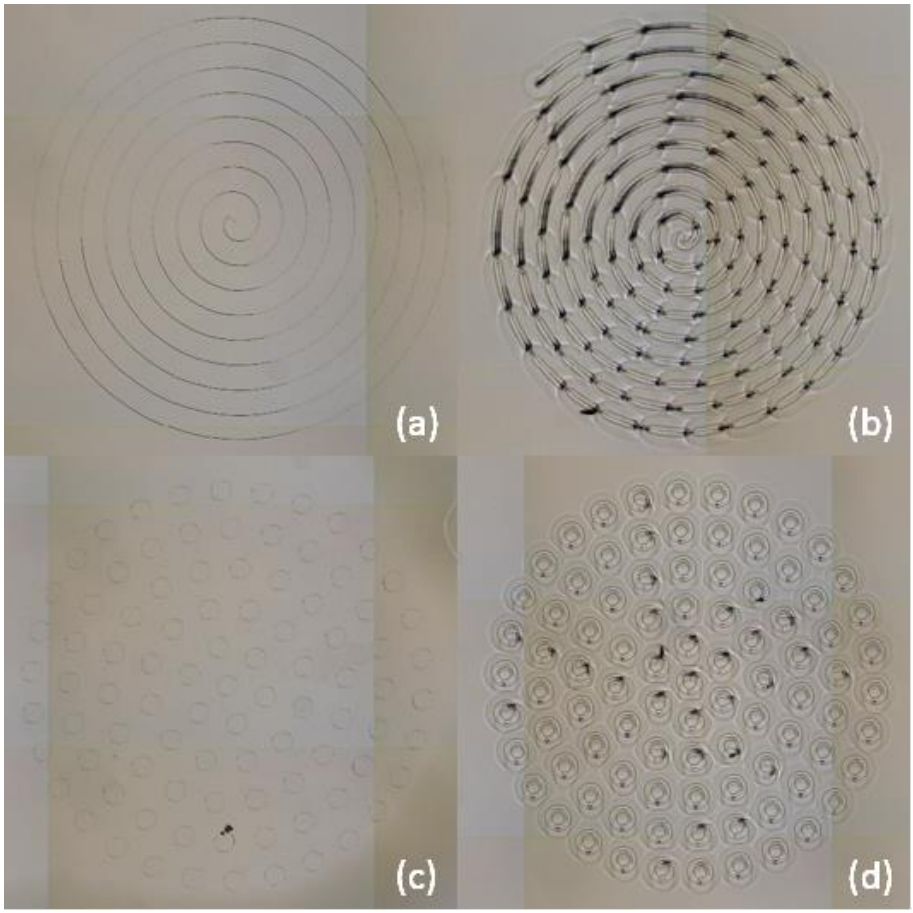

Fig 4.23 Spiral pattern (diameter = 2.7 mm, line separation = 150 μm) and circle array pattern (diameter = 3.15 mm, boundary separation = 150 μm) with power from 1.07 W (a, c) to 3.0 W (b, d).

In order to identify the general trend with regards to strength, groups of four samples were welded with the same parameters. Spiral and circle arrays were evaluated with the laser power varying from apparently non-welded to cracks appearing, as seen in Fig 4.23. The welding area diameters were chosen to keep the same laser scanning path length for the two patterns. Nine different powers were tested with four samples taken for both of the patterns at each power.

Only the weld strength is calculated because the seam width keeps changing for welding with different powers, so the weld strength per unit weld area is not presented here.

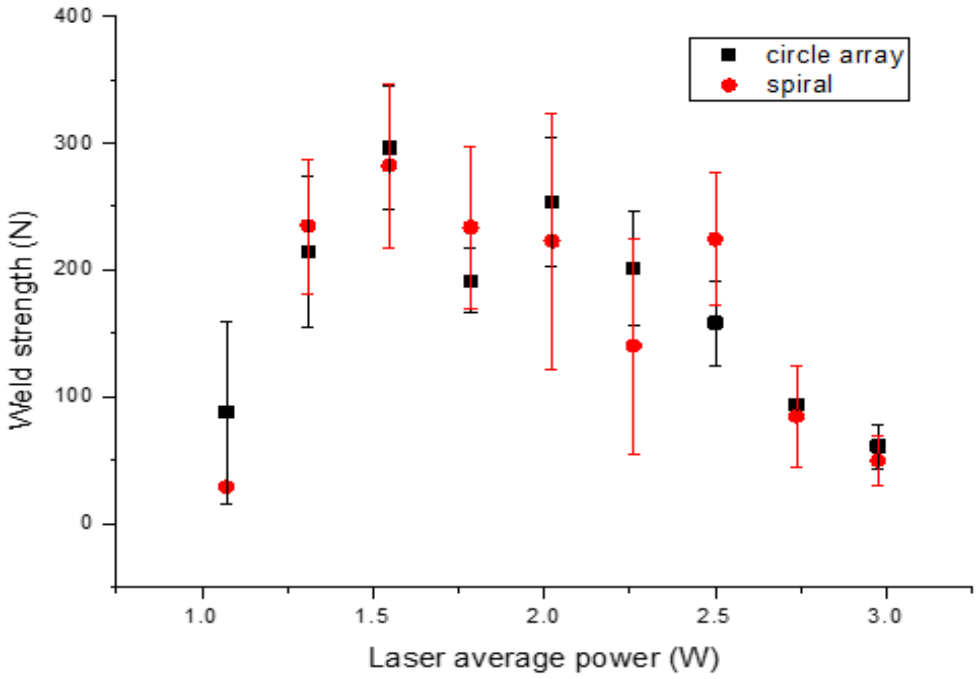

Fig 4.24 Weld strength of borosilicate to borosilicate with different laser powers, with 1 mm/s scan speed and a 10 mm lens.

From Fig 4.24 the two different welding patterns share similar strength values (within the error) for individual laser powers. As the laser power increases, the weld strength increases until the flaws or defects become severe. Then the weld strength decreases again even though there is no obvious cracking (cracks appear from 2.75 W average power) under the microscope. The maximum weld strength presented in the graph indicates the potential for optimising the laser and welding parameters.

4.3.2 Weibull Plot

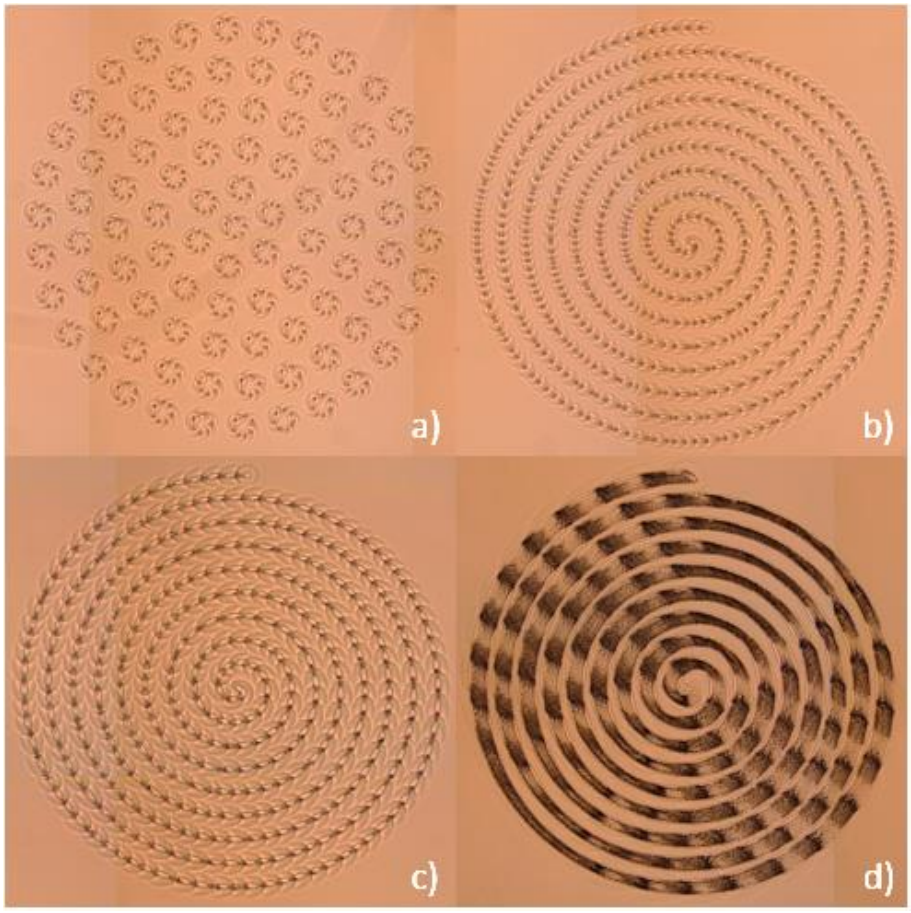

Fig 4.25 Different patterns or powers adopted for Weibull plot test. (a). Circle array with power = 1.6 W, (b). Spiral with power = 1.6 W, (c). Spiral with power = 2.05 W, (d). Vibrating spiral, power = 3.2 W.

In order to ensure the optimum power indicated in Fig 4.24, 20 weld samples as a group of the same parameters were made and shear strength tested, with four groups of different powers or patterns being prepared. In Fig 4.25a and Fig 4.25b the laser power of 1.6 W were chosen for a highest welding strength which is indicated in Fig 4.24; Fig 4.25c is a power slightly higher than optimum power without obvious crack for comparison, and Fig 4.25d is a new spiral pattern with the vibrating focal lens (with the method introduced in Section 6.4) which generates larger HAZ and plasma region with more incident power. The sample preparation method and shear strength test method were the same as described above, with the Weibull plot graph shown in Fig 4.26. Welding of the same pattern and power shares the same welding seam width so the strength of a unit weld area (the area of the weld line) is calculated and present with the Weibull plot in Fig 4.26a and the Weibull plot of the strength of a unit area of the whole region (including the space between the weld lines) is in Fig 4.26b.

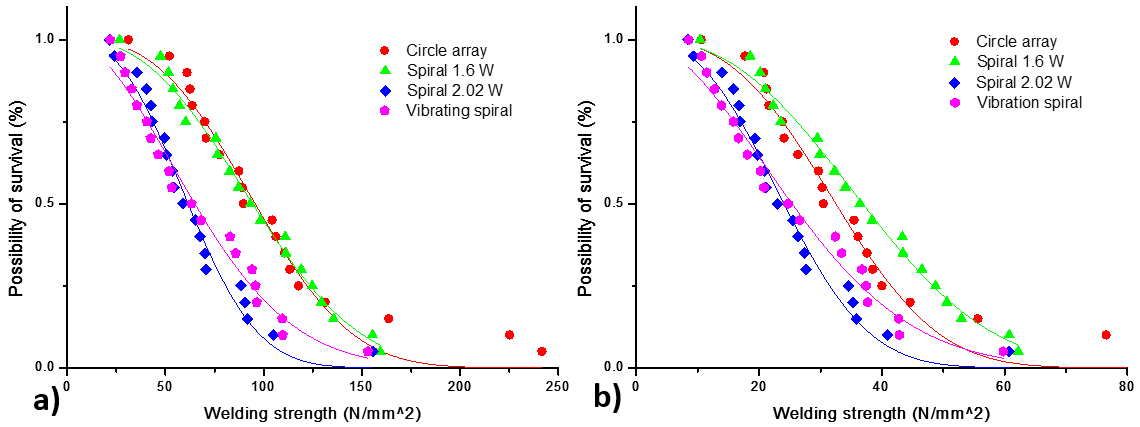

Fig 4.26 Weibull plots of possibility of survival for welding strength of unit area. (a). Welding seam area, (b). The whole weld region.

After the measured data has been plotted, the curves were then fitted with the Weibull distribution using an iterative method (seen in Appendix). The λ and k parameters obtained are shown in Table 4.4. From the graph and table, the weld strength statistic mean are around 108.8 MPa (N/mm^2) at the optimal points (1.6 W average power) indicated in Fig 4.24, with the welding strength 96.3% of the bulk material (113 MPa for borosilicate glass [118]) for the two different patterns (spiral and discrete circle array). As expected the welding strength of 2.05 W spiral is lower than the 1.6 W spiral following the trend in Fig 4.24 and the strength of vibrating spiral as a non-optimised power of 3.2 W, is low as well, but it is clearly higher than the expected 3.2 W spiral based on the trend in Fig 4.24. The Weibull modulus k varies slightly for different patterns as well, which indicates the stability of the welds, with vibrating spiral giving the most stable welds and circle array the lest, and the spiral patterns of different powers shares the similar value.

Table 4.4. Table of Weibull strength test and iterative fit results

Patterns	**Power [W]**	**Weld seam strength**			**Area weld strength**		
		Mean[MPa]	**Median[MPa]**	***k***	**Mean[MPa]**	**Median[MPa]**	***k***
Circle array	1.6	108.828	95.65	2.84	37.002	32.523	2.84
Spiral	1.6	108.887	94.41	2.569	42.543	36.887	2.569
Spiral	2.05	71.023	61.57	2.566	29.75	24.056	2.566
Vibrating spiral	3.2	78.797	64.95	1.896	30.787	25.375	1.896

The curve of Weibull plot and strength per weld region area in Fig 4.26b is plotted to compare the bonding strength of commercial epoxy glue (10-25 MPa [160]), as one can see the average weld stress are nearly 4 times larger than commercial glue, showing the potential of the ultrafast laser welding to replace adhesives as an industrial bonding method.

4.4 Fluorescence Test

As discussed in previous sections, plasma plays a very important role during the welding process, not just for laser power absorption but also the plasma region effectively mixes the materials. To verify this, a Raman confocal fluorescence spectroscope was used to measure the materials components in the weld region. An Nd (4%) doped borosilicate glass sample was welded to an undoped borosilicate glass, with the dopant fluorescent to the Raman laser source.

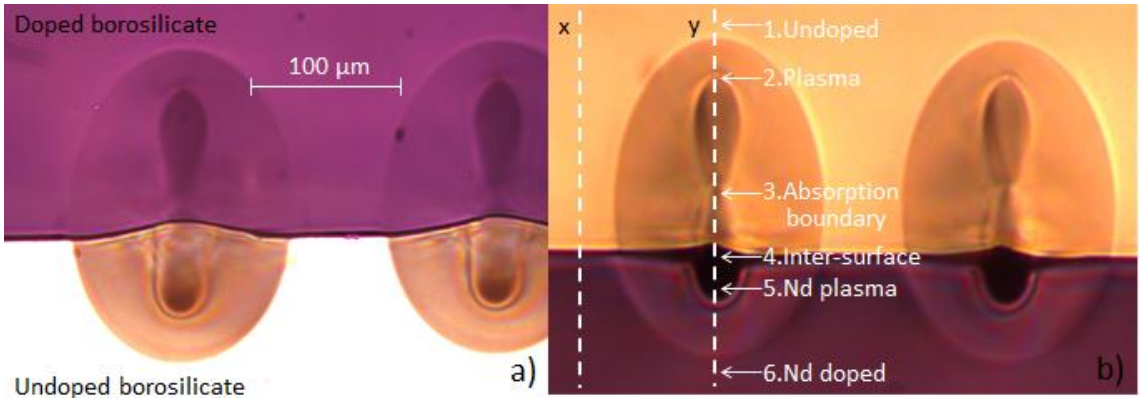

Fig 4.27 Cross-section view of doped (4% Nd) borosilicate glass to undoped borosilicate glass welds. (a). Weld from doped to undoped material, (b). Weld from undoped to doped material.

The cross-section view of the weld is shown in Fig 4.27 with: (i). Laser pulses incident on the interface through the doped borosilicate glass (laser from the top in Fig 4.27), and (ii). Laser pulses incident on the interface through the undoped borosilicate glass. The deformation of the interface can be quite clearly observed from Fig 4.27, comparing of (i) and (ii). This is probably because of the softening point in the two materials are not the same due to the dopant, with the undoped piece expanding further than the doped during the welding process.

Welding of an interface is a little bit different from generating HAZ inside bulk material, as surface defects that scatter and absorb the light play an important role during laser

energy absorption, especially when the interface lies in the position where plasma starts to grow upward and laterally expand. So in this situation an hourglass shape plasma region (Fig 4.27) instead of a cone shape, with the bottom part created by nonlinear and surface absorption and the top part by plasma absorption, for detailed experimental observation and explanation please see 5.2.2.

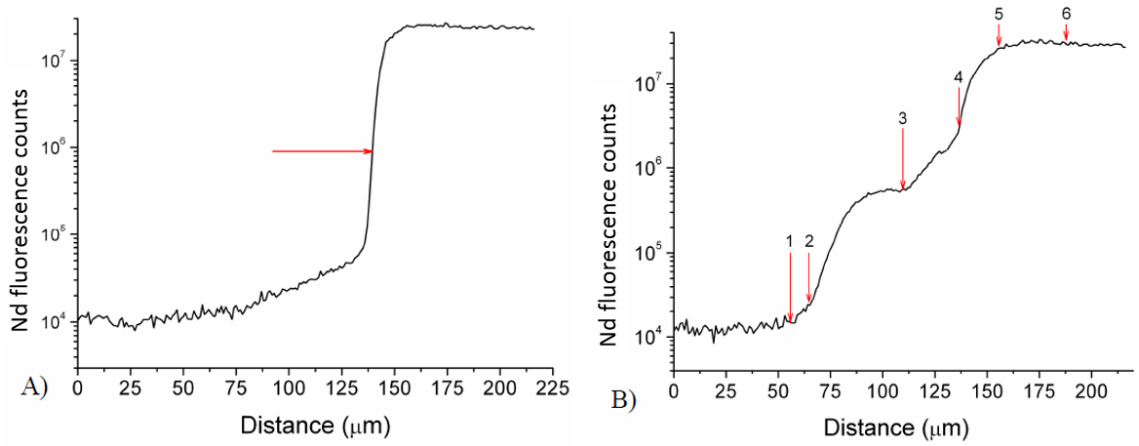

Fig 4.28 Plots of fluorescence spectroscopy scans of sectioned Nd doped to undoped borosilicate welds along paths indicated in Fig 4.27b. (a). Reference scan with no weld (line x), red arrow indicate position of interface between materials. (b). Section across weld centre (line y), arrows indicate position of points of interest from Fig 4.27b.

Plot of fluorescence spectroscopy scanning along paths indicated in Fig 4.27b are shown in Fig 4.28. The numbered points indicate the features of interest points labelled in Fig 4.27. From the Nd fluorescence counts in the reference section Fig 4.28a, a clear dividing line could be seen between the doped and undoped glass. Since the interface is expected to be abrupt the slope of the plot suggests a resolution of the order of 10 μm, which is consistent with the laser spot used for the fluorescence scan.

The weld section gives some interesting information on the mobility of the glass during the welding process. The HAZ in particular shows limited to zero mobility since there is little to no difference between the counts in this region to the non-HAZ region. The plasma zone, (hourglass feature in Fig 4.27) shows considerably more mobility the Nd increases as the trace approaches the interface. There is also a significant difference between the upper and lower lobes of the plasma region, and the doped Nd in lower lobes of the plasma region becomes less dense as well which indicate there is a considerable amount of local intermixing in the plasma region.

4.5 Summary and Conclusion

This chapter presented tests and measurement of ultrafast laser welding parameters for a successful welding of glass to glass and glass to opaque materials.

Nonlinear absorption only occurs in transparent materials where the power density is above a specific threshold (the breakdown point). An ultrashort pulsed laser and high-NA lens are required which allows for an extremely high laser intensity by condensing light temporally and spatially. Nonlinear absorption is a quite low efficiency absorption mechanism, and it needs time to transfer to a plasma absorption (absorption efficiency > 90%) process. Furthermore if the time interval between pulses is comparable or smaller than the thermal diffusion time, thermal accumulation helps through electron or photon assisted absorption in the following pulses.

Several parameters need to be considered for suitable laser energy deposition during the welding process based on the discussion above. Focused laser intensity needs to be high enough for nonlinear absorption by adjusting the laser power and focal lens (focal volume); thermal accumulation needs to be built up between pulses by means of decreasing scan speed and/or increasing pulse repetition rate; pulse energy and pulse duration need to be high to transfer the absorption process from nonlinear to plasma; Sample surface conditions and surface separation also need to be considered to deal with material brittleness and residual stress.

Table 4.5. Table of HAZ change with difference laser parameters inscribing inside bulk glass

Tested Parameter	HAZ
Laser power	HAZ increases with laser power
Scan speed	HAZ slightly decreases with scan speed
Focus lens	Longer focus lens brings larger HAZ, but requires higher breakdown threshold
Laser pulse duration	HAZ decreases with longer pulse duration
Pulse repetition rate	Higher laser repetition rate brings smaller HAZ
materials	Higher material softening point requires more laser power and brings smaller HAZ

For experimentally exploring the influence of parameters, inscriptions inside bulk glass were carried out with different lenses, different laser powers, different scan speeds, different repetition rates and different pulse durations, followed by sample cross-sections and morphology analysis. The relations of HAZ trend with different parameters are shown in Table 4.5.

The investigations of parameters in this chapter help to work out the parameters used for welding. Longer focus lens leads to larger HAZ length/width ratio and lower deposited energy density in the HAZ. The result of different laser powers and scan speeds are quite straightforward: HAZ increases with laser power and decreases with scan speed. Comparing the HAZ of different materials (fused silica and borosilicate glass, the thermal properties are more or less the same except the softening point and transformation temperature) indicates the influence of different material properties on welding parameters.

A laser absorption model together with the cross-sectioning of welds provided us a clear understanding of laser absorption mechanism and morphological formation. When ultrafast laser pulses are focused inside glass, nonlinear absorption will firstly occur at the focus, which appears as an elongated line along the laser vector. This is usually caused by localized chemical bond breaking, but energy absorbed through nonlinear absorption is not sufficient to melt the local region. As the laser power increases (or more pulses come in), plasma is formed and expands to a cone structure. Both laser beam expansion and plasma expansion lead to an absorption region that extends over an area much larger than, and above, the focal volume of the lens. This process continues until the absorbing region has moved so far out of focus that absorption drops to an un-sustainable level. At this point the formation terminates and the process begins again at the geometric focus. During this process material in the plasma affected region mixes and HAZ created due to thermal diffusion, hence a true weld is formed in this area.

Using a carefully prepared set of samples and suitable welding parameters, glass to glass and glass to metals examples were successfully welded. Weld strength tests were carried out to statistically measure the weld strength characteristics with different laser parameters and scanning patterns. Spiral pattern and discrete circle pattern was designed for welding of borosilicate-borosilicate with different powers. As the laser power increases, the weld strength increases until flaws or defects become severe, then the weld strength decreases again even though there is no obvious cracking (cracks appear

from 2.75 W average power) under the microscope. And the Weibull plot of strength tests on 4 different patterns/powers (20 samples for each pattern/sample) show the weld strength (statistic mean) are around 108.8 MPa at the optimal points indicated in Fig 4.24, with the welding strength 96.3% of the bulk material (113 MPa for borosilicate glass [118]). Comparing the bonding strength of commercial adhesives (10~25 MPa [160]), one can see the potential of the ultrafast laser welding to replace glue as an industrial bonding method.

The research of this chapter gives a guide of welding parameter selection and a basic understanding of welding mechanisms. For a future work, an extensive experiment for the investigation of plasma behaviour and laser energy absorption will bring a new insight for ultrafast laser welding, which will introduce more effective ways for the welding work.

Chapter 5 Welding Limit Determination

As discussed in previous chapters, ultrafast laser welding relates to optics, surfaces, materials science and mechanical engineering which require a number of parameters to be considered. Sample preparation methods were discussed in Chapter 3 and parameters investigated and tested in Chapter 4. Using a carefully prepared set of samples and suitable welding parameters, glass to glass and glass to metals were successfully welded, and optimum parameters were investigated via weld strength tests. For industrial applications, it is important that the sample preparation method is straight forward and fit up easy to achieve. Work in this chapter hence focuses on the identification of laser parameters that allow tolerances to be relaxed.

From the parameter tests in bulk material in previous chapters, the trend of HAZ size is indicated by different welding parameters, but those trends are usually misleading when we adopt those parameters for welding. For example, normally a laser power of 1 W can create a HAZ (length: 100 μm) inside borosilicate glass, and as the laser power reaches 2.8 W (HAZ length: 490 μm) there are still no cracks inside the HAZ, as shown in Fig 4.3. But defects and residual stress are greatly increased at this power, and welding with this power will lead to low welding strength or apparent cracking (Fig 4.24). The limitations of laser parameters and welding parameters are discussed in this chapter.

The impact of air gap between the two materials being welded with different welding parameters needs to be investigated. Even with proper clamping, careful surface polishing and cleaning, a large surface separation may still appear due to surface deformations introduced by Van der Waals forces, surface tensions, heat deformations and surface thermal expansion during the welding process. Experimental arrangements using either curved surfaces (cylindrical lens) or etched grooves were thus used to find suitable parameters for weld different gaps. In addition, the impact of different surface preparation techniques was investigated.

5.1 Limitations of Welding Parameters

Limitations of welding parameters need to be considered for a successful weld. In this section the residual stresses inside the weld are discussed and techniques to increase the weld's temperature tolerance and restrain or eliminate cracks in the welding area are investigated.

One of the merits of an ultrafast laser is highly localized heating. With high pulse repetition rate used in this process, an extremely high temperature can be obtained in the very small focus region. The material in this region can thus be melted while still surrounded by cold material. The problem is, energy deposited in the focal region will eventually transfer to the surrounding lattice [161], increasing the temperature and introducing residual stress after welding. Although the residual stress is minimised due to minimal energy deposition using an ultrafast laser, it will still cause cracks or makes the welded area vulnerable to ambient temperature changes. Recent reports suggest annealing can release the stress and reduce the defects introduced by ultrafast laser modification [162], but the annealing temperature is usually too high and not suitable for dissimilar materials.

In general a wider weld seam leads to a larger joining area which implies higher weld strength, but defects or cracks make the weld strength weak. Experiments were carried out by welding borosilicate glass to borosilicate glass with different laser powers. As the laser power increases, a larger seam size is observed, but more defects appear (as voids and microcracks and even large area cracks), as seen in Fig 5.1 below. From the weld strength test in Fig 4.24 one can see the weld strength decreased even through no obvious creaks appear as the laser power was increased. There exists a threshold, as laser power increases, when the joining strength obtains too much influence from defects which weaken bonding to the weld.

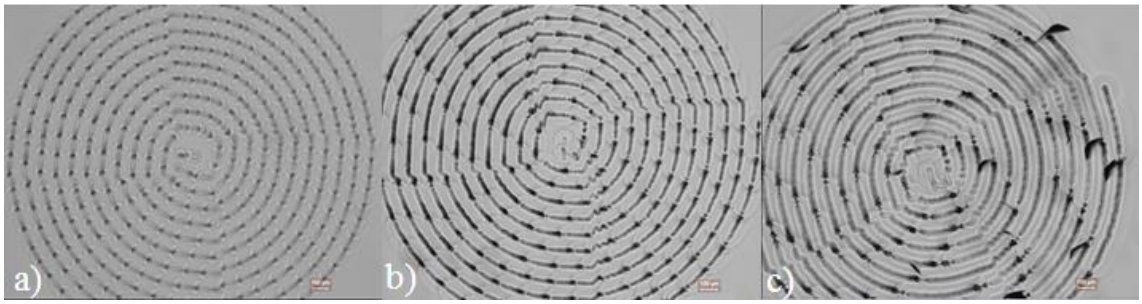

Fig 5.1 Weld seams on borosilicate glass to borosilicate glass with different laser powers, (a).1.57 W, (b).2.06 W, (c). 2.68 W, defects become obvious as laser power increased and cracks appear in higher power(c).

Those high laser power induced cracks are mainly due to a large amount of void generation, high thermal gradients inside the HAZ, and/or HAZ overlapping between different seam lines. Effective methods to eliminate or reduce this kind of defects or

cracks include reducing the laser power, or increasing the seam line separation if the HAZ lines are overlapped.

There is another type of residual stress when two different materials are welded: differences in thermal expansion during the welding process will introduce residual stress. For example, the thermal expansion of stainless steel (17.2×10^{-6} K^{-1}) is much larger than glass (fused silica 0.55×10^{-6} K^{-1}, borosilicate glass 3.3×10^{-6} K^{-1}). After welding, the two materials will contract in a different rate as the temperature returns to ambient. The stress induced can thus become fatal when a large area is welded. Here cracks are generated at the boundary of the weld in the brittle glass (Fig 5.2). Even if no obvious cracks are observed, the residual stress would make the area vulnerable and the cracks can gradually grow around the weld area as a result of ambient temperature changes (e.g. day and night). This residual stress restricts the maximum size that can be welded, which is based on the difference of thermal expansion coefficients, deposited laser energy and the breaking strength of the materials.

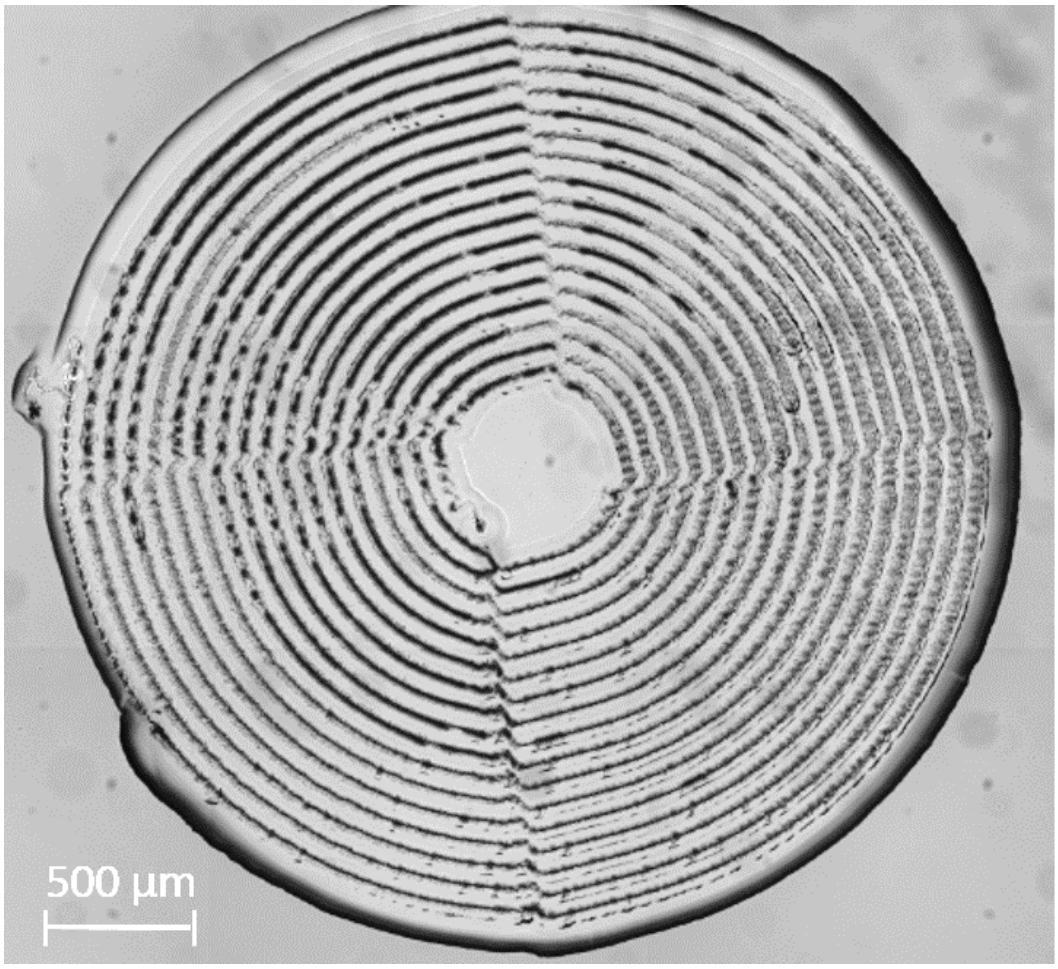

Fig 5.2 Weld with cracks around (borosilicate glass to fused silica, laser power: 1.32 W with scan speed 1 mm/s. weld seam separation is 80 µm).

5.2 Limitations of Surface Separation

For samples with optical contact, ultrafast laser welding results are quite straightforward: non-welded for low laser power and cracking for higher power, as seen in section 4.3. Different speeds, pulse repetition rates and pulse durations share similar results from inspecting cross-section of the HAZ size as discussed in section 4.1.

Welding of sample in optical contact by changing the focal position was carried out by drawing lines along the interface (perpendicular to the cross-section plane shown in Fig 5.3) using the same laser power and scan speed. The gap disappears wherever the HAZ (represent melt region) intersects the interface.

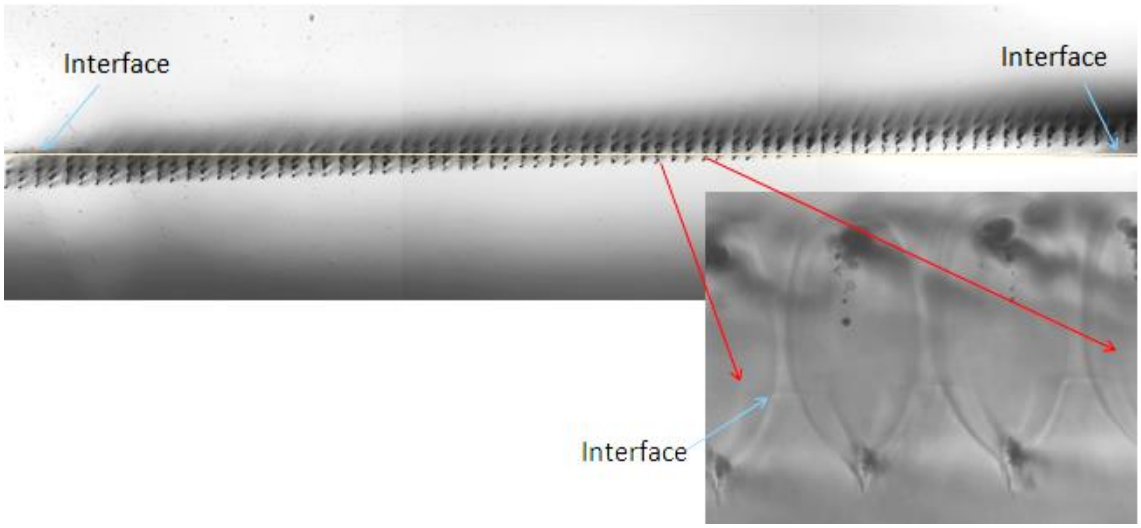

Fig 5.3 Welding of optical contact interface of fused silica to fused silica while varying focal position (laser average power 3.45 W and scan speed 2 mm/s with focal position step of 5 μm).

However, optical contact is hard to achieve across a large area (several hundred square millimetres or larger), even with highly polished surfaces and rigorous cleaning processes, making the process hard to industrialise. Furthermore, the requirement for flat and parallel plates is not always compatible with the geometry of some micro-optical systems, in particular recessed surfaces that are not easy to polish or clean. Hence it is important to determine how large a gap can be bridged.

Two types of sample structure were used to provide controlled and measureable gaps:

(i) an optic with a gently curving surface (long focal length cylindrical lens) together with a flat glass wafer;

(ii) a series of grooves accurately etched into the surface of a flat glass wafer, which was then welded to a another planar glass wafer.

5.2.1 Cylindrical Lens

The cylindrical lens used was a Thorlabs, N-BK7 Plano-Convex Cylindrical Lens, with a 1000 mm focal length, and the glass wafer was Schott, BOROFLOAT®33. Both the wafer and cylindrical lens were cleaned with acetone and methanol then pressed together with a clamp, as shown in the schematic in Fig 5.4. This resulted in a thin optical contact line (*A*, perpendicular to the plane shown), with interference fringes either side of the optical contact area. To generate the welds, the laser beam was scanned across this optical contact line. During this process, the laser spot first encounters a large gap between the materials, which decreases in size to a minimum, before expanding again. Subsequent weld lines were then created in parallel with the first, using a range of average powers (0.98–1.77 W, steps of 0.098 W) and scan speeds (0.5–10 mm/s, steps of 0.5 mm/s).

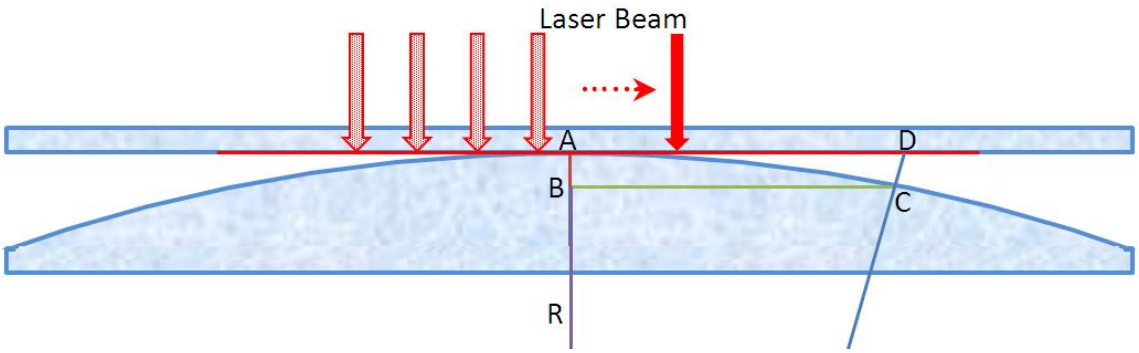

Fig 5.4 Schematic of cylindrical lens setup used for the gap welding experiments. The cylindrical lens is N-BK7 and the flat glass wafer is 1 mm thick borosilicate glass. The lens radius of curvature R is 516.8 mm. Individual weld lines are created perpendicular to the line of optical contact (A) scanning from left to right.

Provided that the radius of the cylindrical lens is sufficiently large in comparison to the weld length (*AD*), the gap (*AB*) at any point (*D*), can be easily calculated by measuring the distance (*AD*) away from the line of optical contact with a geometrical relation:

$$AB = \frac{BC^2}{2R - AB} \approx \frac{AD^2}{2R} \qquad \text{Eq 5.1}$$

Two potential issues with this method are that (a) the glass wafer will bend slightly in the clamp, and (b) previous welding seams may pull (or push) the two surfaces closer together (or further apart), hence the gap distance calculation is subject to some error. Due to these uncertainties, experiments that involve varying the focal position of the laser were not attempted with this setup.

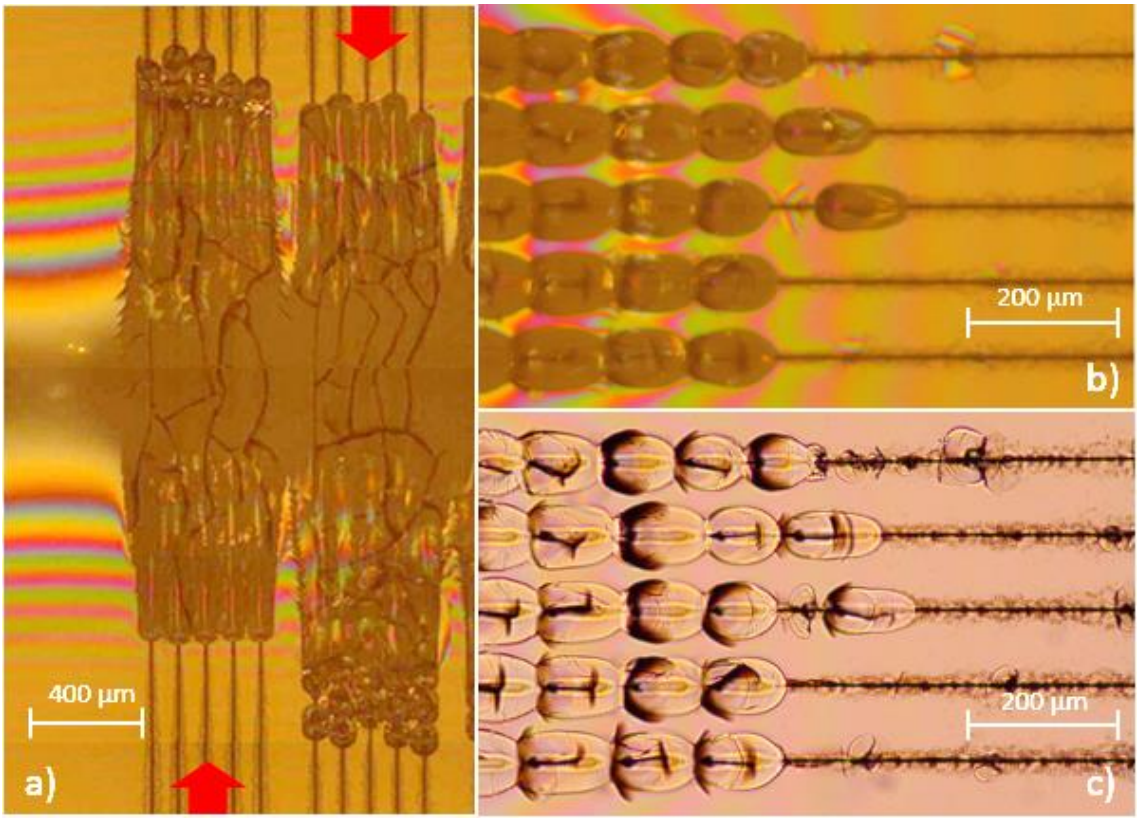

Fig 5.5 (a). Welds of a cylindrical lens to a flat borosilicate glass wafer with different scan directions (labelled with red arrows), (b). Reflection and (c). Transmission images are used to differentiate the true weld from surface ablation. (Laser power 1.18 W with scan speed 1 mm/s).

The impact of weld direction was initially investigated. The cylindrical lens welds shown in Fig 5.5a were made with identical parameters (1.18 W laser power and 1 mm/s scan speed, separation between lines is 0.1 mm), however 5 were in one direction and the other 5 in the opposite direction as indicated by the red arrow on the photo. Fig 5.5b and Fig 5.5c are the enlarged images of the welds with back reflection (b) and transmission (c) microscope mode to differentiate the welded region from ablation. Ablation can be differentiated due to the surface cracks and from the fringe distortion between the weld seams. The fringe distortion indicates that the welds themselves have locally altered the gap between the two glasses, i.e. pulled the glass together or distorted

the inner surfaces. This effect, combined with the bending in the glass slide, results in an uncertainty in the absolute values of the calculation from Eq 5.1. Hence the gap distance calculation is subject to some error. Interference fringes can be clearly observed across the sample, which provide a measure of the gap at any particular point from which the gap calculations could be verified. In b) and c) of Fig 5.5, evidence of ablation is observed, where material escaped and was redeposited.

In Fig 5.5 the weld seam and un-welded (ablated) region can be identified from the width of the HAZ as well as the colour of the reflected top view. The weld-able gaps gap is clearly influenced by the laser scan directions, with a larger gap bridged if the gap is increasing rather than decreasing.

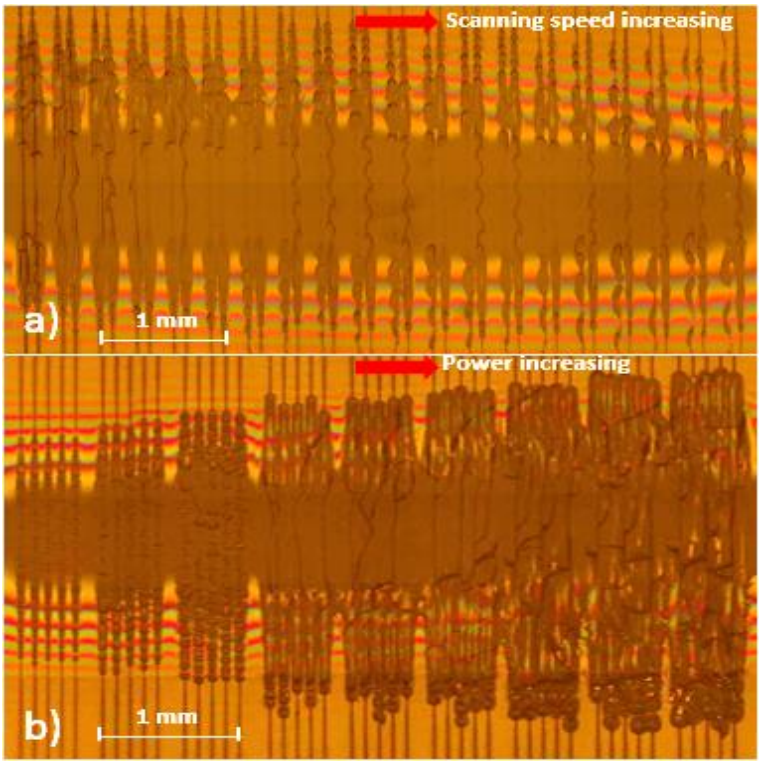

Fig 5.6 Welds of cylindrical lens with different parameters. Each parameter consists of a set of identical welding parameters. (a). 20 sets of welding lines (each set contains 2 lines separated with 100 µm and 200 µm separation between different sets) with an average laser power of 1.18 W, and different scan speeds (left-to-right: from 0.5 mm/s to 10 mm/s with step of 0.5 mm/s). (b). 9 sets of welding lines (each set contains 5 lines separated with 100 µm and 250 µm separation between different sets) with the same scan speed of 1 mm/s, and different average powers (left-to-right 0.98, 1.08, 1.18, 1.28, 1.38, 1.48, 1.57, 1.67 and 1.77 W). The focal position of the laser is 72.7 µm below the bottom surface of the flat glass wafer. In both images, the laser translates from top to bottom.

The results of laser welding of plane glass to a cylindrical lens for a range of laser parameters are presented in Fig 5.6. To investigate the effect of laser spot translation speed, welds were attempted using a constant laser power of 1.18 W, as shown in Fig 5.6a. It can be seen that the weld lines become thinner as the laser spot scan speed is increased. Over the parameter range investigated, however, we observed no obvious trend linking scan speed with the gap that could be successfully welded. This observation is interesting, given that the exposure energy line densities used in this experiment ranged over 20 times, from 2.36 J/mm to 0.12 J/mm although the spot to spot overlap remains extremely high.

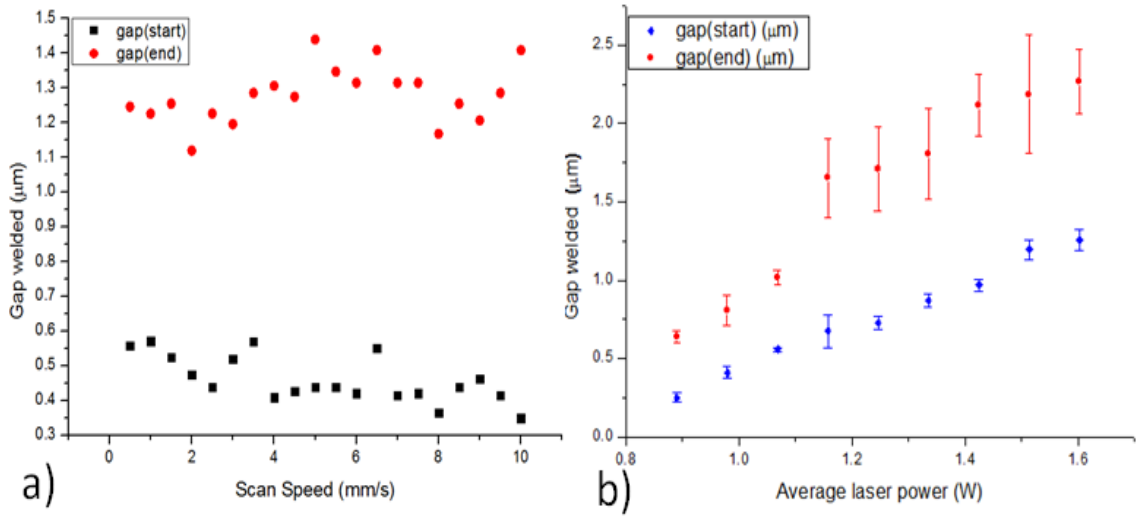

Fig 5.7 Comparison of "gaps (start)" and "gaps (end)" for different incident average powers (a) and scan speed (b) in Fig 5.6. Both graphs indicate that "gaps (end)" are roughly twice as large as "gaps (start)".

To investigate the effect of laser power on the gap size that could be bridged, a constant scan speed of 1 mm/s was used, but the laser power was varied from 0.98 W to 1.77 W, in steps of 0.098 W. As can be seen in Fig 5.6b, higher laser powers enabled successful welds across larger gaps, as might be expected, although we also observed that too high a power also results in cracking in the sample. From Fig 5.6, there appears to be a difference in the size of the gap that can be bridged either side of optical contact in that a larger gap can be bridged if the welding process has already begun. For clarity, we will refer to the size of gap when the weld is initiated as the "gap (start)", and the size of the gap when the weld fails as the "gap (end)". Fig 5.7 presents a comparison of "gaps (start)" and "gaps (end)" calculated from Eq 5.1 using the data obtained from Fig 5.6. As can be seen in Fig 5.7, "gaps (end)" are roughly twice as large as "gaps (start)" for the same welding parameters of both different scan speeds and welding average powers.

Interference fringes can be clearly observed across the sample, which provide a measure of the gap at any particular point from which the gap calculations could be verified. The error bars in Fig 5.7b are based on the standard deviation of the observed results.

5.2.2 Etched Grooves

The etched groove experiment provided a more reliable and repeatable way of generating discrete controlled gaps between the two surfaces to be welded. Reactive-ion etching was used to create a series of grooves on a fused silica wafer with depths from 1 µm to 5 µm (with depth accuracy ±5%). In this experiment we used fused silica rather than borosilicate, however from our previous work [157] we expect the results to be comparable to borosilicate, although a slightly higher average power is required for successful welding.

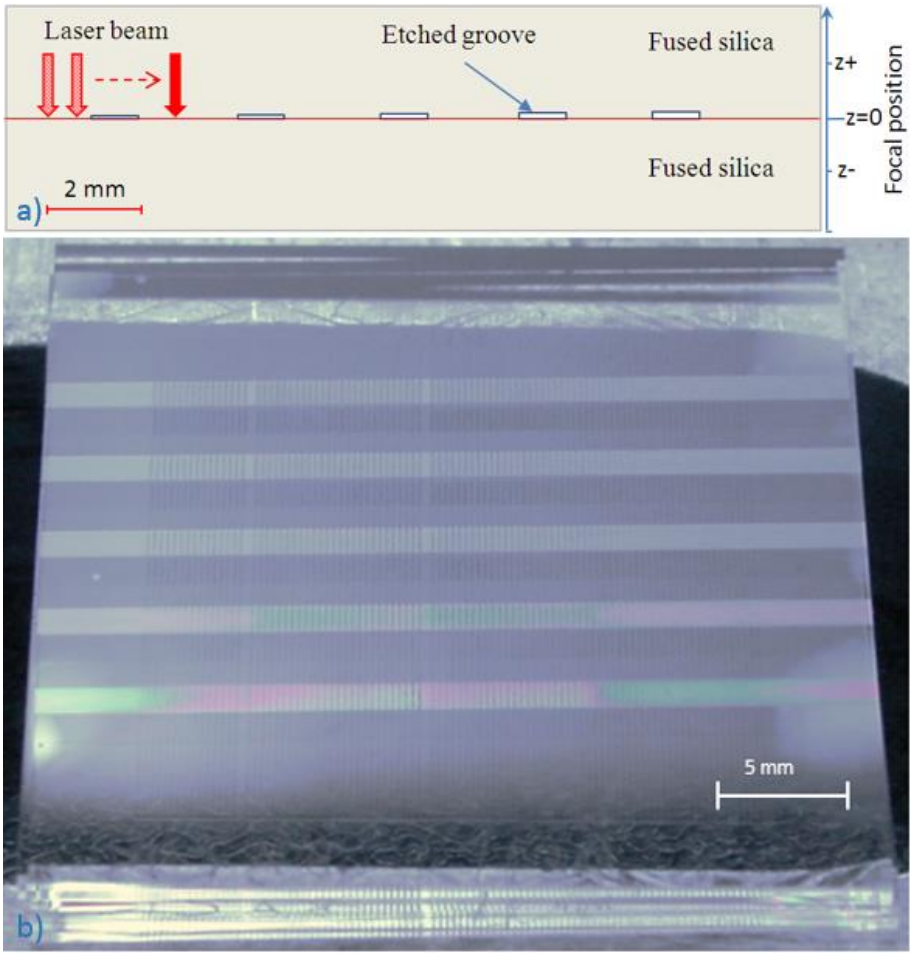

Fig 5.8 Schematic of cross-section of planar substrate arrangement (a) and experiment samples of the groove weld (b). The fused silica wafers are 1 mm thickness, with etched grooves depths of 1.0 µm, 2.0 µm, 3.0 µm, 4.0 µm and 5.0 µm, widths of 1 mm and separations of 2 mm.

The etched and cleaned surface was then clamped against a second fused silica wafer, providing optical contact at all points apart from the etched grooves (Fig 5.8). To create a weld, the laser beam was scanned perpendicular to the grooves. In this arrangement the weld begins and ends in a region of optical contact. Repeated parallel scans with different average laser powers (4.04 W to 8.53 W, in steps of 0.112 W), as well as different focal positions (from -21.2 µm to -172.7 µm in steps of -2.97 µm, Note: zero is defined as the lower surface of the top glass wafer, and a negative focal position is below this interface). All experiments were carried out with constant laser spot scan speed of 2 mm/s.

The etched groove experiment provides a more precisely controlled, albeit discretized, measurement of the gap before welding. It was found that the results obtained could be broadly characterized into one of four states: "plasma ablation", "HAZ ablation", "intermittently welded" and "continuously welded", as illustrated in the inset in Fig 5.9, which was achieved using a 2 µm gap. The "plasma ablation" region appears as a thin clean line, Fig 5.9a; "HAZ ablation" is indicated by a line with material redeposited either side of the ablation line, Fig 5.9b; "Intermittently welded" corresponds to a mixture of HAZ ablation and weld beads with at least 25% of the weld line consisting of beads, Fig 5.9c; For almost all cases of "continuously welded" the weld line becomes thinner and less homogeneous in the gap region, Fig 5.9d. This is likely a combination of distortion to the focal spot caused by the gap and the somewhat rougher etched surface. In most cases there is evidence of a protrusion as the laser first enters the gap. This is most striking in the "continuously welded" example (Fig 5.9d) where the weld seam maintains almost its full cross-section for the first ~100 µm. This effect does not occur as the laser moves from gap to optical contact at the bottom of the etched region (Fig 5.9d).

The classifications outlined above are used in the main part of Fig 5.9 to define a parameter map for these four states as a function of groove (gap) depth and average power at a fixed focal position of -72.7 µm and laser spot scan speed of 2 mm/s. It should be noted that although the gaps tested are 1.0, 2.0, 3.0, 4.0 and 5.0 µm, the average powers tested are at 0.112 W increments giving a total of 41 individual tests per gap size, only those points on the boundaries between classifications have been plotted. Determining the exact boundary between the states is challenging in some cases, particularly with the intermittently welded case, error bars are therefore provided.

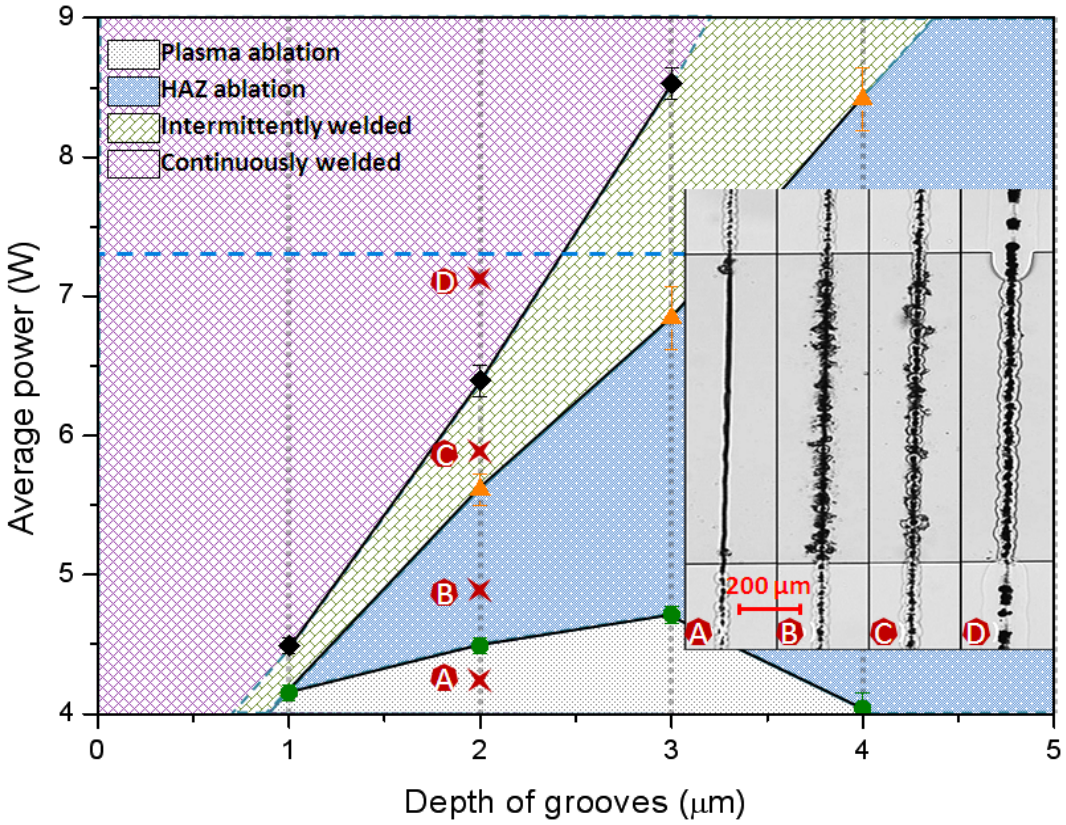

Fig 5.9 Parameter map illustrating the classification of weld results with varying gap distance and average laser power. Plotted points indicate changes between the different process classifications with a resolution of 1.0 μm in depth and 0.112 W of laser average power. The blue dashed line indicates the average power used in Fig 5.10. The inset shows different welding patterns of (a). "Plasma ablation", (b). "HAZ ablation", (c). "Intermittently welded" and (d). "Continuously welded". The cross-sections of those welds are shown in Fig 5.11. The red stars indicate the position of these results.

The results here agree with the cylindrical lens welding experiment: that increased power allows a larger gap to be successfully bridged, with an almost linear relationship. For a particular gap size the welds cycle through all four states which is expected. By increasing the average laser power, an "intermittently welded" or even "HAZ ablation" can become a "continuously welded" region, but at some point material cracking due to excessive laser power will become an issue. It is worth noting that cracking was not observed in any of the etched groove experiments and hence tests with higher average powers are feasible.

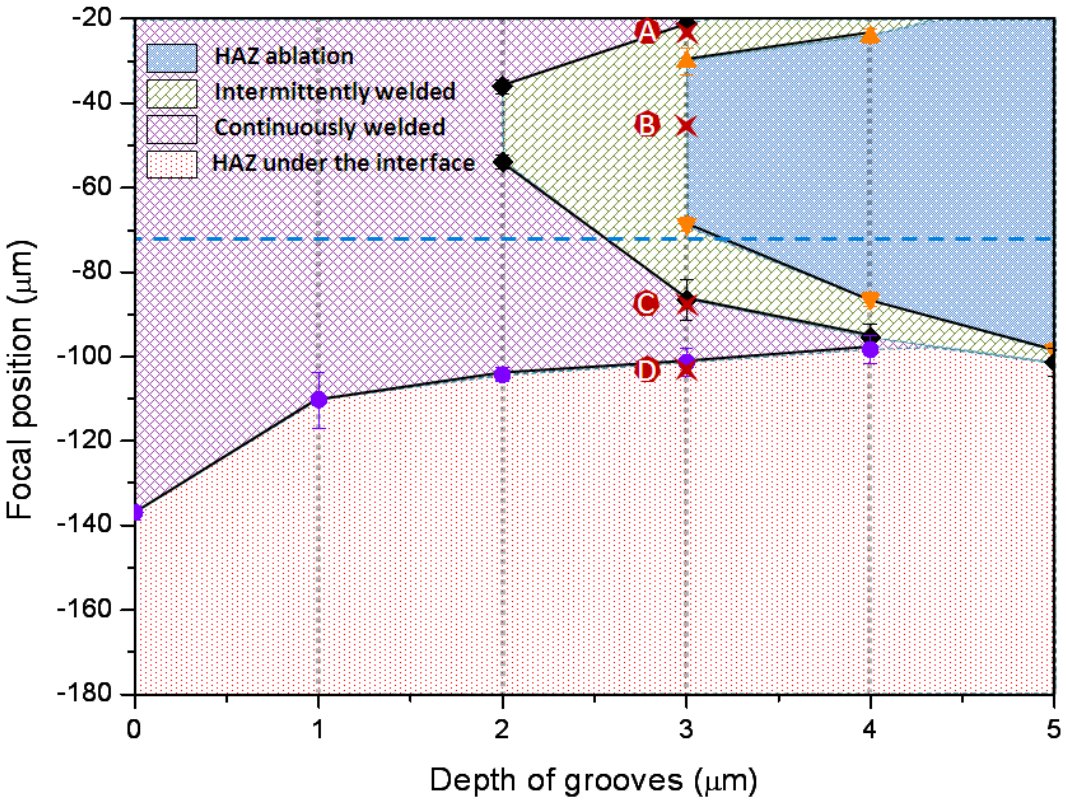

Fig 5.10 Parameter map illustrating classification of weld results with varying gap distance and focal position. Plotted points indicate the position of the change between the different result classifications with a resolution of 1.0 μm in depth and 2.97 μm in focal position. The blue line indicates the focal position used in Fig 5.9. The fifth state appeared when the focal position was too deep and the laser induced modification is below the interface. a, b, c, d in the graph indicate the positions of cross-sections in Fig 5.12.

Fig 5.10 shows a parameter map as a function of groove (gap) depth and focal position with a fixed average power of 7.29 W and speed of 2 mm/s. As the focal position is moved further from the interface a fifth state appears: "HAZ under the interface". This occurs when the HAZ forms far below the interface and the plasma/melt is insufficient to reach the gap area and fill it. There was no observation of the "plasma ablation" state for this experiment.

The graph demonstrates that the ability to weld across a gap changes dramatically with focal depth. From Fig 5.10, the graph could be classified as 3 types of welding mechanisms as the focal position changes: welding from above the interface (-21.2 μm to ~-55 μm), welding from below the interface (~-55 μm to ~-120 μm) and the HAZ fully below the interface (~-120 μm to -172.7 μm). Generally speaking, the different welding mechanisms depend on whether the main laser absorption position is in the

upper sample or in the lower sample (which will be discussed in detail in the discussion below). It should be remembered that Fig 5.9 and Fig 5.10 show two dimensional slices from the three dimensional space of power, focal depth and gap width. From Fig 5.9 it is clear that the "intermittently welded" region and "HAZ ablation" region in Fig 5.10 can, potentially, be changed to "continuously welded" and "intermittently welded" if the average laser power is increased. A combined analysis of Fig 5.9 and Fig 5.10 provides suitable parameters to be used for successful welding.

5.2.3 Results Analysis

Two immediate conclusions can be made from the experiments we have conducted. First, a larger gap can be welded once the weld process has started, as illustrated in Fig 5.7 and as is visible in Fig 5.9d. Secondly, in a non-intuitive and non-trivial manner, the position of the laser focus relative to the gap has a significant influence on the gap that could be bridged.

In section 4.2.2 from Fig 4.15 and Fig 4.16 a theory of plasma evolution and laser energy absorption during the welding process was proposed, to understand the large gap which can be welded once the welding already started. It is known that the HAZ represents the melted glass region [124][151]. Recently it has been shown that even regions outside the melt zone exhibit clear expansion [163]. The ability of this formation to bridge a gap between two surfaces is therefore highly dependent on the size of the HAZ (melt zone) has reached as the formation approaches the gap. This is in turn dependent on the welding parameters and particularly on the focal position.

Fig 5.11 shows the cross-sections of the structures shown in the inset of Fig 5.9 and illustrates the impact of varying incident average power on the evolution of the weld structure. If the laser power is too low then the formation terminates before a HAZ can form (Fig 5.11(1)). This forms plasma modified region which can, depending on the focal position relative to the gap, be entirely subsurface (as shown in Fig 5.11a) or a thin, clean, ablation of the surface.

With increased incident laser power (Fig 5.11(2)) the combination of plasma and melt creates a large amount of ejecta and an ablation line with significant redeposition and surface damage (Fig 5.9b and Fig 5.11b). With a further increase in power there are sufficient ejecta (plasma and melt) to transmit heat across the gap. This transmitted heat

allows the absorption plane to jump the gap without filling it giving rise to ablation from both surfaces (Fig 5.11(3)).

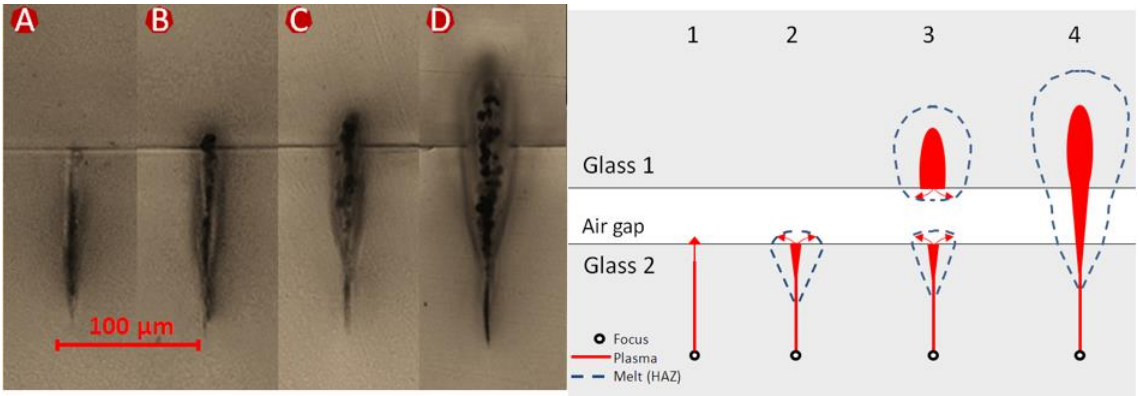

Fig 5.11 Left: cross-sections of different welding patterns of etched grooves experiments label-marked points in Fig 5.9. A to D: power is 4.04 W, 4.49 W, 5.16 W and 7.52 W respectively. Right: illustration of the evolution of the weld structure with varying incident average power. 1). Low power without HAZ; a neat plasma modification line in the bottom glass. 2). Plasma escapes with ejecting melt creating irregular ablation, 3). Plasma generated at both the top and bottom material but neither of them are strong enough to generate a stable bond, 4). Melt bridging the gap providing a bridging corridor for a continuous weld.

If, however, the incident power is sufficiently strong the melt zone will be well enough developed as it approaches the interface to expand and fill the gap ahead of the plasma (Fig 5.11c and Fig 5.11d, also in Fig 5.9); the approaching laser absorption region pushes a bow wave of melt into the gap which initially narrows the gap and eventually fills it forming a bridge which the plasma region can follow. This explains the ability of an already formed weld to bridge a larger gap than an unformed weld in Fig 5.7 and welding protrusion in Fig 5.9d as the melt can be pushed laterally into the gap ahead of the laser translation.

Fig 5.12 illustrates the proposed explanation applied to the 4 types of welding in Fig 5.10 with cross-sections of different typical areas from Fig 5.10 presented in the left of Fig 5.12. If the focal position is close to the interface then the absorption plane will quickly jump the gap and the laser energy is mainly absorbed in the upper glass and an upper HAZ is generated. Here the melt expands downward filling the gap from above and forming a join (Fig 5.12(1)). In this experiment a focal position of between -21.2 µm and -55 µm therefore results in the upper material absorbing the bulk of the laser energy.

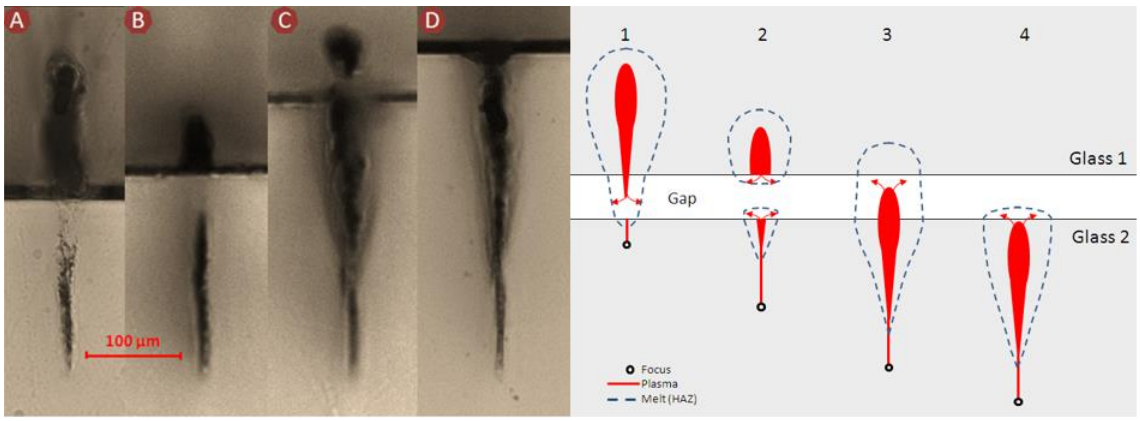

Fig 5.12 Left: cross-sections of different welding patterns of etched grooves experiments label-marked point in Fig 5.10. A to D: focal position is -24.1 µm, -40.0 µm, -86.5 µm and -107.3 µm respectively. Right: diagram illustration of mechanism of left photo.

With a deeper focal position, HAZ is generated from both upper and lower regions. For smaller gaps there is sufficient combined melt from either side to fill the gap and hence the gap still could be welded. For larger gaps the combined melt is insufficient to fill the gap, as seen in Fig 5.12(2), so "intermittently welded" or even "HAZ ablation" regions are formed in Fig 5.10 (typically for a gap $\geq$ 3 µm). As the focal position is further lowered such that the focal region is entirely below the gap, the HAZ forms only in the lower glass. For a small range of focal depths the melt is sufficiently well formed to bridge the gap from only one side forming a true weld. Hence "intermittently welded" and "continuously welded" regions return for deeper focal positions from -55 µm to around -120 µm. With a further deepening in focal position the plasma and melt are too far from the surface to reach the gap, this generates a HAZ either entirely below the interface or with insufficient melt to bridge the gap as the top of the tear drop HAZ formation (> *-120 µm* in Fig 5.10).

This proposed mechanism indicates the importance of choosing appropriate focal position and incident power for bridging gaps. The results are highly significant for ultrashort pulsed laser welding as they significantly relax the requirement for surface preparation and fit-up between parts, which are otherwise prejudicial to the industrial implementation of this otherwise attractive joining process.

5.3 Limitations of Surface Conditions

In section 5.2 we discussed and experimentally investigated the surface separation of glass-glass welding, but for welding of glass-metal there are significantly different

situations to consider: firstly, the metal surfaces are usually not as flat and smooth as commercial glass surfaces, even if highly polished. Hence when the glass and metal are clamped together, there is usually only a small point (area) in optical contact. By applying more force between the two parts a relatively large area can become optically contacted but with a surface deformation and residual stress increasing. As a result for most of the situations involving glass-metal welding the materials are not in optical contact. Secondly, as discussed in section 5.2, different laser parameters are needed to weld different gaps. For relatively rough surfaces, the gap distances over an area are both diverse and random when pressing glass and metal together. Therefore, when the glass-metal interface is welded with a certain average laser power, it is inevitable for some local areas to be over irradiated and some local areas to be under irradiated. Suitable preparation of the metal surface for welding is needed to prevent the welding from cracking due to overheating or failing due to insufficient laser power. Thirdly, during welding of glass-metal, instead of the laser being initially absorbed below the interface, it is absorbed on the metal surface and inside the upper glass, so the plasma from the upper glass filling the gap will dominate the welding mechanism. Because of the high thermal conductivity and high thermal expansion of metal, the glass usually cracks after the welding process. So during glass-metal welding, the weld is judged to be successful if the two samples stick together after weld without apparent cracks.

Based on sample preparation methods and the measured surface roughness, a chart is made shown in Fig 5.13 of what kinds of surfaces can be welded. All those welds were made with borosilicate glass clamped to a metal sample with a particular surface preparation. The laser parameters were chosen to generate suitable HAZ inside the borosilicate glass (based on the HAZ size of previous parameter tests on borosilicate to borosilicate glass welding).

It is clear that a range of metal surfaces can be welded to borosilicate glass through workshop surface preparation methods. However, in contrast to the glass to glass welding prepared earlier where a 3 μm gap can be welded, only a surface roughness of $Ra = 0.3$ μm has been proven weld-able. As discussed above the metal surfaces are usually lacking in terms of flatness and smoothness, even if the surface roughness is only 0.3 μm, a surface separation of over 2 μm is commonly formed as the surface curvature and peaks on the surface will prevent the two surfaces getting close. During the glass-metal welding, increasing the laser average power to weld a large gap is not practical as the huge thermal expansion coefficient compared with glass will introduce

too much residual stress after welding. Also for welds of different materials with apparently different thermal expansion coefficients, crack propagation due to the temperature changes are usually fatal. Furthermore, the elasticity of the metal surface introduces a force to push the two surfaces apart during clamping and after welding, so the welds are usually broken if the weld bond is weak compared with the elastic force of the surface.

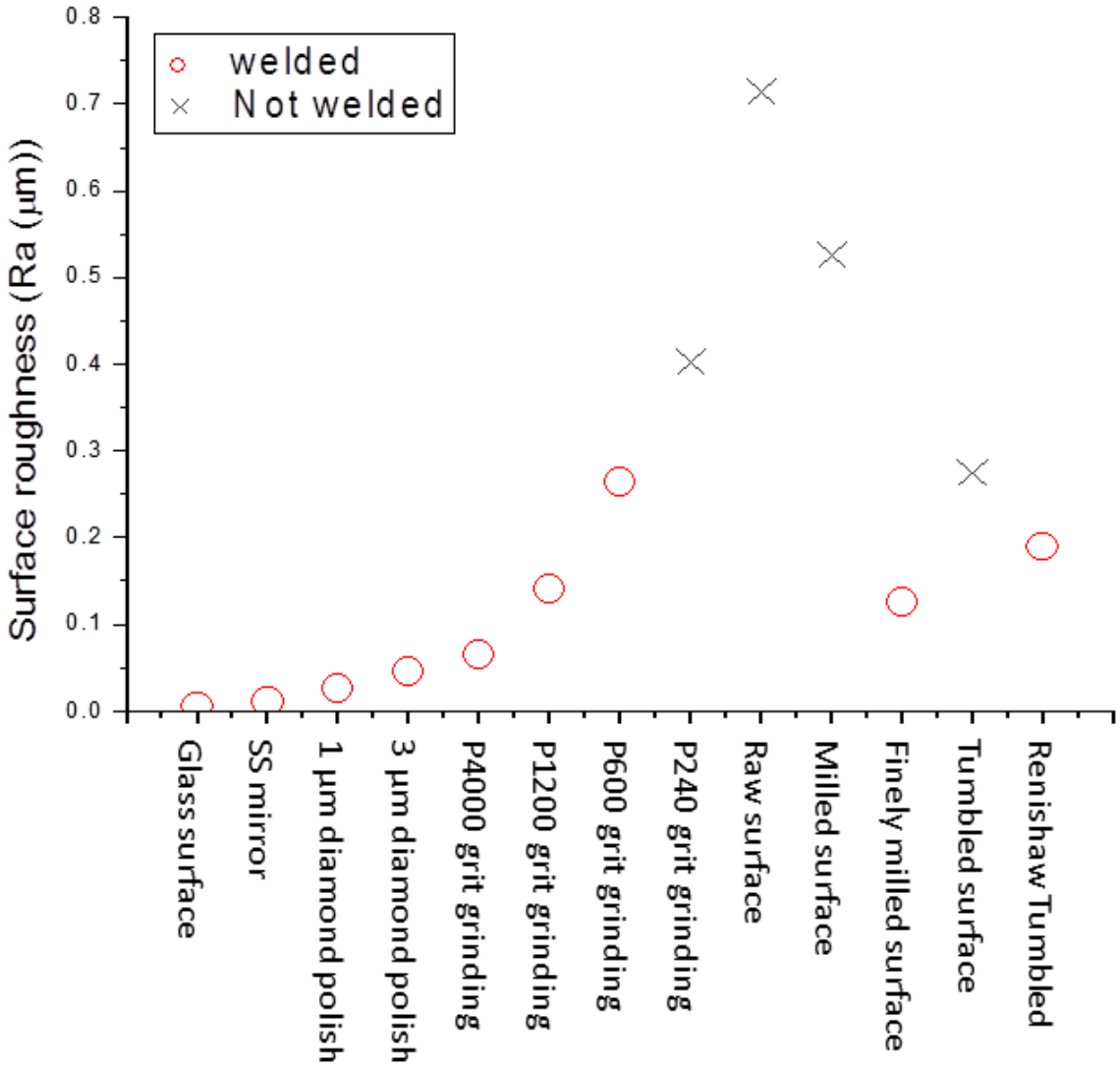

Fig 5.13 Weld-abilities of different surfaces (All surfaces are measured by Alicona and welded with borosilicate glass. The materials of the treated surfaces are aluminium or aluminium alloy except glass and stainless steel mirror (the first two surfaces)).

5.4 Summary and Conclusion

For industrial applications, it is important that the sample preparation method is straight forward and a fit up easy to achieve. Work in this chapter hence focused on the identification of welding parameters that allow tolerances to be relaxed. The work

described in this chapter focused on determining the parameter ranges that generate a successful weld.

The reasons for a weld not being successful were firstly discussed—weak weld strength and large residual stress. Possible reasons for the cracks were discussed and techniques to increase the weld's temperature tolerance and restrain or eliminate cracks in the welding area were investigated. Cracks induced by excessive energy deposition are mainly due to a large amount of void generation, high thermal gradients inside the HAZ, and/or HAZ overlapping between different seam lines. Effective methods to eliminate or reduce this kind of defects or cracks include reducing the laser power, or increasing the seam line separation. While residual stress by different thermal expansion coefficients of the two welded materials can crack the sample after welding or less tolerance to the circumstance temperature change. To eliminate this type of cracks, the weld seams should be narrow and the thermal accumulation needs to be controlled for less temperature increase during the welding process.

Surface separation between the two materials being welded with different welding parameters is equally important for investigation. Two methods of welding of two glass-glass parts with controlled gaps, using either a curved surface (cylindrical lens) or etched grooves, demonstrate the ability of the ultra-short pulsed laser welding process to bridge small gaps. For the cylindrical lens experiment the effect of direction, speed and power were investigated. Power was demonstrated to be critical in determining the weld-able gap while speed, by comparison, appears less critical, at least over the tested range. Most interestingly the experiment demonstrated that the weld-able gap increased, by a factor of two, once the welding process had begun. The etched groove experiment provided a more precise but discretized method to determine the maximum possible weld-able gap. The results for increasing average power agreed well with the cylindrical lens experiment and also demonstrated the key influence of the focal position for larger gap welding. For both experiments roughly 3 μm gaps were successfully welded with borosilicate glass and fused silica. Two parameter maps were made based on the experiment, and specific materials can be successfully welded with the laser power, focus position and surface separation chosen from the maps.

In the third part, ultrafast laser welding glass to metal of different surface preparation methods is demonstrated and we discovered a surface roughness (Ra) of less than 0.3 μm is required for a successful weld.

Chapter 6 Welding Pattern Considerations

Different scan strategies are required during ultrafast laser welding of glass-glass and glass-opaque materials. Welding of the same material is relatively easy, as discussed in section 5.1, so almost all the welding experiments in this thesis use the same simple spiral pattern. But for welding of different materials, the different material thermal properties require special welding pattern designs for successful welding.

Discrete patterns were introduced in this thesis to reduce the stress accumulation at the interface. In this chapter different patterns will be presented for glass-metal welding, and different methods to generate discrete patterns will be proposed and developed.

6.1 Comparison of Different Welding Patterns

6.1.1 Spiral

Initially a spiral pattern was used for welding glass to metal. In this case welds could be obtained, but tended to be cracked or micro-cracked, as seen in Fig 6.1.

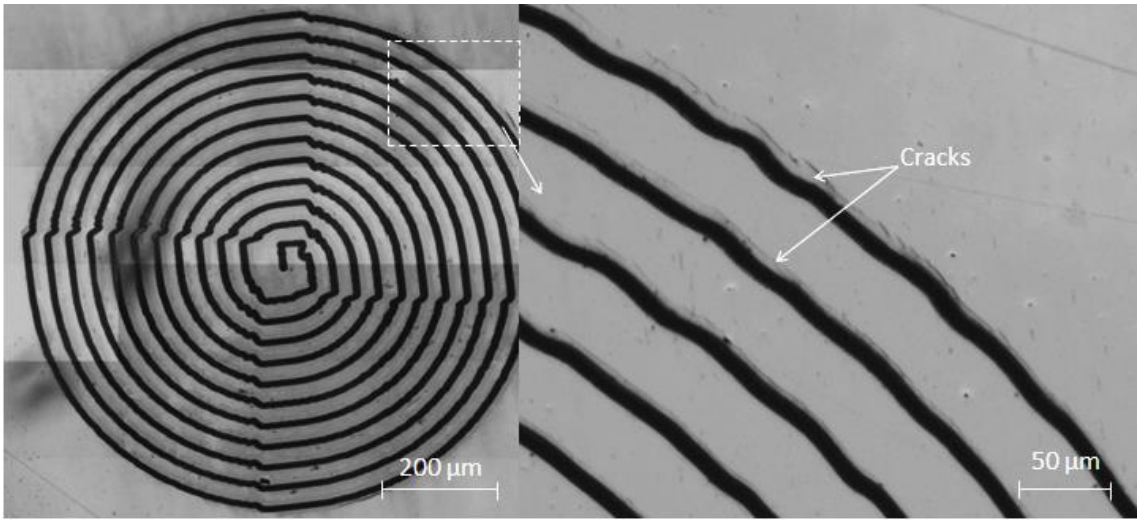

Fig 6.1 Spiral welds of borosilicate glass to stainless steel. (Laser average power 0.9 W and scan speed 1 mm/s), wobbles shown on the graph are due to the stage error.

From the photo, the cracks appear around the edge (outer boundary) of the weld, which represents a stress accumulation as the seams weld outward.

Two methods are usually used to decrease the temperature during the process: decreasing the incident average laser power and increasing the spacing between the seams.

Given that the stress is mainly distributed at the outer boundary of a weld region and it is reduced as the weld seam size decreases, to reduce the likelihood of failure, several methods are considered to solve this problem based on the scan strategy design.

6.1.2 Refined Spiral

One possible route to reduce cracking is to decrease the incident laser power whilst increasing the spiral line separation, which creates lower thermal deposition at the weld region and cracks due to thermal expansion can be effectively reduced, but lowering the laser power results in weaker bonding (Fig 6.2a).

An alternative technique is to create welds with two or more laser powers. As the weld seams expand out, the surface shear stress increases at the boundary of the weld region, and the residual shear stress builds up as the material cools down. As cracks start from the outer boundary of the weld, dual power welding is introduced to keep outer boundary less defects and maintain the bond in the middle strong. Following a higher welding power for the inner spiral if we reduce the laser power for several revolutions at outer boundary (not necessarily commit welding). This will effectively release the stress at the edge of the higher power welding (Fig 6.2b), however, the strength of the weld remains high due to the higher incident power used in the centre.

6.1.3 Inward Spiral

To make it easier to start from an area of optical contact in the clamp rig (see section 3.2.4), an outward spiral pattern from the centre is usually used. Thermal accumulation and thermal expansion is worse as a spiral expands outward (as heat is not easily diffused), and the residual stress grows larger around the edge as it cools down. Hence a third method is to spiral from the outside to the centre. The outer boundary is bonded before significant thermal difference occurs, and provided that the outer seams do not crack during the welding process, the whole weld will be a good one, as the outer welds will have a smaller thermal expansion mismatch, and hence minimum residual internal stress (Fig 6.2c).

6.1.4 Distributed Welding

A line or net pattern can be used to relive the thermal accumulation by distributing laser energy over a relatively large area and also providing time for the energy to diffuse, as seen in Fig 6.2d. The use of long weld lines means that the majority of the heat is

dissipated by the time an adjacent line is welded. Additional cooling time can be provided by using an interlaced welding approach.

6.1.5 Discrete Welding

Instead of welding a large integrated area, which causes the inner stress accumulate at the outer boundary, discrete welding strategies were developed to release the thermal expansion created residual stress and also to stop crack propagation. Arrays of small circles and dots were therefore been welded (Fig 6.2e and Fig 6.2f). Detailed preparation and welding of this part is provided in 6.2.

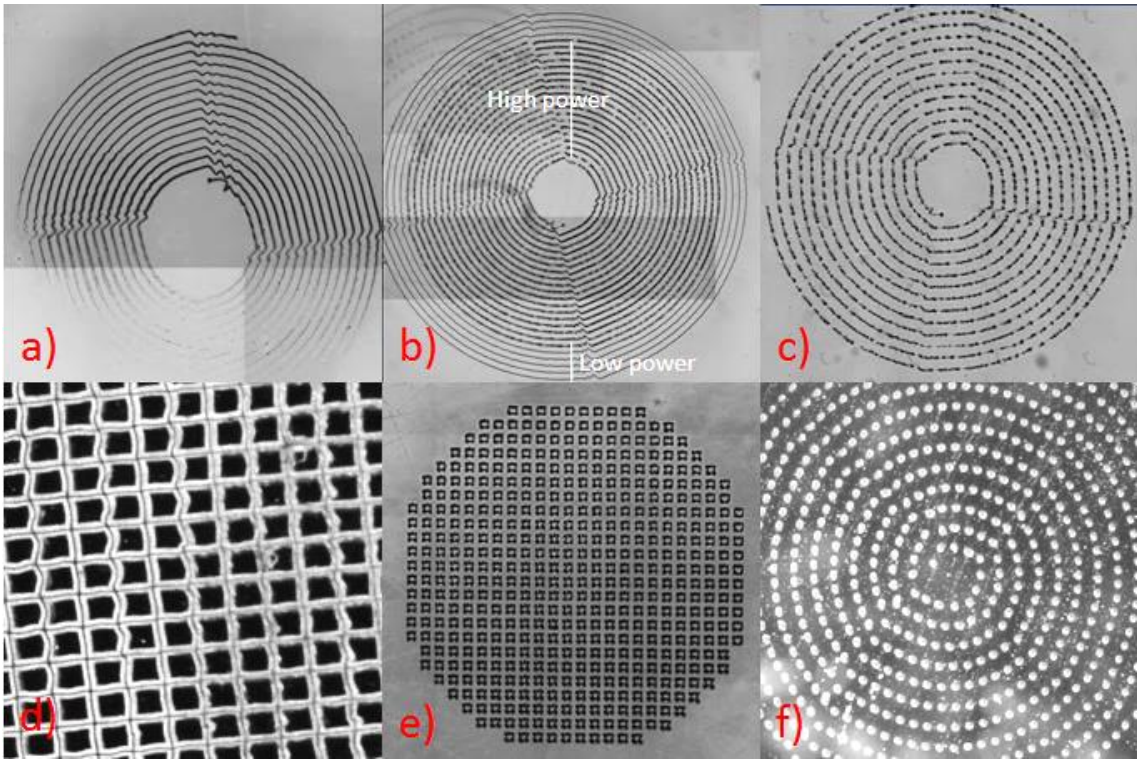

Fig 6.2 Different welding methods dealing with cracks. (a). Lower power, (b). Dual power welding, (c). Inward spiral, (d). Alternative weld geometry pattern, (e), (f). Discrete welding.

6.2 Discrete Patterns

A discrete scan strategy can successfully weld glass to metal without cracking. Two methods can be used to generate such discrete patterns with the motorised stages, the first method is to use the shutter inserted in the beam path (section 3.1.1), where either a dot or a circle (or square) can be generated for each shutter on-off, as seen in Fig 6.2e and Fig 6.2f. The other method is to control the ultrafast pulsed laser source to output

modulated pulses (pulse train). An enveloped pulse train during welding will generate discontinuous welds in a periodic pattern.

6.2.1 On-Off Shutter for Discrete Patterns

In order to generate discrete patterns using the on-off shutter method, different weld shapes and spaces between individual welds were chosen to generate an overall seam area as large as possible in a specific weld region to ensure the weld strength over the weld region remains strong, whilst avoiding weld or HAZ overlap between adjacent welds. Also, in order to reduce the temperature accumulated in a local area, the scanning time sequences of different unit welds (individual welds, such as dash lines or small circles) can also be adjusted. Typical discrete welding patterns are shown in Fig 6.3:

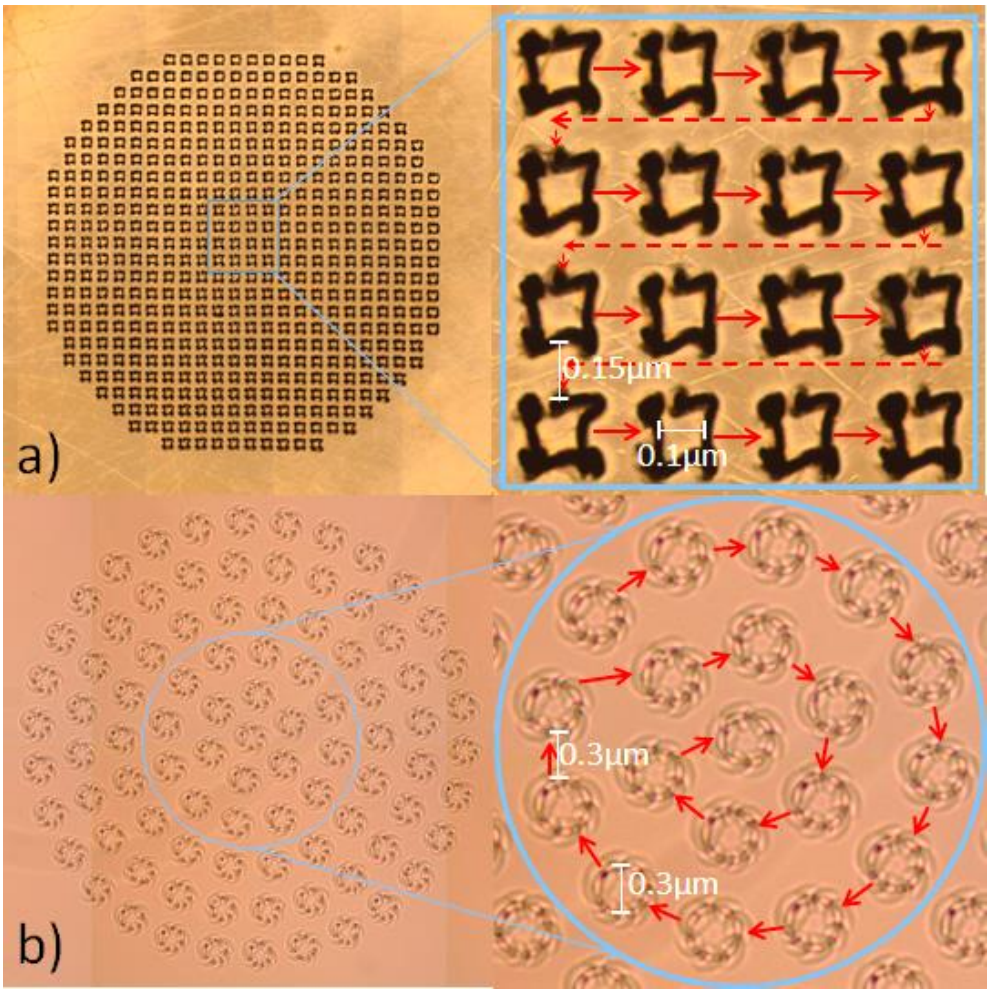

Fig 6.3 Geometrical information and scan sequence of discrete patterns. (a). Borosilicate glass to stainless steel, 1 W average power and 1 mm/s scan speed; (b). Borosilicate glass to borosilicate glass, 1.6 W average power and 1 mm/s scan speed.

Ideally a well-spaced distributed inscription of the individual welds would be better for handling thermal accumulation (section 6.1.4), but this requires a more time consuming process, and more importantly, the previous welds will results in the surrounding surface separation closing, so a successive individual welds is used during the welding process. Compared with Fig 6.1, no obvious micro-cracks appear for the glass-metal welding in the entire welding region. In Fig 6.3, welds with successive scanning are shown in the right of the image, which is an enlargement from the left photo. This demonstrates the scan strategies and the scale for the welds. The narrower HAZ width for borosilicate glass to stainless steel welding enables both a smaller weld pattern and smaller spacing between the welds compared to the borosilicate to borosilicate welding.

6.2.2 Welding with Modulated Pulses

With the shutter method, the stage movement and shutter on-off are well synchronized as both can be controlled through the same software, but is limited by the reaction of the shutter speed. A method of controlling the laser source to output modulated pulses is introduced into generating discrete patterns.

6.2.2.1 Pulse Train Envelop Introduction

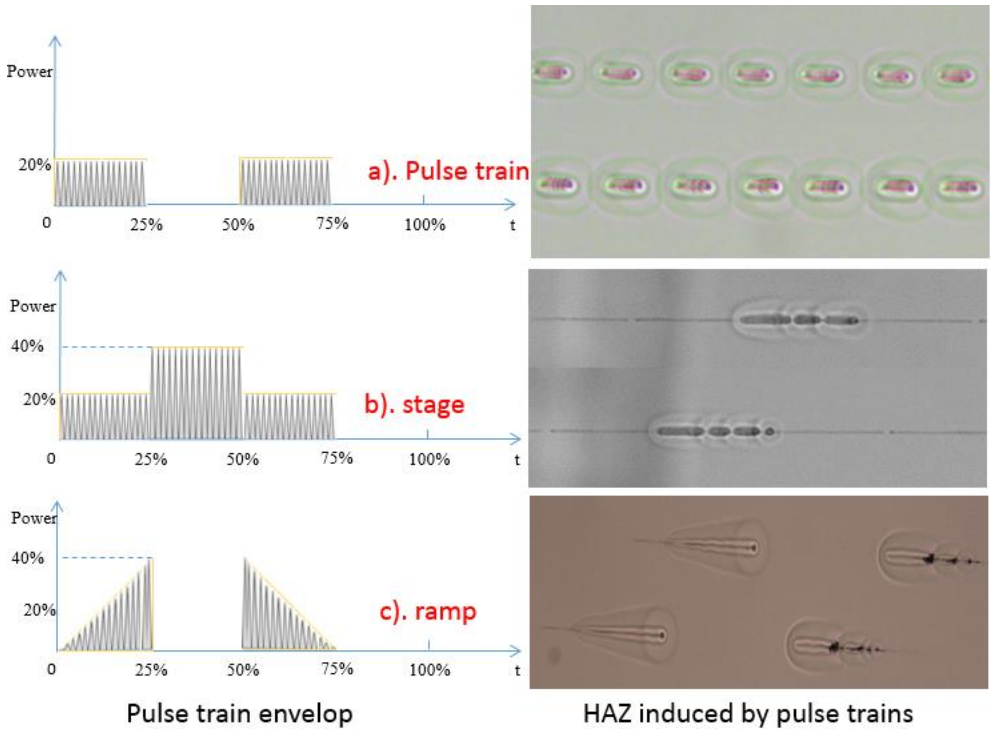

Fig 6.4 Different laser output modulated pulse trains and inscribed HAZ inside borosilicate glass. (a). Pulse train, (b). Stage pulse train, (c). Ramp pulse train. The percentage on the y axis is the percentage of the whole laser output power. (Note that the laser pulses take 3 ms to reach the full power for our laser system).

Normally a repetition rate of 400 kHz continuous pulses is fired out when the picosecond laser works. Also the pulse series can be modulated with deferent envelop through our picosecond laser system. A number of pulses (pulse train) are outputted with a certain pulse train repetition rate and the welds can be discretely generated. Different pulse train envelopes were designed and the HAZ are shown in Fig 6.4. The disadvantage of this method with the available laser is the pulse trains and the stages are separate systems and they cannot work collaboratively. A discrete circle (or square) pattern is impossible in this method instead a dash line pattern with a controlled length can be inscribed with different shear stress releasing patterns.

6.2.2.2 Ramp Pulse Train Plasma Behaviour Investigation

The effect of pulse train on the appearance of weld structures inside bulk borosilicate glass was investigated, in which a 50% duty cycle ramp pulse train was used for a plasma behaviour test, as shown in Fig 6.4c. In a whole period of the pulse train, the laser power increases during the first quarter of the duty cycle and then the laser power is set to zero, and then the third quarter the laser power from a high level gradually decreases to zero, and the power is kept at zero for another quarter of the time period.

In this experiment ramp pulse trains were irradiated inside borosilicate glass with various maximum pulse energies. The HAZ length as the pulse energy rises and falls will reflect the plasma absorption behaviour and the material breakdown threshold.

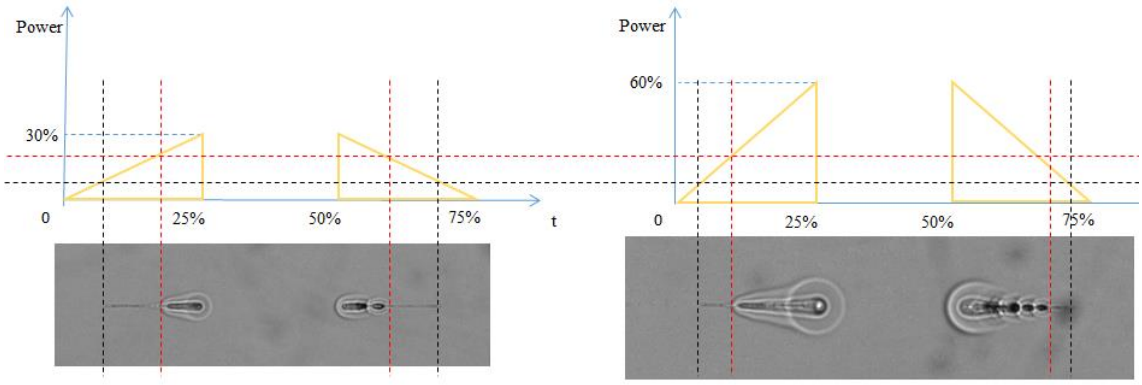

Fig 6.5 Breakdown threshold and plasma absorption threshold of borosilicate glass illustrated by ramp pulse trains of different maximum powers. (Ramp pulse train period=1.6 s, scan speed=1 mm/s and laser power 60%=2.45 W).

Fig 6.5 shows the typical HAZ inscribed by a ramp pulse train with two different laser powers (a. maximum pulse energy 3.1 μJ, b. maximum pulse energy 6.2 μJ). From the

figure, the energy threshold for a permanent refractive index change (nonlinear absorption threshold) is the same whether the pulse energy is increasing or decreasing, which can be calculated to be 0.483±0.005 W (1.207±0.013 μJ per pulse). However the plasma absorption thresholds are different, as seen in Table 6.1. Plasma may be sustained at lower pulse energy as the energy is reduced in comparison to the case where the pulse energy is increased. A possible explanation for this difference is that when plasma is generated by previous pulses, even if it cannot survive between pulses, there still exist free electrons which help plasma formation either by photon or electron assisted absorption. This finding also can explain the larger gap welded in Fig 5.7 and the protrusion presented in Fig 5.9.

Also interestingly the dash HAZ line pattern (Fig 6.5) observed previously (Fig 4.8) appears in the ramp pulse energy decreasing tests but none of them is observed when the pulse energy increases. This phenomenon reflects an unstable plasma state as the pulse energy decreases.

Table 6.1. Table of ramp pulse trains test of pulse energy when breakdown and plasma behaviour (HAZ) start or stop (maximum pulse energy 3.1 μJ and 6.2 μJ).

Ramp pulse trains	**3.1 μJ (maximum pulse energy)**		**6.2 μJ (maximum pulse energy)**	
	Breakdown[μJ]	**HAZ[μJ]**	**Breakdown[μJ]**	**HAZ[μJ]**
Pulse energy rising	1.2±0.04	2.91±0.04	1.21±0.08	2.82±0.02
Pulse energy falling	1.2±0.01	2.74±0.01	1.21±0.1	2.68±0.08

**The absolute number of HAZ threshold reflects the influence of two different maximum pulse energies on HAZ size, not for plasma threshold.*

Fig 6.5 and Table 6.1 are only two different maximum powers. Experiment results of HAZ size start and stop with different laser powers are shown in Fig 6.6, with the HAZ start linear fit equation: $y = 3.728 - 0.192 \times x$, and HAZ stop linear fit equation: $y = 3.471 - 0.165 \times x$.

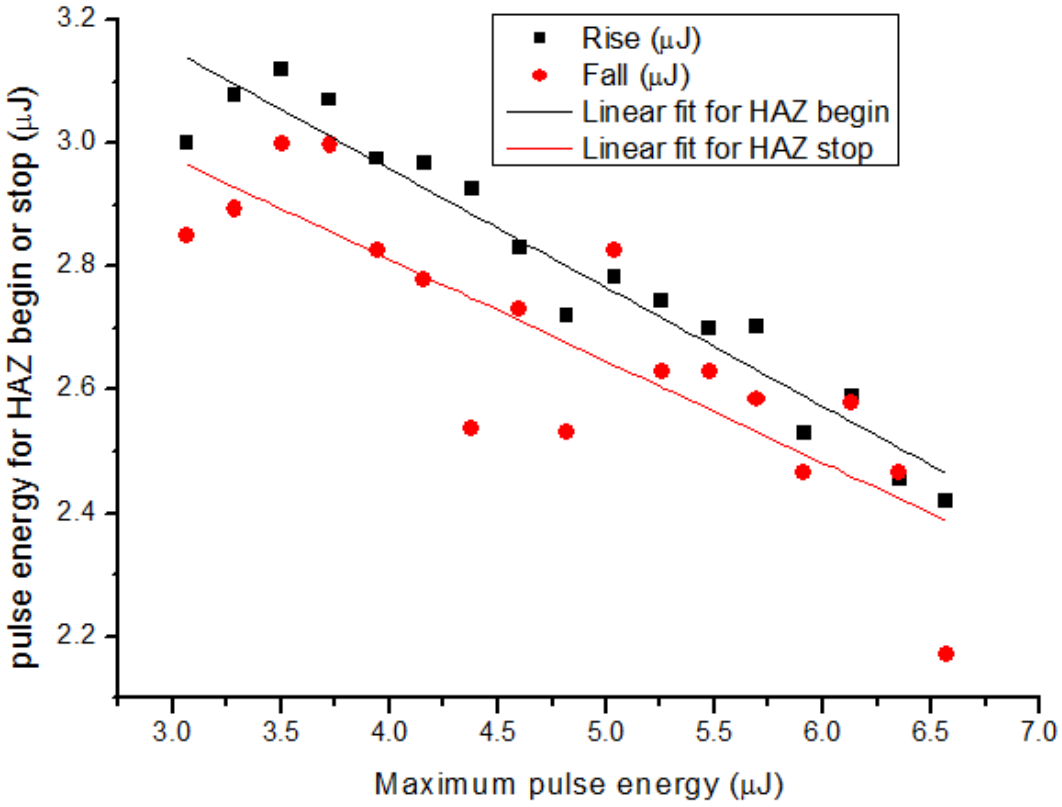

Fig 6.6 Ramp pulse trains measuring the "HAZ beginning pulse energy" when the ramp pulse energy goes up and "HAZ stopping pulse energy" when the ramp pulse energy goes down for different maximum ramp pulse energies (it is not necessarily linear, the linear fit shows the general trend and the clear difference in HAZ, or plasma, absorption in the two cases).

6.2.2.3 Pulse Train Parameters Investigation

Pulse trains (Fig 6.4a) were used to investigate burst pulses interacting with materials. Lines were drawn inside borosilicate glass with the same scan speed 1 mm/s and with pulse trains of the same energy line density (same energy deposited for unit length of each line, shown in Table 6.2) by adjusting the pulse train frequency, pulse train duration and pulse energy. HAZ created by pulse trains of 5 ms duration (with different pulse energies and pulse train repetition rates for the same line energy density) are shown in Fig 6.8.

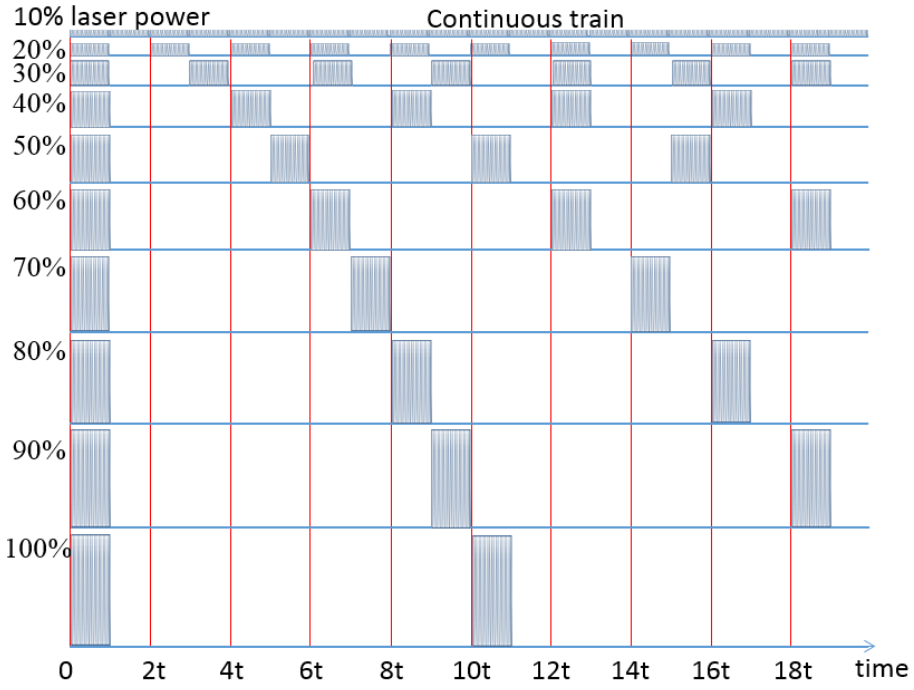

Fig 6.7 Illustration of pulse train parameters experiment with the same line energy density (synchronously adjusts the pulse energy and pulse train repetition rate).

Table 6.2. Pulse train parameters (duration (t), pulse energy (E) and pulse train frequency (f)) for the same laser output power (line energy density for experiment, $t \times f \times E$ = constant) on borosilicate glass HAZ test.

Pulse energy	**0.5 ms pulse train**	**1ms pulse train**	**2ms pulse train**	**3ms pulse train**	**4ms pulse train**	**5ms pulse train**
	Pulse train frequency [Hz]	**Pulse train frequency [Hz]**	**Pulse train frequency [Hz]**	**Pulse train frequency [Hz]**	**Pulse train frequency [Hz]**	**Pulse train frequency [Hz]**
2.7 µJ	Continuous	Continuous	Continuous	Continuous	Continuous	Continuous
5.5 µJ	1000	500	250	167	125	100
8.2 µJ	667	333	167	111	83	67
11 µJ	500	250	125	83	63	50
13.7 µJ	400	200	100	67	50	40
16.5 µJ	333	167	83	56	42	33
19.2 µJ	286	143	72	48	36	29
22 µJ	250	125	63	42	31	25
24.7 µJ	222	111	56	37	28	22
27.5 µJ	200	100	50	33	25	20

Even though the energies deposited per line are the same the HAZ widths are clearly different. Further examples are plotted in Fig 6.9 for different pulse train durations. A rough linear relation could be obtained for HAZ volume and pulse energy.

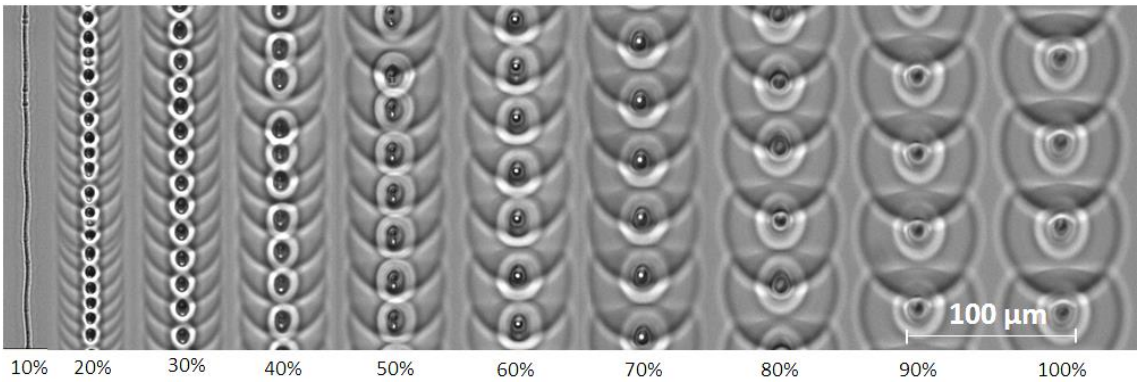

Fig 6.8 Pulse train test of drawing line inside borosilicate glass by the same line energy density (pulse energy of 10% power (0.88 W) is 2.2 µJ). Pulse train duration 5 ms and pulse train repetition rate from 100 Hz for 20% power to 20 Hz for 100% power as seen in Table 6.2 with the same scan speed of 1 mm/s.

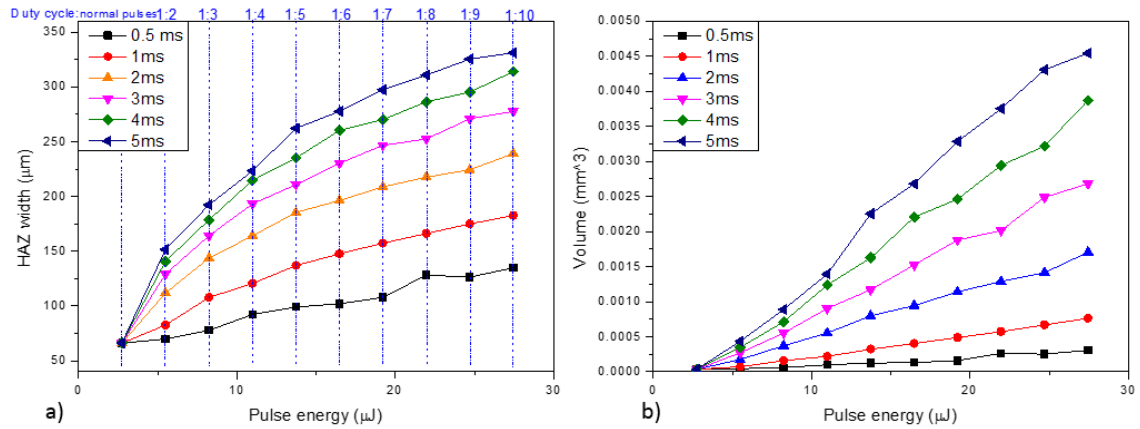

Fig 6.9 (a). HAZ line width of different pulse train pulse energy and repetition rate with different pulse train duration (0.5 ms, 1 ms, 2 ms, 3 ms, 4 ms and 5 ms) for the same energy density, (b). Cube of the HAZ which shows a roughly linear relation with pulse energy.

The huge differences in HAZ size for the same incident energy as a result of different parameters reflects, the influence of several factors:

1. Geometry of HAZ line. As can be seen in Fig 6.8 in the case of low pulse train repetition rate, the weld line is more like a cluster of round balls, this results in errors as we measured the HAZ width or calculate the HAZ volume (we just

cubic the line width in this thesis, which represents the volume), but the influence is limited based on our evaluation (error <20% for 100% power from Fig 6.8);

2. Thermal accumulation. The experiment in this part is similar to the pulse test in section 4.1. For the same line energy density, from Fig 6.9, longer pulse trains give rise to a larger HAZ, and deposits more energy at the region (instead of the energy being homogeneously deposited along the line for normal pulses, pulse trains spatially increase the energy deposition). Further, high pulse energy has a greater effect than repetition rate for the same pulse train duration (a higher pulse energy condenses the energy temporally for a constant flux);

3. Energy absorption. For the same pulse train repetition rate, generally higher pulse energy obtains larger HAZ and this cannot be explained solely by thermal accumulation as shown by the huge HAZ difference between normal pulses (non-enveloped pulses, 400 kHz) and the 5.7 μJ pulse train illustrated in Fig 6.9.

6.2.2.4 Pulse Train Absorption Investigation

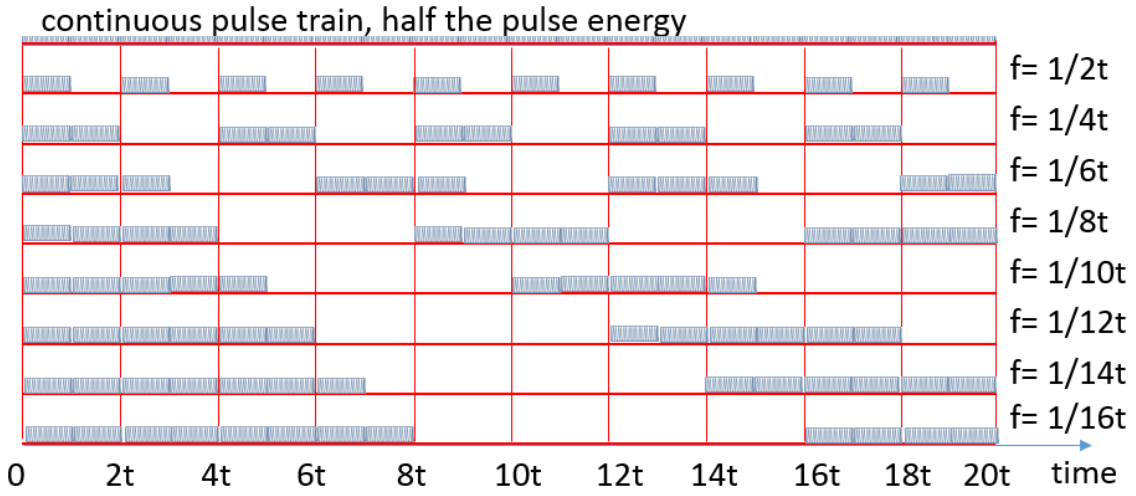

Fig 6.10 Diagram of pulse train duration experiment (keeping the pulse energy, pulse energy duty cycle, and energy density all constant).

In this part another situation is considered: how previous pulses influence energy absorption. From section 5.2 we know energy provided by previous pulses can allow for welding of a larger gap, and from section 6.2.2.2 it helps the plasma survive when the laser power reduces. In this part pulse trains (Fig 6.4a) of different duration (different number of pulses) are used to draw lines inside borosilicate glass, keeping the line

energy density constant by increasing the pulse train duration (t) and reducing pulse train repetition rate (f) (while maintaining a pulse train duty cycle of 50%), as seen in Fig 6.10.

The experiment results are shown in Fig 6.11, two sets of different pulse energies (pulse train energy 5.5 μJ and 6.7 μJ with 50% duty cycle) were measured for comparison. The unmodulated pulses of 2.8 μJ and 3.4 μJ were also tested and the resultant HAZ plotted on the same graph using dashed lines in Fig 6.11. From the figure, when the pulse train duration is shorter than 0.7 ms (280 pulses for our laser system), smaller HAZ is obtained; even if the pulse energy is doubled compared to the unmodulated train. As the pulse train duration increases, the HAZ size increases and finally approaches a maximum value (this is expected to be the HAZ width for unmodulated pulses of the same pulse energy, i.e. the HAZ turns to a line as the pulse train duration becomes longer).

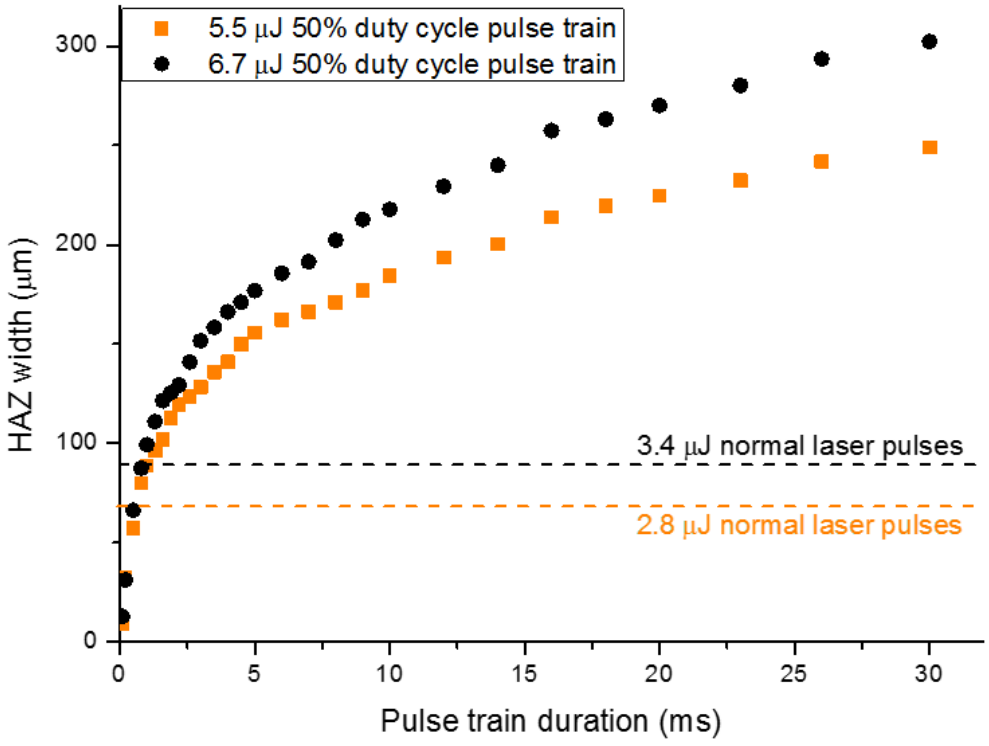

Fig 6.11 HAZ induced by different pulse duration of the same line energy density (with same pulse energy and pulse train duty cycles, with scan speed=1 mm/s).

In Fig 6.11 the HAZ size represents the laser absorption ─ nonlinear and plasma absorption. Consider a series of pulse trains with different durations: the first few pulses in the trains are absorbed through nonlinear absorption as both the localised temperature and the excited free electrons density are low. As further pulses are incident, additional

free electrons are created and the localised temperature increases, giving rise to a stronger plasma absorption which generates more laser energy deposition increases the HAZ size (Fig 6.11). Also from the two different pulse energies, a higher pulse energy helps absorption to increase rapidly with the pulse train duration. This can be modelled using the following equation:

$$E_{Abs} = E_0\beta + E_0(1-\beta)(1-e^{-\alpha t}) \qquad \text{Eq 6.1}$$

here E_{Abs} is the absorbed laser energy, E_0 is the total energy focused inside the material, β is the nonlinearly absorbed energy and $1-e^{-\alpha t}$ is the plasma absorption with α a coefficient for the plasma absorption ability which bases on the localised material conditions (temperature and free electrons density). The relation between volume of HAZ and the number of pulses in the pulse trains is shown in Fig 6.12, fit curves are also presented based on Eq 6.1. From this model maximum HAZ widths for 5.5 µJ pulses and 6.7 µJ pulses could be obtained as 159.3 µm and 260.5 µm respectively, and the nonlinear absorption (also potentially other absorption mechanisms) are 0.15% and 0.27% of the laser power incident into the material.

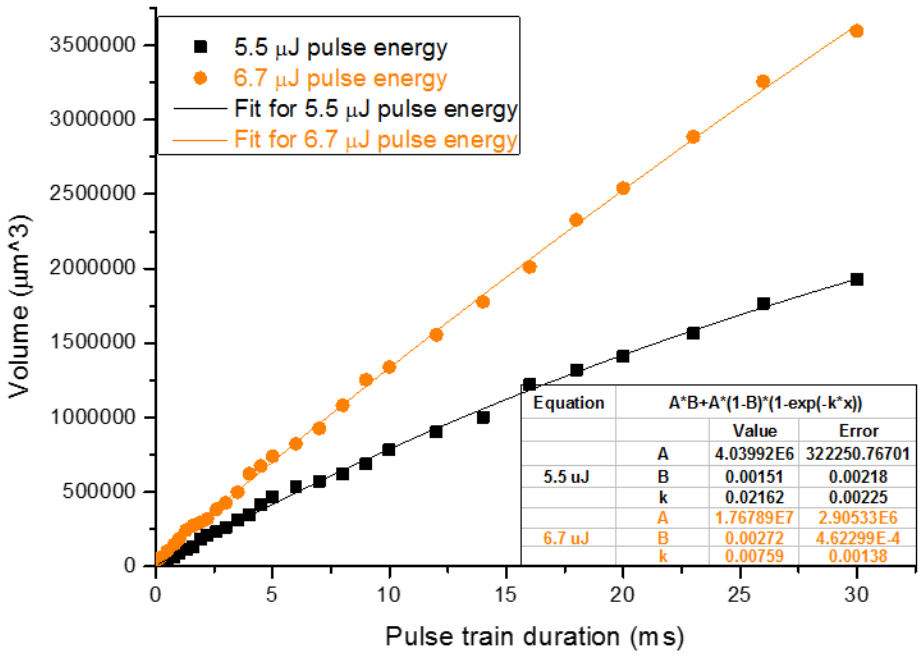

Fig 6.12 Relation of HAZ volume and number of pulses with model fitted curves.

6.2.2.5 Pulse Train Welding

Based on the pulse train parameter investigations from previous sections, a pulse train spiral was welded for glass to metal, as seen in Fig 6.13.

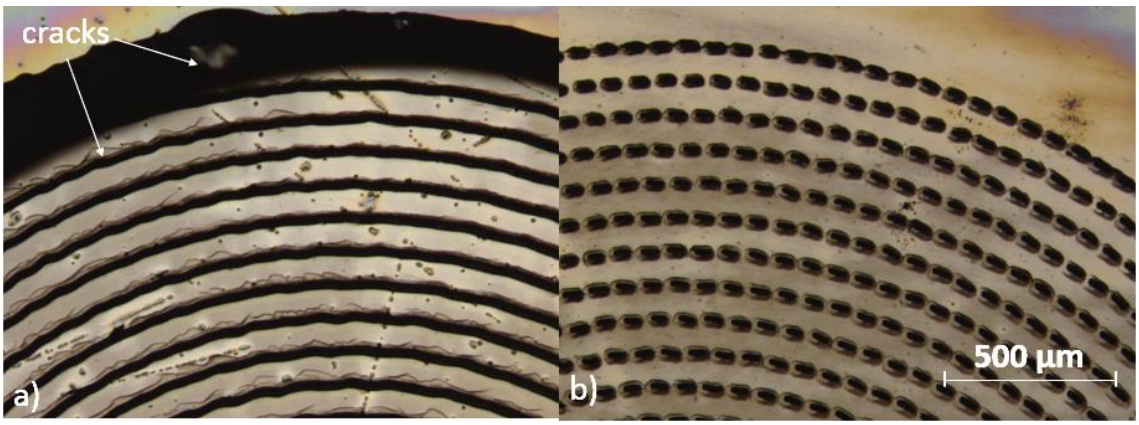

Fig 6.13 (a). Modulated pulse train welding of fused silica with stainless steel (pulse energy: 4.4 µJ, scan speed: 2 mm/s), and (b). 50% duty cycle pulse train welding (pulse energy: 8.8 µJ, pulse train duration: 20 ms, pulse train repetition rate: 25 Hz and scan speed: 2 mm/s).

Both unmodulated pulses and a 50% duty cycle pulse train with the same line energy density were used for welding fused silica to stainless steel. Massive cracks were seen on the outer boundary weld for the unmodulated pulse; however with the 50% duty cycle modulated pulse train, only microcracks were observed around each welding dot.

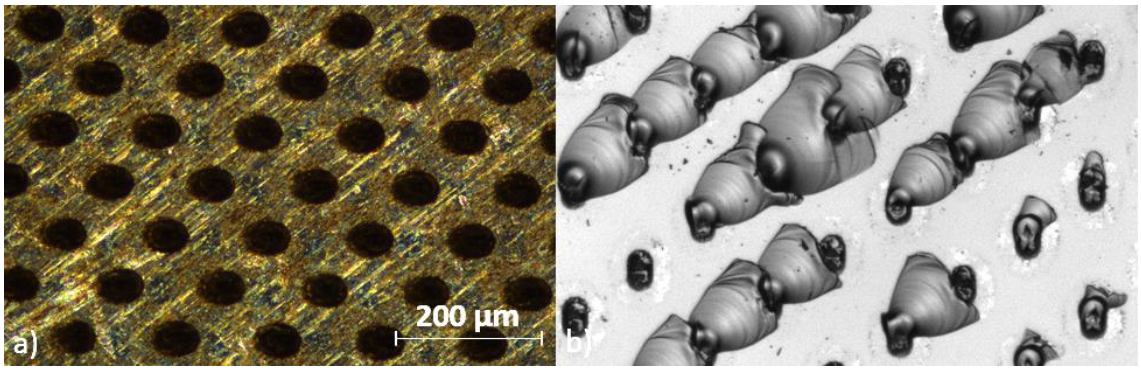

Fig 6.14 Pulse train welding of borosilicate glass with aluminium (a) and peel off image (b). (Pulse energy: 7.5 µJ, pulse duration: 10 ms, pulse train repetition rate: 10 Hz and scan speed: 2 mm/s, with 20 mm focus lens).

Due to the inconsistent metal surface preparation method, no strength test was carried out but a better welding result can be expected (due to fewer cracks). A peeling after welding had been done for pulse train welds of borosilicate glass to aluminium. Glass remains on the surface suggest a true welding on those surfaces in at least some areas (shown in Fig 6.14).

6.3 Welding with Galvo-Scanner

Instead of keeping the focused beam stationary and moving the samples, a scanning beam can be used and provides an alternative welding process. In this section the investigation of a galvo-scanner used to provide a fast scanning beam was carried out which focused the beam on the materials interface with an F-theta. The galvo provides a much more flexible way of creating weld patterns and faster scan speeds. However the focal spot size is large because the short focal length F-theta lenses simply do not exist. As a potential method of ultrafast laser welding for industrial application, this galvo-scanner welding was also investigated in this thesis.

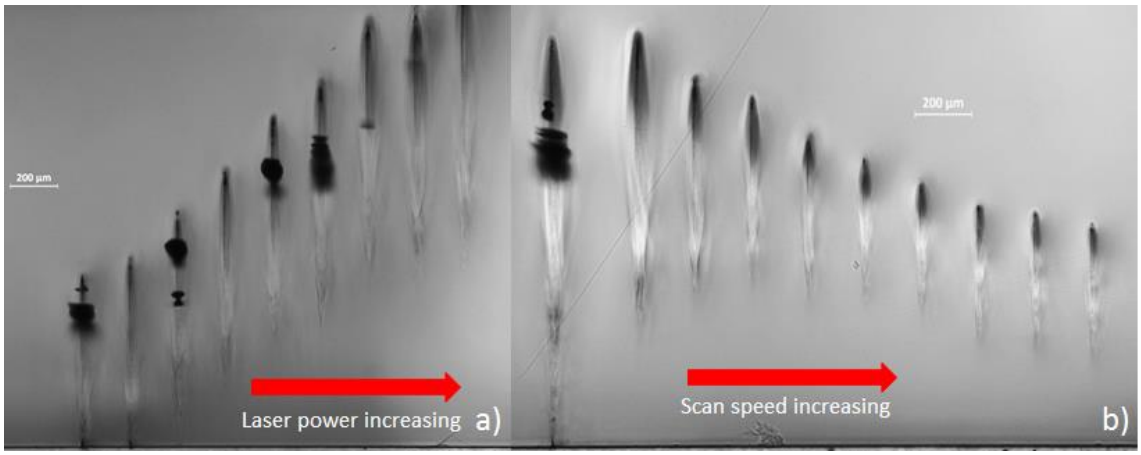

Fig 6.15 Cross-section of galvo-scanner parameters test inside borosilicate glass (line test direction perpendicular to the photo surfaces). (a). Different laser average powers (from 5.94 W to 8.82 W steps of 0.36 W, with scan speed 10 mm/s), and (b). Different speed ((from 5 mm/s to 50 mm/s steps of 5 mm/s, with laser power 6.3 W).

A Hurryscan II galvo scanner was used for the test, with a 163 mm focal length F-theta lens and a 515 nm wavelength (shorter wavelength provides a smaller focal spot size) from the laser which gives a focal spot size of 11.8 µm (diameter). Parameters were investigated by drawing lines inside borosilicate glass, as can be seen in Fig 6.15. Due to the large focal spot size, a higher laser power is required to create absorption inside borosilicate glass (6~9 W). This large spot size and pulse energy also means that a larger HAZ is created, and hence cracks may appear after cross-sectioning. Meanwhile, from Fig 6.15 a laser power related focal position change is observed, with the focus moving towards the lens for increasing laser power; and away from the lens for increasing scan speed.

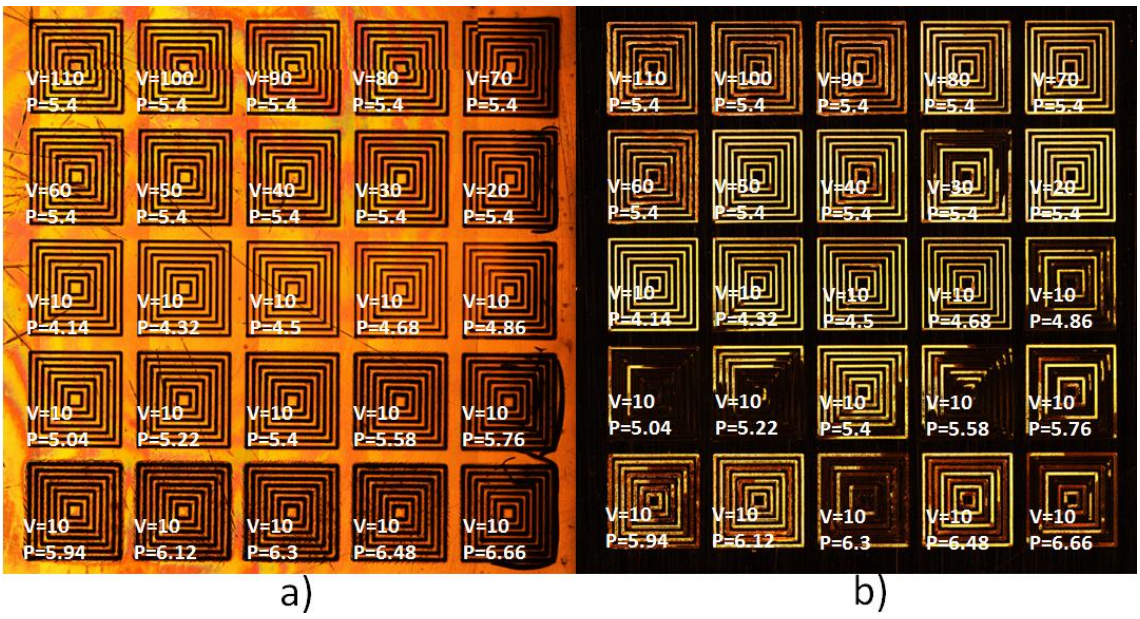

Fig 6.16 Bright field (a) and dark field (b) from microscope illustration of parameter test of welding fused silica to stainless steel with galvo-scanner. Scan speed (v, unit: mm/s) and laser power (p, unit: W) are labelled on the photos.

Fig 6.15 indicated that increasing the scan speed results in a reduction in the deposited energy density, resulting in a smaller HAZ with less chance of cracking. Also, from the figure the focal position changes for different laser average powers and scan speeds making it difficult to determine the optimum focus position for a particular weld geometry. The welding appearances for a range of parameters are presented in Fig 6.16, (a) the reflective image and (b) the dark field image after the weld being peeled off. The bright lines of the dark field image are the glass remnant on the stainless steel, which indicates whether or not the area was truly welded. From the pictures, speeds of up to 110 mm/s can be used but the bonds are weaker due to a reduced energy deposition compared with those at lower speed. As laser power increases, the weld changes from weak welding to a good weld but with subsequent increases the weld becomes unstable.

As Fig 6.15 shows, the focus of the beam keeps changing for different parameters, which makes welding with a galvo-scanner problematic. The impact of focal position on galvo-scanner welding was investigated and is shown in Fig 6.17. This strongly affects the welds, hence it is important to optimise focal position, for the particular combination of laser power and scan speed being used. Successful welding examples are shown in Fig 6.18.

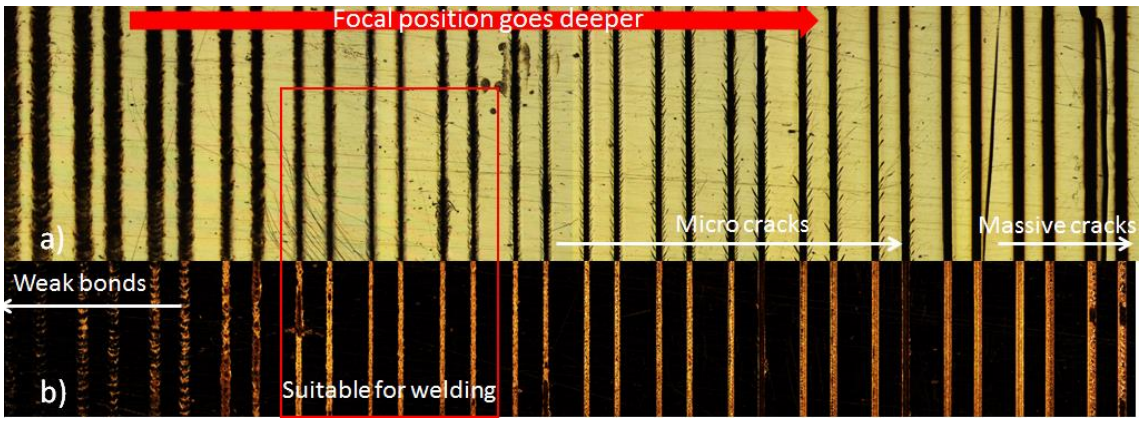

Fig 6.17 Welding test of different focal position for borosilicate glass to stainless steel. Focal position from -1.2 mm to -3.2 mm steps 0.1 mm below the glass-metal interface. (Laser power is 6.8 W and scan speed is 15 mm/s. (a). Reflective view, (b). Dark field view from the microscope).

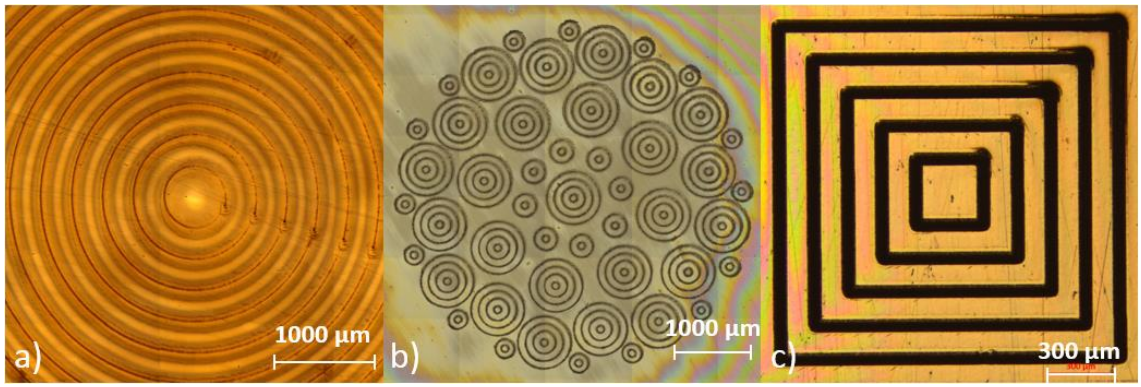

Fig 6.18 Successfully welded samples of borosilicate glass with stainless steel. (a). Concentric circles pattern with laser power 7.1 W, scan speed 10 mm/s and focal position -1.7 mm, (b). Discrete circles pattern with laser power 6.66 W, scan speed 15 mm/s and focal position -2.0 mm and (c). Square pattern with laser power 4.1 W, scan speed 10 mm/s and focal position -2.3 mm).

Over all, ultrafast laser welding with a galvo-scanner provides a higher scan speed, but due to the large focal length lens and the resulting high pulse energy, the weld suffers from weaker bond strength and easily cracks.

6.4 Vibrating Welding

When welding two materials of different thermal expansion, in additional to the residual stress due to different thermal expansion coefficients, the melting, resolidification and local density change introduces another type of residual stress, that is proportional to the thermal gradient during the welding process [128][129][165]. The idea of this section is

therefore to investigate an approach to spread the HAZ/plasma region and hence reduce the thermal gradient by vibrating the focused beam. Two methods were used to generate a fast focus movement. Firstly, a TAG lens [166][167] was used to generate a rapid focal shift in z, whilst secondly a vibrating motor was used to generate a vibrating in the x-y plane.

6.4.1 TAG Lens

For better understanding of the process, Fig 6.19 shows the TAG lens experimental arrangement and the intensity profile after the optics. The Tunable Acoustic Gradient index of refraction lens (or TAG lens) is an adaptive optics device filled with a fluid and driven by an acoustic wave. The very fast refractive index change induced results in a lens with tunable focal length at kHz rates.

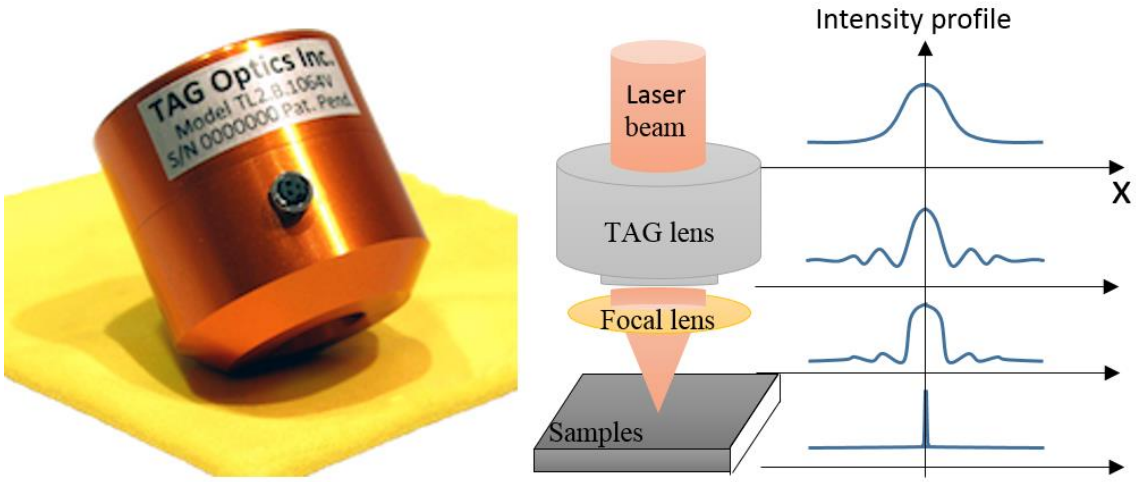

Fig 6.19 TAG lens and the experimental arrangement. Diagram of beam intensity profiles passing through different optics are also illustrated.

In our experiment, the TAG operated at resonant frequencies of 140 kHz and 190 kHz and provided a focal vibrating amplitude of 50 to 115 μm (based on different driving voltages). The experiment consisted of three parts:

1. Low repetition rate, low power, line test to test focal behaviour inside bulk material
2. HAZ induced by stationary laser pulses inside bulk material
3. Welding of borosilicate glass pieces

The laser operated at 1030 nm wavelength and a focal length of 20 mm lens was used for all the TAG experiments. Due to the limited aperture of TAG lens, the telescope (beam expander) was removed from our experiment setup and a laser beam diameter of 6 mm was thus used (focal spot diameter ~6.2 μm).

6.4.1.1 Focus Behaviour Test inside Bulk Material

Based on our previous experiments, a single pulse with enough peak power can generate nonlinear absorption and create a permanent defect inside the material. A very low repetition rate was used to observe the focal behaviour with reduced thermal accumulation and thus interaction between adjacent pulses. In this experiment a 400 Hz pulse repetition rate was used with the laser translated at 1 mm/s focused inside BK7. The laser power was set at 2.08 W, sufficient to generate HAZ even though the focal spot is distorted by the TAG lens, and laser power of 0.94 W which is slightly above the material breakdown threshold.

The experiment used a TAG frequency of around 140 kHz, and changed the TAG driving voltage (to generate focus vibration of different amplitude) to different level and observed the HAZ (or permanent defects) inside BK7 cube. The tests carried out were: "TAG out": Test setup without the TAG in the beam path; "TAG off": TAG lens in the beam path but not working; "TAG on": TAG lens working normally with different parameters. The results are shown below in Table 6.3:

Table 6.3. Defect patterns of different laser powers by different TAG voltage and frequency, Matlab simulation also present to show the location of different pulses (laser frequency 400 Hz and scan speed 1 mm/s inside BK7)

TAG voltage [%]	**TAG Frequency [Hz]**	**P=2.08 [W]**	**P=0.94 [W]**	**Matlab simulation**
TAG off		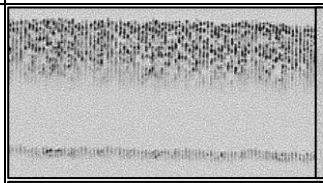		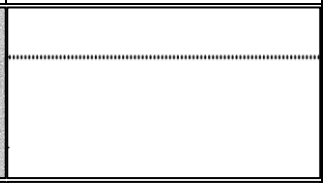
15%	**140780**	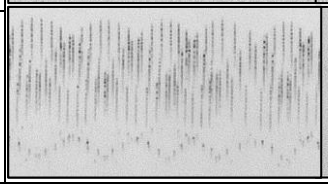	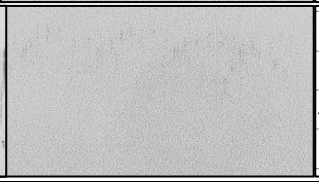	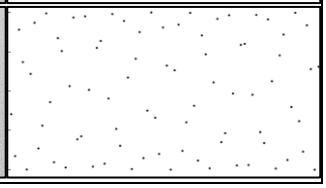

TAG voltage [%]	TAG Frequency [Hz]	P=2.08 [W]	P=0.94 [W]	Matlab simulation
20%	140680	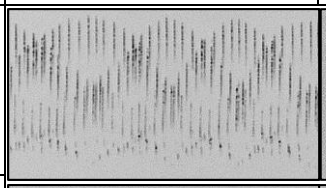	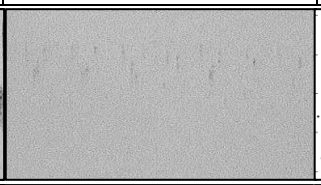	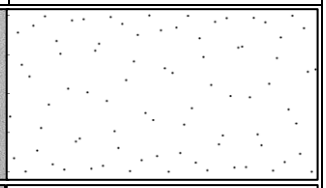
25%	140560	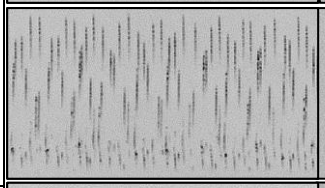	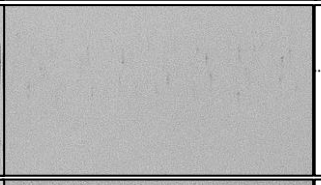	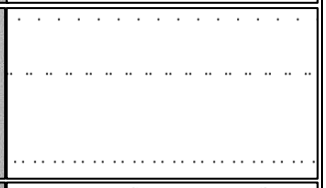
30%	141220	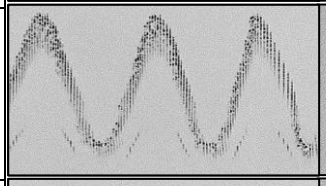	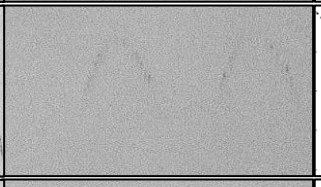	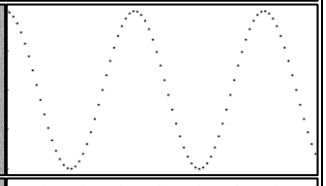
35%	141240	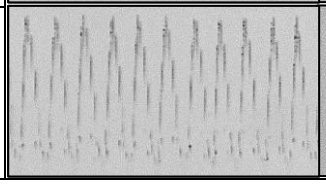	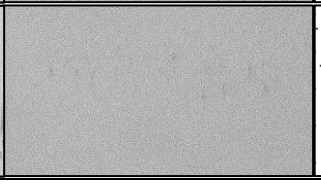	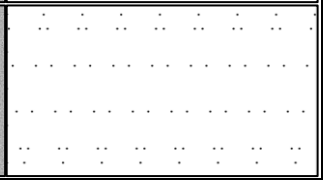

Three conclusions can be made from Table 6.3: firstly, the TAG lens did generate a focus vibration inside the material, where the amplitude was based on the drive voltage and the frequency based on the TAG resonant frequency. The vibrating amplitude could be measured from the laser power 2.08 W, shown in Fig 6.20, which demonstrates a roughly 5.3 μm/*V* of amplitude could be obtained.

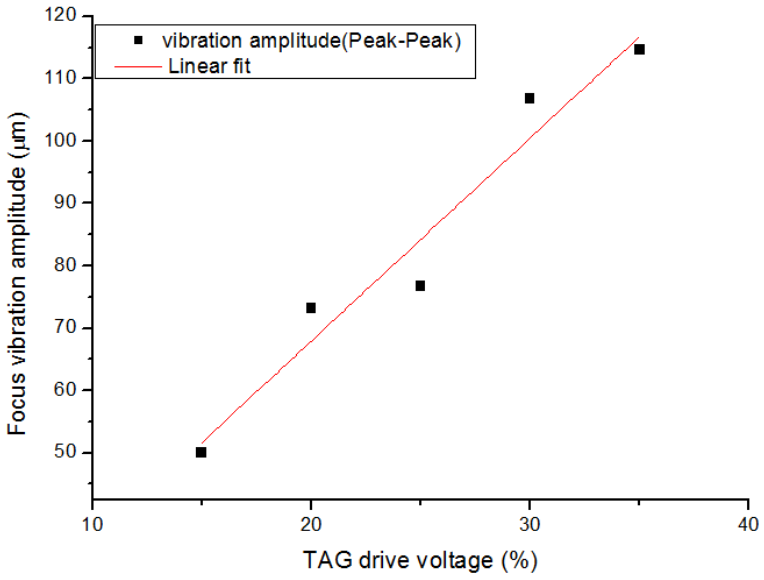

Fig 6.20 Graph of the relation between focus vibration amplitude and the TAG drive voltage. (full voltage is 63 V and linear fit shows a 5.3 μm/V amplitude was obtained)

Secondly, the TAG resonant frequency determined the inscription patterns of the 400 Hz (1 mm/s) pulse irradiation defects (HAZ), although the patterns are highly dependent on the driving frequencies (±0.1 Hz will result in quite different pattern based on our Matlab simulation). Those patterns show where each pulse was located in z axis during the process, which spatially changed the pulse overlap (focused pulses distributed along the vibration direction). This even influences the processing parameters for the 400 kHz pulse repetition rate duration the welding.

Thirdly, the focal spot is deformed when beam passes through the TAG lens, in particular for larger focal shifts, as shown in Table 6.3. Visible material modification at the peaks or valleys of the oscillation can be observed in 2.08 W column photos, but for the laser power at 0.94 W, no modification is observed at the vibration peaks. The deformation when the TAG lens vibrates to a large focal shift results in an intensity below the breakdown threshold.

6.4.1.2 HAZ Comparison of TAG Lens

To investigate the HAZ appearance with a rapidly vibrating focus, a certain number of pulses were irradiated inside BK7 with different TAG parameters while keeping the sample still. The HAZ size was observed under the microscope afterward. The driving frequency used was around 140 kHz with the drive voltages of 10%, 20%, 40% and 60%. The laser was focused 3 mm inside a BK7 cube, and laser average power 2.08 W (pulse energy is 5.2 μJ). The graph for different parameters is shown in Fig 6.21.

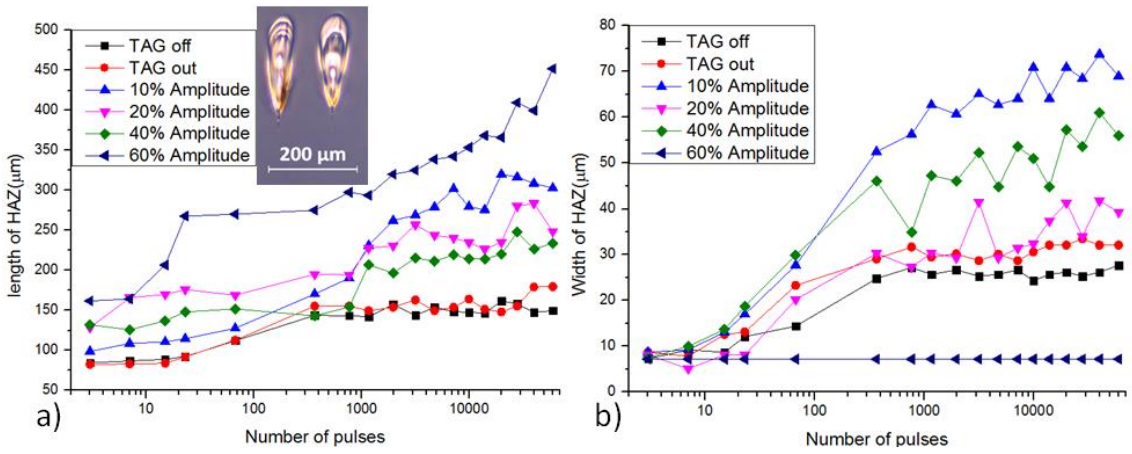

Fig 6.21 HAZ size by number of pulses inside BK7 (pulse energy is 5.2 μJ. (a). Length of HAZ, (b). Width of HAZ), inset photo shows what the HAZ looks like for a vibrating focus inside material.

From the graph, “TAG out” and “TAG off” give similar HAZ sizes which implies that the TAG lens generates little distortion and/or absorption when it is switched off. Overall, the focus vibration results in a larger HAZ inside the material, and as the vibration increases, the HAZ length increases whilst the width decreases, which is easy to understand as the focus vibrating up and down inside the material results in nonlinear and plasma absorption over a large range along the vibrating direction, but less overlap of the adjacent pulses prevents plasma generation. Typically, vibrating peak-peak amplitude of 198.2 μm (60% TAG voltage) resulted in a pulse overlap so low that no plasma absorption could be established.

6.4.1.3 Welding with TAG Lens

To compare the welds with and without TAG on, a suitable TAG lens parameters (140 kHz frequency and 35% amplitude) were chosen to test spiral welding inside borosilicate glass with different laser powers.

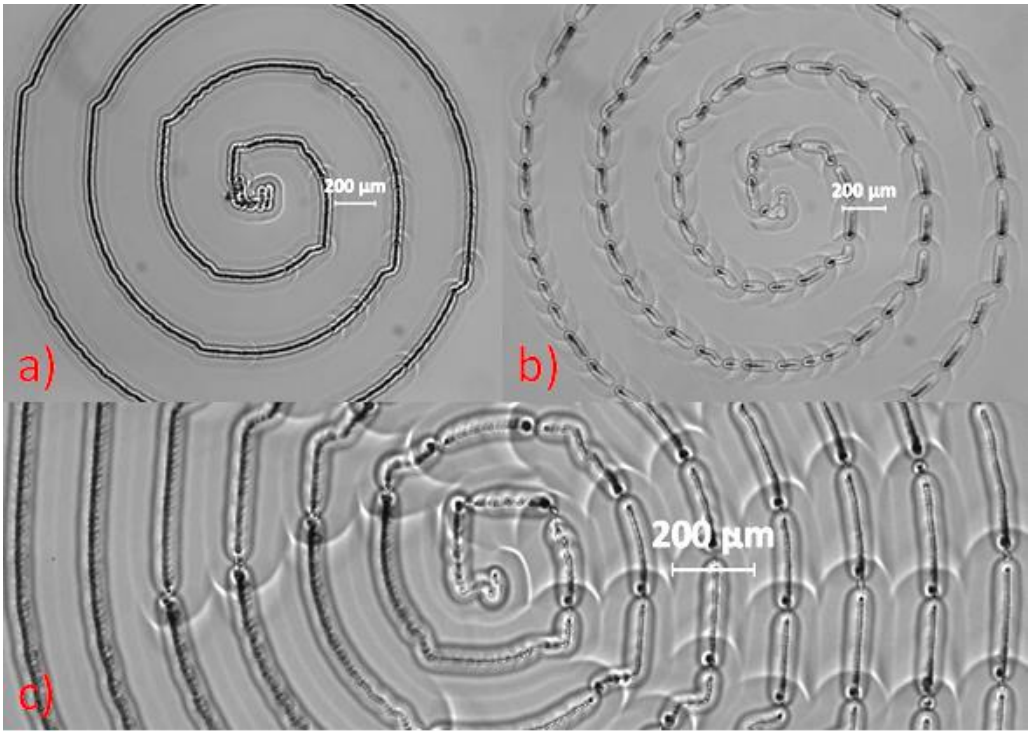

Fig 6.22 TAG lens welding test comparison. (a). “TAG off” with laser power 2.4 W and scan speed 1 mm/s; (b). “TAG on” at 140 kHz and 35% amplitude, with laser power 2.4 W and scan speed 1 mm/s; (c). “TAG on” at 140 kHz and 35% amplitude, with laser power 3.6 W and scan speed 1 mm/s.

example photos generated with 2.4 W laser power and scan speed 1 mm/s with and without TAG vibration are shown in Fig 6.22a and Fig 6.22b. It is clear that the HAZ

size for “TAG on” is obviously larger than “TAG off” as shown. Also, Fig 6.22c shows TAG welding with power as high as 3.6 W; in this case no cracking was observed even through the HAZ clearly overlapped.

The TAG lens results in an increase in the material plasma generation threshold, which is easy to understand as the pulses are less overlapped as the TAG amplitude increases. But once the power is high enough to generate plasma (plasma absorption dominates), the HAZ will become larger compared with the “TAG out” and “TAG off” situation. For welding, when the TAG is on, the plasma region and HAZ are large compared with “TAG off/out” as the focus keeps vibrating, which changes the plasma and heat distribution spatially and greatly eases the thermal gradient of the HAZ, so fewer cracks could be observed even where the HAZ is highly overlapped. When the focus position changes, the focal spot size and shape change as well, this makes laser absorption and HAZ shape unpredictable, especially with different laser powers.

6.4.2 Vibrating Test and Weld with Vibrating Motor

Another method of generating focus vibrations is by applying a motion on the lens. As shown in Fig 6.23, in our demonstration setup a vibrating motor was fastened to the frame cage which mounts the focal lens, the focus hence could be made to oscillate in a circular motion in the x-y plane.

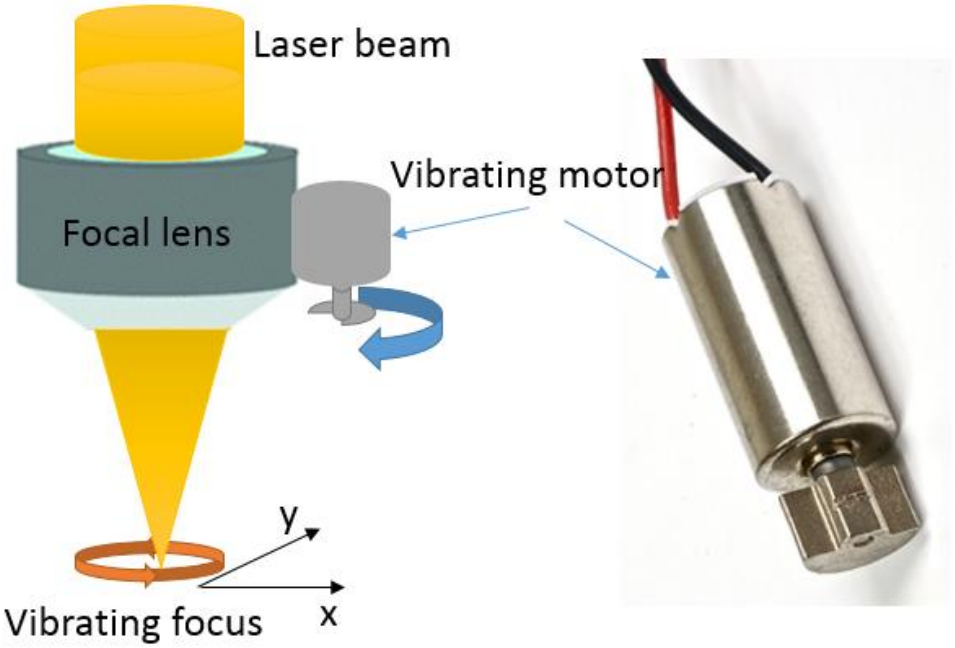

Fig 6.23 Illustration of focus vibration generation at x-y plane by a vibrating motor.

Although it is not easy to control the vibration amplitude dependent on the rigidity of the frame cage (which the focal lens is mounted to), by adjusting the driving voltage of the vibrating motor, the amplitude of movement can be controlled to around hundred micrometres. Hence the laser beam was still paraxial, and an un-deformed focus could be achieved.

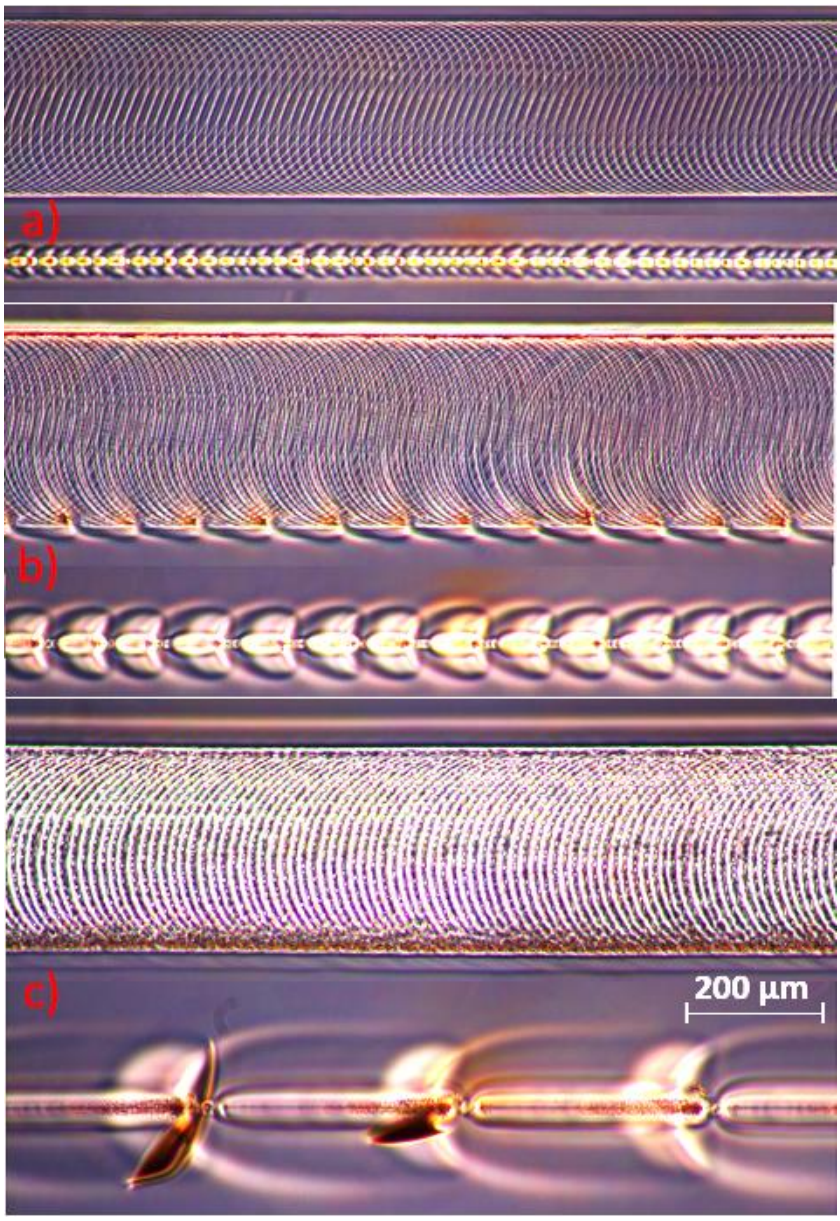

Fig 6.24 HAZ of line test of different powers with or without vibration inside borosilicate glass. (a). Laser power 1.35 W and scan speed 1 mm/s, 10 mm focal lens; (b). Laser power 1.87 W and scan speed 1 mm/s, 10 mm focal lens; (c). Laser power 3.65 W and scan speed 1 mm/s, 10 mm focal lens. The vibration frequency is 65 Hz and p-p amplitude is 265 µm.

HAZ lines were created inside borosilicate glass using a range of powers and a scan speed of 1 mm/s for a vibration frequency of 65 Hz and peak-peak amplitude 265 μm, as shown in Fig 6.24. A combination of forward and circular motion can be observed in the modified material. If a vibration of frequency *f* and p-p amplitude *A* is used, then the focus velocity is $V_{focus} \approx \pi Af + V_{scan} = 55.1\, mm/s$ instead of 1 mm/s without vibration, as shown in Fig 6.24a. However in this case even though a plasma track is clearly created, there was no HAZ of this power level (due to the high scan speed and spatial separation of individual pulses). But as the laser power increased HAZ is observed around the vibrating region as shown in Fig 6.24b at a laser power 1.87 W. If the laser power is further increased the HAZ, without vibrating, induces cracks at 3.65 W (Fig 6.24c) but not when vibrating even with a laser power of 5.6 W.

The cross-section view of different laser powers in Fig 6.25 shows the pattern along the HAZ line along with cross-sections of the HAZ generated by different laser powers. The vibration clearly increases the width of both the plasma modified region and the HAZ. As discussed earlier (section 4.2), this shape of HAZ helps generating a large true weld area.

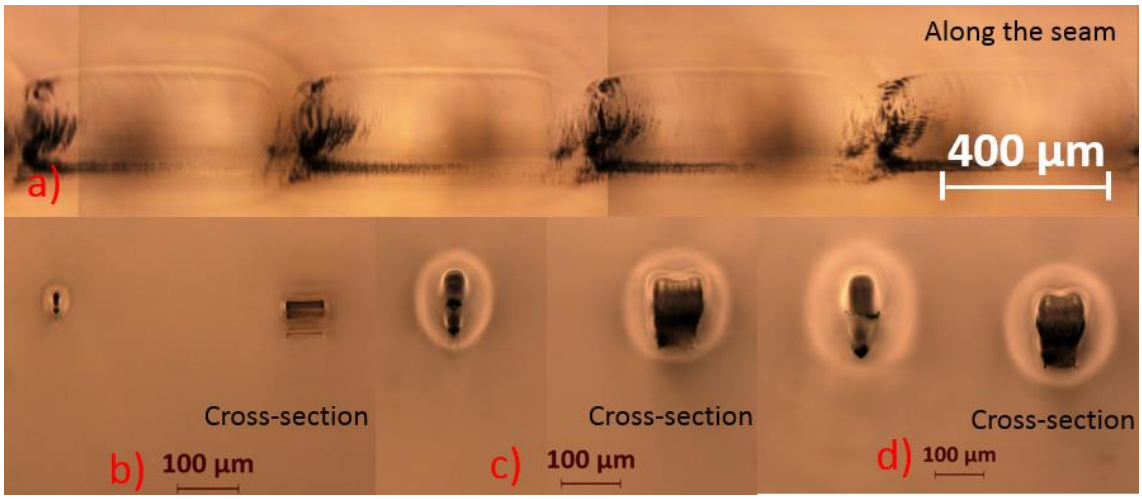

Fig 6.25 Cross-section of vibration HAZ. (a). Typical pattern of sectioning along the HAZ line, laser power 3.12 W; (b). Cross-section of laser power 1.04 W; (c). Cross-section of laser power 2.08 W; (d). Cross-section of laser power 3.12 W. With laser scan speed 1 mm/s with 10 mm lens, vibration frequency 206 Hz and p-p amplitude 59 μm.

Using this vibration approach, welding of borosilicate to borosilicate glass was carried out. As expected, from the results presented above, higher power (as large as 4.16 W)

could be used without cracking, see Fig 6.26. A cross-sectional view of the weld shows that a large weld seam was generated (left of the figure). For comparison a weld made without vibration and half of the laser power (2.08 W, to avoid cracking) is also presented in Fig 6.26. The strength test comparison carried out in section 4.3, for the same laser power, the vibrating weld obtains higher weld strength, but as the laser power used for vibrating welding strength test was not an optimised one, so the comparison is incomplete.

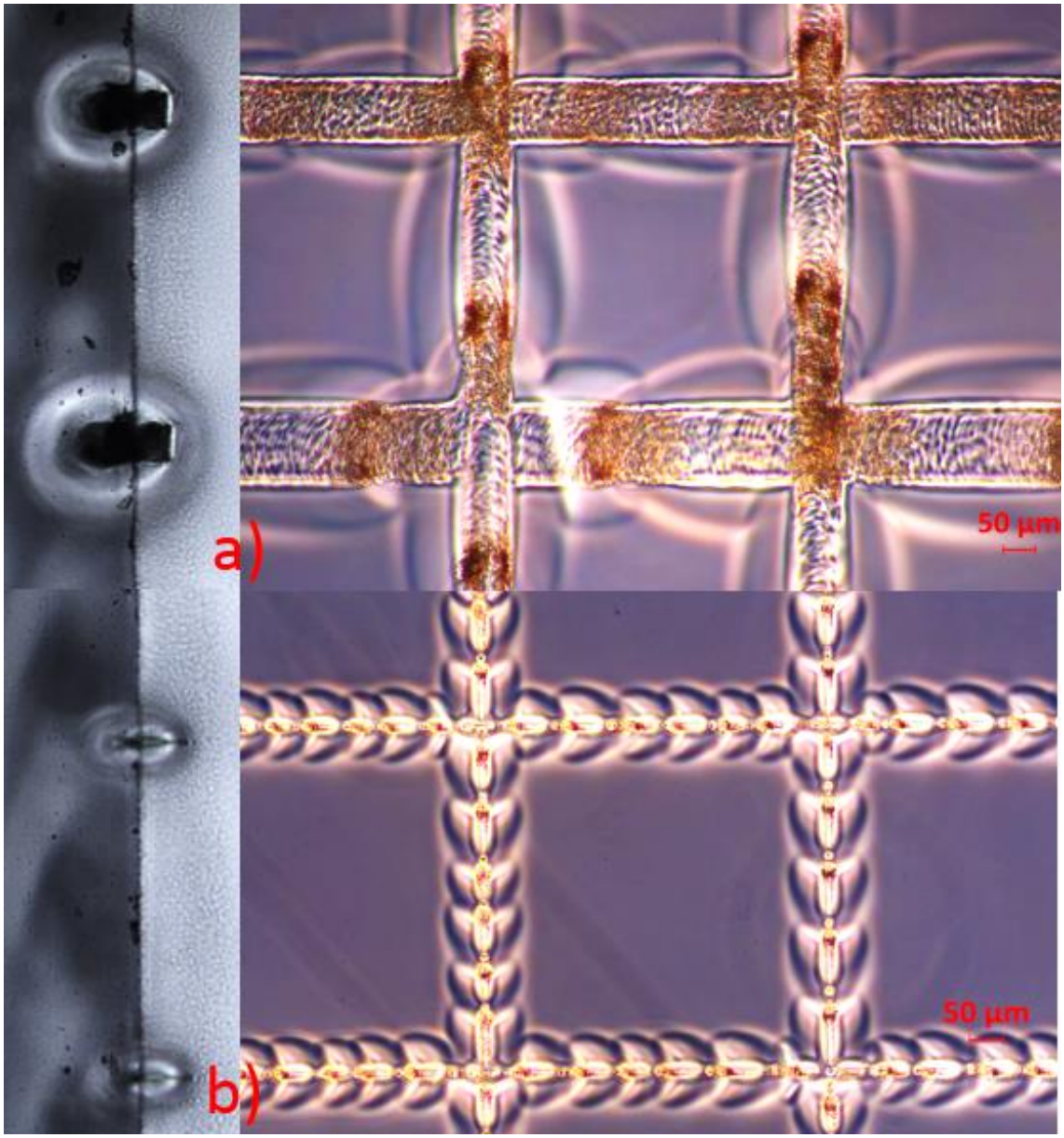

Fig 6.26 Cross-section (left) and top view (right) of vibrating welding (a) (Laser power 4.16 W and scan speed 1 mm/s, with vibrating frequency 137 Hz and p-p amplitude 158 µm) and normal welding (b) (Laser power 2.08 W and scan speed 1 mm/s).

6.5 Summary and Conclusion

In this chapter, different welding patterns were introduced. Residual stresses were firstly investigated and discussed through a stress model, and different scan strategies were put forward to relax stress and eliminate cracks. Also alternative scanning with galvo-scanner was investigated and focus vibrating methods were introduced to provide flexible pattern inscription and strong bond.

The sample cracks due to thermal changes either during the welding process or as temperature varies after welding particularly if a large continuous area is welded, hence discrete patterns are needed to reduce the stress accumulation for glass-metal welding. Based on the analysis above, several methods were used to reduce residual stress: decreasing laser power and increasing seam spacing, dual power welding, scan sequence adjustment and discrete welding (or spot welding), in which discrete welding is the most promising one and we extensively investigated this method.

Two methods of generating discrete welding patterns were discussed and demonstrated, the first method is to use a shutter inserted in the beam path, where either a dot or a circle (or square) can be generated for each shutter on-off. The other method is to control the ultrafast pulsed laser source to output modulated pulses (pulse train). An enveloped pulse trains generate discontinuous welds in a periodic pattern. Those two methods showed effective ways to release residual stress introduced by the thermal expansion coefficient difference inherent in dissimilar material welding.

Welding with a galvo-scanner was also tested as an alternative method for industrial applications. This provides a flexible scanning pattern and high scan speed but the disadvantages of weak welding strength and high residual stress stand out.

As well as reducing the residual stress introduced by different material thermal expansion coefficients, a vibrating focus method was proposed and investigated to reduce the residual stress caused by the thermal gradient during the welding process. Both a TAG lens and a vibrating motor were used to provide focus vibration, and the results showed a promising way of reducing likelihood cracking and expanding the plasma region, albeit at higher laser average power.

Chapter 7 Ultrafast Laser Welding Applications

Existing industrial glass-glass and glass-silicon micro-joining techniques are not reliable. These are usually based on an adhesive agent or interlayer. Mechanical properties and chemical stability are not sufficient for many applications. Tamaki et al (2005) [120] first demonstrated laser welding between two silica glass plates without a light-absorbent intermediate layer using a femtosecond laser, after a decade many applications of glass-glass and glass-metal welding have been explored to replace traditional joining methods [7][8]. The advantages of ultrafast laser welding compared with other joining methods include:

1) Minimal heating outside the weld volume and low heat distortion.

2) Welding of transparent materials without inserting absorbing intermediate layers.

3) Welding dissimilar materials (one of which must be transparent) with significantly different coefficients of thermal expansion.

4) Highly spatial selective welding with few microns precision.

In this chapter an application-orientated investigation was carried out in order to apply ultrafast laser welding to industrial applications.

7.1 Welding over Large Area

It is relatively easy to use an ultrafast pulsed laser to weld identical glasses over a large area without cracking. However, when attempting large glass to metal welds (for example, weld diameter $\geqq 5$ mm), a key difficulty arises; It is hard to provide a metal surface that is both flat and optically smooth over a large area. As calculated in Chapter 6, residual stress increases with weld width and weld area. As the area being welded increases, more energy is deposited at the interface, increasing the material temperatures as a whole (unless a very thick piece of material is used act as a heat sink or a long processing time is adopted to wait for the sample to cool down however this is not practical for industrial manufacturing), which will greatly increase the residual stress caused by differential thermal expansion. For welding glass to metal special scan strategies can be considered (a dot welding or discrete welding approach) to release the stress caused by different thermal expansion coefficients, as well as introducing less energy deposition than a continuous welding process. And if the whole weld strength is

less than required, the welding process can be repeated (while avoiding seams overlapping) for a higher weld strength. Large area welding of identical material and dissimilar material are shown in Fig 7.1.

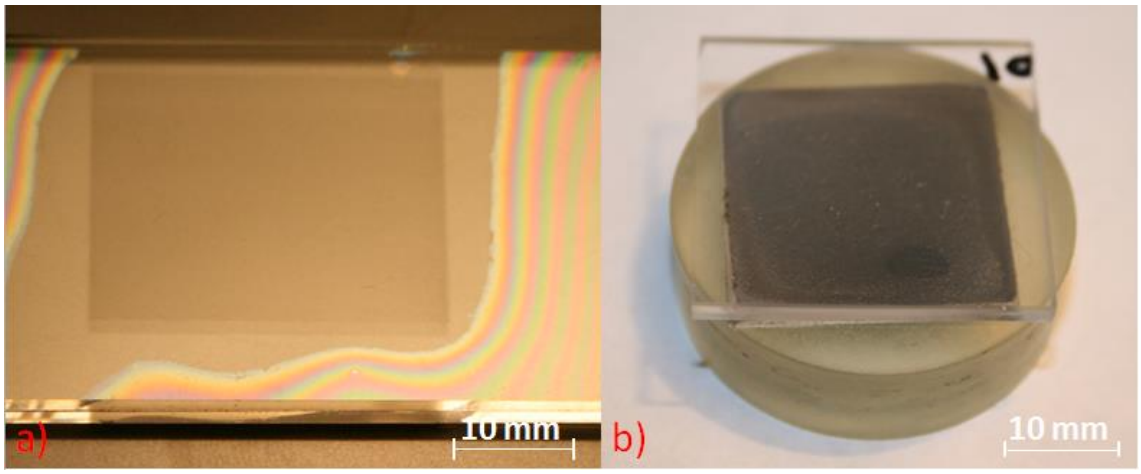

Fig 7.1 Large area welding of identical and highly dissimilar materials. (a). Fused silica welded to fused silica with a normal line scan welding method, weld area is 30 mm × 20 mm, (b). Borosilicate glass welded to aluminium with pulse train spot welding, weld area is 25 mm × 25 mm.

Another advantage of discrete welding is, even if cracks appear at one or several weld units due to local surface conditions, they will not propagate to a large area as the continuous welds usually do. The methods and examples of this part are presented in 6.1 and 6.2.

7.2 Seam Sealing

Seam sealing is a packaging technology typically used for hermetic sealing of chip carrier packages which originated in the electronic industry and sees widespread use, as discussed in section 1.3.2 [168][169]. Ultrafast laser welding provides seam sealing of selective micrometre level direct fusion bonding of a glass cover and glass/metal substrate with just a thin layer (several hundreds of micrometres). As there is no need for an intermediate layer or solder between the materials, only a simple sealing structure is required, as shown in Fig 7.2 and Fig 7.4.

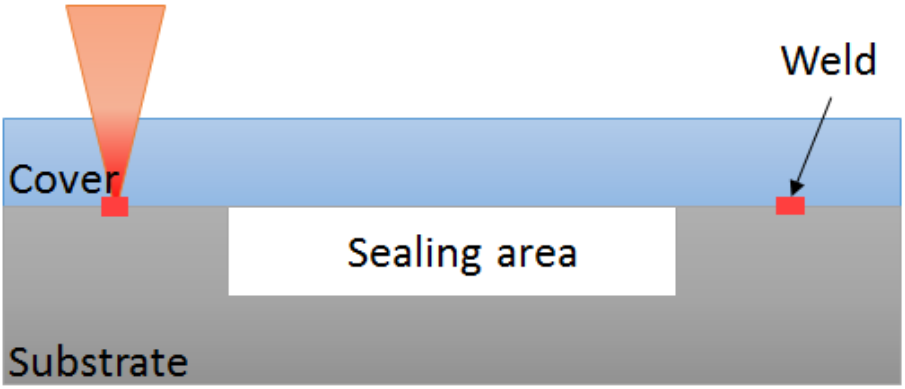

Fig 7.2 Illustration of sealing structure with ultrafast laser welding.

As this sealing is directly welding the cover and substrate materials together—no joining degradation problems are to be expected. No systematic measurement of the hermeticity has been tested, instead a water tightness test was carried out under a weld of 1 μm etched groove with ink filling inside, as shown in Fig 7.3. The water or ink cannot penetrate a single weld seam of 200 μm width, demonstrating the feasibility.

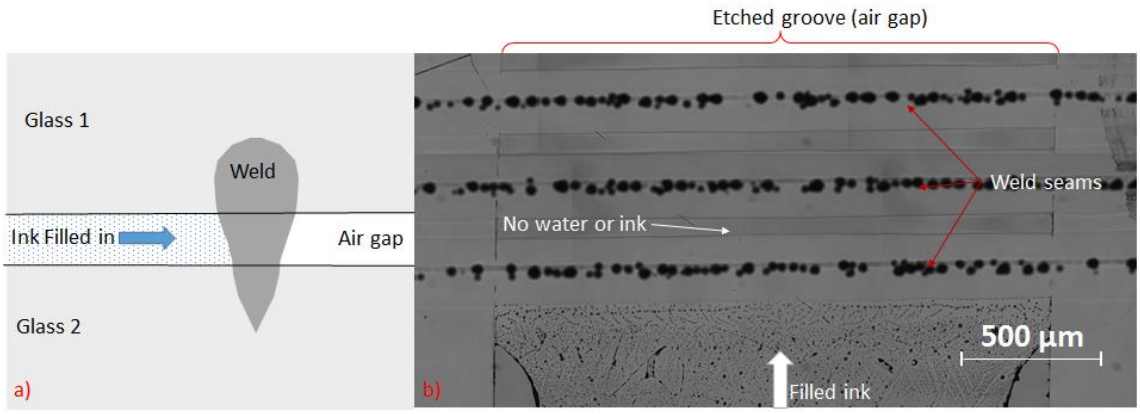

Fig 7.3 Water tightness experiment with filling water to a 1 μm depth groove (a. diagram of cross-section view, b. welds of fused silica to fused silica with laser power 14.04 W and 2 mm/s scan speed).

Different patterns of sealing an area were carried out and an air bubble with ink was sealed as shown in Fig 7.4a and square sealing with different welding patterns is shown in Fig 7.4b.

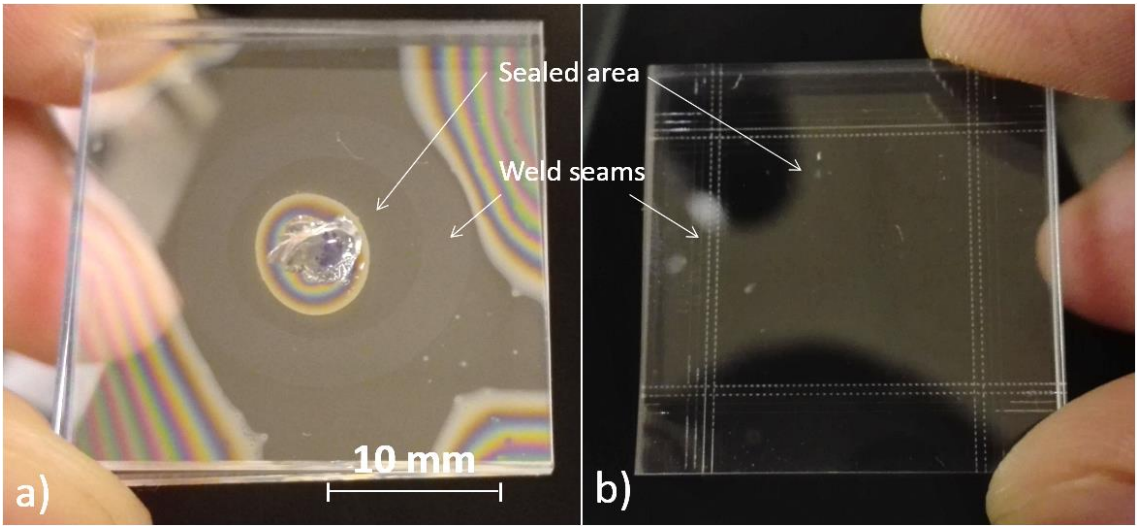

Fig 7.4 Different seam sealing patterns, demonstrated with borosilicate glass to borosilicate glass. (a). Circular seams with an air bubble and ink in the middle, 10 rounds of welds with laser power 1.6 W and scan speed 1 mm/s, and (b). Square sealing with 4 weld lines at each side (inner 2 lines with 4.16 W are vibrating welds and outer 2 lines with end cracks are 2.08 W normal welds, see Fig 6.26).

7.3 Thick/Thin Sample Welding

There are particular issues which arise when welding either thick or ultra-thin pieces of glass to a substrate. Based on Eq 3.4, the focal length should be at least h/n to focus the beam at the interface (h is the thickness of the upper sample and n is its refractive index). Thick glass welding requires a long focal length lens to place the focus at the interface, for example, with our 10 mm focal lens (Thorlabs, AL1210-B the working distance from the focus to the front of the lens is 7.6 mm), a maximum thickness of 11.1 mm of fused silica could be welded with this lens.

As discussed in section 2.1, aberrations arise when focusing a laser beam through a flat glass surface. The impact of these becomes more significant as the laser beam focuses deeper into the glass, causing both the focal spot size and Rayleigh range to increase. To investigate the impact of this on the welding process, the ultrafast pulses were used to generate a HAZ inside borosilicate glass, and the size of this HAZ measured for a range of different focal as shown in Fig 7.5. A 20 mm lens was used with an incident laser power just enough to create HAZ inside the material. Firstly the laser was focused 2 mm inside a borosilicate glass cube, and modification lines were drawn at this height, then the stages move up with 200 μm steps and the lines are repeated, until the focus moved out of the material. The focus position can be measured with a microscope

afterward, and the HAZ photos are also shown in Fig 7.5. The testing result shows a roughly linear trend of HAZ length and focus position, which is predicted through the theoretical calculation in section 2.1.3.3.

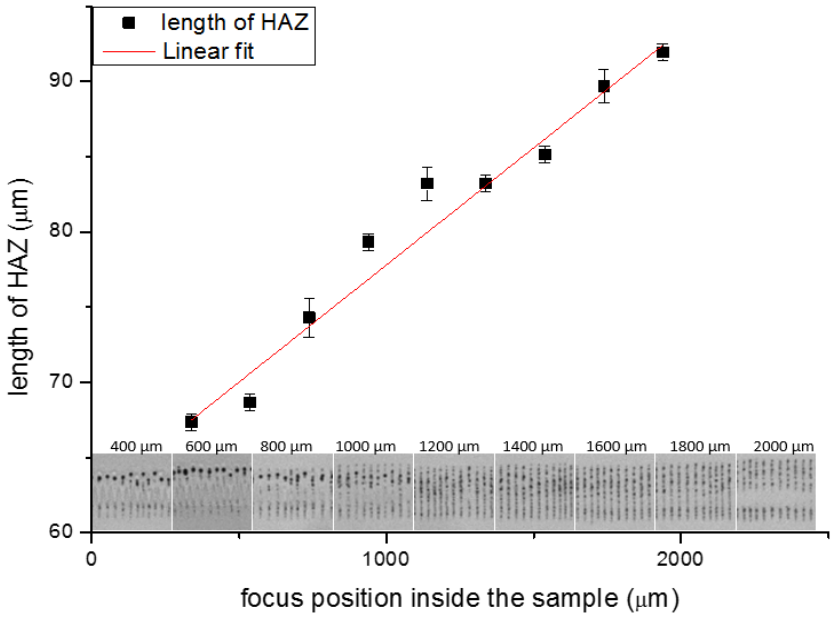

Fig 7.5 Relation of focal position inside the sample and the HAZ length for laser pulse trains (pulse energy was 29 μJ with a 5 ms pulse train duration and 100 Hz repetition rate) with 1 mm/s scan speed and 20 mm lens.

For thick sample welding, it is also necessary to consider that the laser beam may be clipped at the sample edge, resulting in less pulse energy being focused at the interface, as shown in Fig 7.6. For a beam (diameter 12.7 mm) focused by a 10 mm lens through a 10 mm thick fused silica to the interface, the edge clipped length (*d* shown in Fig 7.6) is 3.9 mm based on the geometrical relation.

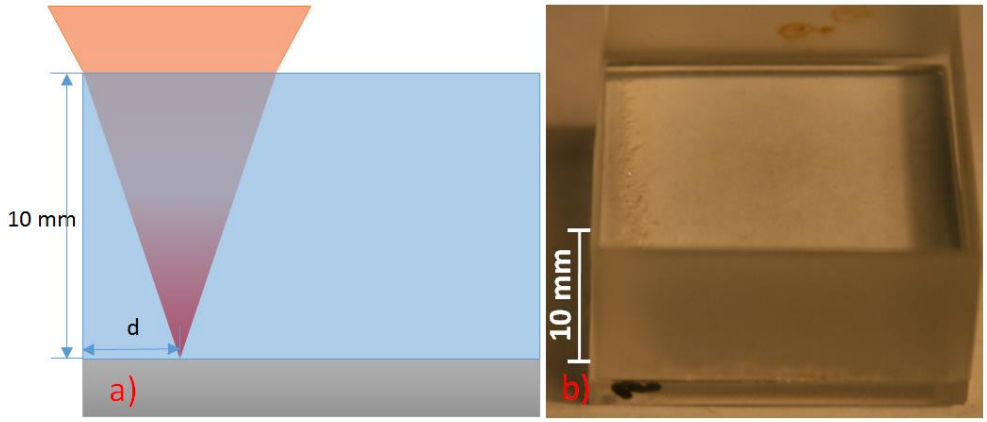

Fig 7.6 Diagram (a) and experimental sample (b) of thick material welding. (b). shows whole area welding through a 10 mm thickness fused silica sample to a 25×25×1 mm borosilicate glass).

For welding thin glass with a substrate, the main problem is glass deformation. When focusing ultrafast pulses inside transparent materials, the plasma generated in the focal region increases the absorption coefficient and results in a fast energy release in a very small volume. A strong shock wave is generated in the interaction region and propagates into the surrounding material [36]. Since the thin glass can easily deform and the strong shock wave will draw the interface out of optical contact. The schematic of clamping during welding thin piece of glass to metal is shown below:

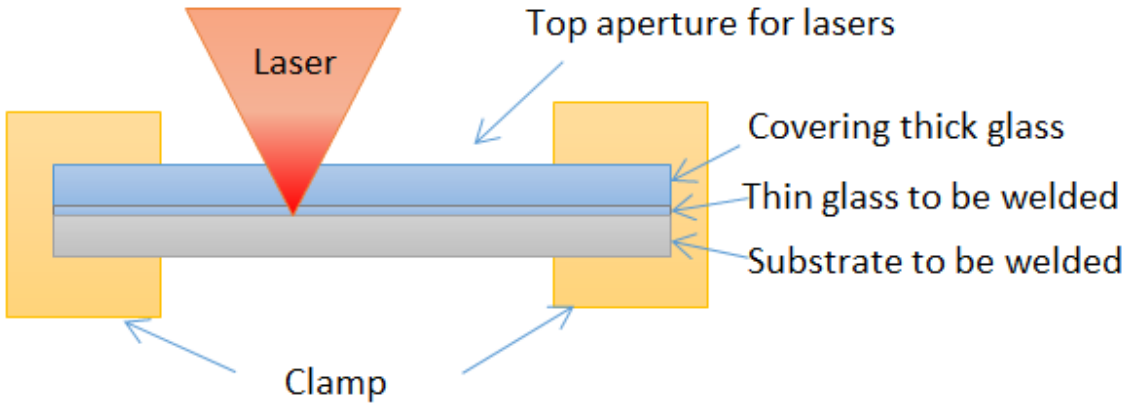

Fig 7.7 Schematic of welding thin glass to metal.

The top thick piece of glass is used to prevent deformation. Laser pulses are thus focused through two layer of the glass to the glass-metal interface. Care must be taken to ensure that the two glass layers are not also welded together, by controlling the focus position and laser power (i.e. to prevent the HAZ from reaching this additional interface).

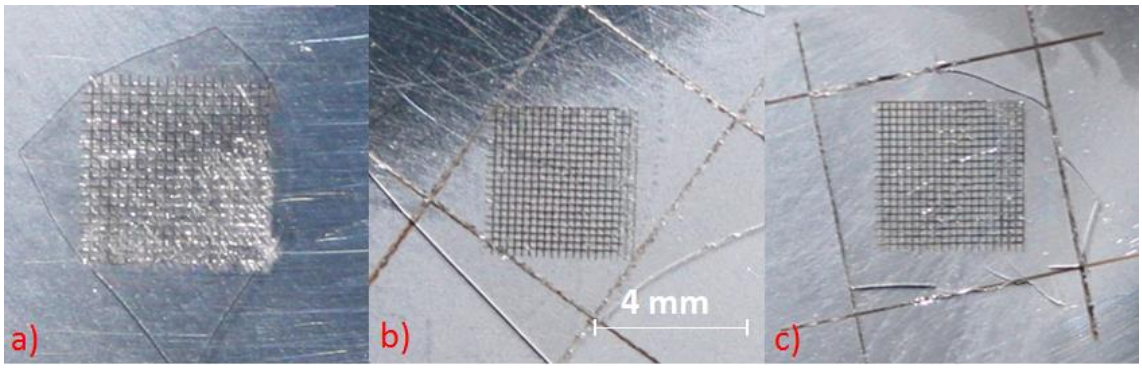

Fig 7.8 Welds of thin piece of glass (fused silica, 100 μm) to aluminium with different powers (net pattern welding area 4 mm × 4 mm, a. 1.84 W, b. 1.67 W, c. 1.49 W with scan speed 2 mm/s).

As a demonstration experiment, thin glass (100 μm fused silica) was welded to aluminium with different powers, as shown in Fig 7.8. The weld experienced welding the top covered glass (Fig 7.8a), perfectly welding (Fig 7.8b), and cracks after welding (Fig 7.8c) cracks are because of the weld not strong enough at lower power) for laser powers of 1.84 W, 1.67 W and 1.49 W respectively.

7.4 Spot Welding of Optical Window

In industrial applications, a piece of glass or sapphire is often required to be fixed in front of a lens or detector as a protection window. Using ultrafast laser welding to bond such a window at a small area is investigated here.

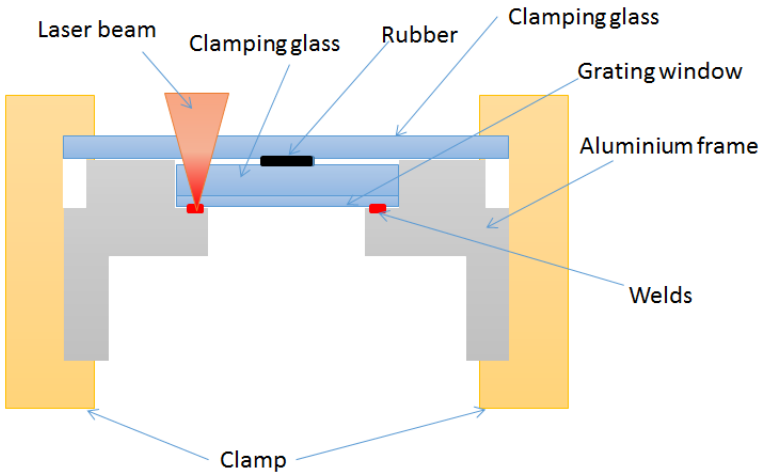

Fig 7.9 Schematic of welding glass optical window to aluminium frame.

The schematic setup for welding a fused silica window to an aluminium frame is shown in Fig 7.9. To smooth the recessed area of the frame, a tumbling method was used. To clamp the glass window and the aluminium part, 2 pieces of glass and a rubber disc was used to provide uniform pressure on the fused silica window. The fused silica window is 5 mm × 3 mm × 0.6 mm and has a 500 μm overlap at each side with the aluminium frame. Multi-spots welding is used for the glass window with the resulting welds shown in Fig 7.10. The glass window was successfully welded with three 0.8 mm diameter spirals as shown in the photos.

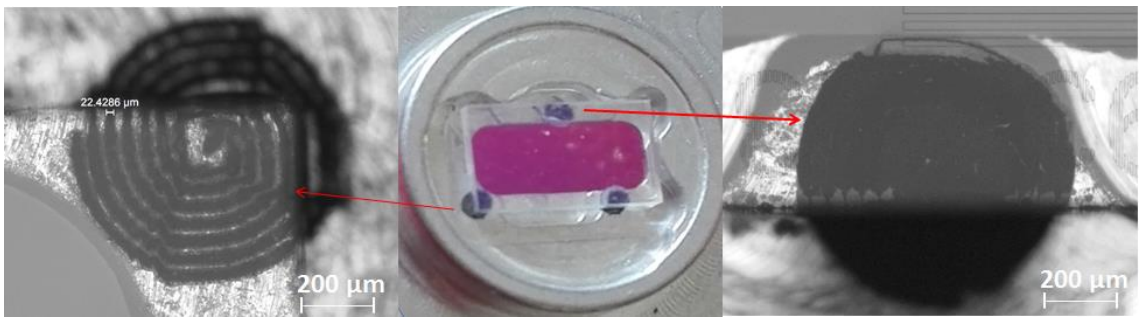

Fig 7.10 Spot welding for fused silica window and aluminium frame and spiral seams (laser power 5.05 W and scan speed 1 mm/s with 20 mm lens).

7.5 Weld with an Angle

Geometrical shape restrictions of industrial applications do not always offer normal transparent surfaces. Thus the welding has to be done by focusing the laser beam through a side face on to the interface. Welding with this method requires the laser beam to be incident on a non-perpendicular front surface (Fig 7.11b), unless an additional prism is placed at the side of the part, as shown in Fig 7.11a.

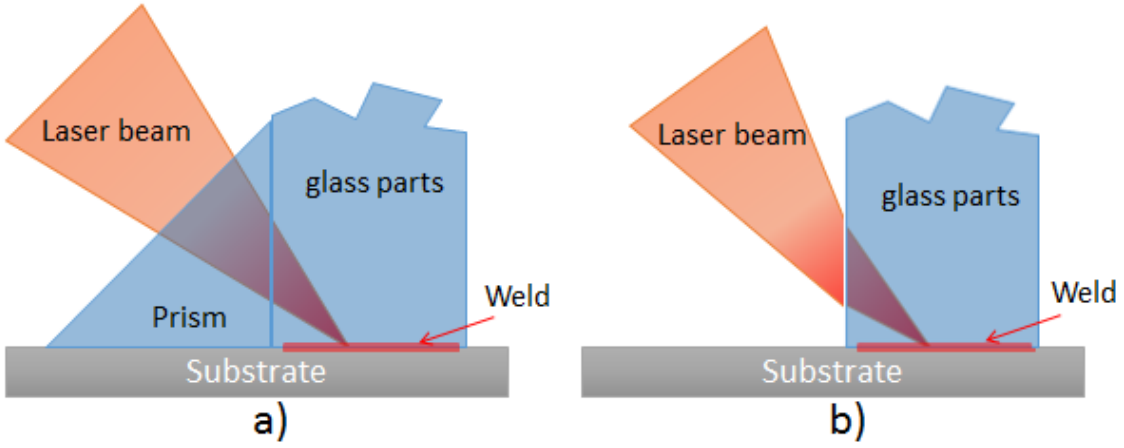

Fig 7.11 Schematic of welding abnormal or non-transparent glass part to substrate. (a). Weld with a prism, (b). Weld without prism.

When welding with a prism, the main problem is the gap between the prism and the glass part, any non-optical contact area can result in a total internal reflection inside the prism, and optical contact at those two surfaces is non-trivial. Fig 7.11b is the more usual schematic used for welding abnormal interfaces. However, aberration is introduced when focusing laser beam inside material with an abnormal angle, results in focal deformation. This will give a line inside the material instead a single point at focus (right side of Fig 7.12, see 2.1 for more detail). To investigate this, firstly an experiment

was setup to measure the transmitted laser power as a function of different incident angles, as shown in Fig 7.12, to determine laser power required to generate a suitably high energy density above the breakdown threshold inside the material.

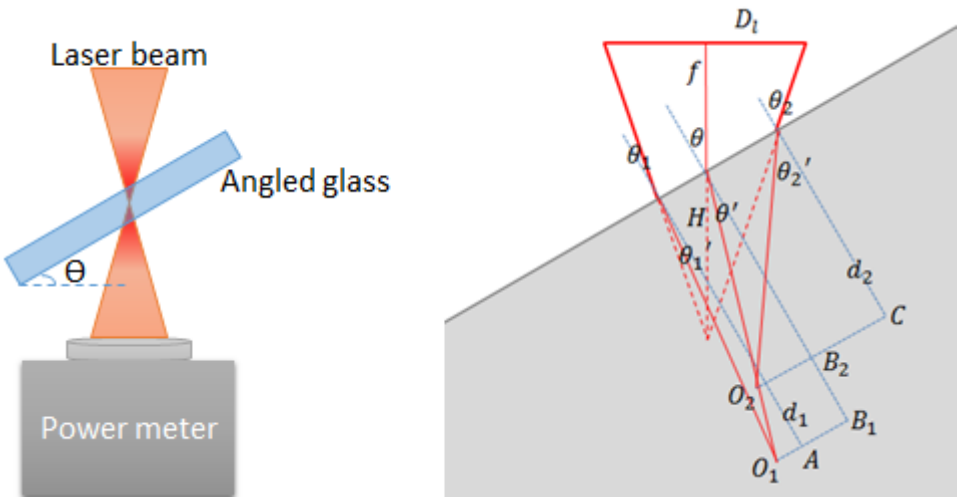

Fig 7.12 Schematic of laser absorption in borosilicate glass with different incident angles, the geometrical diagram is presented at right hand side for aberration calculation, with the details shown in section 2.1.3.2.

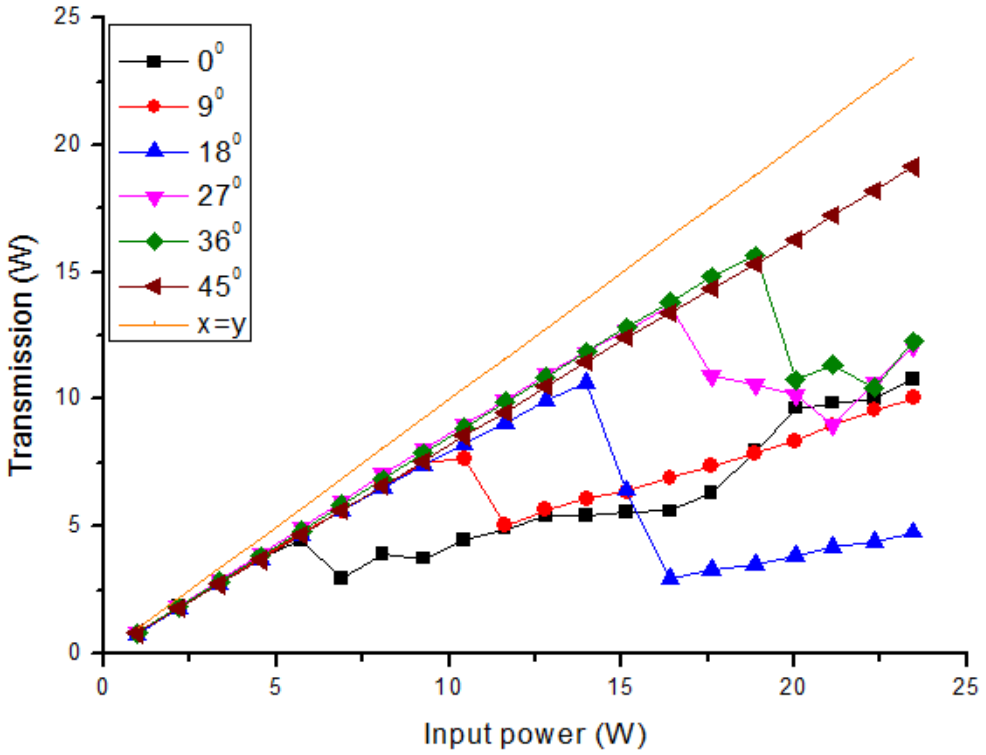

Fig 7.13 Relation of input and output power for different glass angles (x=y line is presented in this graph for comparison), the glass is borosilicate and a 20 mm lens was used for the test.

Once the laser intensity reaches the breakdown threshold, the structure inside the glass changes and absorption or diffraction results in the characteristic transmission change. Before the power reaches breakdown, the relations of transmission-incident power shares the same trend and the gradient could be easily obtained as 0.816, the power loss is mainly due to surface reflection and defect diffraction. Fig 7.14a shows the relation of surface transmission and incident angle based on Snell's law, and the rough relation of breakdown threshold with incident angle inside borosilicate glass for our laser system is shown in Fig 7.14b. A rapid increase in the threshold as a function of angle can be observed from the graph, and indeed the breakdown threshold could not be reached for an angle of 45 degrees even with a laser power of 23.45 W, a factor nearly 5 times higher than that at normal incidence.

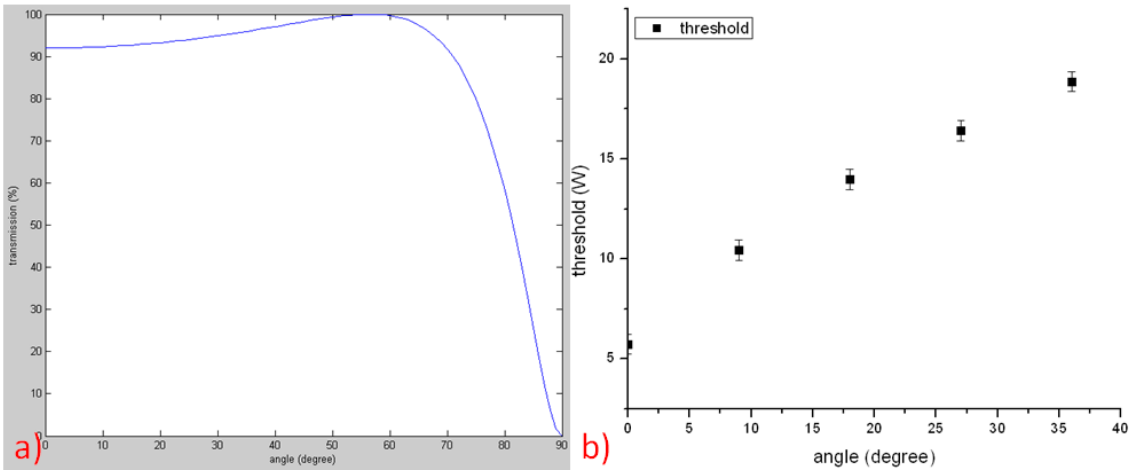

Fig 7.14 (a). Transmission and angle relation based on Snell's law and (b). The breakdown threshold inside borosilicate glass with our laser system for different glass angles.

For ultrafast laser welding with an angle, the laser power should be adjusted based on both the angle and material, but there are still two points we need to consider:

1. Different absorption rates based on interface conditions at the local focus area. Focus aberration of an angled front surface makes the laser power far above normal incident breakdown threshold to generate nonlinear absorption. But whereas the surface defects or other absorption centres will make the absorption start from linear absorption and greatly and quickly increase the absorption rate, create an extreme large HAZ (as the laser power is much higher than that of normal incident), and a much smaller HAZ appears where it initially nonlinear absorbed with no absorption centres. This non-uniform HAZ can easily crack the material. To solve this problem, pulse train welding

was used with increased peak power (far above the breakdown threshold) which will always be highly absorbed but the pulse train stops before too much energy is accumulated creating a large HAZ, a much more homogeneous HAZ train can be obtained via this method.

2. The back-reflection focal positioning method is not applicable for a non-perpendicular laser beam incidence, as the beam is reflected at the air-glass interface at an angle. In addition, the focal depth keeps changing when drawing a pattern at the interface through an angled surface. So a plasma locating method instead of a reflecting method was used for surface positioning. Light emission of a plasma can be observed on the monitoring CCD camera when the laser is focused on the material surface (or inside the material), but not when the focus is in air, so the material front surface can be identified this way. The surface locations (z information) from several different positions (x-y information) on a tilted surface were found in this way, allowing other positions on the surface to be determined by calculating the plane of the interface.

Welding generated by normal laser pulses and pulse trains incident at an angle of 31.7 degrees for borosilicate glass to borosilicate glass welding is shown in Fig 7.15. Compared with photo a) and b), apparently more uniform and less cracked seams could be observed from the one (Fig 7.15b) using the pulse train method.

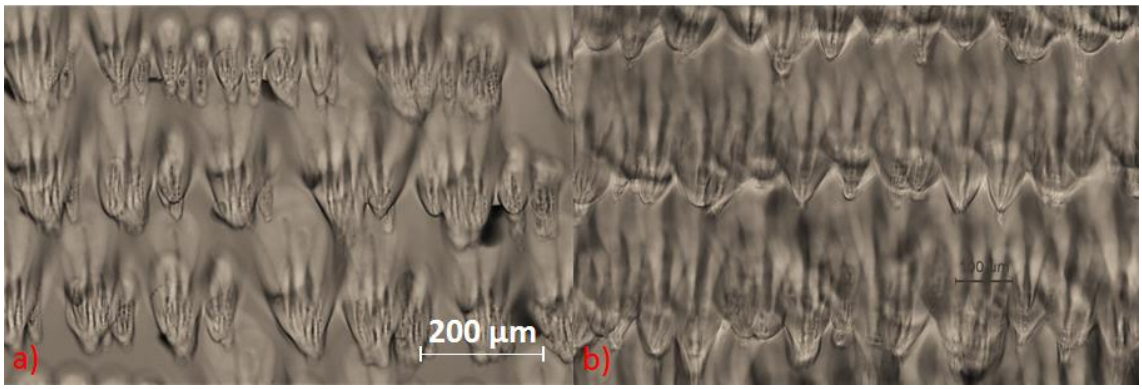

Fig 7.15 Welding an angled borosilicate glass to borosilicate glass with (a) normal laser pulses (a) and (b) with pulse trains. (Glass angle is 31.70 degree (a). normal laser pulses of laser power 16.7 W (pulse energy is 41.8 μJ), with scan speed 2 mm/s, (b). pulse trains with pulse energy 58.8 μJ, pulse train duration 3 ms, frequency 100 Hz, with scan speed 2 mm/s).

The top of the seams are blurred because the HAZ have an angle to the focused interface, in Fig 7.15 the microscope image is focused at the interface of the two

materials. The cross-section image was also obtained for a better view of the angle, as shown in Fig 7.16, massive cracks appearing in the cross-section represent higher residual stress caused by over deposition of energy in the region. The pulse train techniques in Section 6.2.2, however have the potential to eliminate this type of crack.

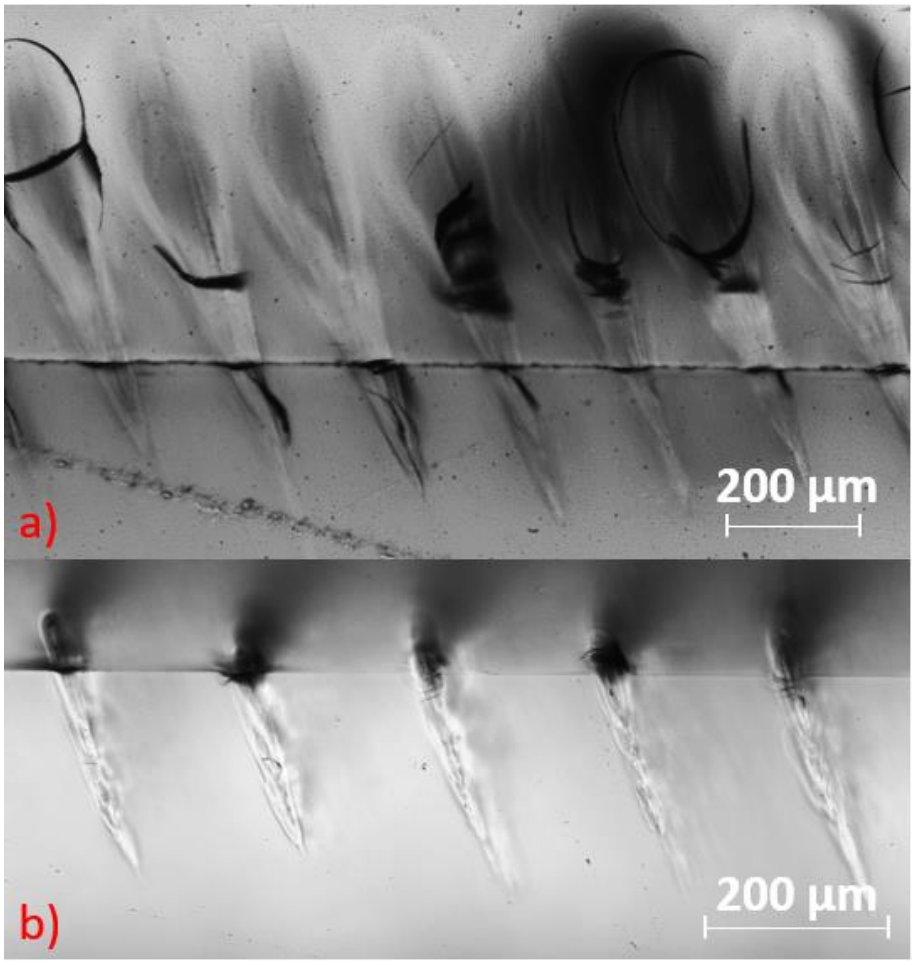

Fig 7.16 Cross-section of angled welding with laser power 21.3 W. (a). Normal laser pulses and (b). Pulse train (duration 3 ms, frequency 100 Hz) with 1 mm/s scan speed and 20 mm lens (angle of incident surface is 31.7 degree and the angle between the HAZ and interface is roughly 21.5 degree).

From the discussion above, angled welding requires more laser power and results in unstable HAZ formation which leads to high residual stress, so angled welding should be avoided if a normal incidence can be used. Alternatively, a prism compensation method can be used to provide normal incidence welding of a tilted interface (Fig 7.11a), provided that total internal reflection is not an issue. An acute angle prism was used for optical path compensation, as shown in Fig 7.17. It would be better to use an original surface of the glass part if there is a suitable surface. In this case we can just rotate the part to get perpendicular incidence (Fig 7.17a). If not, an acute angle prism

can be used to ensure that total internal reflection does not occur in the prism (see the layout in Fig 7.17b).

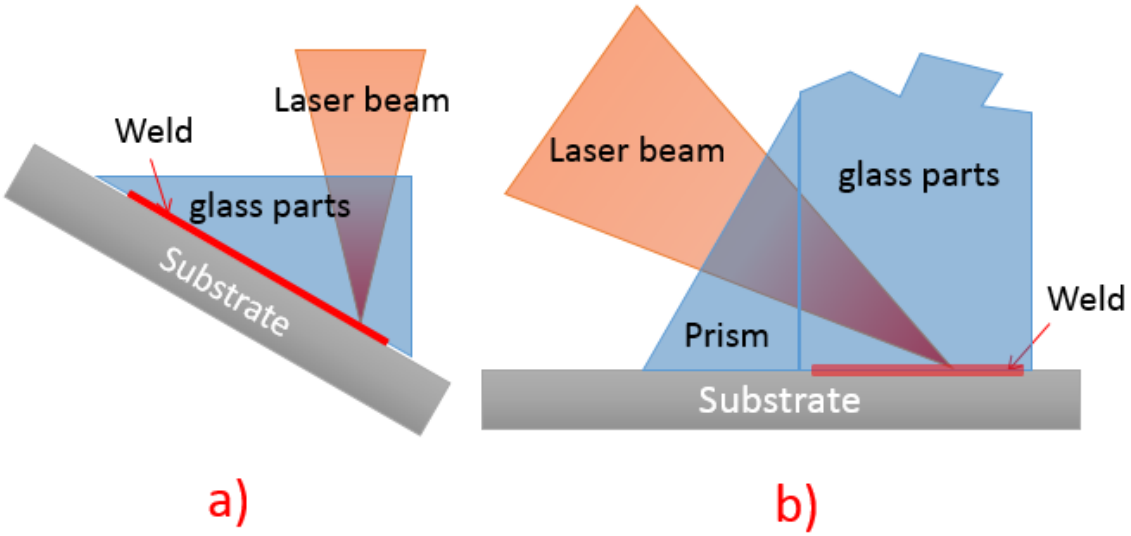

Fig 7.17 Schematics of compensation welding of angled top surface parts to provide a laser beam with normal incidence (a) presenting the part at an angle; and (b) using an acute angle prism for compensation.

7.6 Summary and Conclusion

This chapter discussed ultrafast laser welding of industrially-relevant parts with different, specific application requirements. The experiment results of large area welding, thick/thin sample welding, seam sealing, small recessed area welding and abnormal front surface welding showed a feasible way of manufacturing of industrial parts.

Firstly, based on the investigation from previous chapters, large area welding (25 mm× 25 mm) of borosilicate glass to aluminium is discussed and examples prepared. The main difficulty lies during the large area welding, more energy should be deposited at the interface, increasing the material temperatures as a whole, which will greatly increase the residual stress caused by differential thermal expansion. With a discrete welding method, the surface shear stress was effectively released, also less energy is deposited than in a continuous welding process. Another advantage of discrete welding a large area is, even if cracks appear at one or several weld units due to local surface flaws, they will not propagate to a large area as the continuous welds usually do.

Secondly the feasibility of sealing an area was demonstrated with different sealing methods. Ultrafast laser welding provides seam sealing of selective micrometre level

direct fusion bonding of a glass cover and glass/metal substrate with just a thin layer (several hundreds of micrometres). As there is no need for an intermediate layer or solder between the materials, only a simple sealing structure is required and no joining degradation problems are to be expected.

Thirdly, techniques to weld through thick glass and ultrathin glass are discussed and example samples successfully welded. There are particular issues which arise when welding either thick or ultra-thin pieces of glass to a substrate. Aberrations arise when focusing a laser beam through a thick glass piece, also focused beams may be clipped at sample edges. While deformation becomes severe for thin glass due to the clamp or shock wave during the welding process. Special clamp designs were provided to deal with the deformations and a thickness of 10 mm piece and an ultrathin piece of 0.1 mm were successfully welded to their substrates.

Fourthly, welding a glass window to a frame has been demonstrated. Through a clamp design, a 5 mm × 3 mm × 0.6 mm fused silica window was successfully welded to a recessed region of the aluminium frame (with 500 μm overlap at each side).

Finally, different welding approaches are studied for parts that do not have a glass-air interface parallel to the interface to be welded. Geometrical shape restrictions of industrial applications do not always offer normal transparent surfaces. Thus the welding has to be done by focusing the laser beam through a side face on to the interface. Welding with this method requires the laser beam to be incident on a non-perpendicular front surface or an additional prism for beam path compensation. Aberration is introduced when focusing laser beam inside material with an abnormal angle. To measure the focus laser intensity change caused by focus deformation for different angles, the breakdown threshold inside borosilicate glass was measured with different angles of glass. A rapid increase in the threshold as a function of angle can be observed. For an angle of 45 degrees even with a laser power of 23.45 W, a factor nearly 5 times higher than that at normal incidence the breakdown threshold still could not be reached. Angled welding requires more laser power and results in unstable HAZ formation which leads to high residual stress, angled welding should be avoided if possible. Hence a prism compensation method was introduced to provide normal incidence of a tilted interface during welding.

For future work more specific application requirements can be considered to build a portfolio of techniques suitable for a wide range of industrial applications.

Chapter 8 Conclusions and Outlook

Ultrafast laser welding of glass-glass and glass-opaque material has remained a fast developing area since 2005 due to the advantages of its sub-surface microwelding and ability to join highly dissimilar materials. There has been significant interest from industry for a wide range of applications including semiconductor, micro-optics, biomedical devices and the laser industry. Research in this area covers three main methods: investigation of the welding properties by altering the welding parameters; theoretical calculation and simulation; and morphology analysis, aiming at increasing the weld strength or making the welding process feasible and reliable. However, glass cracking and process stability remain key problems that prevent large scale industrial usage. A number of the underlying issues are addressed in this thesis, whilst others remain unsolved, and also new questions arise from the work. In this chapter, I review some of the key conclusions in this thesis and briefly discuss areas where further work is needed.

8.1 Summary and Conclusions

The work presented in this thesis investigates ultrafast laser welding of similar and dissimilar materials aimed at developing a feasible and reliable welding process for industrial applications. The key factors that influence ultrafast laser welding include laser parameters, material properties and surface conditions. To achieve successful and stable welds, an ultrafast laser welding system based around a Trumpf TruMicro 5x50 picosecond laser system was developed in our lab. A vast range of parameters related to welding were investigated including laser parameters such as power, pulse duration and repetition rate; optical and motion parameters such as focal length, focal position and scan speed; different materials and their surface conditions. The limits of successful welding were determined. Different welding scan strategies were proposed to constrain stresses and eliminate cracks based on the laser absorption investigations and residual stress analysis.

8.1.1 Plasma Behaviour

Theoretical analyses and pulse train investigations were carried out to investigate the plasma behaviour and beam linear and nonlinear propagation into the material. Laser absorption during the welding process can be described as a combination of a filament-like nonlinear absorption and the absorption rates were investigated for different laser

powers. Based on built models and parameter investigations, the absorption mechanisms were depicted. When an ultrashort pulse is focused inside the material, the laser intensity above the material breakdown threshold will first generate a filamental nonlinear absorption volume with the filament length dependent on the laser intensity and the focal lens. Then the nonlinearly absorbed energy locally excites plasma around this filament which absorbs the incident light and grows during the picosecond pulse duration, becoming the dominant absorption mechanism for the reminder of the pulse duration. The plasma continues to grow whilst the absorption is sufficient to sustain the plasma, which appears as a tear-drop with a shape that is dependent on the laser intensity, the focal length, and the pulse duration, and the HAZ due to the thermal diffusion creating bonds and joining the material. Experiments were carried out to verify or support those analyses. The HAZ from irradiating with only a few pulses and with limited laser power inside glass (Fig 4.4 and Fig 4.16 respectively, both of them enable nonlinear absorption while avoiding thermal accumulation for plasma absorption) were demonstrated as thin filaments compared with the tear-drop shape of the higher thermal accumulation case, as predicted in the model presented in section 4.2.1. Thermal accumulation experiments were carried out shown in section 6.2.2, the transfer from nonlinear absorption to plasma absorption can be evaluated based on the laser absorption model set up based on the HAZ generated by different number of pulses.

8.1.2 Impact of Optical Aberrations

Aberrations introduced during the welding process were discussed for a high-NA lens focusing inside a material:

Spherical aberration of the lens is common for a variety of optical systems; for a non-paraxial Gaussian beam, numerical aperture of $NA>0.16$ will bring focal spot size blur larger than the calculated focal spot size for a plano-convex spherical lens.

The aberration that occurs when a laser beam is focused through the flat surface of an optical material, with the effect cancels the spherical aberration. This type of aberration brings great influence on laser beam focusing which depends on the focus position inside glass. Simulation based on the ray optics shows that for a $NA=0.54$ lens focus 2 mm into borosilicate glass, the aberration changes the peak intensity as well as the laser energy distribution. Zemax simulation shows the outer ray diameter can reach to 90 μm at the focus inside the material.

Additional aberration is also created at angled incidence. This aberration rapidly increases with the incident angle of the focused beam. For a 20 mm lens focusing beam inside borosilicate glass with a 30 degree angle, the aberration length can be 0.76 mm. The experiment of breakdown threshold with different incident angle shows the breakdown threshold of 30 degree is 3 times larger than that of normal incidence.

The impact of these aberrations on the laser intensity distribution in the vicinity of the focus was examined using simulations. This analysis demonstrates that the deterioration of focusing increases with the amount of material focused through, and it is instructive to estimate the depth at which focusing at a given NA is no longer diffraction limited.

8.1.3 Experiment Setup and Sample Preparation

Successful welding has been achieved with a reliable laser welding system and sample preparation methods. To ensure that the laser focuses at the interface of the materials to be welded, a CCD camera telescope system was used for focus positioning inspection which can realise a ±10 μm resolution around the interface (good enough to put the HAZ at the interface as the HAZ size is 50~100 μm). A shutter inserted in the beam path synchronised with stage movement provides a flexible scan system for different inscription patterns. Ultrafast laser welding requires close contact of the material surfaces, hence a three ball bearing piston clamp rig was developed to provide highly repeatable close contact in the centre of the workpiece. A range of materials and surface preparation methods were also investigated in order to control the sample inter-surface separation for welding. The surfaces of commercial glass are usually smooth and flat enough for welding, while for most of the metal sample surfaces or industrial parts, milling, grinding, tumbling and polishing were adopted for surface smoothing and the surfaces roughness (*Ra*) were measured. Experiments demonstrated that a surface roughness (*Ra*) of less than 0.3 μm is required for a successful glass to metal weld; this is obtainable using those simple and less expensive surface preparation methods talked above for the industrial applications.

8.1.4 Parameter Investigations

Parameter investigations were carried out to work out suitable parameters for welding different materials and surface conditions. Laser parameters for ps laser, as well as fs lasers were investigated with pulse duration from 162 fs to 10 ps, and repetition rates from 100 kHz which barely provides thermal accumulation, up to 5 MHz. Successfully welds of borosilicate glass were carried out on all the ranges of parameters and

experiments indicated the HAZ decreases for the longer pulse duration, and higher repetition rate for the same average power. Different focus lenses were tested for a better understanding of HAZ generation inside materials and different scan speeds were tested both inside bulk material and for welding. For longer focus lens, the HAZ length/width ratio becomes larger and the energy density in HAZ (laser energy to generate unit HAZ volume) becomes lower. The laser power, scan speed and repetition rate are all effective ways to change the energy density absorbed along the inscription line. The results of different laser powers and scan speeds are quite straightforward: HAZ increases with laser power and decreases with scan speed. Comparing with different materials (fused silica and borosilicate glass) of different laser powers, the thermal properties of the two materials are more or less the same except the softening point and transformation temperature, which probably account for the huge HAZ width difference.

For industrial applications, it is important that the sample preparation method is straight forward and fit up easy to achieve. Conditions for a successful weld were examined to identification of welding parameters that allow tolerances to be relaxed. Parameter maps were generated to predict whether the samples can be welded given certain welding parameters. Experiments results demonstrated that a surface separation of less than 3 μm on glass-glass could be successfully welded, while for glass-metal a surface roughness (R_a) of smaller than 0.3 μm was demonstrated to be weldable.

8.1.5 Weld Strength Tests

Weld strength tests were carried out to statistically measure the weld strength characteristics with different laser parameters and scanning patterns. The strength tests showed that a large HAZ does not necessarily bring higher welding strengths. As the laser power increases, the weld strength increases until the flaws or defects become severe, the weld strength decreases again even though there is no obvious cracking (cracks appear from 2.75 W average power) under the microscope. The maximum weld strength presented in Fig 4.24 indicates the potential for optimising the laser and welding parameters. And the Weibull plot of strength tests on 4 different patterns/powers (20 samples for each pattern/sample) show the weld strength (statistical mean) are around 108.8 MPa at the optimal points (indicated in Fig 4.24), with the welding strength 96.3% of the bulk material. Comparing the bonding strength of commercial adhesives (10~25 MPa), from which one can see the potential of the ultrafast laser welding to replace glue as an industrial bonding method.

8.1.6 Welding Approaches to Minimise Stress and Related Cracking

Based on theoretical analysis, different welding patterns were designed to relax residual stress and eliminate cracks, especially for welding highly dissimilar materials. To achieve this, several methods were considered:

1) Decreasing laser power and increasing seam spacing;
2) Dual power welding;
3) Scan sequence adjustment;
4) Discrete welding (spot welding);
5) Welding with galvo-scanner;
6) Focus vibrating.

Example samples were demonstrated with all of those methods for crack reduction. For the most effective way to release residual stress, discrete welding patterns were extensively used for welding of highly dissimilar materials over a decent large area. Welding with a galvo-scanner was also introduced as an alternative method for industrial applications which provides a flexible scan pattern design and high scan speed but the disadvantages of weak welding strengths and high residual stresses also stand out due to the large laser focal spot size (long focal length to keep large scan range). Apart from reducing the residual stress introduced by the different material thermal expansion coefficients, a vibrating focus method was proposed and illustrated to expand plasma region and reduce the residual stress caused by the thermal gradient during the welding process. A TAG lens method and a vibrating motor method were used to provide the focus vibration for laser-material interaction test and welding, the results show a promising technique to ultrafast laser weld with less cracking and large effective welded area.

8.1.7 Application Examples

Example industrial parts were successfully welded for different application requirements:

1. Large area welding of glass to metal was discussed and example samples were demonstrated with a discrete welding method;

2. The feasibility of hermetic sealing was experimentally demonstrated with different sealing methods;

3. Techniques for ultrafast laser welding through thick/ultrathin pieces of glass to a substrate were discussed and example samples successfully welded;

4. A glass window and a frame have been welded to demonstrate ultrafast laser welding over a small contact area;

5. Non-perpendicular incident welding was introduced to weld those industrial parts which do not offer normal transparent top surfaces. The difference between angled incident welding and normal perpendicular welding was discussed and the main concerns during angled welding were presented.

Overall, this PhD project covers theoretical simulations, welding setup designs, parameter investigations, welding limit determinations, welding pattern designs, welding process development and industrial application considerations. Through the investigation, a range of similar material (glass to glass, sapphire to sapphire) and highly dissimilar materials (glass to sapphire, silicon, aluminium, copper, stainless steel etc.) have been successfully welded using picosecond laser pulses. Directly welding between transparent material and highly dissimilar materials, together with spatially selective welding at interface without degradation suggests the potential of ultrafast laser welding replacing traditional welding methods for industrial applications. And the strength test of the welds showed the welding strength achieved 96.4% of the breaking strength of bulk material and sustainable to the circumstance changes without cracks.

8.2 Outlook

The results presented in this thesis cover the main research areas of ultrafast laser welding of glass-glass and glass-opaque materials, and includes some important steps forward in this area. However, ultrafast lasers have been undergoing fast development in recent years, especially in terms of high power, high repetition rate femtosecond fibre lasers, which are ideal parameters for ultrafast laser welding. The vastness of this subject leaves several areas for future research to investigate.

8.2.1 Theoretical Development of Plasma Behaviour inside Material

Ultrafast laser absorption and plasma build up mechanisms need close investigation for different circumstances. The interactions of ultrafast lasers and materials have been

extensively examined since the development of ultrafast laser direct writing inside glass, but precise details of plasma build up and thermal transfer are still unclear. There are two points in particular which need to be examined:

1. How the absorption changes from nonlinear absorption to plasma based absorption and how this gradually moves to above the focus. Through there are observations on filaments when the laser power is low or only a few laser pulses, and there is a rough model for this there is still no direct evidence on how it works;

2. How previous pulses influence current laser pulse absorption. It is clear the plasma vanishes between pulses for repetition rate of hundreds of kHz or even several MHz, but the clear evidence of pulse train absorption (6.2.2.4) indicates absorption increases for the subsequent pulses, which might because of the heating of the region for a phonon assistant absorption or the residual free electron from the laser pulses directly inducing avalanche ionisation.

8.2.2 Tests on Welded Samples

From this thesis one may notice, quite a lot of welding conditions and welding methods are analysed, but a large number of tests need to be done and welds broken to determine optimum parameters. Also from an application view, many tests should be accomplished for process verification. For example:

1. **Welding strength tests:** for welding of glass with metal, and for different welding methods (pulse train welding, vibrating welding, and welding with different surface conditions);

2. **Sealing test:** how good are the hermetic bonds, and what parameters or scan strategy should be used to generate hermetic bonding to meet application requirements;

3. **Thermal test:** many methods were adopted for highly dissimilar material welding, to release both the residual stress and thermal stress. But the welds need to survive temperature changes for real applications. Thermal tests for different welding strategies and welding strength degradation (due to the cracks) also need to be investigated;

4. **Residual stress test:** the stress distribution inside bulk material and around the weld is another interesting research area. Because transparent materials are involved in ultrafast laser welding, an optical method, like birefringence, could be used.

8.2.3 Further Welding Process Development

Methods proposed and preliminarily tested in this thesis need to be extensively investigated. For example, welding with a galvo-scanner will greatly expand the usage of ultrafast laser welding in industrial applications by increasing the process speed and providing flexible welding patterns. The results presented in this thesis are limited by the available of high-NA, short focal length galvo suitable for ultrafast laser welding. Some welding processes which need to be further investigated are:

1. **Ambient temperature:** the initial temperature greatly influences laser absorption and HAZ formation; also a different initial temperature may affect the weld survival temperature range. For welding different materials, different temperatures and thermal expansions are always a great concern. A suitable heat-sink (or preheating) of one or both pieces during the welding process to compensate for mismatches in thermal expansion or contraction of the two materials to be welded is an interesting area of potential research;

2. **Polarisation:** research on the potential influence of laser polarisation for the welding with an angle during the process, and develop the potential welding process based on this;

3. **Annealing after welding**: residual stress around the welds is always a problem. This makes successfully welded samples crack or break after several days or months. An annealing process should be considered to release the stress. But at the same time, as the welds experience high power during the welding process, how high a temperature the welds can stand should be first investigated. This is also a key point for materials of different thermal expansion coefficient;

4. **Pulse train welding**: pulse train welding to generate discrete patterns for dissimilar material welding needs to be extensively investigated beyond the content of this thesis. Tailoring the thermal stress by altering both the energy and spatial distribution of the laser pulses should be analysed to determine the best distribution to minimise residual stress;

5. **Vibrating weld:** cross-section views of welds (Fig 4.15) show that in a weld a clear gap is observed between interface of the melted region (HAZ except the plasma region), which indicates weak bond or no weld at the region, however, at the plasma region it is surely welded. Welding while vibrating the focus will clearly enlarge the plasma region so as to increase the material exchange. In this thesis the feasibility and possible advantages of doing so are experimentally verified, but systemic experiments and tests should be done for real applications.

Appendix – Weibull distribution

For brittle materials, the maximum stress that a sample can be measured to withstand before failure may vary from specimen to specimen, even under identical testing conditions. This is related to the distribution of physical flaws present in the surface or body of the brittle samples, since the failure processes originate at these weak points. When flaws are consistent and evenly distributed, samples will behave more uniformly than when flaws are clustered inconsistently. This must be taken into account when describing the strength of the material, so strength is best represented as a distribution of values rather than as one specific value. In our case, a Weibull plot is used to determine the probability of survive for a given stress, the accumulative distribution function for the Weibull distribution [159] is:

$$\mathrm{F}(x;k,\lambda) = e^{-\left(x/\lambda\right)^{k}} \qquad \text{A.1}$$

where $k > 0$ is the shape parameter and $\lambda > 0$ is the scale parameter of the distribution and the mean value of the distribution is $\lambda\Gamma(1+1/k)$. The shape parameter k of distribution of strengths is known as the Weibull modulus and is used to describe the variability in the measured material strength of brittle materials. If the measurements show little variation from sample to sample, the calculated Weibull modulus will be high and a single strength value would serve as a good description of the sample-to-sample performance.

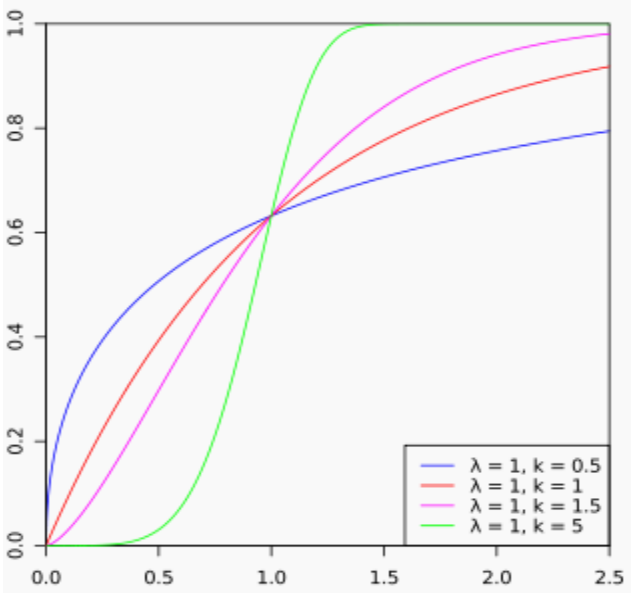

Fig A.1 Accumulated distribution function with different Weibull modulus k.

References

[1] J. Meijer, "Laser beam machining (LBM), state of the art and new opportunities," *J. Mater. Process. Technol.*, vol. 149, no. 1–3, pp. 2–17, 2004.

[2] T. Tamaki, W. Watanabe, and K. Itoh, "Laser micro-welding of transparent materials by a localized heat accumulation effect using a femtosecond fiber laser at 1558 nm," *Opt. Express*, vol. 14, no. 22, p. 10460, 2006.

[3] Y. Ozeki, T. Inoue, T. Tamaki, H. Yamaguchi, S. Onda, W. Watanabe, T. Sano, S. Nishiuchi, A. Hirose, and K. Itoh, "Direct Welding between Copper and Glass Substrates with Femtosecond Laser Pulses," *Appl. Phys. Express*, vol. 1, no. 8, p. 082601, 2008.

[4] S. Richter, S. Nolte, and A. Tünnermann, "Ultrashort Pulse Laser Welding - A New Approach for High- Stability Bonding of Different Glasses," *Phys. Procedia*, vol. 39, pp. 556–562, 2012.

[5] A. Horn, I. Mingaeev, A. Werth, and M. Kachel, "Joining of thin glass with semiconductors by ultra-fast high-repetition laser welding," *Proc. SPIE*, vol. 6880, p. 68800A–68800A–5, 2008.

[6] B. Goss, "Bonding glass and other substrates with UV curing adhesives," *Int. J. Adhes. Adhes.*, vol. 22, no. 5, pp. 405–408, 2002.

[7] A. Utsumi, T. Ooie, T. Yano, and M. Katsumura, "Direct Bonding of Glass and Metal Using Short Pulsed Laser," *JLMN*, vol. 2, no. 2, pp. 2–5, 2007.

[8] W. Watanabe, S. Onda, T. Tamaki, K. Itoh, and J. Nishii, "Space-selective laser joining of dissimilar transparent materials using femtosecond laser pulses," *Appl. Phys. Lett.*, vol. 89, no. 2, p. 021106, 2006.

[9] W. M. Steen and M. J., *Laser Material Processing*. 2010: Springer-Verlag London Limited.

[10] M. Shimizu, M. Sakakura, M. Ohnishi, Y. Shimotsuma, T. Nakaya, K. Miura, and K. Hirao, "Mechanism of heat-modification inside a glass after irradiation with high-repetition rate femtosecond laser pulses," *J. Appl. Phys.*, vol. 108, no. 7, pp. 1–10, 2010.

[11] R. R. Gattass and E. Mazur, "Femtosecond laser micromachining in transparent materials," *Nat. Photonics*, vol. 2, no. 4, pp. 219–225, 2008.

[12] R. W. Boyd, *Nonlinear Optics*. 2008: Academic Press, 3rd edition.

[13] T. Brabec and F. Krausz, "Intense few-cycle laser fields: Frontiers of nonlinear optics," *Rev. Mod. Phys.*, vol. 72, no. 2, pp. 545–591, 2000.

[14] C. B. Schaffer, A. Brodeur, and E. Mazur, “Laser-induced breakdown and damage in bulk transparent materials induced by tightly focused femtosecond laser pulses,” *Meas. Sci. Technol.*, vol. 12, no. 11, pp. 1784–1794, 2001.

[15] D. Du, X. Liu, G. Korn, J. Squier, and G. Mourou, “Laser-induced breakdown by impact ionization in SiO2 with pulse widths from 7 ns to 150 fs,” *Appl. Phys. Lett.*, vol. 64, no. 23, pp. 3071–3073, 1994.

[16] P. P. Pronko, S. K. Dutta, J. Squier, J. V. Rudd, D. Du, and G. Mourou, “Machining of sub-micron holes using a femtosecond laser at 800 nm,” *Opt. Commun.*, vol. 114, no. 1–2, pp. 106–110, 1995.

[17] S. Darvishi, T. Cubaud, and J. P. Longtin, “Ultrafast laser machining of tapered microchannels in glass and PDMS,” *Opt. Lasers Eng.*, vol. 50, no. 2, pp. 210–214, 2012.

[18] Y. Yashkir and Q. Liu, “Experimental and theoretical study of the laser micro- machining of glass using a high-repetition-rate ultrafast laser,” in *Proceedings of SPIE*, 2006, vol. 6190, no. 2006, p. 61900V–61900V–10.

[19] J. Sun, J. P. Longtin, and P. M. Norris, “Ultrafast laser micromachining of silica aerogels,” *J. Non. Cryst. Solids*, vol. 281, no. 1–3, pp. 39–47, 2001.

[20] C. Corbari, A. Champion, M. Gecevičius, M. Beresna, Y. Bellouard, and P. G. Kazansky, “Femtosecond versus picosecond laser machining of nano-gratings and micro-channels in silica glass,” *Opt. Express*, vol. 21, no. 4, p. 3946, 2013.

[21] Y. Liu, L. J. Pyrak-Nolte, and D. Nolte, “Toward 3D microfluidic structures fabricated with two-photon laser machining,” in *Conference on Lasers and Electro-Optics, 2007, CLEO 2007*, 2007.

[22] D. Breitling, A. Ruf, and F. Dausinger, “Fundamental aspects in machining of metals with short and ultrashort laser pulses,” *Phot. Process. Microelectron. Photonics III*, vol. 5339, pp. 49–63, 2004.

[23] P. Simon and J. Ihlemann, “Machining of submicron structures on metals and semiconductors by ultrashort UV-laser pulses,” *Appl. Phys. a-Materials Sci. Process.*, vol. 63, no. 5, pp. 505–508, 1996.

[24] M. D. Perry, B. C. Stuart, P. S. Banks, M. D. Feit, V. Yanovsky, and a. M. Rubenchik, “Ultrashort-pulse laser machining of dielectric materials,” *J. Appl. Phys.*, vol. 85, no. 9, p. 6803, 1999.

[25] H. Varel, D. Ashkenasi, A. Rosenfeld, M. Wähmer, and E. E. B. Campbell, “Micromachining of quartz with ultrashort laser pulses,” *Appl. Phys. A Mater. Sci. Process.*, vol. 65, pp. 367–373, 1997.

[26] K. Sugioka, J. Xu, D. Wu, Y. Hanada, and Z. Wang, “Femtosecond

laser 3D micromachining: a powerful tool for the fabrication of microfluidic, optofluidic, and electrofluidic devices based on glass," *Lab Chip*, vol. 14, no. 18, pp. 3447–58, 2014.

[27] B. Xu, X. Y. Wu, S. Q. Ling, F. Luo, C. L. Du, and X. Q. Sun, "Fabrication of 3D metal micro-mold based on femtosecond laser cutting and micro-electric resistance slip welding," *Int. J. Adv. Manuf. Technol.*, vol. 66, no. 5–8, pp. 601–609, 2013.

[28] T. Shih, M. T. Winkler, T. Voss, and E. Mazur, "Dielectric function dynamics during femtosecond laser excitation of bulk ZnO," *Appl. Phys. A Mater. Sci. Process.*, vol. 96, no. 2, pp. 363–367, 2009.

[29] K. M. Davis, K. Miura, N. Sugimoto, and K. Hirao, "Writing waveguides in glass with a femtosecond laser," *Opt. Lett.*, vol. 21, no. 21, p. 1729, 1996.

[30] Y. Liao, Y. Cheng, C. Liu, J. Song, F. He, Y. Shen, D. Chen, Z. Xu, Z. Fan, X. Wei, K. Sugioka, and K. Midorikawa, "Direct laser writing of sub-50 nm nanofluidic channels buried in glass for three-dimensional micro-nanofluidic integration.," *Lab Chip*, vol. 13, no. 8, pp. 1626–31, 2013.

[31] W. Kautek, J. Krüger, M. Lenzner, S. Sartania, C. Spielmann, and F. Krausz, "Laser ablation of dielectrics with pulse durations between 20 fs and 3 ps," *Appl. Phys. Lett.*, vol. 69, no. 21, p. 3146, 1996.

[32] B. Stuart, M. Feit, S. Herman, a. Rubenchik, B. Shore, and M. Perry, "Nanosecond-to-femtosecond laser-induced breakdown in dielectrics," *Phys. Rev. B*, vol. 53, no. 4, pp. 1749–1761, 1996.

[33] M. Hashida, A. F. Semerok, O. Gobert, G. Petite, Y. Izawa, and J. F. Wagner, "Ablation threshold dependence on pulse duration for copper," in *Applied Surface Science*, 2002, vol. 197–198, pp. 862–867.

[34] N. Bloembergen, "Laser Induced Electric Breakdown in Solids," *IEEE J. Quantum Electron.*, vol. 10, no. 3, pp. 375–386, 1974.

[35] I. M. Burakov, N. M. Bulgakova, R. Stoian, A. Mermillod-Blondin, E. Audouard, A. Rosenfeld, A. Husakou, and I. V. Hertel, "Spatial distribution of refractive index variations induced in bulk fused silica by single ultrashort and short laser pulses," *J. Appl. Phys.*, vol. 101, no. 4, 2007.

[36] E. G. Gamaly, S. Juodkazis, K. Nishimura, H. Misawa, B. Luther-Davies, L. Hallo, P. Nicolai, and V. T. Tikhonchuk, "Laser-matter interaction in the bulk of a transparent solid: Confined microexplosion and void formation," *Phys. Rev. B*, vol. 73, no. 21, p. 214101, 2006.

[37] K. M. Davis, K. Miura, N. Sugimoto, and K. Hirao, "Writing

waveguides in glass with a femtosecond laser," *Opt. Lett.*, vol. 21, no. 21, p. 1729, 1996.

[38] K. Miura, J. Qiu, H. Inouye, T. Mitsuyu, and K. Hirao, "Photowritten optical waveguides in various glasses with ultrashort pulse laser," *Appl. Phys. Lett.*, vol. 71, no. 23, pp. 3329–3331, 1997.

[39] A. M. Streltsov and N. F. Borrelli, "Fabrication and analysis of a directional coupler written in glass by nanojoule femtosecond laser pulses," *Opt. Lett.*, vol. 26, no. 1, pp. 42–43, 2001.

[40] C. B. Schaffer, A. Brodeur, J. F. Garci'a, and E. Mazur, "Micromachining bulk glass by use of femtosecond laser pulses with nanojoule energy," *Opt. Lett.*, vol. 26, no. 2, pp. 93–95, 2001.

[41] C. Florea and K. A. Winick, "Fabrication and characterization of photonic devices directly written in glass using femtosecond laser pulses," *J. Light. Technol.*, vol. 21, no. 1, pp. 246–253, 2003.

[42] V. R. Bhardwaj, E. Simova, P. B. Corkum, D. M. Rayner, C. Hnatovsky, R. S. Taylor, B. Schreder, M. Kluge, and J. Zimmer, "Femtosecond laser-induced refractive index modification in multicomponent glasses," *J. Appl. Phys.*, vol. 97, no. 8, 2005.

[43] M. Will, S. Nolte, B. N. Chichkov, and A. Tunnermann, "Optical properties of waveguides fabricated in fused silica by femtosecond laser pulses," *Appl. Opt.*, vol. 41, no. 21, pp. 4360–4364, 2002.

[44] R. Osellame, N. Chiodo, V. Maselli, A. Yin, M. Zavelani-Rossi, G. Cerullo, P. Laporta, L. Aiello, S. De Nicola, P. Ferraro, A. Finizio, and G. Pierattini, "Optical properties of waveguides written by a 26 MHz stretched cavity Ti : sapphire femtosecond oscillator," *Opt. Express*, vol. 13, no. 2, pp. 612–620, 2005.

[45] S. M. Eaton, H. Zhang, M. L. Ng, J. Li, W.-J. Chen, S. Ho, and P. R. Herman, "Transition from thermal diffusion to heat accumulation in high repetition rate femtosecond laser writing of buried optical waveguides.," *Opt. Express*, vol. 16, no. 13, pp. 9443–9458, 2008.

[46] L. Tong, R. R. Gattass, I. Maxwell, J. B. Ashcom, and E. Mazur, "Optical loss measurements in femtosecond laser written waveguides in glass," *Opt. Commun.*, vol. 259, no. 2, pp. 626–630, 2006.

[47] S. Nolte, M. Will, J. Burghoff, and A. Tuennermann, "Femtosecond waveguide writing: A new avenue to three-dimensional integrated optics," *Appl. Phys. A Mater. Sci. Process.*, vol. 77, no. 1, pp. 109–111, 2003.

[48] M. Kamata, M. Obara, R. R. Gattass, L. R. Cerami, and E. Mazur, "Optical vibration sensor fabricated by femtosecond laser micromachining," *Appl. Phys. Lett.*, vol. 87, no. 5, 2005.

[49] A. Radke, T. Gissibl, T. Klotzbücher, P. V. Braun, and H. Giessen, “Three-dimensional bichiral plasmonic crystals fabricated by direct laser writing and electroless silver plating,” *Adv. Mater.*, vol. 23, no. 27, pp. 3018–3021, 2011.

[50] N. Sherwood-Droz and M. Lipson, “Scalable 3D dense integration of photonics on bulk silicon.,” *Opt. Express*, vol. 19, no. 18, pp. 17758–65, 2011.

[51] a M. Kowalevicz, V. Sharma, E. P. Ippen, J. G. Fujimoto, and K. Minoshima, “Three-dimensional photonic devices fabricated in glass by use of a femtosecond laser oscillator.,” *Opt. Lett.*, vol. 30, no. 9, pp. 1060–1062, 2005.

[52] G. D. Marshall, M. Ams, and M. J. Withford, “Direct laser written waveguide-Bragg gratings in bulk fused silica,” *Opt. Lett.*, vol. 31, no. 18, p. 2690, 2006.

[53] M. Mikutis, T. Kudrius, G. Slekys, D. Paipulas, and S. Juodkazis, “High 90% efficiency Bragg gratings formed in fused silica by femtosecond Gauss-Bessel laser beams,” *Opt. Mater. Express*, vol. 3, no. 11, pp. 1862–1871, 2013.

[54] B. Li, L. Jiang, S. Wang, H. L. Tsai, and H. Xiao, “Femtosecond laser fabrication of long period fiber gratings and applications in refractive index sensing,” *Opt. Laser Technol.*, vol. 43, no. 8, pp. 1420–1423, 2011.

[55] X. Sun, P. Huang, J. Zhao, L. Wei, N. Zhang, D. Kuang, and X. Zhu, “Characteristic control of long period fiber grating (LPFG) fabricated by infrared femtosecond laser,” *Front. Optoelectron.*, vol. 5, no. 3, pp. 334–340, 2012.

[56] A. Martinez, M. Dubov, I. Khrushchev, and I. Bennion, “Direct writing of fibre Bragg gratings by femtosecond laser,” *Electron. Lett.*, vol. 40, no. 19, p. 1170, 2004.

[57] S. Kroesen, W. Horn, J. Imbrock, and C. Denz, “Electro-optical tunable waveguide embedded multiscan Bragg gratings in lithium niobate by direct femtosecond laser writing.,” *Opt. Express*, vol. 22, no. 19, pp. 23339–48, 2014.

[58] G. D. Marshall, A. Politi, J. C. F. Matthews, P. Dekker, M. Ams, M. J. Withford, and J. L. O’Brien, “Laser written waveguide photonic quantum circuits.,” *Opt. Express*, vol. 17, no. 15, pp. 12546–12554, 2009.

[59] A. Crespi, R. Osellame, R. Ramponi, D. J. Brod, E. F. Galvão, N. Spagnolo, C. Vitelli, E. Maiorino, P. Mataloni, and F. Sciarrino, “Integrated multimode interferometers with arbitrary designs for photonic boson sampling,” *Nat. Photonics*, vol. 7, no. 7, pp. 545–549,

2013.

[60] K. Sugioka and Y. Cheng, “Ultrafast lasers—reliable tools for advanced materials processing,” *Light Sci. Appl.*, vol. 3, no. 4, p. e149, 2014.

[61] A. Marcinkevičius, S. Juodkazis, M. Watanabe, M. Miwa, S. Matsuo, H. Misawa, and J. Nishii, “Femtosecond laser-assisted three-dimensional microfabrication in silica,” *Opt. Lett.*, vol. 26, no. 5, pp. 277–279, 2001.

[62] M. Masuda, K. Sugioka, Y. Cheng, N. Aoki, M. Kawachi, K. Shihoyama, K. Toyoda, H. Helvajian, and K. Midorikawa, “3-D microstructuring inside photosensitive glass by femtosecond laser excitation,” *Appl. Phys. A Mater. Sci. Process.*, vol. 76, no. 5, pp. 857–860, 2003.

[63] Y. Li, K. Itoh, W. Watanabe, K. Yamada, D. Kuroda, J. Nishii, and Y. Jiang, “Three-dimensional hole drilling of silica glass from the rear surface with femtosecond laser pulses,” *Opt. Lett.*, vol. 26, no. 23, pp. 1912–1914, 2001.

[64] Y. Liao, Y. Ju, L. Zhang, F. He, Q. Zhang, Y. Shen, D. Chen, Y. Cheng, Z. Xu, K. Sugioka, and K. Midorikawa, “Three-dimensional microfluidic channel with arbitrary length and configuration fabricated inside glass by femtosecond laser direct writing.,” *Opt. Lett.*, vol. 35, no. 19, pp. 3225–3227, 2010.

[65] Y. Liao, J. Song, E. Li, Y. Luo, Y. Shen, D. Chen, Y. Cheng, Z. Xu, K. Sugioka, and K. Midorikawa, “Rapid prototyping of three-dimensional microfluidic mixers in glass by femtosecond laser direct writing.,” *Lab Chip*, vol. 12, no. 4, pp. 746–9, 2012.

[66] Y. Liao, Y. Shen, L. Qiao, D. Chen, Y. Cheng, K. Sugioka, and K. Midorikawa, “Femtosecond laser nanostructuring in porous glass with sub-50 nm feature sizes.,” *Opt. Lett.*, vol. 38, no. 2, pp. 187–9, 2013.

[67] Y. Liao, Y. Cheng, C. Liu, J. Song, F. He, Y. Shen, D. Chen, Z. Xu, Z. Fan, X. Wei, K. Sugioka, and K. Midorikawa, “Direct laser writing of sub-50 nm nanofluidic channels buried in glass for three-dimensional micro-nanofluidic integration.,” *Lab Chip*, vol. 13, no. 8, pp. 1626–31, 2013.

[68] B. N. Chichkov, C. Momma, S. Nolte, F. von Alvensleben, and A. Tünnermann, “Femtosecond, picosecond and nanosecond laser ablation of solids,” *Appl. Phys. A Mater. Sci. Process.*, vol. 63, no. 2, pp. 109–115, 1996.

[69] A. Y. Vorobyev and C. Guo, “Femtosecond laser nanostructuring of metals.,” *Opt. Express*, vol. 14, no. 6, pp. 2164–2169, 2006.

[70] A. Y. Vorobyev and C. Guo, “Femtosecond laser structuring of titanium implants,” *Appl. Surf. Sci.*, vol. 253, no. 17, pp. 7272–7280, 2007.

[71] E. Stratakis, V. Zorba, M. Barberoglou, C. Fotakis, and G. A. Shafeev, “Femtosecond laser writing of nanostructures on bulk Al via its ablation in air and liquids,” *Appl. Surf. Sci.*, vol. 255, no. 10, pp. 5346–5350, 2009.

[72] A. Y. Vorobyev and C. Guo, “Direct femtosecond laser surface nano/microstructuring and its applications,” *Laser and Photonics Reviews*, vol. 7, no. 3. pp. 385–407, 2013.

[73] C. a Zuhlke, T. P. Anderson, and D. R. Alexander, “Formation of multiscale surface structures on nickel via above surface growth and below surface growth mechanisms using femtosecond laser pulses,” *Opt. Express*, vol. 21, no. 7, pp. 8460–8473, 2013.

[74] G. D. Tsibidis, M. Barberoglou, P. A. Loukakos, E. Stratakis, and C. Fotakis, “Dynamics of ripple formation on silicon surfaces by ultrashort laser pulses in subablation conditions,” *Phys. Rev. B - Condens. Matter Mater. Phys.*, vol. 86, no. 11, 2012.

[75] M. Birnbaum, “Semiconductor surface damage produced by ruby lasers.,” *J. Appl. Phys.*, vol. 36, pp. 3688–3689, 1965.

[76] D. C. Emmony, R. P. Howson, and L. J. Willis, “Laser mirror damage in germanium at 10.6 μm,” *Appl. Phys. Lett.*, vol. 23, no. 11, pp. 598–600, 1973.

[77] A. Y. Vorobyev and C. Guo, “Metal colorization with femtosecond laser pulses (a),” *SPIE*, vol. 7005, no. Lambda 900, p. 70051T–70051T–8, 2008.

[78] J. Bonse, J. Krüger, S. Höhm, and a. Rosenfeld, “Femtosecond laser-induced periodic surface structures,” *J. Laser Appl.*, vol. 24, no. 4, p. 042006, 2012.

[79] P. M. Fauchet and A. E. Siegman, “Surface ripples on silicon and gallium arsenide under picosecond laser illumination,” *Appl. Phys. Lett.*, vol. 40, no. 9, pp. 824–826, 1982.

[80] S. Sakabe, M. Hashida, S. Tokita, S. Namba, and K. Okamuro, “Mechanism for self-formation of periodic grating structures on a metal surface by a femtosecond laser pulse,” *Phys. Rev. B - Condens. Matter Mater. Phys.*, vol. 79, no. 3, 2009.

[81] J. Reif, F. Costache, M. Henyk, and S. V. Pandelov, “Ripples revisited: Non-classical morphology at the bottom of femtosecond laser ablation craters in transparent dielectrics,” in *Applied Surface Science*, 2002, vol. 197–198, pp. 891–895.

[82] A. Borowiec and H. K. Haugen, “Subwavelength ripple formation on the surfaces of compound semiconductors irradiated with femtosecond laser pulses,” *Appl. Phys. Lett.*, vol. 82, no. 25, pp. 4462–4464, 2003.

[83] C. Wang, H. Huo, M. Johnson, M. Shen, and E. Mazur, “The thresholds of surface nano-/micro-morphology modifications with femtosecond laser pulse irradiations.,” *Nanotechnology*, vol. 21, no. 7, p. 75304, 2010.

[84] V. R. Bhardwaj, E. Simova, P. P. Rajeev, C. Hnatovsky, R. S. Taylor, D. M. Rayner, and P. B. Corkum, “Optically produced arrays of planar nanostructures inside fused silica,” *Phys. Rev. Lett.*, vol. 96, no. 5, 2006.

[85] G. Miyaji and K. Miyazaki, “Origin of periodicity in nanostructuring on thin film surfaces ablated with femtosecond laser pulses.,” *Opt. Express*, vol. 16, no. 20, pp. 16265–16271, 2008.

[86] T. H. Her, R. J. Finlay, C. Wu, S. Deliwala, and E. Mazur, “Microstructuring of silicon with femtosecond laser pulses,” *Appl. Phys. Lett.*, vol. 73, no. 12, pp. 1673–1675, 1998.

[87] L. Rayleigh, “A Study of Glass Surfaces in Optical Contact,” *Proc. R. Soc. A Math. Phys. Eng. Sci.*, vol. 156, no. 888, pp. 326–349, 1936.

[88] F. Niklaus, G. Stemme, J. Q. Lu, and R. J. Gutmann, “Adhesive wafer bonding,” *Journal of Applied Physics*, vol. 99, no. 3. 2006.

[89] Y. S. Choi, J. S. Park, H. D. Park, Y. H. Song, J. S. Jung, and S. G. Kang, “Effects of temperatures on microstructures and bonding strengths of Si-Si bonding using bisbenzocyclobutene,” in *Sensors and Actuators, A: Physical*, 2003, vol. 108, no. 1–3, pp. 201–205.

[90] Y. K. Kim, E. K. Kim, S. W. Kim, and B. K. Ju, “Low temperature epoxy bonding for wafer level MEMS packaging,” *Sensors Actuators, A Phys.*, vol. 143, no. 2, pp. 323–328, 2008.

[91] F. Niklaus, P. Enoksson, E. Kälvesten, and G. Stemme, “Low-temperature full wafer adhesive bonding,” *J. Micromechanics Microengineering*, vol. 11, no. 2, pp. 100–107, 2001.

[92] J. Oberhammer, F. Niklaus, and G. Stemme, “Sealing of adhesive bonded devices on wafer level,” in *Sensors and Actuators, A: Physical*, 2004, vol. 110, no. 1–3, pp. 407–412.

[93] Y. C. Lin, M. Baum, M. Haubold, J. Fromel, M. Wiemer, T. Gessner, and M. Esashi, “Development and evaluation of AuSi eutectic wafer bonding,” in *TRANSDUCERS 2009 - 15th International Conference on Solid-State Sensors, Actuators and Microsystems*, 2009, pp. 244–247.

[94] R. F. Wolffenbuttel and K. D. Wise, “Low-temperature silicon wafer-to-wafer bonding using gold at eutectic temperature,” *Sensors Actuators A. Phys.*, vol. 43, no. 1–3, pp. 223–229, 1994.

[95] A. W. Y. Tan and F. E. H. Tay, “Localized laser assisted eutectic bonding of quartz and silicon by Nd:YAG pulsed-laser,” *Sensors Actuators, A Phys.*, vol. 120, no. 2, pp. 550–561, 2005.

[96] P. Elenius and L. Levine, “Comparing Flip-Chip and Wire-Bond Interconnection Technologies,” *Chip Scale Review*, 2000. [Online]. Available: http://processsolutionsconsulting.com/pdf/Flip_Bump/csr-7-00.pdf.

[97] D. Stavrov and H. E. N. Bersee, “Resistance welding of thermoplastic composites-an overview,” *Compos. Part A Appl. Sci. Manuf.*, vol. 36, no. 1, pp. 39–54, 2005.

[98] S. Aslanlar, A. Ogur, U. Ozsarac, E. Ilhan, and Z. Demir, “Effect of welding current on mechanical properties of galvanized chromided steel sheets in electrical resistance spot welding,” *Mater. Des.*, vol. 28, no. 1, pp. 2–7, 2007.

[99] G. Wallis and D. I. Pomerantz, “Field assisted glass-metal sealing,” *J. Appl. Phys.*, vol. 40, no. 10, pp. 3946–3949, 1969.

[100] T. M. H. Lee, I. M. Hsing, and C. Y. N. Liaw, “An improved anodic bending process using pulsed voltage technique,” *J. Microelectromechanical Syst.*, vol. 9, no. 4, pp. 469–473, 2000.

[101] T. Rogers and J. Kowal, “Selection of glass, anodic bonding conditions and material compatibility for silicon-glass capacitive sensors,” *Sensors Actuators A Phys.*, vol. 46, no. 1–3, pp. 113–120, 1995.

[102] J. . Lancaster, “The physics of welding,” *Phys. Technol.*, vol. 15, no. 2, pp. 73–79, 1984.

[103] D. Grewell and A. Benatar, “Welding of plastics: Fundamentals and new developments,” in *International Polymer Processing*, 2007, vol. 22, no. 1, pp. 43–60.

[104] Michael J Troughton, “Friction Stir Welding,” *Weld. J.*, vol. 8, no. 6, pp. 131–134, 2009.

[105] R. S. Mishra and Z. Y. Ma, “Friction stir welding and processing,” *Materials Science and Engineering R: Reports*, vol. 50, no. 1–2. 2005.

[106] X. He, F. Gu, and A. Ball, “A review of numerical analysis of friction stir welding,” *Prog. Mater. Sci.*, vol. 65, pp. 1–66, 2014.

[107] W. Callister and D. Rethwisch, *Materials science and engineering: an introduction*. 2007: John Wiley & Sons.

[108] S. Fukumoto, A. Hirose, and K. F. Kobayashi, “Application of Laser-Beam Welding to Joining of Continuous Fiber-Reinforced Composite to Metal,” *Mater. Sci. Technol.*, vol. 9, pp. 264–271, 1993.

[109] L. Quintino, P. Vilaca, R. Rodrigues, and L. Bordalo, “Laser beam welding of automobile hinges,” *Weld. J.*, vol. 80, no. 11, p. 261s–267s, 2001.

[110] J. Zhou and H. L. Tsai, *Handbook of Laser Welding Technologies*. 2013: Woodhead Publishing Limited.

[111] W. M. Steen, “Arc augmented laser processing of materials,” *J. Appl. Phys.*, vol. 51, no. 11, pp. 5636–5641, 1980.

[112] M. Sieben and F. Brunnecker, “Laser-hybrid welding, an innovative technology to join automotive body parts,” in *Physics Procedia*, 2010, vol. 5, no. PART 2, pp. 61–68.

[113] G. Turichin, E. Valdaytseva, I. Tzibulsky, A. Lopota, and O. Velichko, “Simulation and technology of hybrid welding of thick steel parts with high power fiber laser,” in *Physics Procedia*, 2011, vol. 12, no. PART 1, pp. 646–655.

[114] J. Dutta Majumdar and I. Manna, “Laser material processing,” *Int. Mater. Rev.*, vol. 56, pp. 341–388, 2011.

[115] E. Schubert, M. Klassen, I. Zerner, C. Walz, and G. Sepold, “Light-weight structures produced by laser beam joining for future applications in automobile and aerospace industry,” *J. Mater. Process. Technol.*, vol. 115, no. 1, pp. 2–8, 2001.

[116] K. Itoh and T. Tamaki, “Ultrafast laser microwelding for transparent and heterogeneous materials,” *Proc. SPIE*, vol. 6881, p. 68810V–68810V–9, 2008.

[117] I. Miyamoto, “Local Melting of Glass Material and Its Application to Direct Fusion Welding by Ps-laser Pulses,” *J. Laser Micro/Nanoengineering*, vol. 2, no. 1, pp. 7–14, 2007.

[118] S. Richter, F. Zimmermann, S. Döring, a. Tünnermann, and S. Nolte, “Ultrashort high repetition rate exposure of dielectric materials: Laser bonding of glasses analyzed by micro-Raman spectroscopy,” *Appl. Phys. A Mater. Sci. Process.*, vol. 110, pp. 9–15, 2013.

[119] D. Hélie, M. Bégin, F. Lacroix, and R. Vallée, “Reinforced direct bonding of optical materials by femtosecond laser welding,” *Appl. Opt.*, vol. 51, no. 12, p. 2098, 2012.

[120] T. Tamaki, W. Watanabe, J. Nishii, and K. Itoh, “Welding of Transparent Materials Using Femtosecond Laser Pulses,” *Jpn. J. Appl. Phys.*, vol. 44, no. No. 22, pp. L687–L689, 2005.

[121] Y. P. Raĭzer, “Breakdown and Heating of Gases Under the Influence

of a Laser Beam," *Sov. Phys. Uspekhi*, vol. 8, pp. 650–673, 1966.

[122] L. Jiang and H.-L. Tsai, "Energy Transport and Nanostructuring of Dielectrics by Femtosecond Laser Pulse Trains," *J. Heat Transfer*, vol. 128, no. 9, p. 926, 2006.

[123] J. Cheng, C. S. Liu, S. Shang, D. Liu, W. Perrie, G. Dearden, and K. Watkins, "A review of ultrafast laser materials micromachining," *Opt. Laser Technol.*, vol. 46, no. 1, pp. 88–102, 2013.

[124] I. Miyamoto, K. Cvecek, Y. Okamoto, and M. Schmidt, "Novel fusion welding technology of glass using ultrashort pulse lasers," *Phys. Procedia*, vol. 5, pp. 483–493, 2010.

[125] S. Richter, S. Döring, A. Tünnermann, and S. Nolte, "Bonding of glass with femtosecond laser pulses at high repetition rates," *Appl. Phys. A Mater. Sci. Process.*, vol. 103, pp. 257–261, 2011.

[126] L. Hallo, C. Mézel, A. Bourgeade, D. Hébert, E. G. Gamaly, and S. Juodkazis, "Laser-Matter Interaction in Transparent Materials : Confined Micro-explosion and Jet Formation," *Extrem. Photonics Appl.*, pp. 121–146, 2010.

[127] L. Cerami, E. Mazur, S. Nolte, and C. B. Schaffer, "Femtosecond Laser Micromachining," in *Ultrafast Nonlinear Optics*, 2013, pp. 287–321.

[128] K. Cvecek, I. Alexeev, I. Miyamoto, and M. Schmidt, "Defect formation in glass welding by means of ultra short laser pulses," *Phys. Procedia*, vol. 5, pp. 495–502, 2010.

[129] P. Kongsuwan, G. Satoh, and Y. L. Yao, "Transmission Welding of Glass by Femtosecond Laser: Mechanism and Fracture Strength," *J. Manuf. Sci. Eng.*, vol. 134, no. February, p. 011004, 2012.

[130] M. Born and E. Wolf, "Principles of optics," *Principles of Optics Electromagnetic Theory of Propagation INterference and Diffraction of Light 2nd edition by Max Born Emil Wolf New York NY Pergamon Press 1964*. pp. 1–952, 1999.

[131] H. Haus, *Waves and Fields in Optoelectronics*. 1985: Prentice Hall.

[132] Z. Ulanowski and I. K. Ludlow, "Scalar field of nonparaxial Gaussian beams.," *Opt. Lett.*, vol. 25, no. 24, pp. 1792–4, 2000.

[133] J. Ashcom, "The role of focusing in the interaction of femtosecond laser pulses with transparent materials," *Harvard Univeristy*, p. 158, 2003.

[134] E. Hecht, *Optics 4th edition*. 2001: Addison-Wesley.

[135] J. H. Marburger, "Self-focusing: Theory," in *IQEC, International Quantum Electronics Conference Proceedings*, 2005, vol. 2005, p. 1593.

[136] C. B. Schaffer, “Interaction of Femtosecond Laser Pulses with Transparent Materials,” no. May, p. 193, 2001.

[137] A. Gaeta, “Catastrophic Collapse of Ultrashort Pulses,” *Phys. Rev. Lett.*, vol. 84, no. 16, pp. 3582–3585, 2000.

[138] J. J. Sakurai, “Modern Quantum Mechanics,” *American Journal of Physics*, vol. 54. p. 668, 1986.

[139] S. C. Jones, P. Braunlich, R. T. Casper, X.-A. Shen, and P. Kelly, “Recent progress on laser-induced modifications and intrinsic bulk damage of wide-gap optical materials,” *Opt. Eng.*, vol. 28, no. 10, pp. 1039–1068, 1989.

[140] K. Mishima, M. Hayashi, J. Yi, S. Lin, H. Selzle, and E. Schlag, “Generalization of Keldysh’s theory,” *Physical Review A*, vol. 66, no. 3. p. 033401, 2002.

[141] P. Y. Yu and M. Cardona, *Fundamentals of Semiconductors*. 2010: Springer.

[142] E. G. Gamaly, A. V. Rode, B. Luther-Davies, and V. T. Tikhonchuk, “Ablation of solids by femtosecond lasers: Ablation mechanism and ablation thresholds for metals and dielectrics,” *Phys. Plasmas*, vol. 9, no. 3, p. 949, 2002.

[143] M. E. Fermann, A. Galvanauskas, and G. Sucha, *Ultrafast lasers - Technology and Applications*. 2003: CRC Press.

[144] J. I. Pankove and D. A. Kiewit, “Optical Processes in Semiconductors,” *J. Electrochem. Soc.*, vol. 119, no. 5, p. 156C, 1972.

[145] C. Schaffer, N. Nishimura, E. Glezer, A. Kim, and E. Mazur, “Dynamics of femtosecond laser-induced breakdown in water from femtoseconds to microseconds.,” *Opt. Express*, vol. 10, no. 3, pp. 196–203, 2002.

[146] M. Sakakura and M. Terazima, “Initial temporal and spatial changes of the refractive index induced by focused femtosecond pulsed laser irradiation inside a glass,” *Phys. Rev. B - Condens. Matter Mater. Phys.*, vol. 71, no. 2, 2005.

[147] E. N. Glezer, M. Milosavljevic, L. Huang, R. J. Finlay, T. H. Her, J. P. Callan, and E. Mazur, “Three-dimensional optical storage inside transparent materials.,” *Opt. Lett.*, vol. 21, no. 24, pp. 2023–2025, 1996.

[148] W. M. Steen and J. Mazumder, “Laser Welding,” in *Laser Material Processing*, vol. 22, no. 8, 2010, pp. 199–249.

[149] a. Mermillod-Blondin, I. Burakov, Y. Meshcheryakov, N. Bulgakova, E. Audouard, A. Rosenfeld, A. Husakou, I. Hertel, and R.

Stoian, “Flipping the sign of refractive index changes in ultrafast and temporally shaped laser-irradiated borosilicate crown optical glass at high repetition rates,” *Phys. Rev. B*, vol. 77, no. 10, p. 104205, 2008.

[150] R. Tadmor, “The London-van der Waals interaction energy between objects of various geometries,” *J. Phys. Condens. Matter*, vol. 13, no. 9, pp. L195–L202, 2001.

[151] I. Miyamoto, K. Cvecek, and M. Schmidt, “Crack-free conditions in welding of glass by ultrashort laser pulse,” *Opt. Express*, vol. 21, no. 12, pp. 14291–14302, 2013.

[152] T. L. Teng, P. H. Chang, and W. C. Tseng, “Effect of welding sequences on residual stresses,” *Comput. Struct.*, vol. 81, no. 5, pp. 273–286, 2003.

[153] A. Guevara-Morales and U. Figueroa-López, “Residual stresses in injection molded products,” *Journal of Materials Science*, vol. 49, no. 13. pp. 4399–4415, 2014.

[154] D. Ashkenasi, G. Müller, A. Rosenfeld, R. Stoian, I. V. Hertel, N. M. Bulgakova, and E. E. B. Campbell, “Fundamentals and advantages of ultrafast micro-structuring of transparent materials,” *Appl. Phys. A Mater. Sci. Process.*, vol. 77, no. 2003, pp. 223–228, 2003.

[155] T. G. Cowling, “Approximate theories of thermal diffusion,” *J. Phys. A Gen. Phys.*, vol. 3, no. 6, p. 774, 1970.

[156] K. I. Morozov, “Thermal diffusion in disperse systems,” *Journal of Experimental and Theoretical Physics*, vol. 88, no. 5. pp. 944–946, 1999.

[157] R. M. Carter, J. Chen, J. D. Shephard, R. R. Thomson, and D. P. Hand, “Picosecond laser welding of similar and dissimilar materials,” *Appl. Opt.*, vol. 53, no. 19, pp. 4233–4238, 2014.

[158] F. Zimmermann, S. Richter, S. Döring, A. Tünnermann, and S. Nolte, “Ultrastable bonding of glass with femtosecond laser bursts.,” *Appl. Opt.*, vol. 52, no. 6, pp. 1149–54, 2013.

[159] M. Ashby and D. Jones, *Engineering Materials 2: An Introduction to Microstructures and Processing and design*. 2012: Butterworth-Heinemann.

[160] S. G. Prolongo, G. Del Rosario, and A. Ureña, “Comparative study on the adhesive properties of different epoxy resins,” *Int. J. Adhes. Adhes.*, vol. 26, no. 3, pp. 125–132, 2006.

[161] D. Ivanov and L. Zhigilei, “Combined atomistic-continuum modeling of short-pulse laser melting and disintegration of metal films,” *Phys. Rev. B*, vol. 68, pp. 1–22, 2003.

[162] J. J. Witcher, W. J. Reichman, L. B. Fletcher, N. W. Troy, and D. M.

Krol, “Thermal annealing of femtosecond laser written structures in silica glass,” *Opt. Mater. Express*, vol. 3, no. 4, p. 502, 2013.

[163] K. Cvecek, R. Odato, S. Dehmel, I. Miyamoto, and M. Schmidt, “Gap bridging in joining of glass using ultra short laser pulses,” *Opt. Express*, vol. 23, no. 5, pp. 5681–5693, 2015.

[164] W. Chen and C. Nelson, “Thermal stress in bonded joints,” *IBM J. Res. Dev.*, 1979.

[165] V. Jain, A. Sidpara, R. Balasubramaniam, G. Lodha, V. Dhamgaye, and R. Shukla, “Micromanufacturing: A review--Part I,” *Proc. Inst. Mech. Eng. Part B J. Eng. Manuf.*, vol. 228, no. 9, pp. 973–994, 2014.

[166] E. McLeod and C. B. Arnold, “Multiscale bessel beams from tunable acoustic gradient index of refraction lenses,” in *Conference on Lasers and Electro-Optics, 2007, CLEO 2007*, 2007.

[167] “TAG lens.” [Online]. Available: http://www.tag-optics.com/. ©*2012 TAG Optics Inc*.

[168] M. Antelius, A. C. Fischer, F. Niklaus, G. Stemme, and N. Roxhed, “Hermetic integration of liquids using high-speed stud bump bonding for cavity sealing at the wafer level,” *J. Micromechanics Microengineering*, vol. 22, no. 4, p. 45021, 2012.

[169] S. Aono, K. Ohmori, M. Furuya, and T. Takakura, “Newly developed micro-parallel seam joining equipment and its applications,” *Yosetsu Gakkai Ronbunshu/Quarterly J. Japan Weld. Soc.*, vol. 7, no. 4, pp. 3–9, 1989.